Ph.D. Dissertation

On-line coupling of volcanic ash and aerosols transport with global and regional meteorological models

A thesis submitted to the Universitat Politècnica de Catalunya

in partial fulfillment for the degree of

Doctor of Philosophy

Alejandro Martí Donati

Director: Dr. Arnau Folch Duran - Barcelona Supercomputing Center (BSC)

Coordinator: Dr. Santiago Gassó Domingo - Universitat Politècnica de Catalunya (UPC)

Universitat Politècnica de Catalunya

Doctoral Program in Civil and Environmental Engineering

Barcelona, May 29, 2017

For my family, Laura and Paco…

“All models are wrong, some are useful.”

- G.P.E. Box (1992)

Acknowledgments

The research leading to these results has received funding from the European Union Seventh Framework Programme (FP7/2007-2013): People, ITN Marie Curie Actions Programme (2012-2016) under the project NEMOH (REA grant agreement n° 289976).

First of all, my sincerest gratitude to my Ph.D. supervisor, Dr. Arnau Folch, for his guidance and strong support during the project. The scientific advice and comments from Dr. Folch were key to making this project a success. I also want to thank Dr. Oriol Jorba for his support during the first stages of this project and for his help with the NMMB-MONARCH model. In addition, thanks to the Barcelona Supercomputing Center – Centro Nacional de Supercomputación (BSC-CNS), and the CASE director Dr. José Maria Cela, for hosting me during my Ph.D. thesis. Support provided by the BSC-CNS and associated staff was very helpful and appreciated. I also want to acknowledge the great work from all those researchers at the Earth Science Department at the BSC-CNS who have been involved in the development of the NMMB-MONARCH model prior to this thesis. Special thanks to Dr. Santiago Gassó and the staff at the "Unitat Doctorat - UTG Àmbit Camins" from the UPC for all their help in preparing and submitting my Ph.D. thesis. I would like to thank the BSC-CNS's Severo Ochoa mobility program for funding several of my research visits.

I would also like to thank those I had the pleasure and luck to work with in my secondment at the National Institute of Geophysics and Volcanology (Istituto Nazionale di Geofisica e Vulcanologia - INGV) in Italy. Special thanks go to Dr. Antonio Costa for giving me this opportunity and being my supervisor during this visit (*Anto, grazie mille per il tuo autentico tutoraggio e amicizia*). In that same context, I would like to thank the National Centers for Environmental Prediction (NCEP) in the U.S. for hosting me several times and for supporting the completion of this project. Additionally, my warmest thanks to Dr. Zavisa Janjic (and his wife Gordana) for his mentoring and priceless advice both at professional and personal level.

I would like to acknowledge all the co-authors of the publications written in the framework of this thesis, including: Dr. Arnau Folch, Dr. Antonio Costa, Dr. Samantha Engwell and the visualization team and the BSC-CNS for their incredible work in the Campanian Ignimbrite reconstruction; also Dr. Arnau Folch, Dr. Oriol Jorba and Dr. Zavisa Janjic for their massive support in developing NMMB-MONARCH-ASH; and Dr. Folch for the pioneering comparison between on-line and off-line models for volcanic ash. In that same context, it was a pleasure to collaborate with Dr. Adelina Geyer, Dr. Santiago Giralt and Dr. Arnau Folch in the promising work regarding the threat of Antarctic volcanoes; and with Mr. Matthieu Poret, Dr. Antonio Costa and Dr. Arnau Folch on the modeling work at Mt. Etna.

This Ph.D. was also possible thanks to the collaboration of many scientists from many different institutions, including Dr. Carlos Perez (NASA-GISS / BSC-CNS), Ms. Soledad Osores (Servicio Meteorológico de Argentina), Dr. Geoff DiMego (NCEP), Dr. João Zilhão (Universitat de Barcelona), Dr. Costanza Bonadonna (Université de Genève), Dr. Maria Gonçalves (BSC-CNS). In addition, my most sincere gratitude also goes for all the NEMOH staff: Dr. Paolo Papale (project coordinator), Raffaela Pignolo and Alessandro Fornaciai (project assistants) for their incredible mentoring and personal support; all the senior scientist and professors I was fortunate to work with and learn from; and, of course, the NEMOH fellows who made this training experience to be exceptionally fun. I would also like to express my gratitude to Dr. Francisco Artigas for all these years of mentoring and friendship (it's always good to remember where are you coming from...).

At the personal level, I would like to start by dedicating this work to my father, the reason why I started this journey and came back "home". I know that you are watching and this will make you smile. Also, to my family and especially to my grandmother (*yaya!*), who has always been a constant pillar in my life. To my uncles who stepped up when I needed them most. I would like to share this special moment with Laura and her family who have become part of my family and have encouraged me to see this project through – words don't come close to describe my gratefulness. To my four-legged friend Paco who, believe it or not, kept me sane during many difficult stages in the past few years. To my friends here in Spain and in the U.S.- it takes true friends to able to pick up our friendship like it was yesterday regardless how long it has been or how far away they live. To my co-workers and friends at the BSC-CNS, which I shared this Ph.D. journey with: thanks to Matias for all those talks at 8am at the gym and not letting me skip Thursdays; to Alfonso for being my roommate and not getting mad when I temporarily cancelled my subscription to your issues ;) ; to Jordi for still trying to convince me to start doing yoga; to Chiara for leading the way; to all the "pasto" folks for our conversations at lunch and outings together; to Mónica for helping me focus on the real objective till the end and for sharing your entrepreneurship mentality; to Mohammad, Dani and Abel for our many nights as "arraplegats"; to Simon for being "a nice French", to Maria for making me feel that I was a workaholic; to Guille and Fer for putting the magic in science; to Maria Cristina and Mónica M. for their nice non-Ph.D. conversations; to Margarida to be so calm all the time; to Laura G. for all her admin support, always accompanied with a smile; to the rest of the CASE group; to the night-security "dude" that made me feel as I wasn't alone at night while working late at the BSC… To all of you, thank you!

Abstract

Explosive volcanic eruptions can eject large quantities of particulate matter that, along with other aerosol droplets and trace gases, are carried upwards into the atmosphere by the buoyant eruption column and then dispersed by winds aloft. The presence of volcanic ash in the atmosphere is a sporadic yet important factor that can threaten human health, affect the urban built environment, disrupt aerial navigation and, for very large eruptions, alter both atmospheric composition and chemistry. Once volcanic ash is injected into the atmosphere, it can be transported over great distances, even circumnavigating the entire planet. Volcanic ash modeling systems are used to simulate the atmospheric dispersion of volcanic ash and to generate operational short-term forecasts to support civil aviation and emergency management. The efficiency of response and mitigation actions is directly associated to the accuracy of the volcanic ash cloud detection.

Volcanic ash modeling systems normally require an emission or source term model to characterize the eruption column; a dispersal model to simulate the atmospheric transport, dispersion and ground deposition of ash particles; and a meteorological model for the description of the atmospheric conditions. Traditional forecasts for volcanic ash build on off-line coupled modeling systems, where meteorological variables are only updated at the specified coupling intervals. Although this approach is computationally advantageous is some cases, there is a concern that it can lead to a number of accuracy issues and limitations that can be corrected by on-line modeling strategies. Despite these concerns, to date, no on-line coupled model is available for the operational forecast of volcanic ash. In addition, the quantification of the limitations associated to the off-line systems has received no attention.

This Ph.D. thesis describes and evaluates NMMB-MONARCH-ASH, a novel fully coupled on-line multiscale meteorological and atmospheric transport model designed to predict ash cloud trajectories, concentration of ash at relevant flight levels, and the expected deposit thickness for both regional and global domains in research and operational set-ups. The thesis document focuses on four main activities:

The first activity targeted a model validation against several well-characterized events including, the Mt. Etna 2001, Eyjafjallajökull 2010, and Cordón Caulle 2011 eruptions. The model has shown to be robust, scalable, and capable to reproduce the spatial and temporal dispersal variability of the ash cloud and tephra deposits, showing promising results and improving the performance from well-known off-line operational models.

The second activity quantified the model shortcomings and systematic errors associated to traditional off-line forecasts employed in operational set-ups. NMMB-MONARCH-ASH demonstrated that off-line forecasts could fail to reproduce up to 45-70% of the ash cloud of an on-line forecast, considered to be the

best estimate of the true outcome. The uncertainty associated to off-line systems was found to be as relevant (same order of magnitude) as those uncertainties attributed to the source term.

The third activity focused on a global application of NMMB-MONARCH-ASH to analyze the potential impacts of ash dispersal from Antarctic volcanoes. Numerical simulations suggested that volcanic ash emitted from Antarctic volcanoes could potentially encircle the globe, leading to significant consequences for global aviation safety.

The last activity included a novel computational inversion method to account, for the first time, for the Plinian and co-ignimbrite phases of the 39 ka Campanian Ignimbrite super-eruption. This particular application employed the off-line coupled FALL3D model, found to be more suitable from a computational point of view.

The outcome of this Ph.D. thesis encourages operational groups responsible for real-time advisories for aviation to consider employing computationally efficient on-line coupled dispersal models for volcanic ash.

Resumen

Las erupciones volcánicas explosivas pueden emitir una gran cantidad de material que, junto con otros aerosoles y gases traza, son inyectados en la atmósfera por la columna eruptiva para luego ser dispersados por los vientos en altura. La presencia en la atmósfera de cenizas volcánicas es un factor esporádico aunque importante, que puede llegar a amenazar la salud humana, afectar las infraestructuras urbanas, interrumpir la navegación aérea y, en el caso de grandes erupciones, alterar la composición atmosférica y química. Una vez inyectada en la atmósfera, la ceniza volcánica puede ser transportada a grandes distancias, llegando incluso a circunnavegar todo el planeta. Los sistemas de modelado de cenizas volcánicas se utilizan para simular la dispersión atmosférica de estas partículas, y para generar pronósticos operacionales a corto plazo empleados para dar soporte a la aviación civil y a la gestión de emergencias. La eficacia para responder a estos eventos y mitigar su potencial impacto está directamente asociada a la precisión de detección y simulación del transporte de las nubes de cenizas volcánicas.

Los sistemas de modelado de cenizas volcánicas normalmente requieren un modelo de emisión de partículas (o término fuente) para la caracterización de la columna eruptiva; un modelo de dispersión para la simulación del transporte atmosférico, la dispersión y la deposición de partículas de cenizas; y de un modelo meteorológico para la descripción de las condiciones atmosféricas. Los pronósticos tradicionales de ceniza volcánica se basan en sistemas de modelado desacoplados (*off-line*), donde las variables meteorológicas sólo se actualizan a intervalos de tiempo especificados. Aunque este enfoque presenta ventajas desde el punto de vista computacional, existe la preocupación de que puede estar asociado a una serie de limitaciones y problemas de precisión que, por el contrario, pueden ser corregidos mediante estrategias de modelado acoplado (*on-line*). A pesar de estas preocupaciones, hasta la fecha no hay un modelo acoplado *on-line* disponible para el pronóstico operativo de las cenizas volcánicas. Además, tampoco existe una cuantificación de las limitaciones asociadas a los sistemas *off-line*.

Este doctorado describe y evalúa NMMB-MONARCH-ASH, un modelo de transporte meteorológico y atmosférico multiescalar (regional/global) completamente acoplado *on-line*, para su uso en investigación y servicios de predicción operacional. El modelo está diseñado para predecir trayectorias de nubes de cenizas volcánicas, concentración de ceniza en niveles de vuelo (*flight levels*) relevantes, y el correspondiente espesor de depósito. El documento de doctorado se centra en cuatro actividades principales:

La primera actividad de esta tesis se centra en la validación de modelo mediante varias erupciones bien caracterizadas. Estas incluyen las erupciones del Mt. Etna 2001, Eyjafjallajökull 2010, y del Cordón Caulle 2011. El modelo ha demostrado ser robusto, escalable y capaz de reproducir la variabilidad de la

dispersión espacial y temporal de los depósitos y de las nubes de ceniza, mostrando resultados prometedores y mejorando el rendimiento de modelos operacionales como el FALL3D.

La segunda actividad cuantifica las deficiencias y errores sistemáticos asociados a los pronósticos *off-line* tradicionalmente empleados en configuraciones operacionales. NMMB-MONARCH-ASH demuestra que los pronósticos *off-line* podrían no reproducir hasta un 45-70% de la nube de cenizas de un pronóstico on-line, considerado éste último como la mejor estimación de la realidad. Esta actividad concluye que la incertidumbre asociada a los sistemas *off-line* puede llegar a ser en algunos casos tan relevante (mismo orden de magnitud) como aquellas incertidumbres atribuidas al término fuente.

La tercera actividad se centra en una aplicación global de NMMB-MONARCH-ASH para analizar los posibles impactos de la dispersión de cenizas asociado a los volcanes antárticos. Las simulaciones numéricas sugirieren que las cenizas volcánicas emitidas por estos volcanes pueden llegar a rodear el globo, conduciendo a consecuencias significativas para la seguridad de la aviación a nivel mundial.

La última actividad incluye un nuevo método de inversión computacional para identificar, por primera vez, las fases Pliniana y co-ignimbrita de la super-erupción de la Ignimbrita Campaniana (39 ka). Para esta aplicación, se empleó el modelo FALL3D off-line, que resultó ser más adecuado desde un punto de vista computacional.

El resultado de este Ph.D. anima a los grupos operacionales responsables de dar soporte al sector de la aviación durante una erupción, a considerar el uso de modelos eficientes de dispersión acoplados on-line para las cenizas volcánicas.

Publications derived from thesis

International Journals Included in the Science Citation Index (SCI):

1. **Marti, A**., Folch, A., Costa, A., Engwell, S. Reconstructing the plinian and co-ignimbrite sources of large volcanic eruptions: A novel approach for the Campanian Ignimbrite. *Sci. Rep.* **6**, 21220; doi: 10.1038/srep21220, 2016.
2. **Marti, A.,** Folch, A., Jorba, O., and Janjic, Z.: Volcanic ash modeling with the online NMMB-MONARCH-ASH v1.0 model: model description, case simulation, and evaluation, Atmos. Chem. Phys., 17, 4005-4030, doi:10.5194/acp-17-4005-2017, 2017.
3. **Marti, A.,** Folch, A.: Volcanic ash modeling with the NMMB-MONARCH-ASH model: quantification of off-line modeling errors, Atmos. Chem. Phys. Discuss., doi:10.5194/acp-2017-354, 2017.
4. **Marti, A.:** Volcanic ash modeling with the on-line NMMB-MONARCH-ASH model: model description, applications, and quantification of off-line modeling errors, *in review*.
5. Geyer, A., **Marti, A**., Giralt, S., Folch, A.: Antarctic volcanoes: A remote but significant hazard. Sci. Rep., *submitted.*
6. Poret, M., Costa, A., Folch, A., **Marti, A**.: Modeling tephra dispersal and ash aggregation: 26 April 1979 eruption, La Soufrière St. Vincent, J Volcanol Geotherm Res., *submitted*.

International conference proceedings and workshops:

1. Geyer, A., **Marti, A**., Giralt, S., Folch, A.: Antarctic volcanoes: A remote but significant hazard, Geophysical Research Abstracts Vol. 19, EGU General Assembly 2017, EGU2017-6667, Vienna, Austria.
2. **Marti, A**., De Mier, M.: SOlutions in Real-Time for air traffic management: A case for ash and dust flight conditions. Electronic Flight Bag Users Forum, EFB2016-S2P4, Munich, Germany, 2016.
3. **Marti, A**., Folch, A., Jorba, O., Janjic, Z.: Volcanic ash modeling with the online NMMB/BSC-ASH-v1.0: A novel multiscale meteorological model for operational forecast, Geophysical Research Abstracts Vol. 18, EGU General Assembly 2016, EGU2016-927, Vienna, Austria.
4. **Marti, A**.: The NMMB/BSC-ASH: description and results. The second NOAA Nonhydrostatic Multiscale Model on the B-grid (NMMB) Workshop. U.S. National Centers for Environmental Prediction, 2016.

5. **Marti, A**., Folch, A., Costa, A. and Engwell, S.: Reconstructing the volume and tephra dispersal for each phase of the Campanian Ignimbrite super-eruption, Geophysical Research Abstracts Vol. 17, EGU General Assembly 2015, EGU2015-11244-2, Vienna, Austria.
6. **Marti, A**., Folch, A., Costa, A. and Engwell, S.: Plinian and co-ignimbrite phases of the Campanian Ignimbrite super-eruption, 26th International Union of Geodesy and Geophysics, General Assembly, IUGG2015-VS17, Prague, Czech Republic, 2015.
7. **Marti, A**., Folch, A., Costa, A. and Engwell, S.: A novel approach to reconstruct the plinian and co-ignimbrite phases of large eruptions - Campanian Ignimbrite, 2nd International BSC Doctoral Symposium 2015, Conference proceedings, page 81, Barcelona, Spain, 2015.
8. **Marti, A**., Folch, A., Jorba. O.: On-line coupling of volcanic ash and aerosols transport with multiscale meteorological models, Geophysical Research Abstracts Vol. 16, EGU General Assembly 2014, EGU2014-12834, Vienna, Austria, 2014.
9. **Marti, A**., Folch, A., Jorba. O.: A new approach for the transport and sedimentation of volcanic particles. Cities on Volcanoes - International Association of Volcanology and Chemistry of the Earth's Interior (IAVCEI), Jakarta, Indonesia, 2014.
10. **Marti, A**.: A Development of on-line meteorological models for the dispersion of volcanic aerosols. Severo Ochoa Seminars, 2014.
11. **Marti, A**., Folch, A., Jorba. O.: Coupling TTDMs on-line with meteorological models. 2nd IUGG-WMO Workshop on Ash Dispersal Forecast and Civil Aviation, Geneva, Switzerland, 2013.
12. **Marti, A**., Folch, A., Jorba. O.: On-line coupling of volcanic ash and aerosols transport with multiscale meteorological models. International Association of Volcanology and Chemistry of the Earth's Interior. IAVCEI General Assembly, Kagoshima, Japan, 2013.

NEMOH-related presentations and reports:

1. **Marti, A**.: NEMOH final report: Results from three years of research as an ESR within the Numerical, Experimental and stochastic Modeling of vOlcanic processes and Hazard project (NEMOH), Catania, Italy, 18th November 2015.
2. **Marti, A**., Folch, A., Jorba. O.: Progress on NMMB-BSC/ASH. NEMOH Workshop Dublin: Inverse methods in geophysics and volcanology, Dublin, Irland, 2014

1. **Marti, A**.: NEMOH Mid-Term Review: Preliminary results as a NEMOH ESR, Rome, Italy, 18th October 2013.

Table of contents

List of figures

List of Tables

List of acronyms

ADS	**A**dvection**–D**iffusion**–S**edimentation
AMS	**A**merican **M**eteorological **S**ociety
AOD	**A**erosol **O**ptical **D**epth
ATM	**A**ir **T**raffic **M**anagement
BSC-CNS	**B**arcelona **S**upercomputing **C**enter – **C**entro **N**ational de **S**upercomputación
CTM	**C**hemical **T**ransport **M**odel
DRE	**D**ense **R**ock **E**quivalent
ECMWF	**E**uropean **C**entre for **M**edium-**R**ange **W**eather **F**orecasts
EPA	**E**nvironmental **P**rotection **A**gency
ESMF	**E**arth **S**ystem **M**odeling **F**ramework
ESP	**E**ruption **S**ource **P**arameter
GCM	**G**lobal **C**limate **M**odels
IAVW	**I**nternational **A**irways **V**olcano **W**atch
INGV	**I**stituto **N**azionale di **G**eofisica e **V**ulcanologia
IUGG	**I**nternational **U**nion of **G**eodesy and **G**eophysics
JMA	**J**apanese **M**eteorological **A**gency
LES	**L**arge **E**ddy **S**imulations
MER	**M**ass **E**ruption **R**ate
MPI	**M**essage **P**assing **I**nterface
MER	**M**ass **E**ruption **R**ate
MONARCH	**M**ultiscale **O**n-line **N**onhydrostatic **A**tmosphe**R**e **CH**emistry model
NASA	**N**ational **A**eronautics and **S**pace **A**dministration
NAM	**N**orth **A**merican **M**esoscale
NBL	**N**eutral **B**uoyancy **L**evel
NCEP	**N**ational **C**enters for **E**nvironmental **P**rediction
NEMS	**N**OAA **E**nvironmental **M**odeling **S**ystem
NEMOH	**N**umerical, **E**xperimental and stochastic **M**odeling of v**O**lcanic processes and **H**azard
NMMB	**N**on-hydrostatic **M**ultiscale **M**odel on a **B** grid
NOAA	**N**ational **O**ceanic and **A**tmospheric **A**dministration
NPWM	**N**umerical **W**eather **P**rediction **M**odel
PBL	**P**lanetary **B**oundary **L**ayer
RAM	**R**andom-**A**ccess **M**emory
RRTM	**R**apid **R**adiative **T**ransfer **M**odel
SMN	**S**ervicio **M**eteorológico **N**acional (Argentina)
SDS-WAS	**S**and and **D**ust **S**trom **W**arning Advisory and **A**ssessment **S**ystem
SSA	**S**tratospheric **S**ulfate **A**erosol
TDM	**T**ransport and **D**ispersion **M**odels
TGSD	**T**otal **G**rain **S**ize **D**istribution

TKE	**T**urbulent **K**inetic **E**nergy
TTDM	**T**ephra **T**ransport and **D**ispersion **M**odel
USGS	**U**nited **S**tates **G**eological **S**urvey
VAA	**V**olcanic **A**sh **A**dvisory
VAAC	**V**olcanic **A**sh **A**dvisory **C**enter
VAG	**V**olcanic **A**sh **G**raphic
VATDM	**V**olcanic **A**sh **T**ransport and **D**ispersal **M**odel
VIIRS	**V**isible **I**nfrared **I**maging **R**adiometer **S**uite
WRF	**W**eather **R**esearch and **F**orecast model

*other specific symbols are defined in the text.

Introduction

Background

Explosive volcanic eruptions can eject large quantities of particulate matter (tephra) that, along with other aerosol droplets and trace gases, are carried upwards into the atmosphere by the buoyant eruption column and then dispersed downstream by winds aloft (e.g. Sparks et al., 1997). Tephra particles smaller than 2 mm in diameter, technically defined as volcanic ash (Schmid, 1981), can spread over large distances away from the source forming ash clouds that jeopardize air traffic (Casadevall, 1993), airports (Guffanti et al., 2009) and, for very large eruptions, alter both atmospheric composition and chemistry (Myhre et al., 2013; Self, 2006). The recent eruptions of Eyjafjallajökull (Iceland) in 2010 and Cordón Caulle (Chile) in 2011 have reinforced the importance of volcanic ash dispersal in the context of global aviation safety. Particularly, the former event prompted a rapid change in the management of hazards to aviation from volcanic ash clouds, triggered by the use of safety concentration thresholds for flight. In addition, these eruptions have driven the improvement of volcanic ash detection and forecasting techniques that allow Volcanic Ash Advisory Centers (VAACs) to issue more accurate advice to aviation authorities.

Volcanic ash modeling systems are used to simulate the atmospheric transport, dispersion and ground deposition of tephra, and to generate operational short-term forecasts to support civil aviation and emergency management. Conventionally, these modeling systems require of: i) a source term model to characterize the emission of ash depending on the so-called Eruption Source Parameters (ESPs); ii) a Numerical Weather Prediction Model (NWPM) for the description of the atmospheric conditions, and; iii) a Volcanic Ash Transport and Dispersal Model (VATDM) to forecast the particle transport and deposition mechanisms. These systems are vital during efforts to prevent aircraft flying into ash clouds, which could result in catastrophic impacts (Miller and Casadevall, 2000). In addition, other model applications include the reconstruction of past eruptive events, probabilistic hazard assessments or simulation of recent eruptions for model evaluation purposes.

Traditionally, VATDMs have evolved decoupled (off-line) from the driving NWPM. In an off-line modeling system, the NWPM runs *a priori* and independently from the VATDM to produce the required meteorological fields at regular time intervals (e.g. every 1 or 6 hours for typical mesoscale and global operational NWPM outputs and reanalysis data, respectively). Meteorological fields are then furnished to the VATDM, which commonly assumes constant values for these fields during each time coupling interval or, at most, performs a linear interpolation in time. This approach is convenient in terms of computing time because different VATDM executions are possible without re-running the meteorological component, e.g. to update the source term whenever the eruption conditions vary, for inverse modeling of ash emissions (Marti et al., 2016; Webster et al., 2012), or to perform an ensemble forecast (e.g. Galmarini et al., 2010) in which all the ensemble members share the same meteorological conditions.

However, off-line systems introduce model and numerical errors due to non-synchronized time stepping, use of unaligned grids and projections, and/or inconsistencies in the numerical schemes. In contrast, in an on-line coupled system, the NWPM and the VATDM run concurrently and consistently and the particle transport is automatically tied to the model resolution time and space scales. This strategy results in a more realistic particle dispersal representation as highlighted by the experience from other communities (e.g. air quality; Baklanov, 2014; Zhang, 2008).

Despite these experiences, to date, all operational ash forecast systems follow the off-line modeling approach. However, the increase of computational power in recent years and the fact that the total computing time required to run an on-line coupled model is actually not substantially larger (e.g. Grell and Baklanov, 2011; Marti et al., 2017), imply that the benefits of the traditional off-line systems are at question. Seemly, it is also surprising that the quantification of modeling errors and shortcomings associated to the off-line coupling strategy has received no attention in volcanology despite the lessons learned from other communities.

Motivation and context of the Ph.D.

This research project aims to implement a fast and reliable on-line meteorological and atmospheric transport model to pioneer research and operational forecast of volcanic ash. Three primary questions are raised to motivate this research line:

I. What are the best available models for volcanic ash operational forecast?

II. How can we improve the accuracy of traditional off-line modeling systems for volcanic ash?

III. What are the advantages of the on-line coupled chemistry transport models over traditional off-line modeling systems for volcanic ash?

In order to answer these questions, this research project is separated into three main areas. The first area explores and validates the traditional off-line approach assumed by all operational volcanic ash dispersion models. The second area focuses on the implementation of a novel on-line modeling system to pioneer the future operational forecast of volcanic ash. The final research area evaluates the differences between the traditional off-line and the novel on-line modeling strategies for volcanic ash forecast. In the context of these research areas, the three main objectives proposed for this Ph.D. thesis are:

1. Investigate the VATDMs currently available and select a suitable model to be coupled on-line with the Non-hydrostatic Multiscale Model on a B grid (NMMB) meteorological model.

2. Implement and evaluate NMMB-MONARCH-ASH: a fast and reliable on-line meteorological and atmospheric transport model to pioneer research and operational forecast for volcanic ash.

3. Quantify the systematic errors and shortcomings associated to traditional off-line modeling systems employed for operational volcanic ash forecast.

To achieve these and other objectives, the author of this thesis was funded as an Early Stage Researcher at the Barcelona Supercomputing Center for a period of 36 months under NEMOH: an Initial Training Network in the framework of the European Community FP7 Marie-Curie Programme. The objective of this Marie-Curie ITN was to form the next generation of European volcanologists, capable of extending further the knowledge and understanding of volcano dynamics and the methods and paradigms for volcanic hazard evaluation. As a Marie-Curie fellow, Alejandro Martí was hosted for a three month-long international secondment from the 1st of June to the 1st of September 2014 at the Geophysical Fluid Dynamics unit of the Istituto Nazionale di Geofisica e Vulcanologia (INGV) in Bologna, Italy. The main objective of the secondment was to carry out research activities under the supervision of Dr. Antonio Costa in the field of numerical modeling of volcanic ash and aerosols. During the secondment, a novel computational approach was developed to reconstruct, for the first time, the duration and contribution of the two phases of the Campanian Ignimbrite super-eruption. The primary contribution from this secondment included the publication of this novel computational approach on *Scientific Reports* journal form the publishers of *Nature* (see Chapter 5 for detailed description of data, methodology, and results from this study).

Organization of the Ph.D. thesis

This **Introduction** sets the background, the motivation and the structure of the Ph.D. thesis. Airborne volcanic ash presents a well-publicized threat to aviation, health, and agriculture. In consequence, a central goal of volcano science is focused on volcanic ash, including both its atmospheric transport during a volcanic crises and its eventual deposition over the ground and sea. The state of the science has advanced rapidly, in large part due to the interest generated by the high economic cost and the disruptions caused to aviation stakeholders by the 2010 Eyjafjallajökull eruption in Iceland and the 2011 Cordón Caulle eruption in Chile. On the scientific front, these events have prompted a notable increase in volcanic-cloud research. A burst of scientific articles have been published, including special journal issues (e.g. Hasager et al., 2010; Langmann et al., 2012). Despite this significant progress, to date, no operational on-line coupled dispersal model is available to forecast volcanic ash. In light of the above, the objective of this Ph.D. thesis is to implement the NMMB-MONARCH-ASH model: a fast and reliable on-line meteorological and atmospheric transport model to pioneer research and operational forecast for volcanic ash.

Chapter 1 summaries the scientific context of this Ph.D. thesis. The chapter starts with a general introduction about volcanic ash and its properties, leading to a comprehensive description of the meteorological and atmospheric transport components typically employed in a volcanic ash modeling

system. This description gives way to a historical evolution and recent developments of the transport and dispersal models conventionally used to simulate the atmospheric transport, dispersion and ground deposition of volcanic ash. The operational FALL3D dispersal model is selected for extensive review, and it is designated as the VATDM model to be embedded in the Multiscale Online Nonhydrostatic AtmospheRe CHemistry model (NMMB-MONARCH; formerly known as NMMB/BSC-CTM). To conclude, this chapter discusses the advantages and limitations of traditional off-line modeling systems, and highlights the benefits of using on-line strategies reported by other communities (e.g. air quality, climate) and their current state-of-the-art.

Chapter 2 describes and evaluates NMMB-MONARCH-ASH, a new on-line multi-scale meteorological and transport model that attempts to pioneer the forecast of volcanic aerosols at operational level. The model forecasts volcanic ash cloud trajectories, concentration of ash at relevant flight levels and the expected deposit thickness. The ash module coupling in NMMB-MONARCH-ASH can be turned on or off, depending on the solution required (on-line vs. off-line). The regional and global configurations of the model are validated against two well-characterized events (2011 Cordón Caulle and 2001 Mount Etna eruptions). The numerical performance of the model is calculated in terms of its parallel speed-up and its scaling efficiency. The computational efficiency of NMMB-MONARCH-ASH and its application results compare favorably against other long-range tephra dispersal models (FALL3D), supporting its operational implementation.

Chapter 3 employs the coupling strategies available in the NMMB-MONARCH-ASH model presented in **Chapter 2** to quantify the systematic errors and shortcomings associated to traditional off-line modeling systems by employing different quantitative and categorical evaluation scores. The skills of the off-line coupling strategy are compared against those from an on-line forecast considered to be the best estimate of the true outcome. Case studies are considered for a synthetic eruption with constant eruption source parameters and for two historical events, which suitably illustrate the severe aviation disruptive effects of European (2010 Eyjafjallajökull) and South-American (2011 Cordón Caulle) volcanic eruptions. Evaluation scores indicate that systematic errors credited by off-line modeling can be of the same order of magnitude that those associated to the source term uncertainties. In particular, traditional off-line forecasts employed in operational model setups can result in significant uncertainties, failing to reproduce, in the worst cases, up to 45-70% of the ash cloud of an on-line forecast. These inconsistencies are anticipated to be even more relevant in scenarios where the meteorological conditions change rapidly in time. The outcome of this chapter encourages operational groups responsible for real-time advisories for aviation to consider employing computationally efficient on-line dispersal models or, at least, short coupling intervals ($\leq$ 1h).

Chapter 4 presents a global application of the on-line coupled NMMB-MONARCH-ASH model to analyze the potential impacts of ash dispersal and fallout from Antarctic volcanoes. The chapter focuses on Deception Island as a case study, one of the most active Antarctic volcanoes with multiple eruptions in the last 10,000 years. Numerical simulations using NMMB-MONARCH-ASH demonstrate that volcanic ash emitted from Antarctic volcanoes could potentially encircle the globe, leading to significant consequences for global aviation safety. Results obtained in this chapter recall the need to perform a proper hazard assessment on Antarctic volcanoes, and are crucial to understanding the patterns of ash distribution at high southern latitudes with strong implications for tephrostratigraphy, pivotal to synchronize palaeoclimatic records.

Chapter 5 presents a particular application where employing off-line coupled modeling systems is recommended from a computational point of view. This chapter employs a computational inversion method that explicitly accounts, for the first time, for the Plinian and co-ignimbrite phases of the 39 ka Campanian Ignimbrite (CI) super-eruption, the largest volcanic eruption of the past 200 ka in Europe. In addition, this chapter also evaluates the effect of gravitational spreading of the umbrella cloud by coupling FALL3D (introduced in **Chapter 2**) with a model that accounts for the gravity-driven transport in the umbrella cloud. To verify the consistency of the novel two-phase reconstruction, an additional single-phase inversion was performed using an independent thickness dataset. The better-fitting two-phase model suggests a higher mass eruption rate than previous studies, and estimates that 3/4 of the total fallout volume is co-ignimbritic in origin. Gravitational spreading of the umbrella cloud dominates tephra transport only within the first hundred kilometers due to strong stratospheric winds in the best-fit wind model. Finally, tephra fallout impacts would have interrupted the westward migration of modern human groups in Europe, possibly supporting the hypothesis of prolonged Neanderthal survival in South-Western Europe during the Middle to Upper Palaeolithic transition.

Chapters 3, 4 and **5** are presented in a similar form as they have been published or submitted to an international SCI journal and include their own introduction, specific methodology, results, discussion and conclusions. Because part of the methodological aspects and data are common in different chapters, some adjustments have been performed with respect to the journal version in order to avoid unnecessary repetitions. However, there is still some overlap between the introductive sections for some chapters, with the objective that each chapter has a comprehensive background and can be read independently from the rest of the thesis. **Chapter 6** includes the main harmonized conclusions of this thesis, and the recommendations for future research considering the specific conclusions exposed in **Chapters 3**, **4** and **5**. Finally, all references are compiled at the end of this thesis.

Research at the Barcelona Supercomputing Center

The research leading to this work has been carried at the Barcelona Supercomputing Center – Centro Nacional de Supercomputación (BSC-CNS) Computer Applications in Science and Engineering (CASE) Department in the capacity of an Early-Stage Researcher within the framework of the NEMOH-ITN: an Initial Training Network under the European Community FP7 to train the next generation of European volcanologists.

This research builds on the work of two BSC-CNS in-house models:

i. The Multiscale On-line Nonhydrostatic AtmospheRe CHemistry model (NMMB-MONARCH; formerly known as NMMB/BSC- CTM; Badia et al., 2017a; Haustein et al., 2012; Jorba et al., 2012; Pérez et al., 2011; Spada et al., 2013, 2015), an on-line chemical weather prediction system conceived for both the regional and the global scale. The model is developed and maintained by the Earth Sciences Department at the BSC-CNS.

ii. The FALL3D model, a 3-D time-dependent Eulerian model for the transport and deposition of volcanic ash and lapilli (Costa et al., 2006; Folch et al., 2009). The model is developed and maintained by the Computer Applications in Science and Engineering at the BSC-CNS in collaboration with the INGV.

Numerical simulations included in this thesis were performed at the Barcelona Supercomputing Center with the MareNostrum III Supercomputer using 8x4 GB DDR3-1600 DIMMS (2GB/core) Intel Sandy Bridge processors, iDataPlex Compute Racks, a Linux Operating System, and an InfiniBand interconnection.

Chapter 1

1 SCIENTIFIC CONTEXT

1.1 General introduction to volcanic ash

There are numerous excellent volcanological resources on volcanic ash and its properties, including Heiken's (1974) classic Atlas of Volcanic Ash and two data-rich textbooks from the 80's: Fisher and Schmincke's (1984) *Pyroclastic Rocks* and Cas and Wright's (1987) *Volcanic Successions: Modern and Ancient.* More recently, Mackie et al. (2016) provided a comprehensive overview on the volcanic ash formation, its physical characteristics, and spatial variations in ash properties within a range of volcanic deposits. The effects of volcanic ash on the global environment have also been recently described by Schmidt et al. (2015). The objective of this section is to provide a general introduction to volcanic ash, its transport and the associated impact on air traffic management.

The term volcanic ash refers strictly to all particles ejected by an explosive eruption that are 2 mm or less in diameter, regardless of its composition. It is thus a subset of the entire population of fragmented or eroded (clasts) particles produced by an explosive volcanic eruption, material that is broadly termed tephra, a collective term for pyroclasts derived from a Greek term used by Aristotle for volcanic ash. This work follows this convention and uses the term "tephra" when referring to the entire ensemble of explosively erupted particles, and "ash" when referring specifically to the small size fraction. Thorarinsson (1944) classified, for the first time, tephra particles according to their size as: volcanic bombs or blocks, lapilli, coarse ash, and fine ash (Figure 1).

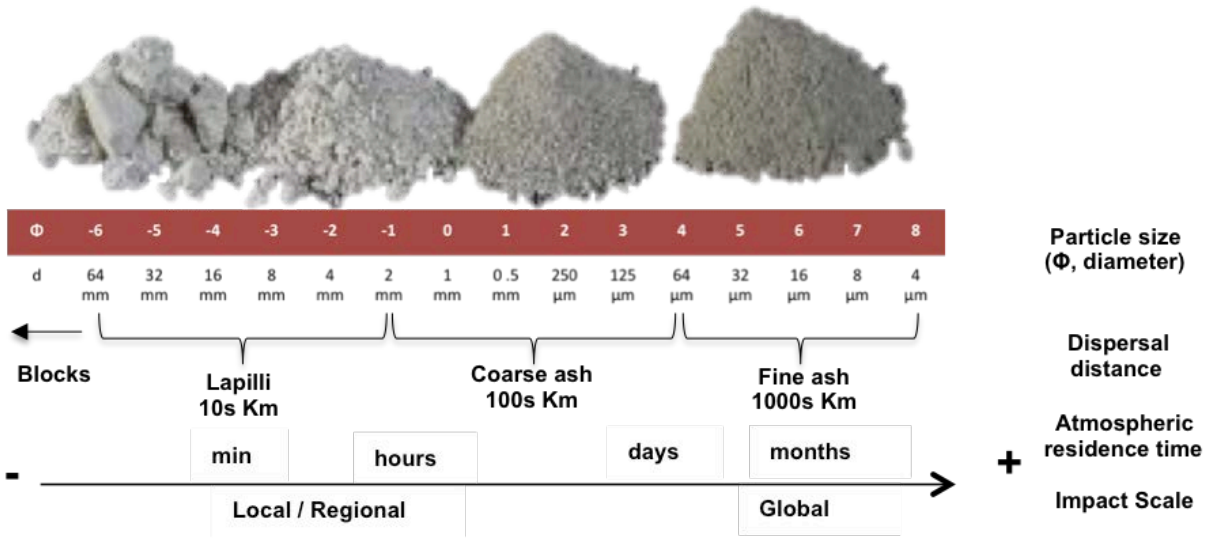

Figure 1. Tephra particle size representation: volcanic bombs or blocks ($\boldsymbol{d \geq 64}$mm or $\boldsymbol{\Phi \leq -6}$), lapilli ($\boldsymbol{2}$mm $\boldsymbol{\leq d < 64}$mm or $\boldsymbol{-1 \geq \Phi > -6}$), coarse ash ($\boldsymbol{64}$ µm $\boldsymbol{\leq d <}$ 2mm or $\boldsymbol{4 \geq \Phi > -1}$), and fine ash ($\boldsymbol{d < 64}$µm or $\boldsymbol{\Phi > 4}$), where $\boldsymbol{d}$ is the diameter of the particle and $\boldsymbol{\Phi \equiv -log_2 d}$ (mm).

Juvenile tephra forms when magma fragments during explosive eruptions. Fragmentation transforms magma from a continuous liquid phase with dispersed gas bubbles to a gas phase with dispersed magma fragments (Cashman and Rust, 2016). Once created, volcanic particles are transported within, and deposited from, hot plumes that rise up to tens of kilometers above the volcanic vent. Tephra deposits formed from volcanic plumes have spatial extents and thickness variations that reflect both eruption and transport conditions (Scollo et al., 2008). These deposits preserve information on the size and strength of the eruption.

The focus here, however, is on volcanic ash, which comes in many sizes, compositions, shapes, and densities and, as a result, has a wide range of optical characteristics and transport dynamics. This variability has important implications for detecting, tracking, and forecasting the behavior of ash transported within volcanic plumes. Particle size is the main parameter in controlling tephra sedimentation velocity; blocks and larger lapilli follow ballistic and non-ballistic trajectories settling in minutes to few hours near the volcano. In contrast, very fine ashes can remain entrapped at higher atmospheric levels for days to months and disperse at continental or even at global scales.

Once volcanic ash is injected into the atmosphere, it can be transported over great distances, even circumnavigating the entire planet, such as the Mt. Pinatubo eruption in 1991. Volcanic ash transport and dispersion models (VATDM) have been developed to comprehensively forecast volcanic ash clouds. A detailed description of the available VATDMs currently available is provided in Sect. 1.3. The primary users of these VATDMs are those stakeholders involved in the provision of operational forecast of the future trajectory of an ash cloud. These include, for example, those agencies involved in the International Airways Volcano Watch (IAVW), known as Volcanic Ash Advisory Centers (VAACs). In addition, VATDMs are also important for reconstructing ground deposit data after a volcanic eruption in an attempt to better understand the event and to provide new methods for improving the capabilities of the models for future use.

The presence in the atmosphere of volcanic ash is a sporadic yet important factor that can threaten human and animal health; affect the urban built environment; or disrupt aerial navigation. In addition, volcanic ash is a hazard to aircraft because it can degrade engine performance and navigational and operational instrumentation. For example, the presence of airborne volcanic ash at low and jet-cruise atmospheric levels compromises the safety of aircraft operations and forces re-routing of aircraft to prevent encounters with volcanic ash clouds. A full review on the influence of volcanic ash on aircraft engine components is provided by Chen and Zhao (2015), and a re-evaluation of the engine manufacturers ash concentration threshold for safe aircraft operation (‘Safe-to-Fly’ chart) was reported by Clarkson et al. (2016). Past events have shown the difficulty to access to atmospheric hazard dispersal information useful for Air Traffic Management (ATM). For example, due to the extent of the ash clouds generated by the 2010

Eyjafjallajökull volcano eruption in Iceland, more than 100,000 flights were cancelled and over 300 airports in about two-dozen countries, and a correspondingly large airspace, were closed in Europe during 16-21 April. This disruption caused a loss of more than $1.7 billion USD airline revenues and more than 10 million stranded passengers according to an analysis by Oxford Economics.

1.2 Atmospheric transport models for volcanic ash

Atmospheric transport models are used to simulate the transport of particles and gases, comprising those of natural (e.g. volcanic particles and aerosols, mineral dust, sea salt), biogenic (e.g. biomass burning), and anthropogenic origin (e.g. aerosol and particulate matter pollutants, radionuclides). All models involve three different components (Russell and Dennis, 2000) regardless of the nature of the substance being transported (Fig. 2):

i. An emission or source term model, which describes the "release" of the airborne substance, both in time and space;
ii. A Numerical Weather Prediction Model (NWPM; also known as Meteorological Models), which describes the state and evolution of the atmosphere in which the emissions are introduced. Meteorological codes are classified based on their different spatial and temporal scales;
iii. A transport and dispersal model (TDM), which describes the substance transport and deposition mechanisms. TDMs require the definition of an additional source/sink term when particles experience transformations during transport (e.g. particle aggregation, chemical or photochemical reactions).

In particular, volcanic ash modeling systems are atmospheric transport models specifically employed to simulate the atmospheric dispersion of volcanic ash and to generate operational short-term forecasts to support civil aviation and emergency management. These systems require of: i) an eruption source term model to characterize the emission of ash depending on the so-called Eruption Source Parameters (ESPs); ii) a meteorological model (NWPM) for the description of the atmospheric conditions, and; iii) a Transport and Dispersal Model to forecast the particle transport and deposition mechanisms of volcanic ash. The accuracy of the model forecast is highly dependent on the input parameters to the model simulations, such as the accuracy of the meteorological data (wind, temperature, precipitation rate) and the determination of the emissions from the volcano (the source term). Models to simulate tephra dispersal in atmosphere are called Tephra Transport and Dispersal Models (TTDMs). TTDMs are often referred as Volcanic Ash Transport and Dispersal Models (VATDMs), which are actually a sub- group of TTDMs especially adapted to model volcanic ash (particles with 2mm or less in diameter).

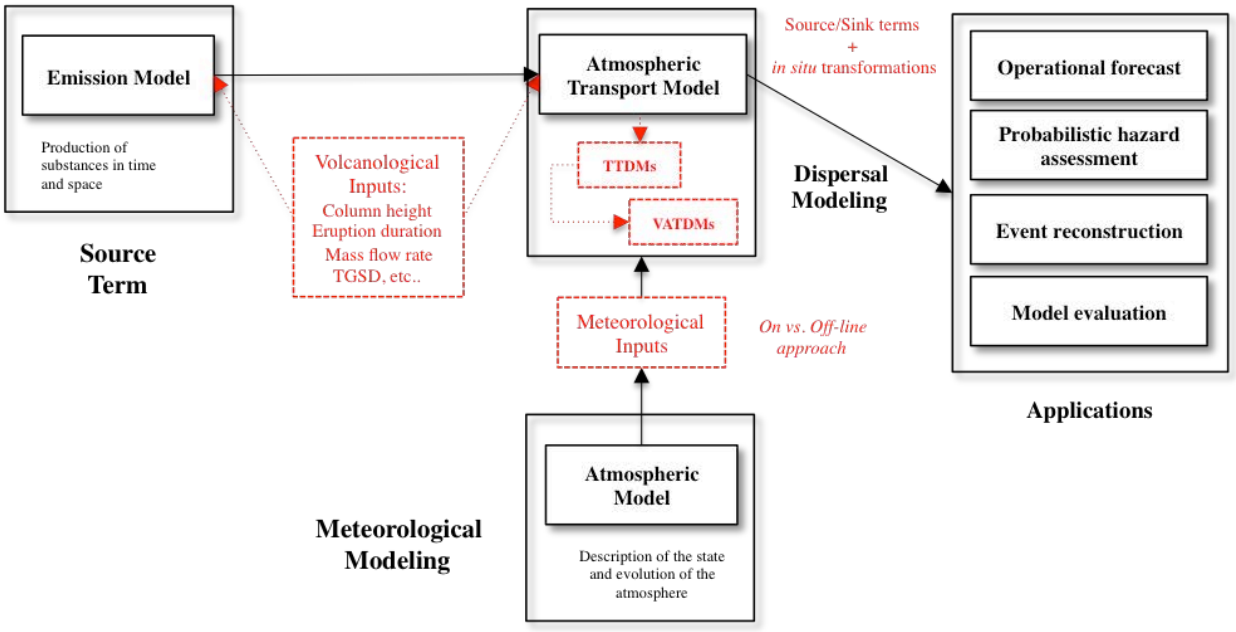

Figure 2. Schematic representation of the main components of an Atmospheric Transport Model. Red text shows model specifications for the transport of volcanic ash (modified from Marti et al., 2017).

The following sections provide a brief overview about the volcanological source term, describe different types of meteorological and atmospheric transport models, and discuss the possible NWPM-TDM coupling strategies.

1.2.1 Source term model

In general terms, the source model consists of a model for the eruption plume (or column; these terms are used interchangeably in this document), which furnishes the TTDM with a spatio-temporal distribution of particles (mass) along the eruption column. Source term models used by TTDMs may range from simple geometric distributions to complex multi-component and multi-phase flow models. To complete the volcanological characterization of the source term model, it is necessary to describe the parameters for the source term quantification, commonly known as Eruption Source Parameters (ESPs). These include the eruption start and duration, the determination of the eruption column height, the mass eruption rate (MER) and the total particle grain size distribution (TGSD). These parameters, not only vary from one eruption to another, but also during the different eruptive phases of a single event.

Strategies for quantifying these physical parameters may differ whether they are estimated in real time or a posteriori implying, therefore, different uncertainty levels. On one end, real-time dispersal forecasts employ a combination of geophysical and modeling strategies to define ESPs parameters with different application limits and resolutions. On the other end, the a posteriori ESP definition relies on the exhaustive study of tephra deposits and provides probability density functions for selected activity scenarios. These outputs are used both to compile long-term hazard assessments, and to help with preliminary real-time simulations of dispersal forecasting when no real-time data are available. Typically,

the eruption starting time, duration and column height are inferred/constrained in real-time from visual (direct ground observation or Pilot reports; not accurate for large columns), ground-based instrumentation (e.g. C-band weather radar, transportable X and L-band radars, lidars, thermal cameras, etc.), or satellite observations. Model input values for MER are commonly inferred from column height. A common option is to use field-based relationships between column height and averaged MER (e.g. Mastin et al., 2009; Sparks et al., 1997). However, such estimations can have up to a factor 10 of uncertainty. Recent studies have shown the importance of accounting for wind effects in the determination of MER using either numerical models or analytical relationships (Bursik, 2001; Degruyter and Bonadonna, 2012;Woodhouse et al., 2013). A comprehensive description of the most relevant source term parameterizations is presented in Section 2.2.3.1. Finally, the total grain size distribution (TGSD) of particles ejected by the source term is normally reconstructed from tephra deposits using both field studies and numerical inversion strategies. It is important to mention that, to date, no real-time technique is capable to provide the erupted mass associated with the whole particle size's spectrum.

For those eruptive events where ESPs are not readily available, model inputs must be inferred from previous events of similar characteristics. Mastin et al. (2009) compiled an ESP database with information on volcanoes around the world including the vent location (latitude, longitude and height) and the corresponding ESPs for the eruptive events associated to each volcano. Finally, for ancient eruptions, where ESPs are not available, values can be estimated from tephra deposits (e.g. Carey and Sparks, 1986; Pyle, 1989) or by best-fitting tephra deposit by means of inverse modeling techniques (e.g. Connor and Connor, 2006; Costa et al., 2012; Marti et al., 2016).

1.2.2 Meteorological model classification

Meteorological phenomena occur over a wide range of space and time scales. Based on its scale resolution, meteorological models can be classified from global, to meso- to microscale. As defined in the American Meteorological Society's (AMS) *Glossary of Meteorology*, mesoscale models include domains ranging from ~100 to 2000 kilometers, and typically use structured rectilinear mesh with nested grids and finite-difference methods in all three dimensions. Horizontal grid cell sizes may range from few to tens of kilometers, while vertical resolution may be of the order of meters near the surface and stretch to hundreds of meters or more above the boundary layer. Operational mesoscale models are typically run by National Weather Services for their region of interest. Examples include NMMB (Janjic, 2005, 2009; Janjic and Gall, 2012), WRF-NMM (Skamarock et al., 2008), or WRF-ARW (Michalakes et al., 2000). Global models, on the other end, cover the entire Earth and often use spectral methods for the horizontal dimensions and finite-difference methods for the vertical dimension. For forecasting purposes, the most utilized global models are the Global Forecast System (GFS; Kalnay et al., 1990), the Integrated Forecast System (IFS; Michalakes et al., 2000) or the JMA Global Spectral Model (GSM), run by the National Oceanic and Atmospheric Administration (NOAA), the European Centre for Medium-Range Weather

Forecasts (ECMWF), and the Japanese Meteorological Agency (JMA), respectively. All systems can run operationally or as members of an ensemble of meteorological models, and provide daily forecasts and reanalysis datasets.

1.2.3 Transport model classification

Atmospheric transport models are classified as Eulerian, Lagrangian or Gaussian-puff models, based on the way they solve the advection, diffusion, and sedimentation processes. Eulerian models numerically solve the discretized version of the Advection–Diffusion equation at specific reference points in a gridded system using finite differences or finite elements. Eulerian solvers can be adapted to account for deposition, agent decay, and gravitational settling by solving the Advection–Diffusion–Sedimentation (ADS) equation. Multiple equations need to be solved for multiple particle bins. Lagrangian models, on the other hand, track "particles" (virtual puffs accounting for several real particles) along their trajectory. Finally, Gaussian puff models, allow for a hybrid modeling solution where the trajectory of the puff centroid is computed and then used to obtain the particle concentration assuming Gaussian diffusion. The following sections summarize the general physics for each modeling approach.

1.2.3.1 Eulerian models

Eulerian models describe how an airborne particle is advected by wind, diffused by atmospheric turbulence and deposited by gravity, by means of their scalar concentration ADS equation (Eq. 1). This equation also includes the source and sink terms corresponding to the generation and destruction of particles, respectively. Neglecting the particle inertia effects and the interaction between particles, the general expression of the ADS equation is:

$$\frac{\partial C}{\partial t} = -\nabla(uC) + \nabla(\mathbb{K}\nabla \mathrm{C}) - \nabla(u_s\, C) + S_o + S_k \qquad (1)$$

where C is the particle mass concentration, t represents time, $u = (u_x, u_y, u_z)$ is the wind velocity, $\mathbb{K}$ is the turbulent eddy diffusivity tensor, u_s is the particle sedimentation velocity, $S_o(x, y, z, t)$ is the source term (accounting for the production of particles per time-step), and $S_k(x, y, z, t)$ is the sink term (accounting for the destruction of particles per time-step). The advection-diffusion solver typically uses the three components of the wind field computed by a NWPM as input. Many solvers use an eddy diffusivity or $\mathbb{K}$-theory gradient diffusion turbulence model to approximate turbulent mixing.

Transport and dispersal models for volcanic ash based on this approach group ash particles with comparable size, density, and shape in particle classes on bins. These groups are characterized by sharing the same sedimentation velocity. Eulerian models are very convenient for steady particle size distribution,

employing different ADS equations for each particle class. However, this approach is no longer valid for those events where the particle size distribution evolves with time, e.g. with the occurrence of particle aggregation. Some examples of Eulerian models employed for the transport and deposition of volcanic particles include: FALL3D (Costa et al., 2006; Folch et al., 2009), ASH3D (Schwaiger et al., 2012), or ATHAM (Herzog et al., 2003).

1.2.3.2 Lagrangian models

Lagrangian models track maker "particles" released in the air using the mean wind field. Neglecting the particle mixing and inertia effects, the movement of a particle between time-steps t_1 and t_2 is given by:

$$r(t_2) = r(t_1) + \int_{t_1}^{t_2} [u(r,t) + u'(r,t) + u_s(r,t)]\, dt \qquad (2)$$

where t is the time, r is the position vector, u and u_s are the wind and particle sedimentation velocities, and u' is the unresolved-scale wind turbulent fluctuations. A typical solution to resolve turbulent fluctuations is to employ the standard random-walk expression for the horizontal and vertical components of u'. This approach is capable to handle the influence of spatially complex wind and turbulent fields on the ash cloud transport and dispersion by introducing random perturbations in the trajectory of a particle (Boughton et al., 1987; Legg and Raupach, 1982).

Examples for volcanic ash Lagrangian models include HYSPLIT (Stein et al., 2015), PUFF (Searcy et al., 1998), NAME (Jones et al., 2007), MLDP0 (D'Amours et al., 2010), or FLEXPART (Stohl et al., 2005). It is relevant to mention that models that merely consider the advection term are known as Lagrangian tracers, whereas those considering diffusion and particle deposition mechanisms are know as Lagrangian transport models.

1.2.3.3 Gaussian puff models

Gaussian puff models also track puffs using the mean wind field from a meteorological model, increasing the puff size with time to mimic turbulent diffusion. The puff travels with the wind at the puff centroid. The rate of growth of the puff depends on the atmospheric turbulence and, as the puff grows, it is possible that it splits if significant wind variations occur. For this particular case, concentrations within the puff are described by a 3D Gaussian distribution, where the size of the puff is proportional to the travel time and the magnitude of turbulence.

Gaussian puff models can be interpreted as a hybrid Lagrangian-Eulerian solution, in the sense that the model tracks the puffs in a Lagrangian way but, computes the concentration at fixed receptors by summing up the contribution of all puffs on each receptor as in an Eulerian model. This approach is

capable to simulate the effect of turbulent spreading of the ash cloud faster than random-walk models since the puff growth is accomplished through a Gaussian equation requiring fewer puffs. Similar to Eulerian models, Puff models can be adapted to account for deposition, gravitational settling, and agent decay, and are ideally suited to buoyant rise and dense gas applications. A typical Gaussian puff transport model employed for volcanic ash dispersal is the VOL-CALPUFF (Barsotti et al., 2008) transport model.

1.2.4 Coupling strategies (off vs. on-line)

This section introduces the different NWPM-TDM coupling strategies available, their limitations, and their possible implementation methods, using the nomenclature approach found in most air quality and chemistry models. In general terms, the NWPM-TDM coupling can be performed either off-line or on-line (Fig. 3).

1.2.4.1 Off-line models

In an off-line modeling system, the NWPM runs *a priori* and independently from the TDM to produce the required meteorological fields at regular time intervals. Meteorological fields are then furnished to the TDM, which commonly assumes constant values for these fields during each time coupling interval or, at most, performs a linear interpolation in time.

At present, all operational ash forecast systems follow the off-line approach and the few existing on-line atmospheric chemistry and transport models adapted to volcanic ash, e.g. NMMB-MONARCH-ASH (Marti et al., 2017), ICON-ART (Rieger et al., 2015) or WRF-Chem (Stuefer et al., 2013) are still restricted to a research level. However, notwithstanding the increase of computational power in recent years and the fact that the total computing time required to run an on-line coupled model is actually not substantially larger (e.g. Grell and Baklanov, 2011; Marti et al., 2017) the benefits of the traditional off-line systems are at question.

The off-line approach is convenient in terms of computing time because different TDM model executions are possible without re-running the meteorological component, e.g. to update the source term whenever the eruption conditions vary, for reconstructing the ESP corresponding to past events employing inverse modeling methods (see section 5.3.3) of ash emissions (e.g. Marti et al., 2016; Webster et al., 2012), or to perform an ensemble forecast (e.g. Galmarini et al., 2010) in which all the ensemble members share the same meteorological conditions. However, off-line modeling systems can lead to a number of issues due to inheritance uncertainties. NWPM and TDM codes frequently use different input datasets (e.g. underlying terrain, land use/land cover), occasionally are set-up in different projections (e.g. Universal Transverse Mercator vs. Lambert Conformal vs. model specific projections). Additionally, they have non-aligned grid meshes, non-synchronized time stepping, and/or inconsistent physical parameterizations and

numerical schemes that can lead to a loss of potentially important information about atmospheric processes that often have a time scale much smaller than the meteorological model output frequency (e.g. wind speed and directional changes, PBL height variations, cloud formation, and rainfall). This may be especially important when meteorological conditions change rapidly in time or when feedbacks between the ash cloud and meteorology are important. These limitations can be corrected by using an on-line approach, specially, with on-line integrated systems allowing feedbacks between the TDM and the NWPM.

1.2.4.2 On-line models

In contrast, in an on-line modeling system, the NWPM and the TDM run concurrently and consistently and the particle transport is automatically tied to the model resolution time and space scales, resulting in a more realistic transport representation. In most cases, both the NWPM and TDM are embedded in the same code and run using a single executable. Depending on the degree of integration of the on-line system, on-line models can be further distinguished between on-line integrated or on-line access modeling systems (Baklanov et al., 2014). On-line integrated models are defined as those where the NWPM and TDM are fully integrated in one unified modeling system using one main time-step for integration (e.g. consistent spatial and temporal interpolation, map projections, dataset inputs, numerical schemes, etc.). On the other end, on-line access models use independent meteorology and transport models but exchange information between them on a regular and frequent basis. In this case, the transport model is embed it into an existing meteorological code but models use different input datasets and map projections, dissimilar algorithms for computing identical quantities, and distinct numerical schemes and/or computational grids. That is, the TDM and NWPM are put into the same code and share input and output information via memory but, in all other respects, models are run equivalently to an off-line system. For the purpose of this document, the term “on-line” is used to refer to “on-line integrated models”.

This modeling approach might also include two-way interactions (also referred to as feedbacks) at each model time-step. These models, commonly known as (two-way) feedback modeling systems, are useful to estimate the effect of volcanic aerosols on the radiative budget. Despite that for most volcanic eruptions the influence on the radiative budget is minor (no effect or minor local/regional effects), in some cases (e.g. large explosive eruptions, super-eruptions) the impact of tropospheric volcanic aerosol can be significant, becoming a regional or even global radiative forcing of climate (Schmidt et al., 2015).

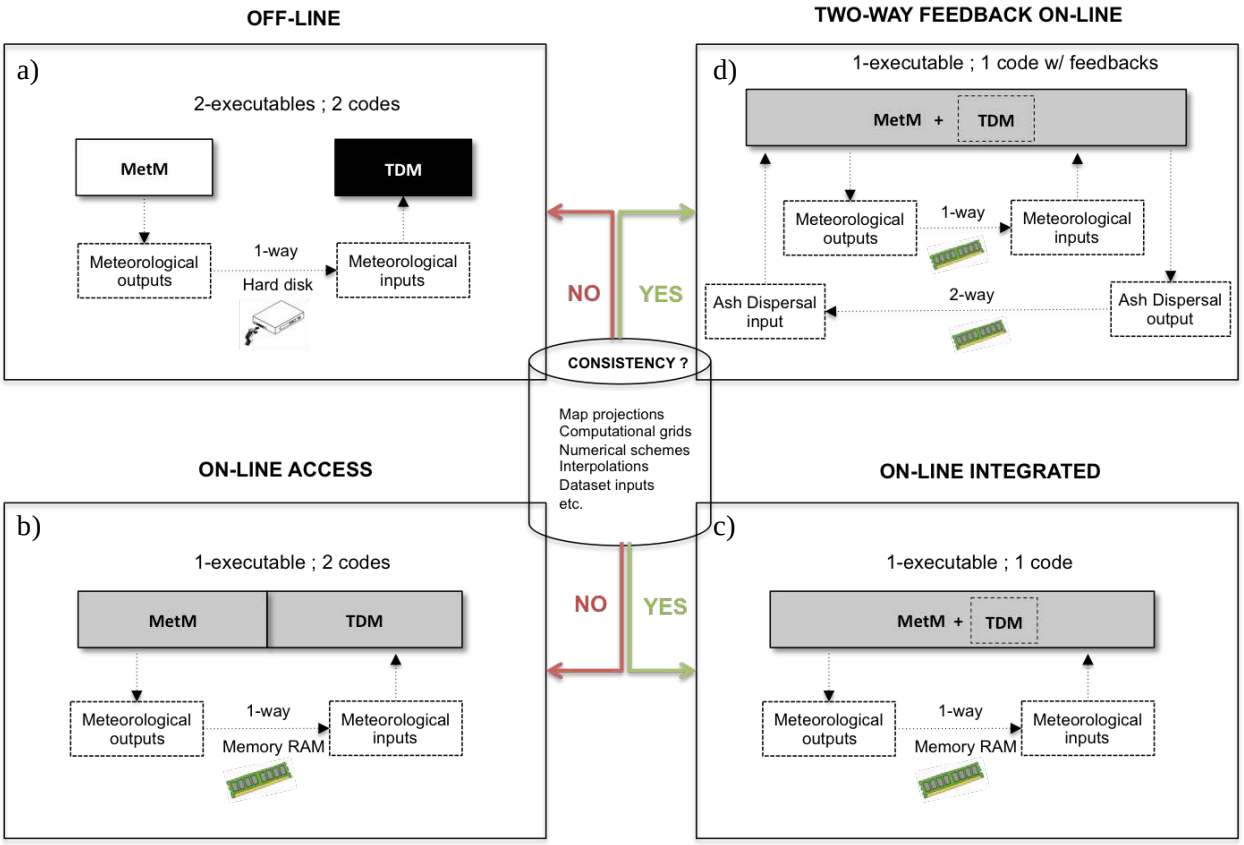

Figure 3. Schematic representation of the different coupling approaches for the meteorological (NWPM) and transport and dispersal (TDM) models. Green and red arrows describe whether data consistency is preserved or not, respectively.

1.3 Historical evolution of TDMs for volcanic ash

Historically, different scientific communities had modeled volcanic ash dispersal based on the particle size and dispersal distance. On one end, volcanologists developed families of models suitable for lapilli and coarse ash (see Fig. 1). These models aim at computing fallout deposits and provide probabilistic hazard assessments. In contrast, meteorologists and atmospheric scientists have conventionally used other TDMs dealing with finer ash particles for tracking motion of volcanic ash clouds and, eventually, for computing airborne ash concentrations. This section builds on the review of Folch (2012), who provided a comprehensive review of the evolution and characteristics of different families of TDMs for volcanic ash. Despite the exiting overlap in some cases, this review follows a chronological structure, starting with the early models built on simple particle sedimentation parameterizations for plumes, followed by the development of Tephra TDMs (TTDMs) and Volcanic Ash TDMs (VATDMs), which represent a specific sub-group of TTDMs used to model long-range transport of fine ash. To conclude, this chronological review includes a brief overview on recent efforts to employ Chemical Transport Models for volcanic ash forecast.

1.3.1 Sedimentation models

The first models to quantify tephra transport were mainly focused on reproducing ground measurements obtained by volcanologists (isopleths and isopachs – contours of equal largest clasts or equal mass per unit area/thickness, respectively). These models are commonly known as sedimentation models (e.g. Carey and Sparks, 1986; Wilson, 1976; Wilson and Walker, 1987). During the mid 1980's, Carey and Sparks (1986) and Wilson and Walker (1987) pioneered the first sedimentation model for pyroclastic fallout. The model was capable to calculate the trajectory of an isopleth by defining support envelopes; a surface where the column vertical velocity (Turner, 1973) equals the terminal velocity of a clast type. Given a specific support envelope, the isopleth morphology is defined by a unique combination of plume height and wind speed, allowing for a simple calculation of the clast trajectories under a given wind profile by inverting these two parameters. Despite its limitations (e.g. assumptions of steady eruption and wind conditions, restrictions in clast size definition, *etc.*), this approach was widely used by field geologists as a first approximation to reconstruct a deposit. This groundbreaking work led the development of sedimentation models throughout the decade. During the 1990's, sedimentation models shifted their focus to the atmospheric transport phenomena. In that framework, seminal works such as Sparks et al. (1992) or Bursik et al. (1992) were key to add novel parameterizations for convective transport of the plume and gravitation spreading of the umbrella cloud.

Starting with the new millennia, research works such as Bonadonna et al. (1998), Bonadonna and Phillips (2003) or Bonadonna and Houghton (2005) built on Sparks et al. (1992) sedimentation model to describe relevant features of tephra deposits such as: particle aggregation, plume strength or the dependencies between the terminal fall velocity and Reynolds number dependencies. Despite these improvements, sedimentation models were still mainly used for the reconstruction of proximal deposits. In 2001, however, following the original work from Armienti et al. (1988), Koyaguchi and Ohno (2001) proposed a sedimentation model that accounted for the amount of fine ash particles at the top of the eruption column. This work can be considered and inflexion point in the historical evolution of TDM for volcanic ash, opening the door, for the first time, for the reconstruction of more distal deposits with sedimentation models.

1.3.2 Tephra Transport and Dispersion Models

In parallel, a different family of modeling strategies focused explicitly on the particle (tephra) transport phenomena also gained relevance amongst volcanologists during the late 90's, setting the bases of what is today know as Tephra Transport and Dispersion Models (TTDMs). These models can be classified as Eulerian or Lagrangian models (or a hybrid of both). As previously introduced in Sect. 1.2.3 the main difference between these two approaches is that Eulerian models use a fixed three-dimensional grid (typically Cartesian), whereas Lagrangian models calculate the trajectories of particles within the computational domain. Eulerian models can be further classified depending on their Advection-Diffusion-Sedimentation (ADS) equation solution as Semi-analytical (also called Gaussian models) and Numerical

models. In terms of validation, TTDMs are normally validated against well-characterized tephra deposit. Validation is typically performed through isomass/isopach model-to-data semi-quantitative comparisons, log–log plots of observed versus computed values of load and thickness at discrete points, or ground measurements of tephra accumulation rates. For a complete list of the available numerical TTDMs, refer to Table 1.

1.3.2.1 Semi-analytical (Gaussian) Models

These models describe the dispersion of particles using an analytical solution of the ADS equation in the form of a Gaussian function. This is possible if one assumes a negligible vertical diffusion and settling velocity divergence, a constant and homogenous horizontal wind advection and turbulent diffusion, and a sufficient eruption column height to neglect terrain effects. Gaussian TTDMs were born after the seminal works of Suzuki (1983) and Armienti et al. (1988). The first semi-analytical Gaussian model for tephra dispersion to become popularly used amongst the volcanological community was HAZMAP (Macedonio et al., 2005; Pfeiffer et al., 2005), a model originally developed to simulate ground load and probabilistic mass accumulation given a wind profile. The model also allowed the possibility to compute the mass accumulation probabilities given a set of wind profiles. Further developments on HAZMAP led to – ASHFALL (Hurst, 1994), TEPRHA2 (Bonadonna et al., 2005) – versions of the model. Gaussian models have been mainly used to elaborate probabilistic hazard maps. Additionally, thanks to their low computation cost, these models are also suitable to constrain eruption source parameters (ESP) by means of inversion analysis (Connor and Connor, 2006). However, despite these advantages, Gaussian models are limited to several assumptions that are not always satisfied, including: i) the dispersal from strong plumes (high eruptions columns to neglect terrain effects); ii) proximal tephra dispersal (to meet the homogenous requirements for the wind field) and, iii) short-lasting eruptions (to meet the time-constant atmospheric conditions).

1.3.2.2 Numerical Models

Numerical TTDMs, on the other side, are able to overcome these limitations by numerically solving the ADS equation, which allow the transport and deposition of any particle size, including fine ash. One of the first numerical models specifically developed for tephra transport was FALL3D (Costa et al., 2006; Folch et al., 2009). This multi-scale Eulerian TTDM is coupled off-line with several mesoscale and global NWPM and re-analysis datasets, allowing the forecast of both particle concentration in the atmosphere (i.e. ash cloud evolution) and particle loading at ground level. Its multi-purpose core, allows for operational forecast applications (e.g. Buenos Aires Volcanic Ash Advisory Center), reconstruction of recent (e.g. Folch et al., 2012) and historical eruption events (Costa et al., 2012; Marti et al., 2016), or performing probabilistic hazard assessments (Folch and Sulpizio, 2010; Scaini et al., 2012). A couple of years after, Barsotti et al. (2008) presented VOL-CALPUFF, a semi-Lagrangian puff model built on

adapting the pollutant transport model CALPUFF to simulate the transport and deposition of volcanic particles. The model has been mainly applied at Mt. Etna for modeling volcanic clouds (Barsotti et al., 2008) and to assess volcanic ash hazards (Barsotti et al., 2010). More recently, Schwaiger et al. (2012) and Mastin et al. (2013) added ASH3D to this list; a finite-volume Eulerian model developed and employed by USGS scientist and U.S. volcano observatories.

1.3.3 Volcanic Ash Transport and Dispersion Models

The establishment of the International Airways Volcano Watch (IAVW) Programme in 1987, and the subsequent creation of the Volcanic Ash Advisory Centers (VAACs) in 1994, extenuated the need to further develop TTDMs to be able of tracking and forecasting fine ash from volcanic ash clouds. With this objective in mind, the volcanology and atmospheric communities started to adapt existing atmospheric Lagrangian models (e.g. atmospheric tracers, aerosol transport models) to forecast distal dispersal of fine ash. These efforts led to the development of the first Volcanic Ash Transport and Deposition Models (VATDMs), which were used for civil aviation safety purposes, by simply identifying the location of the volcanic ash cloud.

However, in the aftermath of the April–May 2010 Eyjafjallajökull eruption and the subsequent inclusion of ash concentration thresholds, required VATDMs to shift towards a more quantitative modeling approach (absolute ash mass concentrations). Since then, many VATDMs have been used to operationally forecast tephra dispersal around the world: HYSPLIT (Stein et al., 2015 - United States), NAME III (Witham et al., 2007 - United Kingdom), FALL3D (Costa et al., 2006; Folch et al., 2009 - Argentina). MOCAGE-accident (Martet et al., 2009 - France), JMA (Iwasaki et al., 1998 - Japan) or, the MLDP0 (D'Amours et al., 2010 - Canada) model, just to name a few. Table 1 illustrates the model characteristic for the vast majority of VATDM existing worldwide.

	ASH3D	ATHAM	FALL3D	FLEXPART	HYSPLIT	JMA-GATM JMA-RATM	MLDP0	MOCAGE	NAME	PUFF	TEPHRA2	VOL-CALPUFF
Operational												
Approach [1]	E/H	E	E	L	H	L	L	E	LH	L	E	H
Method [2]	N	N	N	N	N	N	N	N	N	N	A	S
Coverage [3]	LRG	L	LR	LRG	LRG	RG	LRG	G	LRG	LRG	L	LR
Physics												
Topography												
H wind advection												
V wind advection												
H atm. diffusion								See [5]				
V atm. diffusion												
Particle sed.												
Other dry dep.												
Wet deposition												
Dry part. aggregation												
Wet part. aggregation												
Variable part. shape												
Gas species												
Chemic. processes												
Granulometry												
Variable size class.												
Variable GS distr.												
Variable size limits												
Source term												
Mass distribution [4]	PS/U/ LN	O	ALL	PS/L/U/P/O	PS/L/U/P/LN	PS/L/LN	PS/L/U/P/O	PS/L	PS/L/U/BP/ O	PS/L/U/P /O	L/U/LN/O	PS/BP

Table 1. Comparison of existing TTDMs (IUGG-WMO, 2013b. Colored/white cells indicate that the option is available/not available for the TTDM, respectively.
(1) L=Lagrangian, E=Eulerian, H=Hybrid
(2) A=Analytical, S=Semi-analytical, N-Numerical

(3) L=Local, R=Regional, G=Global
(4) PS=Point Source, L=Linear, U=Umbrella-type, P=Poisson, LN=Log-Normal, BP= Buoyant-Plume, O=Other
(5) Neglected. Diffusion of numerical origin appears to be sufficient, with particularly good results at 0.5°.

1.3.3.1 FALL3D

FALL3D (Costa et al., 2006; Folch et al., 2008) is an Eulerian model for the transport and deposition of volcanic ash and lapilli. The model solves the advection–diffusion–sedimentation (ADS) equation on a structured terrain-following grid using a second-order finite differences explicit scheme. The model code can be compiled either as serial or parallel using Message Passing Interface (MPI). Model inputs include meteorological data, topography, vent coordinates, Eruption Source Parameters (i.e. MER, eruption duration, and TGSD). Model outputs are tephra ground load/thickness, airborne ash concentration and other related variables. Several parameterizations can be chosen to describe eruption source geometry and physics, particle terminal settling velocity, eddy diffusivity tensor, and ash aggregation. FALL3D employs an off-line strategy to furnish meteorological variables from independent models or datasets. The model can be used to reproduce features of past eruptions, as a tool for short-term ash dispersal forecasting, and for volcanic fallout hazard assessment. The FALL3D model is used at the Buenos Aires and Darwin Volcanic Ash Advisory Centers (VAAC) in operational forecasts.

This thesis work partially builds on the most recent release of FALL3D – version 7.1 (Folch et al., 2016b). Current developments in FALL3D 8.0 (expected by the end of 2017) replace the classical Lax-Wendorff (LW) central scheme for solving the ADS equation, known to introduce numerical dissipation leading to over-diffusive results, for the high-resolution Kurganov-Tadmor scheme (KT). This scheme is combined with a fourth-order explicit Runge-Kutta method to advance in time, as opposed to the second-order (first-order for big gradients) time-marching Euler method implemented in the previous versions of the code. In addition, version 8.0 will include nesting and several model performance implementations.

FALL3D sources and a list of scientific publications employing the model are available at: http://datasim.ov.ingv.it/models/fall3d.html.

1.3.4 Chemical Transport Models for volcanic ash

During the last decade, and mainly as a result of the 2010 Eyjafjallajökull eruption, scientists have started to apply exiting Eulerian chemistry aerosol models to study the dispersion of volcanic ash and sulfur/sulfate aerosol. Chemical Transport Models (CTM) are capable of simulating the long-range transport of small particles in the atmosphere provided the necessary input parameters (e.g. accurate 3-D meteorological and emission fields).

Traditionally, CTM were mainly developed to study specific processes. However, the latest generation of CTMs have gravitated towards the representation of most processes associated to changes in the atmospheric composition in terms of aerosols and trace gases, including all types of emissions – i.e. anthropogenic, biogenic, mineral dust, sea salt, vegetation fires, etc. In a recent article Baklanov et al. (2014) provided a comprehensive review of the current research status of online coupled meteorology and atmospheric chemistry modeling within Europe.

The review of all available CTMs is beyond the scope of this section. This section provides a brief description of those CTMs capable to simulate the transport and deposition of volcanic ash. It is worth mentioning that most of these CTMs have not been developed with the objective of providing cost-efficient and reliable operational forecasts for volcanic ash. In fact, CTMs that forecast volcanic ash transport are normally limited to specific research purposes and, in many cases, use a version of the model that was originally developed for mineral dust or other aerosol simulations. Some of these models include:

i. MCCM (Grell et al., 2000): a meso-scale on-line coupled meteorology atmospheric chemistry model capable to produce flow simulation and weather forecast model based on the 5th-generation Penn State/NCAR Mesoscale Model (MM5). The model is frequently used for weather, climate and air quality forecasts. For the simulations of the volcanic ash dispersion, ash is attributed entirely to the coarse mode and handled as mineral dust in MADE/SORGAM (Emeis et al., 2011).
ii. COSMO-MUSCAT: a regional CTM system consisting of the non-hydrostatic model COSMO (Doms et al., 2011) as meteorological driver, and the online-coupled 3-D chemistry tracer transport model MUltiScale Chemistry Aerosol Transport Model (MUSCAT; Renner and Wolke, 2010). Similar to the previous case, volcanic ash transport is simulated with a version of the model that was originally developed for Saharan dust simulations (Heinold et al., 2012).
iii. WRF-CMAQ (Community Multi-scale Air Quality modeling system): In this case the WRF model is coupled with an Eulerian chemistry transport model developed by the U.S. Environmental Protection Agency (EPA) Atmospheric Science Modeling Division. The CMAQ modeling system has been used as a VATDM to model ash dispersion over Europe for the 2010 Eyjafjallajökull eruption (Matthias et al., 2012).
iv. REMOTE (Langmann, 2000): is a regional scale Eulerian atmosphere-chemistry and aerosol model coupled on-line with the former regional weather forecast system of the German Weather service (DWD). The model has been applied to study the local dispersion of SO_2 volcanic emissions and volcanic ash.

In few cases, chemistry transport models include specific parameterizations (e.g. compute the total mass flux emitted according to empirical fits) to characterize volcanic emission. Despite this, CTM models in the literature are still limited in the way they characterize the volcanological source term and lack the representation of certain critical processes (e.g. mass distribution in the column, aggregation, particle settling velocity, etc.). Some models including basic parameterizations to characterize the volcanological source term are:

i. WRF-Chem (Grell et al., 2005; Stuefer et al., 2013): The Weather Research and Forecast (WRF; http://www. wrf-model.org/) model coupled with Chemistry (WRF-Chem; Grell et al., 2005) provides the capability to simulate chemistry and aerosols from cloud scales to regional scales. WRF-Chem is a community model. The development is led by NOAA/ESRL with multiple collaborating agencies. The initial release of WRF-Chem uses the emission PREP-CHEM-SRC emission tool (Freitas et al., 2011), originally developed to characterize trace gases and aerosol emissions and to provide the volcano location and the total erupted mass, which is empirically derived from the column height according to Mastin et al. (2009). The preprocessor allows only for three options to characterize volcanic ash i) use the four finest ash species as invariant tracers that are being transported, deposited and settled only; ii) selecting a number of 10 ash variables, which also includes coarse ash species for estimates of ash fall; and iii) only 2 different ash species with feedback processes implemented within WRF-Chem. The model has been tested for the simulation of ash transport for the 2010 Eyjafjallajökull eruption.

ii. CHIMERE-2016 (Mailler et al., 2016): this CTM has evolved from its original box-modeling of regional atmospheric composition design to a 3D Eulerian model capable to run from local to continental domains. As in WRF-Chem, the source term for volcanic emissions only computes the total erupted mass following the Mastin et al. (2009) empirical fits. Its global forecast capabilities have been recently tested for a simulation of the circumpolar transport of volcanic ash plume from the Cordón Caulle volcanic eruption in June 2011 in Chile, and employing the WRF meteorological mode as a NWPM.

iii. ICON-ART: in a joint development with the Max-Plank-Institute of Meteorology Hamburg (MPI-M), the German Weather service (DWD) is working on the dispersion of volcanic ash particles and radioactive tracers for operational forecast with ICON-ART; an extension of ICON (ICOsahedral Nonhydrostatic model) to enable the simulation of gases, aerosol particles and related feedback processes in the atmosphere. The future implementation of ICON-ART will include a parameterization that only depends on the top of the plume height and employs an inversion modeling approach based on Stohl et al. (2011) to derive vertical profiles of the emissions of volcanic ash. In its current stage, ICON-ART is capable of simulating mineral dust and sea salt aerosol and the interactions of these aerosol types with clouds (Rieger et al., 2015).

While atmospheric Chemistry Transport Models might be very useful in future operational set-ups, to date, no CTM is capable to match the specific VADTM volcano emissions. In addition, CTM currently assume all particles to be spherical in shape. While this may be suitable for fine particles (volcanic ash), this approach is not adequate for bigger tephra particles such as lapilli, limiting therefore the representation of the sedimentation processes of these models. At the time of this review, all VAACs employ traditional VADTM models coupled off-line with NWPM. In light of the above, the focus on developing a computational efficient online CTM model specific for volcanic ash capable to provide robust operational forecasts is timely.

1.3.5 Review of existing on-line modeling efforts in other communities

To date, most TTDMs and VATDMs are off-line systems. However, other communities involved in modeling atmospheric transport and dispersion have highlighted the importance of on-line strategies for different applications. This section discusses current state-of-the-art of on-line systems in the fields of: i) air quality; ii) climate and, iii) plume transport and dispersal models.

1.3.5.1 Regional air quality and photochemical transport models

In the regional photochemical community, on-line systems have been (and continue to be) developed primarily to improve the reliability of the air quality predictions through the inclusion of two-way feedback mechanisms. In this context, Grell et al. (2004) described the feedback effects between air pollutants and meteorology on both short-term and climatic time scales. Aerosol concentrations have an impact on the radiative forcing and meteorological events (e.g. precipitation, thunderstorms, etc.) through the availability and distribution of cloud condensation nuclei. Table 2 summarizes the chemistry-meteorology impacts described by Baklanov et al. (2014) for air quality.

Aerosols	- Modulate radiation transfers (SW scattering/absorption, LW absorption and scattering by large particles like dust) - Affect boundary layer meteorology (temperature, humidity, wind speed and direction, ABL height, stability) - Extraordinary high concentrations can affect stability and wind speed - Influence cloud formation, since they act as cloud condensation nuclei
Aerosols physical properties	- Influence cloud droplet and crystal number and hence cloud optical depth and hence radiation - Modulate cloud morphology (e.g. reflectance) - Influence precipitation (initiation, intensity) - Affect haze formation and atmospheric humidity - Influence scattering /absorption
Soot deposited on ice	- Influences albedo
Radiative active gases	- Modulate radiation transfers

Table 2 Aerosol impacts (feedbacks) on meteorology (Baklanov et al., 2014)

Presently, most of the coupled photochemical meteorological models include simple direct effects of aerosols on meteorological processes in which aerosols scatter, absorb and reemit incoming shortwave

radiation (e.g., COSMO LM-ART and MCCM). Grell and Baklanov (2011) and Zhang, (2008) provided comprehensive reviews on integrated models to forecast weather and air quality in Europe and United States, respectively. According to Baklanov et al. (2014) only two mesoscale on-line integrated modeling systems (WRF-Chem and Enviro-HIRLAM) consider both the first and the second indirect feedbacks.

Finally, in the context of photochemical modeling, several authors (e.g. Baklanov et al., 2011; Grell and Baklanov, 2011; Zhang, 2008) have listed the following advantages for employing on-line modeling systems:

- Only one grid for both the Met and scalar concentration advection-diffusion solver.
- No interpolation in space and time.
- Identical physical parameterizations and numerical schemes, i.e., no inconsistencies.
- Availability of all 3-D meteorological variables at the right time, i.e., each time step.
- Possibility to consider feedback mechanisms, e.g., aerosol forcing.
- No need for meteorological pre/postprocessors.

1.3.5.2 Global Climate community

Similarly than in the air quality community, global climate models (GCM's) use the on-line approach to efficiently account for the feedback of greenhouse gases and aerosols onto the radiation balance, the atmospheric and surface energy budget, and the meteorology (e.g Cox et al., 2000).

Larson et al. (2005) discussed the strengths and weaknesses of coupled global climate modeling systems. Their work summarizes the main aspects to consider in the choice of the coupling technique, including for example: the physics of the problem, the needed solution accuracy, and the elements of software implementation. According to Larson et al. (2005), the physics of the problem determines:

- The connectivity, i.e., the model-model interactions determined by the physics and solution algorithms of the coupled system (e.g., ocean and atmosphere interactions).
- The domain overlap, i.e., the simulation space across which two or more models must exchange either driving or boundary condition data, which may be as simple as subsets of physical meshes, or as complex as interactions across spectral spaces or between Eulerian and Lagrangian models (e.g., the evaporation rate from the ocean model is a source term for the atmospheric model).
- The coupling cycle, i.e., the period over which all models in the system exchange data (e.g., hourly, daily).
- The coupling frequency, i.e., the temporal exchange rate for a given model pair.
- The "tightness," i.e., the ratio of the effort (e.g., wall-clock time) spent by a component executing model-model interactions vs. integrating the model mass, momentum, and energy conservation

equations (e.g., time spent transferring data between models over a distributed-memory multiprocessor network vs. computing the equations).

They also identified the following software implementation characteristics to consider:

- Component scheduling, i.e., the order of execution for the individual models in the coupled system, which can be sequential, concurrent, or a combination of both.
- Resource allocation, i.e., the number of processors and threads allocated to each component in the system.
- Number of executables, i.e., the number of executable images in the coupled system – either single or multiple executables.
- Coupling mechanism, i.e., the way models exchange information, either directly or through an intermediate entity (e.g., a preprocessor, a centralized server).

Finally, independently from the coupling strategy, they described the following additional issues that need to be addressed when linking models:

- Data structures, i.e., two modules that need to exchange data can have different internal data structures. This is true, for instance, any time two modules were developed independently from different groups and then forced to work together.
- Data transformation, i.e., the spatiotemporal interpolation from an original to a target grid and variable transformation to infer the set of physical quantities required by the target module starting from a different set of variables. In case of a distributed memory parallel program, distributed inter-grid interpolation algorithms are needed.
- Data transmission, i.e., the act of moving data from one module to another. In a distributed memory parallel program, data could be decomposed differently on different sets of processors; therefore they will need to be transmitted from the original network node to the target node(s) potentially resulting in performance degradation and lack of scalability.

1.3.5.3 Mesoscale plume transport and dispersal modeling

Extensive use of on-line systems has been reported within the mesoscale plume transport and dispersal modeling community. Some examples include the COAMPS, OMEGA, and TAPM models. The Navy's COAMPS code is the only one that includes aerosol feedback on the cloud microphysics with plans for further integration with radiation balance schemes (Smith et al., 2012). The model accounts for the impact of volcanic emissions, fires, and dust storms on regional weather to predict the reduction in visibility to support military operations. OMEGA and TAPM are on-line integrated modeling systems that do not currently include plume feedback onto the meteorological fields.

1.4 Recent developments

The recent eruptions of Eyjafjallajökull (Iceland) in 2010 and Cordón Caulle (Chile) in 2011 have shed light into the importance of tephra dispersal in the context of aviation safety. Moreover, the unsuccessful implementation of the zero-ash tolerance criterion for high capacity European Air Space during long-lasting eruptions required the employment of a new volcanic ash contingency plan. In the aftermath of these events, a new multidisciplinary international community was created to promote stronger interactions between the volcanological and the operational forecasting communities and to provide a robust and reliable response to societal needs. As a result of the recommendations from the IUGG-WMO workshops on Ash Dispersal Forecast and Civil Aviation (Bonadonna et al., 2012, 2014), significant progress has been accomplished to improve the accuracy of dispersal models for volcanic ash and to lessen their associated uncertainties. In general, this progress has led to a series of recent developments including new methods and techniques to improve: i) the characterization of the source term; ii) physical processes for particle transport and deposition; iii) model validation and; iv) the operational implementation of models. In addition, the European Research Council (ERC) has also pioneered different Initial Training Networks (ITN) to prepare the next generation of volcanologists. This section provides an overview on the research progress achieved in each area in the last 5 years.

1.4.1 Source term (plume models)

The description of physical parameters from explosive eruptions is necessary to characterize eruptive behavior of active volcanoes and assess their hazards. In that context, several datasets are for the characterization of eruptive events of the past 10.000 years (e.g. Global Volcanism Program, GVP, http://www.volcano.si.edu/; LaMEVE database, http://www.bgs.ac.uk/vogripa/view/controller.cfc?method=lameve). In addition, collaborative efforts are currently underway to review and restructure the Eruption Source Parameters (ESPs) Database for the world's volcanoes (Engwell et al., 2016) originally proposed by Mastin et al. (2009).

Accurate characterization of the initial plume height, mass eruption rate (MER) and total grain size distribution (TGSD) is key to characterize the source term and to determine the height at which volcanic plumes spread in the atmosphere. The height to which a volcanic plume (or column; these terms are used interchangeably in this document) may rise is greatly influenced by the surrounding atmospheric characteristics and it is widely investigated for hazard mitigation. Traditionally, simple relationships between the source mass flux and plume height in a wind field have been used to characterize the eruption column. However, such empirical formulations (0-D) can be inaccurate and can underestimate rates in windy conditions (Mastin, 2014). This section focuses on the most recent developments regarding plume modeling.

Noteworthy progress has been reported in the development of new empirical formulations and eruptive plume models. In a recent work, Costa et al. (2016b). compared and evaluated one-dimensional (1-D) and

three-dimensional (3-D) numerical models of volcanic eruption columns in a set of different inter-comparison exercises. Model variability in plume height was estimated to be within ~20% for the weak plume and ~10% for the strong plume (Costa et al., 2016b). Results from this work also suggest that 1D models are considered adequate for weak plumes but recommend the use of more complex 3D models for strong plumes (Fig 4). This section provides a conceptual overview of the existing plume modeling solutions (empirical, 1-D and 3-D) and the most recent developments for each approach. It is worth mentioning that, despite the progress presented by 1-D and 3-D models, recent studies have also highlighted the uncertainty associated to plume models, (e.g. Dioguardi et al., 2016; Macedonio et al., 2016; Mastin, 2014). In light of the above, better understanding of the source conditions and how these affect the development and evolution of eruptive plumes is still required to reduce uncertainties in ash dispersion modeling.

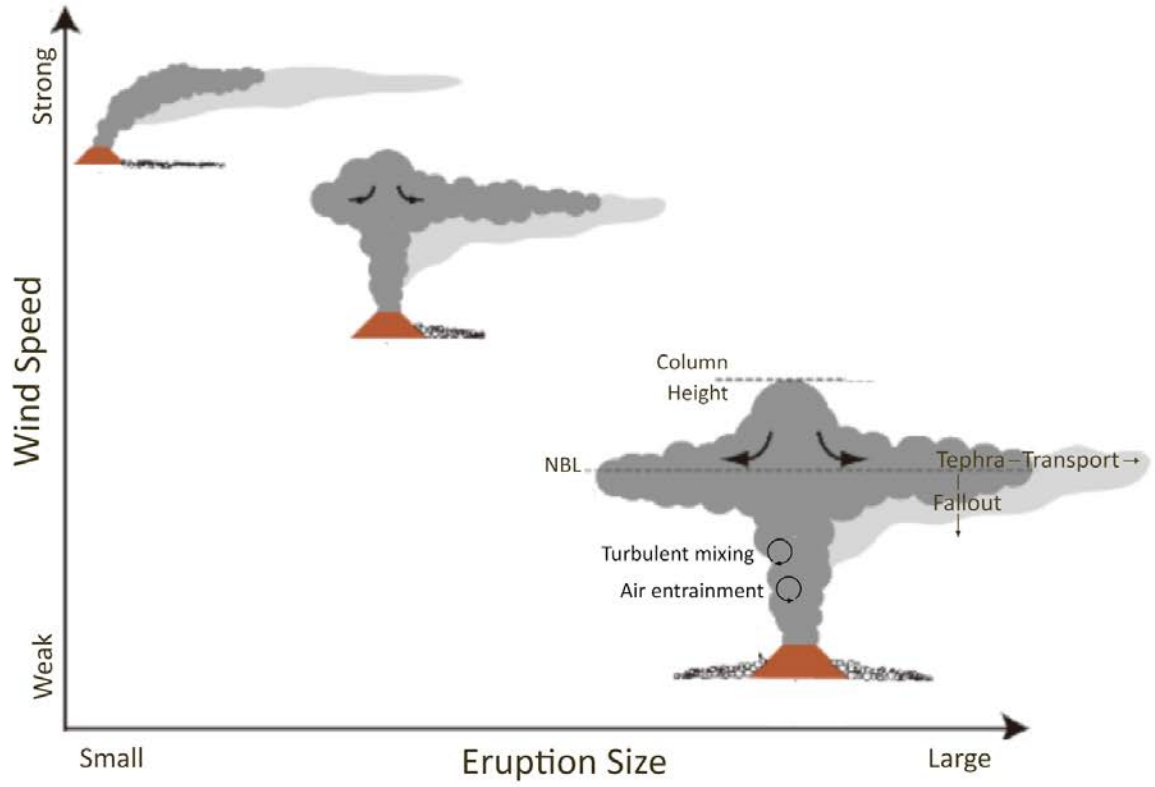

Figure 4. Schematic representation of weak and strong plumes according to eruption size (modified from Costa et al., 2016b)

1.4.1.1 Empirical formulations (0-D)

Historically, empirical formulations provided the relationship between plume height and mass eruption rate based exclusively on field observations (e.g. Mastin et al., 2009). Despite their goodness of fit (Fig. 5), these relationships result in significant uncertainty when used to estimate mass flux in windy conditions (Mastin, 2014). Recent developments have led to explicitly account for the effects of wind. For

example, Degruyter and Bonadonna (2012) and Woodhouse et al. (2013) incorporated the effects of the atmospheric temperature, wind profile, source thermodynamic properties, and values of the entrainment coefficient into this relationship.

More recently, Carazzo et al. (2015) used analogue experiments from strong and weak plumes to account for wind velocity. Despite their advantages, several authors (e.g. Mastin, 2014) have argued that the actual eruption rate could have been 1 to 2 orders of magnitude greater than the empirical relations would suggest, and could be more accurately estimated using one-dimensional plume models.

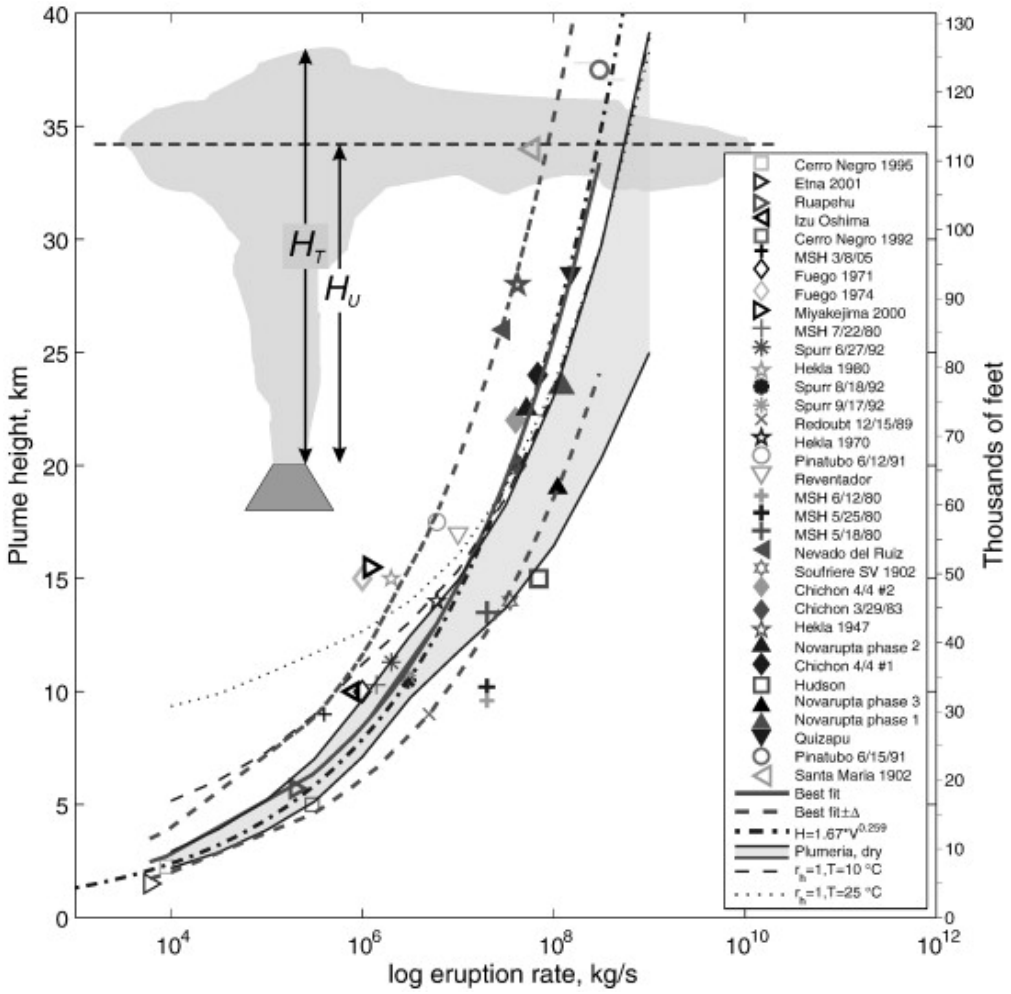

Figure 5. Column height and MER relationship based on field observations (extracted from Mastin et al. 2009).

1.4.1.2 1-D Plume Models

Despite their simplicity, 1-D models have been remarkably successful at describing buoyant plumes. These employ different applications of the mathematical description of turbulent buoyant plumes (Morton et al., 1956), hereafter referred to as Buoyant Plume Theory (BPT). Most 1-D models use the formulation of Woods (1988) who built his plume theory on Wilson (1976) by assuming ambient pressure and homogeneous mixture of all phases. The inclusion of additional atmospheric processes a few years later,

such as humidity (Mastin, 2007), wind (Bursik, 2001) and profiles in temperature, allowed 1-D models to start reflecting real atmospheric conditions. More recently, models adopted different entrainment coefficients values based on their specific formulations or calibration studies (e.g. Devenish et al., 2010). Finally, Folch et al. (2016a) presented FPlume: a 1-D cross-section averaged plume model which accounts for plume bent over, entrainment of ambient moisture, effects of water phase changes on the energy budget, particle aggregation, particle fallout and re-entrainment by turbulent eddies, as well as variable entrainment coefficients fitted from experiments. FPlume has been implemented in NMMB-MONARCH-ASH. Currently, 1-D models currently offer the best tool for operational use and broad exploratory investigations (Costa et al., 2016b; Devenish, 2013). Table 3 (top) summarizes, in chronological order, 1-D models developed (or updated) in the last 5 years.

1.4.1.3 3-D Plume Models

Three-dimensional (3-D) plume models are designed to resolve the detailed turbulence structure of volcanic plumes using a time-dependent solution of the turbulent Navier–Stokes equations for the conservation of mass, momentum, and energy. Different numerical solutions exist depending on the way models describe the eruptive mixture or solve the governing equations. In any case, to initialize these models it is necessary to provide a description of the flux of volcanic ash and gases into the atmosphere. These multiphase and multicomponent models, while computationally more expensive, have shown to provide critical information on the interaction of the plume with the surrounding atmosphere. Suzuki et al. (2016) provided a thorough inter-comparison of three-dimensional models of volcanic plumes. Table 3 (bottom) summarizes (in chronological order) the most commonly used 3-D models developed (or updated) in the last 5 years.

Table 3. Recent (5 years or less) developments in plume modeling. Top: 1-D models; Bottom: 3-D models (Costa et al., 2016b)

Model (Year)		***Refs.***	***Model type***	***Air entrainment***	***Wind***	***Particle fallout***	***Particle re-entrainment***	***Moisture entrainment***	***Water latent heat***
Puffin	2001-2016	1	1D	α=0.15 β=1.0	Yes	Yes	Yes	No	No
Plumeria	2007-2014	3	1D	α=0.09 β=0.5	Yes	No	No	Yes	Yes
Degruyter	2012	3	1D	α=0.10 β=0.5	Yes	No	No	Yes	Yes
PlumeRise	2013	4	1D	α=0.09 β=0.9	Yes	No	No	Yes	Yes
Devenish	2013	5	1D	α=0.10 β=0.5	Yes	No	No	Yes	Yes
PPM	2014	6	1D	α=f(Ri) β=0.5	Yes	Yes	No	No	No
PlumeMoM	2015	7	1D	α=0.09 β=0.6	Yes	Yes	No	No	No
FpluMe	2016	8	1D	α=f(Ri) β=g(Ri)	Yes	Yes	Yes	Yes	Yes
ASH1D	2015	9	1D	α=0.10 β=0.0	No	No	No	No	Yes

ATHAM	1998-2016	10	3D	LES	Yes	Yes	Yes	Yes	Yes
PDAC	2007-2015	11	3D	LES	No	Yes	Yes	No	No
SK-3D	2005-2009	12	3D	DNS-LES	Yes	No	No	No	No
ASHEE	2016	13	3D	LES	No	Yes	Yes	Yes	Yes

Refs: 1—Bursik (2001), Pouget et al. (2016); 2—Mastin (2007, 2014); 3- Degruyter and Bonadonna (2012); 4—Woodhouse et al. (2013); 5—Devenish (2013); 6—Girault et al. (2014);7—De'Michieli Vitturi et al. (2015); 8—Folch et al. (2016a); 9—Cerminara (2015); 10—Oberhuber et al. (1998),(Savre et al., 2016); 11—Esposti Ongaro et al. (2007), Esposti Ongaro and Cerminara (2015); 12—Suzuki (2005), Suzuki and Koyaguchi (2009); 13—Cerminara et al. (2016).

1.4.2 Dispersal model physics

Recent contributions in the physics of ash dispersal models include developments mostly in three fronts: i) experimental and modeling work on aggregation of volcanic ash; ii) description of the gravitational spreading of the umbrella cloud; iii) modeling work on sedimentation processes, and; iv) re-suspension of volcanic ash. This section offers a brief overview of recent contributions on each front.

1.4.2.1 Aggregation processes

A substantial fraction of finer tephra particles (diameters up to 100 μm; fine ash roughly) often falls as different aggregates types. Particle aggregation is a fundamental process that controls the dispersal and sedimentation of ash with diameter <100 μm. Model accuracy is limited by the fact that fine ash aggregates alter patterns of deposition. Experimental work on sedimentation and aggregation of volcanic ash has been (and is being) undertaken by a number of groups. Brown et al. (2012) provided a compressive review on recent volcanic ash aggregation developments during the past few decades. More recently, Mackie et al. (2016) dedicated a chapter to provide an overview of aggregates observed falling out of recent volcanic clouds, aggregates found in deposits, and key formation mechanisms. Since the review of Brown et al. (2012), a significant number of aggregation papers have been published. Some of that progress is highlighted here.

At modeling level, Costa et al. (2010) and Folch et al. (2010) developed a pioneer aggregation model based on a fractal relationship to describe the rate particles are incorporated into ash aggregates. Later, Langmann (2013) reported suitable algorithms for volcanic ash aggregation and wet deposition during long-range transport to be used in standard off-line volcanic ash forecast models. Van Eaton et al. (2015) proposed a mechanism of hail-like ash aggregation, based on previous laboratory experiments (Van Eaton et al., 2012a), that contributes to the anomalously rapid fallout of fine ash and occurrence of concentrically layered aggregates in volcanic deposits. More recently, Mastin et al. (2016) developed a simple, computationally-efficient aggregation parameterization scheme for use in operational model forecasts. The data resulting from these new developments have been included in the IAVCEI Commission for Tephra Hazard Modeling database for ash aggregates and it is currently being used in

different TTDMs. That same year, Costa et al. (2016a) attempted, for the first time, to assess TGSD on the basis of pivotal physical quantities, such as magma viscosity and plume height. Their proposed empirical strategy represented a valuable step forward towards a better evaluation of ESPs when more rigorous data are not available, e.g. real-time forecasting during volcanic crisis and fast hazard assessments. In addition, several works have illustrated observational and modeling perspectives on aggregation processes for specific recent eruptions – e.g. the 2010 Soufrière Hills eruption - Burns et al., (2017), the 2011 Grímsvötn eruption - Prata et al. (2017), or pre-historical events such as the 25.4 ka Oruanui supereruption from Taupo volcano, New Zealand (Van Eaton and Wilson, 2013).

Despite the significant progress presented above, aggregation processes remain a major source of uncertainty both in ash dispersal forecasting and interpretation of eruptions from the geological record. New integrated observations that combine remote sensing studies of ash clouds with field measurements and lab experiments are required to fill current gaps in knowledge surrounding ash aggregation processes. It is worth mentioning that with the exception of the FALL3D model, no operational model considers aggregation in their forecasts. Instead, aggregation is accounted for by either setting a minimum settling velocity in the code or, in the model input, adjusting particle-size distribution by replacing some of the fine ash with aggregates of a specified density, shape, and size range.

1.4.2.2 Gravitational spreading umbrella cloud

The complex interplay among cloud gravitational spreading, atmospheric diffusion, and wind advection of volcanic clouds have recently been topics of lively debates within the international community. For example, Costa et al. (2013) presented a novel analytical model to describe the radial growth of the umbrella cloud and the conditions when the dominant transport regime is gravity-current, passive, or mixed in terms of the cloud Richardson number. The model was implemented in FALL3D to evaluate the relative importance of gravity current effects during large volcanic eruptions (e.g. comparing model results to satellite imagery showing the 1991 Pinatubo umbrella cloud). In a later work, Mastin et al. (2014) replicated this work in Ash3D by calculating turbulent diffusion through an adjusted Crank-Nicolson formulation to match the observed rate of downwind widening of a deposit or ash cloud in simulations. In that same context, Johnson et al. (2015) suggested the need to re-evaluate the interpretations of Costa et al. (2013) grounded on the assumption that the radius of a continuously supplied intrusion (r_f) should grow in time (t) as $r_f \sim t^{3/4}$ rather than $r_f \sim t^{2/3}$.

More recently, Pouget et al. (2016a) presented a new model for radial, gravity-driven intrusion of volcanic ash and gas into the atmosphere in the umbrella cloud. The model increased the number of regimes described in Costa et al. (2013) to four spreading regimes based on type of resistance force (i.e. buoyancy-inertial or turbulent) and type of release (i.e. instantaneous or continuous).

1.4.2.3 Sedimentation (particle settling velocity)

Particle settling velocity is a complex function of particle size, density, and shape. These parameters control the residence time of tephra in the atmosphere and, consequently, tephra deposition. For simplicity, it is commonly assumed that tephra particles in volcanic clouds settle at their terminal velocity, which is derived from the balance between gravity, buoyancy, and drag forces. The precise determination of the aerodynamic drag forces requires a detailed parameterization of particle shape (e.g., Ganser, 1993). A large amount of experimental aerodynamic data exists for simple regular shapes. However, just a few studies have directly measured the terminal velocities of irregular volcanic particles (non-spherical), which is typical from most volcanic eruptions. In that context, the seminal work of Ganser (1993) has been considered to be the most accurate model available for predicting drag coefficient of non-spherical particles.

A review presented by Alfano et al. (2011) compared and assessed the use of Ganser's model along with various existing particle settling velocity models considering different morphological characterizations (i.e., 2D and 3D). A couple of years later, Bonadonna et al. (2013) provided a review of the main approaches to model tephra sedimentation from volcanic plumes. This work concluded that more sophisticated numerical models do not necessary provide better accuracy in terms of ground depositions, but they can provide crucial information not possible with analytical models. This review also emphasized that models of all levels of sophistication would benefit from better parameterization of critical sedimentation processes such as particle aggregation and from the quantification of uncertainties associated with input parameters. More recently, Bagheri and Bonadonna (2016) summarized the current state of methods for characterizing size, shape, and aerodynamics of volcanic particles. Their review confirmed that particle shape governs both size parameters and particle aerodynamics (i.e. drag coefficient, settling velocity), and that the spherical approximation of volcanic particles introduces large errors. In a complementary work, Bagheri and Bonadonna (2016b) presented a novel model to predict the drag coefficient of non-spherical solid particles of different shapes (settling in gas or liquid) valid for sub-critical particle Reynolds numbers (i.e. $Re < 3\times10^5$). Finally, Dioguardi et al. (2017) presented new drag laws as a function of 3D fractal dimension and 3D sphericity measurements taken with X-ray microtomography.

Despite recent progress, the prediction of the drag coefficient for volcanic particles continues to be a major source of uncertainty. In that context, the seminal work of Ganser (1993) has been considered to be the most accurate model available for predicting drag coefficient of non-spherical particles and it is currently employed in most VATDMs.

1.4.2.4 Re-suspension

Re-suspension of fine ash has long been recognized as an issue for aviation and air quality in some regions of the world (e.g. Alaska, Argentina and Iceland). For the past five years, research groups focusing on re-suspension have worked to classify the source of re-suspended material and identify methodologies to include it as an area source within VATDMs. To define the source term emission schemes for mineral dust have been tested for volcanic ash in Iceland (Leadbetter et al., 2012; Liu et al., 2014); Argentina (Folch et al., 2014; Ulke et al., 2016; Reckziegel et al., 2016; Toyos et al., 2017). In a recent work, Beckett et al. (2016) employed a different approach by using satellite-based measurements in combination with radiative transfer and dispersion modeling to quantify the total mass of ash re-suspended during the 16–17 September 2013 strong surface winds in southern Iceland.

1.4.3 Model validation

Strategies to develop timely and quantitative products for use in real-time observations of the dispersing cloud, were discussed at the "2nd IUGG-WMO Workshop on Ash Dispersal Forecast and Civil Aviation workshop" (Bonadonna et al., 2014). In recent years, a significant number of model validation papers were published as a consequence of the extensive observational data gathered during Eyjafjallajökull (2010), Cordón Caulle (2011) and Grimsvötn (2011) eruptions. In general, TTDM can be validated against ground deposits and ash cloud measurements, expecting point-to-point differences to lie within a factor 5 on average when model inputs are well constrained. In contrast, VATDM have traditionally been validated using satellite imagery, providing a qualitative location and extend of the ash cloud (e.g. Prata, 1989). More recently, satellite retrievals (e.g. Pavolonis, 2016; Pavolonis et al., 2013), space-based remote sensing techniques (e.g. Dacre et al., 2011, Folch et al., 2012), or X-ray microtomography (tephra deposits preserved within marine sediments; e.g., Griggs et al., 2015) have been used to identify tephra deposits.

Traditional passive satellite algorithms were recently evaluated during the Volcanic Ash Algorithm Intercomparison SCOPE-Nowcasting PP2 (Pavolonis, 2016). This study considered more than 20 passive satellite sensor algorithms from institutions and groups all over the world to improve knowledge of satellite-based detection and quantification of volcanic ash, and explore the nowcasting applications for volcanic ash forecast. The six volcanic eruptions considered in the intercomparison were Eyjafjallajökull (2010), Grimsvötn (2011), Sarychev Peak (2009), Kelut (2014), Cordón Caulle (2011) and Kirishimayama (2011). The study revealed the improvement in volcanic cloud monitoring and highlighted the forecasting capabilities of these data to improve the safety and economic hazards that volcanic eruptions pose on aviation. Despite these improvements, the study exposed the need for additional scientific development of algorithms and more detailed comparisons between datasets within an organized international framework.

In response to the needs presented by Pavolonis (2016), the aftermath of the 2010 Eyjafjallajökull eruption generated an unprecedented validation dataset that triggered the development of alternative algorithms. In addition to the European EARLINET network (Pappalardo et al. 2013), validation datasets and algorithms have been reported including observations from satellite-based infrared (e.g. Zhu et al. 2017) and ultraviolet (e.g. Carn and Krotkov, 2016) measurements, thermal cameras (e.g., Clarisse and Prata, 2016; Prata and Bernardo, 2014), lidar ceilometers deployed for monitoring of meteorological clouds (e.g. Geisinger et al., 2016; Mona and Marenco, 2016), single or multi-wavelength aerosol lidars (e.g. Ansmann et al., 2010), dedicated satellite-derived ash plume measurements (e.g. (Balis et al., 2016) or from in situ measurements using particle counters mounted on aircrafts (e.g. Schumann et al., 2011) and on ground stations (e.g. Flentje et al., 2010).

In addition, the IAVCEI Commission for Tephra Hazard Modeling completed a benchmarking exercise for plume models of both strong and weak plumes (Costa et al., 2016b) and collaborates with the ICAO Volcanic Ash Scientific Advisory Group (VASAG) in building a database including satellite data, NWPM results and ESPs for recent eruptions. These efforts will constitute the first open dataset for VATDM validation.

1.4.4 ERC Training Networks

The 2010 Eyjafjallajökull eruption also stressed the associated threats to volcanic eruptions and emphasized that Europe has and is surrounded by active volcanoes and, therefore, must be prepared for similar future events. In that context the European Research Council (ERC) has pioneered two Initial Training Networks (ITN) under the FP7 Framework to form the next generation of European volcanologists and modelers. These networks account for a unique and innovative portfolio of partners from academia, research institutes and the private sector from several European countries.

1.4.4.1 NEMOH - Numerical, Experimental and stochastic Modeling of vOlcanic processes and Hazard (FP7/2007-2013 - REA grant agreement n° 289976)

NEMOH was an Initial Training Network under the European Community FP7 running from 2012 to 2016. The objective of the network was that of forming the next generation of European volcanologists, capable of extending further the knowledge and understanding of volcano dynamics and the methods and paradigms for volcanic hazard evaluation. The NEMOH consortium was made of nine full Network Partners (Institutions playing a leading European and world-wide role in volcano research, volcanic hazard forecasting, and management of volcanic crises), plus four Associated Partners (including two SMEs - Small/Medium Enterprises) that fully participated to the network activities and contributed to the definition and development of the research and training programs under the network. The network was

conceived for the appointment of 18 Early Stage Researcher (ESRs) for a total of 528 person months (PM).

NEMOH targeted mainly seven research activities:

i. Laboratory determination of single-phase and multiphase magma-rock properties
ii. Analogue modeling
iii. Numerical simulation of magma and eruption dynamics
iv. Fluid-Rock interaction dynamics and rock transfer functions;
v. Source models and inversion procedures;
vi. Mixed deterministic/stochastic approach for the simulation of volcanic processes;
vii. Volcanic hazard assessment.

The training part of the network was conceived to be developed in the context of internationally coordinated research structured in closely interconnected research activities, including: i) the physical mechanisms of volcanic eruptions; ii) the numerical techniques for both the solution of complex space-time-dependent equations that describe the physical processes, and their constrain through inverse modeling of large datasets, and; iii) the techniques to deal with the uncertain, stochastic nature of volcanic processes and hazard.

More information of NEMOH objectives, deliverables and outcomes can be found at http://www.nemoh-itn.eu/.

1.4.4.2 VERTIGO - Volcanic ash: FiEld, expeRimenTal and numerIcal investiGations of prOcesses during its lifecycle (FP7/2013-2017 - REA grant agreement n° 607905)

VERTIGO is an on-going Initial Training Network under the European Community FP7 running from 2014 to 2018. The objective of the network is to address the challenging mission of providing an encompassing mechanistic and quantitative understanding of the physico-chemical processes during the lifecycle of volcanic ash: from formation in a volcano, through changes during the dispersal in the atmosphere to the impacts on life and society.The VERTIGO consortium was made of nine full Network Partners (Institutions playing a leading European and world-wide role in volcano research, volcanic hazard forecasting, and management of volcanic crises), plus fourteen Associated Partners (involving academia, research institutions and the private sector from eight European countries). The network was conceived for the appointment of 13 Early Stage Researcher (ESRs) for a total of 468 person months.

VERTIGO targets mainly five research activities:

i. Direct observation of explosive eruptions and characterization of proximal deposits;
ii. Experimental simulation of explosive eruptions and proximal deposition;

iii. Experimentally constraining the physico-chemical processes in the eruption column and the atmosphere;

iv. Numerical simulation of physico-chemical processes during explosive magma fragmentation and in eruption plumes;

v. Impact of volcanic ash on life.

More information of VERTIGO objectives, deliverables and expected outcomes can be found at http://www.vertigo-itn.eu.

Chapter 2

2 Description and evaluation of the NMMB-MONARCH-ASH v1.0 model

2.1 Introduction

This chapter describes and evaluate NMMB-MONARCH-ASH (Marti et al., 2017), a new on-line meteorological and atmospheric chemistry transport model to simulate the emission, transport and deposition of tephra particles released from volcanic eruptions. The final objective in developing NMMB-MONARCH-ASH is two-fold. On one hand, at a research level, this chapter aims at studying the differences between the on-line/off-line modeling strategies. On the other hand, at an operational level, it aims to develop a robust and low-cost computational model that can be applied for more accurate on-line operational forecasting of volcanic ash clouds. The chapter is organized as follows; Section 2.2 describes the main characteristics of the meteorological core and the volcanic ash module. Section 2.3 describes the observational data and introduces the model evaluation strategy. Section 2.4 discusses the performance of the model and its cost-benefit analysis. Section 2.5 introduces the model operational set-up. Finally, Section 2.6 includes the conclusions of this chapter.

2.2 Model description

NMMB-MONARCH-ASH predicts ash cloud trajectories, concentration of ash at relevant flight levels, and the expected deposit thickness for both regional and global domains. The novel on-line coupling in the model allows solving both the meteorological and aerosol transport concurrently and interactively at every time-step. This coupling strategy aims at improving the current state-of-the-art of tephra dispersal models, especially in situations where meteorological conditions are changing rapidly in time, two-way feedbacks are significant, or distal ash cloud dispersal simulations are required. The model builds on the Multiscale Online Nonhydrostatic AtmospheRe CHemistry model (NMMB-MONARCH; formerly known as NMMB/BSC-CTM; Badia et al., 2017a; Haustein et al., 2012; Jorba et al., 2012; Pérez et al., 2011; Spada et al., 2013, 2015) to represent the transport of volcanic particles. The following subjects present a comprehensive description of the meteorological and volcanic ash components of the model.

2.2.1 Meteorological core

Its meteorological core, the Non-hydrostatic Multiscale Model on a B grid (NMMB; Janjic and Black, 2007; Janjic and Gall, 2012; Janjic, 2005; Janjic et al., 2011), is a fully compressible meteorological model with a non-hydrostatic option that allows for nested global-regional atmospheric simulations by using consistent physics and dynamics formulations. The non-hydrostatic dynamics were designed to avoid over-specification. The cost of the extra non-hydrostatic dynamics is about 20% of the cost of the hydrostatic part, both in terms of computer time and memory (Janjic, 2001, 2003).

The numerical schemes for the hydrostatic and nonhydrostatic options available in the NMMB dynamic solver were designed following the principles found in Janjic (1977) and developed and modified thereafter (Janjic, 1979, 1984, 2003), and are summarized in Janjic and Gall (2012). The Arakawa B-grid horizontal staggering is applied in the horizontal coordinate employing a rotated latitude-longitude coordinate for regional domains and latitude-longitude coordinate (Janjic, 2003) with polar filtering for global domains. Rotated latitude-longitude grids are employed for regional simulations in order to obtain more uniform grid distances. In this particular case, the equator of the rotated system runs through the middle of the integration domain, reducing the longitudinal grid-size as the southern and the northern boundaries of the integration domain are approached (Janjic and Gall, 2012). In the vertical, the Lorenz staggering vertical grid is used with a hybrid sigma-pressure coordinate. The general time integration philosophy in NMMB uses explicit schemes when possible for accuracy, computational efficiency and coding transparency (e.g., horizontal advection), and implicit for fast processes that would otherwise require a restrictively short time-step for numerical stability with explicit differencing (e.g., vertical advection and diffusion, vertically propagating sound waves).

NMMB is placed within the NOAA Environmental Modeling System (NEMS) infrastructure: a shared, portable, high performance software superstructure for use in operational prediction models at the National Centers for Environmental Prediction (NCEP). The NEMS architecture is based on the Earth System Modeling Framework (ESMF; Janjic and Black, 2007), and follows the general modeling philosophy of the NCEP regional WRF-NMM (Weather Research and Forecasting framework – Non-hydrostatic Mesoscale Model; Janjic et al., 2001; Janjic, 2003). The NMMB model became operational in October of 2011 as the NCEP North American Mesoscale (NAM) meteorological model, and it has been computationally robust, efficient and reliable in operational applications and pre-operational tests since then. In high-resolution NWP applications, the efficiency of the model significantly exceeds those of several established state-of-the-art non-hydrostatic models (e.g. Janjic and Gall, 2012).

The following sections include a comprehensive description of the model dynamics, numeric, and physics employed by the model. The standard physical and numerical schemes employed in NMMB are summarized in Table 4.

Meteorological Solver	*Scheme*	*Reference*
Spatial discretization		
Multi-scale domain ranging from large eddy simulations (LES) to global simulations		Janjic (2005)
Conservativeness		
Conservation of mass, momentum, energy, enstrophy and a number of other first order and quadratic quantities. Positive definiteness and monotonicity are preserved by tracer advection		Janjic (1984)
Coordinates /Grid		
Horizontal coordinate	Rotated latitude-longitude for regional domains, and latitude-longitude coordinate with polar filter for global domains	Janjic et al. (2009); Janjic and Gall, (2012)
Vertical coordinate	Terrain following hybrid sigma-pressure	Simmons and Burridge, (1981)
Horizontal grid	Arakawa B-grid staggering	Janjic, 2005; Janjic and Black, 2007)
Vertical grid	Lorenz staggering	Lorenz, (1960)
Time integration schemes		
Horizontally propagating fast-waves	Forward-backward scheme	Ames, (1969); Gadd, (1974); Mesinger, (1977); Janjic, 1979)
Vertically propagating sound waves	Implicit scheme	Janjic and Gall, (2012)
Horizontal advection & Coriolis terms	Modified (Stable) Adams-Bashforth scheme	
Vertical advection	Crank-Nicolson scheme	Janjic, (1977,1984)
TKE generation and dissipation	Iterative	
Advection terms		
Horizontal	Energy and enstrophy conserving, quadratic conservative, second order	Janjic and Gall, (2012)
Vertical	Quadratic conservative, second order	Janjic and Gall, (2012)
Diffusion terms		
Vertical	Surface layer scheme	Janjic (1994, 1996)
Lateral	Smagorinsky non-linear approach	Janjic (1990)
Physics Options		
Microphysics/Clouds	Ferrier (Eta)	Ferrier et al. (2002)
Short and Longwave Radiation	Rapid Radiative Transfer Model (RRTM)	Mlawer et al. (1997); Pérez et al. (2011)
Surface Layer	NMMB similarity theory scheme: Based on Monin-Obukhov similarity theory with Zilitinkevich thermal roughness length	Monin and Obukhov (1954); (Zilitinkevich, 1965a); Janjic (1994, 1996)
Land Surface, Heat & moisture surface flux	LISS model	Vukovic et al. (2010)
Planetary Boundary layer / free atmosphere	Mellor-Yamada-Janjic scheme	Mellor and Yamada, (1982); Janjic (1996, 2001)
Convective adjustments	Betts-Miller-Janjic scheme	Betts and Miller, (1986); Janjic (1994, 2000).

Table 4. Main characteristics of the NMMB-MONARCH-ASH meteorological solver.

2.2.1.1 The NMMB dynamics

The NMMB dynamics solver together with various options for physics, initialization and post processing are combined within the NEMS framework to produce end-to-end multiscale simulations. The solver includes fast waves, advection, thermodynamic processes, a nonhydrostatic add-on module, lateral

diffusion, horizontal divergence damping, coupling of the sub-grids of the semi-staggered grid B, boundary conditions, polar filtering and nesting capabilities. In addition, it also includes transport of various components of the atmosphere such as moisture variables and other tracers Janjic and Gall (2012).

This section provides a brief overview of the atmospheric fluid dynamic equations implemented in NMMB dynamics solver. For a full review of the scientific and algorithmic approaches in the NMMB dynamics refer to the Janjic and Gall (2012) technical note. The NMMB dynamics solver equations are characterized for being fully compressible, Eulerian and nonhydrostatic with a hydrostatic option.

The hydrostatic mass continuity equation is obtained from:

$$\left[\frac{\partial}{\partial t}\left(\frac{\partial \pi}{\partial s}\right)\right] + \nabla_s + \left(\boldsymbol{v}\frac{\partial \pi}{\partial s}\right) + \frac{\partial}{\partial s}\left(\dot{s}\frac{\partial \pi}{\partial s}\right) = 0 \qquad (3)$$

where π is the hydrostatic pressure; s denotes a generalized mass based terrain following vertical coordinate that varies from 0 at the model top to 1 at the surface (e.g. Eckermann, 2009); $\boldsymbol{v}$ represents the horizontal velocity vector; and $\dot{s}$ is the vertical velocity and the subscripts indicate the variable that is kept constant while the differentiation is performed.

The nonhydrostatic dynamics extension in NMMB is implemented through an add–on nonhydrostatic module. This module can be turned on and off depending on resolution in order to eliminate the computational overhead at coarse and transitional resolutions where the impact of nonhydrostatic effects is not detectable $\Delta x \sim \Delta y > 10\text{Km}$. The nonhydrostatic option in NMMB was designed to avoid over-specification, reducing about 20% of the cost of the hydrostatic dynamics both in terms of computer time and memory.

The following equations summarize the relaxed hydrostatic approximation used in NMMB. The hypsometric equation $\frac{\partial \phi}{\partial \pi} = -\alpha$, relates the geopotential ϕ to the hydrostatic pressure π. If the atmosphere is assumed to be dry, the specific volume is related to the temperature T and actual pressure p by the ideal gas law $\alpha = {}^{RT}/_{p}$ (R being the gas constant). Note that the ideal gas law does not involve the hydrostatic pressure but rather the actual pressure, p, hereafter referred to as nonhydrostatic pressure. Using the hypsometric equation, the third (vertical) equation of motion may be written as:

$$\frac{\partial p}{\partial \pi} = 1 + \varepsilon \qquad (4)$$

which defines the relationship between the hydrostatic and the nonhydrostatic pressures, and where $\varepsilon \equiv \frac{1}{g}\frac{\partial w}{\partial t}$, defines the ratio of the vertical acceleration (w) and gravity (g). As can be seen from Eq. (4) should ε vanish, the pressure and the hydrostatic pressure become equivalent.

In the hydrostatic s coordinate system, the nonhydrostatic continuity equation takes the form:

$$w = \frac{1}{g}\left[\left(\frac{\partial \phi}{\partial t}\right)_s + \boldsymbol{v} \cdot \nabla_s \phi + \left(\dot{s}\frac{\partial \pi}{\partial s}\right)\frac{\partial \phi}{\partial \pi}\right] + W_{(\lambda,\varphi,t)} \tag{5}$$

i.e., reduces to the definition of the vertical velocity w. Where W denotes an integration constant that may depend on horizontal coordinates and time; $\dot{s}$ is the vertical velocity and the subscripts indicate the variable that is kept constant while the differentiation is performed.

In the hydrostatic s coordinate system, the time derivative of a fluid property q following the motion of an air parcel may be written as:

$$\frac{dq}{dt} = \left(\frac{\partial q}{\partial t}\right)_s + \boldsymbol{v} \cdot \nabla_s q + \left(\dot{s}\frac{\partial \pi}{\partial s}\right)\frac{\partial q}{\partial \pi} \tag{6}$$

The operator presented in Eq. (6) is applied to the nonhydrostatic continuity Eq. (5) to obtain the vertical acceleration $\frac{dw}{dt}$. Then, from vertical acceleration and gravity ratio:

$$\varepsilon = \frac{1}{g}\frac{dw}{dt} = \frac{1}{g}\left[\left(\frac{\partial w}{\partial t}\right)_s + \boldsymbol{v} \cdot \nabla_s w + \left(\dot{s}\frac{\partial \pi}{\partial s}\right)\frac{\partial w}{\partial \pi}\right] \tag{7}$$

The inviscid nonhydrostatic equation for the horizontal part of the wind (momentum equation) takes the form:

$$\frac{d\boldsymbol{v}}{dt} = -(1+\varepsilon)\nabla_s \phi - \alpha \nabla_s p + f\mathbf{k} \cdot \mathbf{v} \tag{8}$$

Finally, the thermodynamic equation takes the form:

$$\frac{\partial T}{\partial t} = -\boldsymbol{v} \cdot \nabla_s T - \left(\dot{s}\frac{\partial \pi}{\partial s}\right)\frac{\partial T}{\partial \pi} + \frac{\alpha}{c_p}\left[\frac{\partial p}{\partial t} + \boldsymbol{v} \cdot \nabla_s p + \left(\dot{s}\frac{\partial \pi}{\partial s}\right)\frac{\partial p}{\partial \pi}\right] \quad (9)$$

where T denotes temperature, and c_p is the specific heat at constant pressure.

The parameter ε is the key factor of the extended, nonhydrostatic dynamics in NMMB. The presence of nonzero ε in (Eq. 4), (Eq. 8) and (Eq. 9) indicates where, how, and to what extent are the familiar hydrostatic equations affected by relaxing the hydrostatic approximation. This approximation can be safely used for meso- and large scales where atmospheric flows $\varepsilon << 1$ (vertical acceleration is much smaller than the gravitational field). Previous works (Janjic and Gall, (2012) and reference therein) have shown that impact of nonhydrostatic dynamics becomes detectable at resolutions <10km, and is important at resolutions of about 1km.

2.2.1.2 The NMMB numerics

Horizontal domain. NMMB is discretized on an Arakawa semi-staggered B grid (Fig. 6), a form of spatial horizontal grid characterized for its accuracy in calculating the inertial-gravity waves (Arakawa and Lamb, 1977; Janjic et al., 2003) of the atmosphere and a better stability of the model.

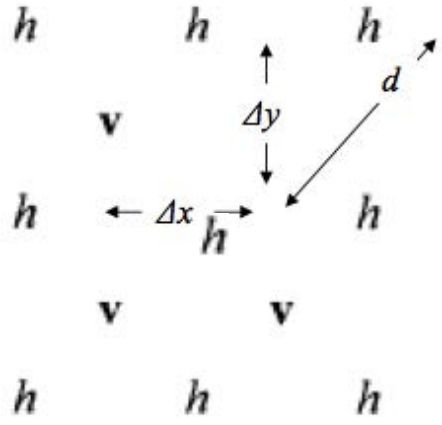

Figure 6. Arakawa semi-staggered B grid, where $\boldsymbol{h}$ represents mass points (temperature, pressure, height, any scalar variable) and v represents the horizontal velocity vector. The grid distances $\Delta \boldsymbol{x}, \Delta \boldsymbol{y}$ and d are also shown (extracted from Janjic and Gall, 2012).

The B-grid uses a regular latitude-longitude coordinate system for the global domain, and a rotated latitude-longitude system for regional applications (Fig. 7). The rotated regional domain is centered at the equator to obtain more uniform grid distances. In this particular case, the equator of the rotated system runs through the middle of the integration domain, reducing the longitudinal grid-size as the southern and the northern boundaries of the integration domain are approached (Janjic and Gall, 2012).

Figure 7. Horizontal coordinate system in NMMB for a domain centered at 38N, 92W. On the left side: domain plotted on a regular latitude longitude map background. On the right: the same domain is projected on a rotated latitude longitude map background (extracted from Janjic and Gall, 2012).

Vertical domain. NMMB uses a hybrid pressure-sigma vertical coordinate option (Eckermann, 2009; Simmons and Burridge, 1981) for consistency with NCEP's global spectral model. Hybrid σ-pressure coordinate schemes combine σ-denominated layers at the bottom (following terrain) with isobaric (pressure-denominated) layers aloft. In the hybrid coordinate system, the hydrostatic pressure can be obtained from:

$$\begin{aligned} \pi_{(x,y,s,t)} &= \pi_T + \sigma_1(s)\Pi + \sigma_2(s)\mu_{(x,y,t)} \\ \textit{at } \sigma\textit{-levels} \quad &= \pi_T + \Pi + \sigma_2(s)\mu_{(x,y,t)} \\ \textit{at p-levels} \quad &= \pi_T + \sigma_1(s)\Pi \end{aligned} \tag{10}$$

where π is the hydrostatic pressure, taking values of π_{sfc} at surface and π_T at the top of the model atmosphere; μ is the difference between π_{sfc} and π_T. The hydrostatic pressure depends on the horizontal (x, y), and terrain following vertical coordinate (s) - which varies from 0 at the model top to 1 at the surface, and time (t). Π is the constant depth of the hydrostatic pressure coordinate layer at the top of the model atmosphere. σ_1 is zero at the top and the bottom of the model atmosphere, and σ_2 increases from 0 to 1 from top to bottom (Fig. 8 left).

The Lorenz staggering of the variables (Lorenz, 1960) is used in the vertical (Fig. 8 right). The nonhydrostatic pressure and the geopotential are defined at the interfaces of the vertical layers, while the three components of the velocity and temperature are provided in the middle of the model layers

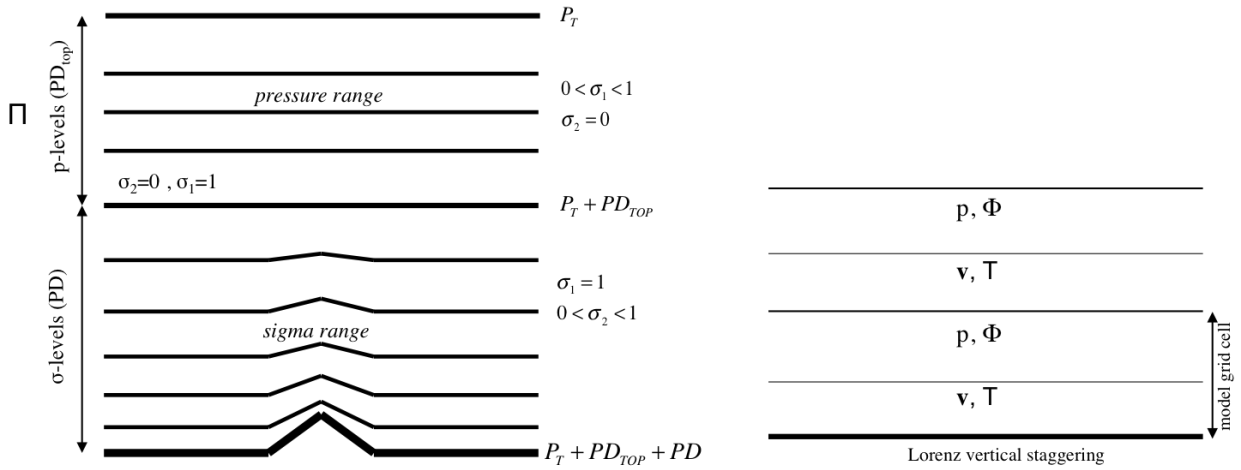

Figure 8. Vertical coordinate system in NMMB. On the left side: the vertical hybrid σ-pressure coordinate system. On the right the Lorentz vertical staggering of the variables. Solid lines represents the atmospheric layers while dotted lines represent middle levels within the layers (modified from Janjic and Gall, 2012).

Time stepping. The general time integration philosophy in NMMB is:

Explicit where possible for accuracy, computational efficiency and coding transparency of:

- Horizontal advection of u , v, T
- Advection of various other variables such as water vapor mixing ratio, cloud water, and turbulent kinetic energy (TKE)
- Adjustment terms (gravity-inertia waves)

Implicit for very fast processes that would require a restrictively short time-step for numerical stability with explicit differencing:

- Vertical advection
- Vertically propagating sound waves

For the basic dynamic variables the NMMB uses four types of time integration: (i) modified Adams-Bashforth for horizontal advection of u , v, T and tracers, and for Coriolis terms (f), (ii) Crank Nicholson for vertical advection of u , v, T and tracers, (iii) forward-backward scheme for adjustment terms and (iv) time integration for vertically propagating sound waves hidden inside the implicit algorithm used to solve the full model equations (Janjic and Gall, 2012).

2.2.2 The NMMB Physics

The physical package in NMMB is composed by: i) the Mellor-Yamada-Janjic (MYJ) (Mellor and Yamada, 1982; Janjic, 2001) level 2.5 turbulence closure for the treatment of turbulence in the planetary boundary layer (PBL) and in the free atmosphere (Janjic et al., 2001); ii) the surface layer schemes are based on the Monin-Obukhov similarity theory (Monin and Obukhov, 1954) with introduced viscous sublayer over land and water (Zilitinkevich, 1965; Janjic, 1994) and the NCEP Global Forecasting

System (GFS) scheme; iii) the Noah land surface model (Pan and Mahrt, 1987; Ek et al., 2003) or the LISS model (Vukovic et al., 2010) for the computation of the heat and moisture surface fluxes, iv) the RRTM longwave and shortwave radiation (Mlawer et al., 1997; Pérez et al., 2011); v) the Ferrier gridscale clouds and microphysics (Ferrier et al., 2002); and vi) the cumulus parameterization schemes based on the Betts-Miller-Janjic convective adjustment scheme (Betts and Miller, 1986; Janjic, 1994, 2000), or the Simplified Arakawa-Schubert scheme (Han and Pan, 2011). Vertical diffusion is handled by the surface layer scheme and by the PBL scheme (Janjic, 1994). Lateral diffusion is formulated following the Smagorinsky non-linear approach (Janjic, 1990). Isotropic horizontal finite volume differencing is employed so a variety of basic and derived dynamical and quadratic quantities are conserved (Janjic, 1984).

2.2.3 The volcanic ash module

The ash module is embedded within the NMMB meteorological model and solves the mass balance equation for volcanic ash taking into account: i) the characterization of the source term (emissions); ii) the transport of volcanic particles (advection/diffusion); and iii) the particle removal mechanisms (sedimentation/deposition). The coupling strategy of this module can be turned on or off, depending on the solution required (on-line vs. off-line). The on-line version of the model solves both the meteorological and ash transport concurrently and consistently (on-line coupling). This strategy allows the particle transport to be automatically tied to the model resolution time and space scales, resulting in a more realistic representation of the meteorological conditions. To ensure consistency with the meteorological solver, the ash bins are advected at the corresponding time step of the meteorological tracers using the same numerical schemes implemented in the NMMB. In contrast, the off-line approach uses an “effective wind field” in which meteorological conditions (e.g. wind velocity, mid-layer pressure, etc.) are set to constant, and are only updated at specific coupling intervals. This strategy replicates the off-line coupling effect of traditional ash dispersal models used at operational level (e.g. coupling intervals of 1h or 6h). The conservativeness of the model is evaluated to ensure that the ash transport scheme is consistent with the mass conservation equation.

2.2.3.1 Source term

2.2.3.1.1 Mass eruption rate

The Mass Eruption Rate (MER) gives the mass released by unit of time and defines the eruption intensity. Its characterization in NMMB-MONARCH-ASH is achieved by employing a series of empirical correlations between (observed) column height and MER, which, according to the buoyant plume similarity theory, scales roughly as the 4^{th} power of height. Because of this strong dependence, uncertainties within 20% in the determination of column height can translate into uncertainties up to 70%

for the MER (e.g., Biass and Bonadonna, 2011). Averaged column heights of eruptions that have not been directly observed are typically derived from characteristics of tephra deposits (e.g. Bonadonna and Costa, 2013; Carey and Sparks, 1986; Pyle, 1989), or derived from model inversion (e.g. Connor and Connor, 2006; Marti et al., 2016; Pfeiffer et al., 2005).

The empirical correlations to estimate MER in the model are based either on fitting observations (e.g. Mastin et al., 2009), or more sophisticated fits accounting for wind bent-over effects (e.g. Degruyter and Bonadonna, 2012; Woodhouse et al., 2013). The mathematical representation of these empirical fits is described next. In addition, MER can also be derived using a more sophisticated 1-D plume model (see section 2.3.1.5), which, in addition, give the vertical distribution of mass.

Mastin et al. (2009) estimated MER using empirical correlations based on column height observation taken from the field:

$$MER = \bar{\rho}\left[\frac{0.5H_{plume}}{10^3}\right]^{\frac{1}{0.241}} \tag{11}$$

where $\overline{\rho}$ represents the density (2500 kg m^{-3}), and H_{plume} is the column height above the vent (m).

A more sophisticated fit to estimate MER was presented by Degruyter and Bonadonna (2012). This estimation accounts for the bent-over effects of winds on the eruption column:

$$MER = \pi\frac{\rho_{a0}}{g'}\left(\frac{\alpha^2\overline{N}^3}{z_1^4 n}H_{plume}^4 + \frac{\beta^2\overline{N}^2\bar{v}}{6}H_{plume}^3\right) \tag{12}$$

where ρ_{a0} is the atmospheric density at the vent (1,105 kg m^{-3}), $\overline{N}$ is the average Brunt-Väisälä buoyancy frequency (s^{-1}), $\bar{v}$ represents the average wind velocity across column height (m s^{-1}), z_1 is the maximum non-dimensional height, and α and β are the radial and crossflow entrainment coefficients taking values of 0.1 and 0.5, respectively. Finally, g' in Eq. (12) corresponds to the value for the reduced gravity, which is computed as:

$$g' = g\left(\frac{c_0\theta_0 - c_{a0}\theta_{a0}}{c_{a0}\theta_{a0}}\right) \tag{13}$$

where g is the gravitational acceleration (9.81 m s^{-2}), c_0 denotes the mixture specific heat capacity (1250 J kg^{-1} K^{-1}), c_{a0} is the specific heat capacity of the atmosphere (998 J kg^{-1} K^{-1}), θ_0 represents the source temperature (1200 K), and θ_{a0} is the atmospheric temperature (268.7 K).

Finally, Woodhouse (2013) followed the parameterizations presented by Degruyter and Bonadonna (2012) to include the bent-over effects of wind employing the following function for wind strength (W_S) as follows:

$$f(W_s) = {}^{1.44\dot{\gamma}}/_{\overline{N}} \tag{14}$$

where $\dot{\gamma}$ represents the shear rate of atmospheric wind (s^{-1}). The resulting dimensionless value for the wind strength is then used to find MER as follows

$$MER = 0.35\alpha^2 f(W_s)^4 \frac{\rho_{a0}}{g'} \overline{N}^3 H_{plume}^4 \tag{15}$$

In this case, Woodhouse (2013) computed the value for the reduced gravity (g') in Eq. (15) as follows:

$$g' = g\left(\frac{c_v n_0 + c_s(1-n_0)\theta_0 - c_a\theta_{a0}}{c_a\theta_{a0}}\right) \tag{16}$$

where c_s, c_a and c_v are the specific heat of solids, dry air and water vapor (J kg^{-1} K^{-1}), respectively.

2.2.3.1.2 Vertical distribution of mass

The vertical distribution of mass in the column at the vent location is key when representing the plume, especially if wind shear exists above the volcano (Lin, 2012). To determine the vertical distribution of mass, NMMB-MONARCH-ASH allows for the following geometrical distributions: i) point source, where mass is released as a single source point at a certain height above the vent, H_{plume}; ii) top-hat, where mass is released along a umbrella-type slab of user-defined thickness, and iii) the so-called Suzuki distribution (Suzuki, 1983; Pfeiffer et al., 2005), which assumes a more complex vertical distribution of mass release along the eruption column;

$$S = MER\left\{\left(1 - \frac{z}{H_{plume}}\right)\exp\left[A\left(\frac{z}{H_{plume}} - 1\right)\right]\right\}^{\lambda} \tag{17}$$

where $S(z)$ is the mass per unit of time (kg s^{-1}) released at a given height z above the vent, MER is the total mass eruption rate, H_{plume} is the column height above the vent and A and λ are the so-called Suzuki parameters. The parameter A dictates the height of the maximum particle release (typically taking values of 4 or 9 for Plinian or co-ignimbrite eruptions, respectively), whereas λ controls how closely mass distributes around this maximum. Any of the previous options (i.e. point, top-hat or Suzuki) above can be combined independently with the different fits for MER estimation. It is important to highlight that in

NMMB-MONARCH-ASH, the terrain following hybrid sigma-pressure vertical levels of the model are converted to elevations at each model integration time-step in order to interpolate MER from the discrete source points into the nodes of the model grid.

2.2.3.1.3 Total grain size distribution

The impact of explosive volcanic eruptions on climate and air traffic strongly depends on the concentration and grain size distribution (GSD) of pyroclastic fragments injected into the atmosphere (e.g. Girault et al., 2014). Grain size distribution is normally reconstructed by volcanologists from grain size data at individual outcrops, ranging from basic unweighted average of the GSD at individual sparse outcrops, to various integration methods of grain size data (e.g. Rose and Durant, 2009). The particle grain size distribution in NMMB-MONARCH-ASH is specified through an input file, which defines each particle bin properties (bin mass fraction, diameter, density and shape factor). In volcanology, grain size distributions are given in terms of the Φ-number, defined as $d = 2^{-\Phi}$, where d is the particle diameter in mm. The granulometry file in the model can be furnished by the user (typically derived from field data) or generated by an external utility program which produces Gaussian and Bi-Gaussian distributions in Φ (log-normal in diameter d) (Costa et al., 2016a; Folch et al., 2009).

2.2.3.1.4 Particle aggregation

The total grain size distribution (TGSD) erupted at the vent can be altered in case of particle aggregation, which dramatically impacts particle transport dynamics thereby reducing the atmospheric residence time of aggregating particles and promoting the premature removal of fine ash. For computational purposes, particle aggregation in NMMB-MONARCH-ASH is assumed to take place mainly in the eruption column, where particle concentration and water contents are higher (the subsequent formation of aggregates downstream in the ash cloud under the appropriate atmospheric conditions is not contemplated by the model). The model considers aggregates as another particle class (bin), introduced as a standard source term by considering either: i) a series of simple analytical expressions based on field observations or, ii) a more sophisticated wet aggregation model originally proposed by Costa et al. (2010). In this particular case, the source term must be computed with the plume model (see section 2.3.1.5).

The analytical expressions available in the model modify the user-given particle grain size distribution by assuming that a certain mass fraction of each granulometric class forms a new aggregate class that is added to the TGSD. Despite the obvious limitations (obviates the physics of aggregation processes), these field-based simplistic approaches are advantageous in that only the source term has to be modified in order to account for aggregation. Table 5 provides an overview of these options.

Name	***New aggregate class***	***Default aggregation properties***	***Reference***
NONE	No aggregation processes	n/a	n/a

CORNELL	50% of the 63–44 μm class aggregate 75% of the 44–31 μm class aggregate 100% of the < 31 μm class aggregate	Diameter = 250 μm Density = 350 kg m^{-3} Sphericity = 0.9	Based on Cornell et al. (1983) Campanian Ignimbrite's deposit (Y5 ash layer)
PERCENTAGE	Takes a user-defined fixed percentage from each particle class	Diameter = 250 μm Density = 350 kg m^{-3}	Based on Sulpizio et al. (2012)

Table 5. Ash aggregation options in NMMB-MONARCH-ASH from from field observations. Default aggregate properties can be modified by the user.

In addition to these empirical aggregation schemes, NMMB-MONARCH-ASH also includes a wet aggregation model originally proposed by Costa et al. (2010) and (Folch et al., 2010). This option allows for wet aggregation in the column providing an intermediate solution between the unaffordable all-size class approach and the empirical solutions presented before. The model is based on a solution of the classical Smoluchowski equation, obtained by introducing a similarity variable and a fractal relationship for the number of primary particles in an aggregate. It also considers three different mechanisms for particle collision: Brownian motion, ambient fluid shear, and differential sedimentation. The governing equations of this wet aggregation model are as presented below.

The number of particles (Δn_f) of a class j per unit of volume that aggregate during a time interval Δt is approximated by:

$$\Delta n_f \approx \frac{\Delta n_{tot} N_j}{\sum_k N_k} \quad (k = k_{min}, \dots, k_{max}) \tag{18}$$

where Δn_{tot} corresponds to the number of particles that decay per time interval, and N_k and N_j are the number of particles with diameter k and j in an aggregate, respectively. The number of aggregated particles with diameter j is computed employing a fractal prefactor ($k_f \approx 1$) and a fractal exponent ($D_f \leq 3$) as follows:

$$N_j = k_f \left(\frac{d_A}{d_j}\right)^{D_f} \tag{19}$$

where d_A is the aggregate diameter.

The total particle decay (Δn_{tot}) per unit volume during the interval Δt is obtained by integrating the coagulation kernel over all particle sizes:

$$\Delta n_{tot} = \alpha_m \left(A_B n_{tot}^2 + A_S \emptyset^{3/D_f} n_{tot}^{2-3/D_f} + A_{DS} \emptyset^{4/D_f} n_{tot}^{2-4/D_f}\right) \Delta t \tag{20}$$

where $\emptyset$ is the solid volume fraction, n_{tot} corresponds to the total number of particles that can potentially participate in the aggregation process per unit volume ($\sum_j \frac{6C_j}{\pi \rho_j d_j^3}$ $(j = j_{min}, \ldots, j_{max})$), and α_m denotes the sticking efficiency mean (size class averaged) calculated as:

$$\alpha_m = \frac{\sum_i \sum_j f_i f_j \alpha_{ij}}{\sum_i \sum_j f_i f_j} \tag{21}$$

where f_k is the class mass fraction, α_{ij} is the sticking efficiency between the classes i and j, and the addition on i and j is performed over the aggregating classes between k_{min} and k_{max}. Equation (20) considers the product of Eq. (21) times a collision frequency function which accounts for Brownian motion (A_B), laminar and turbulent fluid shear (A_S), and differential sedimentation (A_{DS}):

$$\begin{aligned} A_B &= -\frac{4k_b T}{3\mu_o} \\ A_S &= \frac{2\Gamma_S \mathcal{E}^4}{3} \\ A_{DS} &= -\frac{\pi(\rho_m - \rho_a) g \mathcal{E}^4}{48\mu_o} \end{aligned} \tag{22}$$

where k_b is the Boltzmann constant (1.38 × 10^{-23} m^2 kg s^{-2} K), T is the absolute temperature, μ_o symbolizes the dynamic viscosity of air, Γ_S is the fluid shear, $\mathcal{E}$ is the particle diameter to volume fractal relationship, ρ_m is the class averaged mean particle density, and ρ_a is the air density.

2.2.3.1.5 FPlume model

A more sophisticated approach to obtain MER and the vertical mass distribution in the column from the conditions at the vent consists of solving a 1-D radially averaged BPT model for mass, momentum, and energy. These 1-D plume models are more useful in operational roles and broad exploratory investigations (Costa et al., 2016b; Devenish et al., 2012). For that reason, NMMB-MONARCH-ASH is coupled with the 1-D FPlume model (Folch et al., 2016a); a 1-D cross-section averaged plume model which accounts for plume bent over, entrainment of ambient moisture, effects of water phase changes on the energy budget, particle fallout and re-entrainment by turbulent eddies, as well as variable entrainment coefficients fitted from experiments. The model also accounts for particle aggregation in presence of liquid water or ice that depends on column dynamics, particle properties, and amount of liquid water and ice existing in the column (Folch et al., 2010). This allows the plume model to predict an "effective" grain size distribution depleted in fines with respect to that erupted at the vent. For a complete definition of the governing equations of FPlume, refer to Folch et al. (2016a). FPlume has two solving strategies where the model: i) solves directly for column height for a given MER; or ii) solves iteratively for MER

for a given height. For any case, the following inputs need to be provided to the ash input file in NMMB-MONARCH-ASH: eruption start and duration, vent coordinates and elevation, conditions at the vent (exit velocity, temperature, magmatic water mass fraction, and total grain size distribution) and total column height or MER.

2.2.3.2 Particle advection and diffusion

Transport of volcanic ash by advection and turbulent diffusion is analogous to that of atmospheric tracers (e.g. moisture Janjic et al., 2009) in NMMB (see section 2.2.1), and follows the initial model developments focused on the implementation of the mineral dust aerosol component (NMMB/BSC-Dust; Haustein et al., 2012; Pérez et al., 2011). Tracer advection is Eulerian, positive-definite and monotone, maintaining a consistent mass conservation of the chemical species within the domain of study. The Adams-Bashforth scheme is used for horizontal advection and the implicit Crank-Nicolson scheme for vertical advection. In addition, particle advection in NMMB is coupled with a model to account for the gravity-driven transport above the vent in the umbrella region of the column, typically associated to high-intensity explosive eruptions. For the horizontal diffusion, the model uses a second order scheme with two types of parameterized dissipative processes: explicit lateral diffusion (often called horizontal diffusion, a 2nd order nonlinear Smagorinsky-type approach; Janjic, 1990) and horizontal divergence damping (Janjic and Gall, 2012).

2.2.3.2.1 Gravity-driven transport

Plumes from high-intensity eruptions can be injected high into the stratosphere, reaching a maximum column height and intruding laterally at the neutral buoyancy level (NBL) as a gravity current (Sparks et al., 1997). This gravity current can spread at velocities exceeding those of the surrounding winds, affecting tephra transport and deposition near the source. As larger particles are removed by deposition and air is entrained, the plume density decreases and momentum reduces such that, at a certain distance, atmospheric turbulence and wind advection become the dominant atmospheric transport mechanisms (Baines and Sparks, 2005). To account for this phenomena, NMMB-MONARCH-ASH is coupled with the model of Costa et al. (2013) describing cloud spreading as a gravity current. This parameterization calculates an effective radial velocity of the umbrella spreading (u_b) as a function of time (t) or cloud radius (R).

$$u_b(t) = \frac{2}{3}\left(\frac{3\lambda \bar{N} q}{2\pi}\right)^{1/3} t^{1/3} \tag{23}$$

$$u_b(R) = \left(\frac{2\lambda \bar{N} q}{3\pi}\right)^{1/2} \frac{1}{\sqrt{R}} \tag{24}$$

where λ is an empirical constant ($\lambda \approx 0.2$; Suzuki and Koyaguchi, 2009), $\overline{N}$ corresponds to the frequency of Brunt-Väisälä due to the ambient stratification of the atmosphere, and t is time. Finally, q symbolizes the volumetric flow rate into the umbrella region and can be estimated as a function of the efficiency of air entrainment, k, the MER, and the location of the eruption C:

$$q = C\sqrt{k}\frac{MER^{3/4}}{N^{5/8}} \tag{25}$$

$$C\begin{cases} 0.5\times10^{4}\ \mathrm{m^3kg^{-3/4}s^{-7/8}} & \text{for tropical eruptions} \\ 1.0\times10^{4}\ \mathrm{m^3kg^{-3/4}s^{-7/8}} & \text{for midlatitude and polar eruptions} \end{cases}$$

The effective radial velocity of the umbrella spreading is then combined with the wind field velocity (u_w) centered above the vent in the umbrella region to calculate the contribution of the gravitational spreading (ct) to the total cloud spreading:

$$ct = \left(\frac{u_b}{u_b + u_w}\right) \times 100 \tag{26}$$

To estimate the radial distance at which the critical transition between gravity-driven and passive transport occurs, the umbrella front velocity is compared with the mean wind velocity at the Neutral Buoyancy Level (NBL) estimating the Richardson number, Ri (gravity-driven regime when $Ri > 1$, passive transport regime for $Ri < 0.25$, and an intermediate regime in between these values):

$$Ri = \frac{u_b^2}{u_w^2} = \frac{4}{9u_w^2}\left(\frac{3\lambda N q}{2\pi}\right)^{2/3} t^{-2/3} \tag{27}$$

Finally from Eq. (24), the critical time-scales characterizing the passive t_p and gravity-driven t_b transport can be estimated:

$$\begin{aligned} t_p &= \frac{32\lambda N q}{9\pi u_w^3} \\ t_b &= \frac{4\lambda N q}{9\pi u_w^3} \end{aligned} \tag{28}$$

Neglecting the gravitational spreading of the umbrella cloud in tephra dispersal simulations could misrepresent the interaction of the volcanic ash cloud and the atmospheric wind field for high-intensity eruptions and for proximal deposition of tephra (Mastin et al., 2014).

2.2.3.3 Particle sedimentation

2.2.3.3.1 Particle settling velocity

Particle sedimentation in NMMB-MONARCH-ASH is governed by the terminal velocity of settling particles. This fall velocity is sensitive to particle size and atmospheric conditions, determining the residence time of ash particles in the atmosphere. NMMB-MONARCH assumes that the settling velocities of aerosols (mineral dust, sea salt, etc.) follow the Stokes law for spherical particles corrected by the Cunningham slip factor. The Stokes law applies to the creeping or Stokes flow regime, in which the drag force is proportional to particle velocity, and holds only for Reynolds numbers, $Re \lesssim 0.1$. This regime is justified for small particles and aerosols (< 20 μm). However, calculating settling velocities using the Stokes Law is less adequate for coarse ash (> 64 μm), which sediments much faster. In addition, ash particles are not spherical, which complicates and further slows fallout. In order to simulate properly a wider spectrum of particle sizes, NMMB-MONARCH-ASH adds a new sedimentation module that covers the turbulent regime ($Re \gtrsim 1000$) in which the drag force is proportional to the square of the particle velocity. In this case, the gravitational particle settling velocity, v_s ($m\ s^{-1}$), can be expressed as:

$$v_s = \sqrt{\frac{4g\left(\rho_p - \rho_a\right)d}{3C_d\rho_a}} \tag{29}$$

where ρ_a and ρ_p denote air and particle density, respectively, d is the particle equivalent diameter, and C_d is the drag coefficient (based on the Reynolds number). Strictly, the expression above is valid for spherical particles in the turbulent regime but it is often generalized to the whole range of Re numbers and particle shapes by defining the drag coefficient properly.

The different settling velocity models available in NMMB-MONARCH-ASH depend on the empirical evaluation of drag coefficient (C_d) and the assumed particle shape. In the framework of Eq. (29), the available sedimentation models in NMMB-MONARCH-ASH is presented next. First, the model includes a simple solution to compute the drag coefficient, assuming that all particles are spherical in shape. In that context, Arastoopour et al. (1982) defined the empirical evaluation of the drag coefficient as:

$$C_d = \begin{cases} \frac{24}{Re}\{1 + 0.15Re^{0.687}\} & Re \leq 988.947 \\ 0.44 & Re > 988.947 \end{cases} \tag{30}$$

This assumption for irregular particles only holds in the case of a laminar sedimentation regime (Bonadonna and Costa, 2013b). However, this approach is largely used in tephra dispersal modeling.

In order to provide analytical solutions of settling velocity specifically for irregular particles, NMMB-MONARCH-ASH relies on simple parameterizations of particle morphology, such as the ratio of the three orthogonal axes (Wilson and Huang, 1979) and sphericity (Dellino et al., 2005; Ganser, 1993). In particular, Ganser (1993) gives a fit valid over a wide range of particle sizes and shapes covering the spectrum of volcanic particles considered in volcanic column models (lapilli and ash):

$$C_d = \frac{24}{ReK_1}\{1 + 0.1118(ReK_1K_2)^{0.6567}\} + \frac{0.4305K_2}{1 + \frac{3305}{ReK_1K_2}} \tag{31}$$

where $K1$ and $K2$ are two shape factors depending on the particle orientation and particle sphericity, ψ, which is defined as:

$$K_1 = \frac{3}{\left[\left({}^{d_n}/_{d}\right)\right] + 2\psi^{-0.5}} \tag{32}$$

$$K_2 = 10^{1.8148(-Log\psi)^{0.5743}} \tag{33}$$

where d is the sphere of equivalent volume, d_n is the average between the minimum and maximum axis. The particle sphericity (ψ) takes the value of 1 for spherical particles, while for other shapes is provided as an input parameter by the user.

Following a similar approach than Ganser (1993), the Wilson and Huang (1979) model used the interpolation suggested by Pfeiffer et al. (2005) to provide suitable C_d valid for different particle sizes and shapes:

$$C_d = \begin{cases} \frac{24}{Re}\varphi^{-0.828} + 2\sqrt{1.07 - \varphi} & Re \leq 10^2 \\ 1 - \frac{1 - C_d|_{Re=10^2}}{900}(10^3 - Re) & 10^2 \leq Re \leq 10^3 \\ 1 & Re \leq 10^3 \end{cases} \tag{34}$$

where $\varphi = (b + c)/2a$ is the particle aspect ratio ($a \geq b \geq c$ denote the particle semi-axes).

Finally, NMMB-MONARCH-ASH also includes the Dellino et al. (2005) sedimentation model focused to describe the sedimentation of larger particles:

$$v_s = 1.2605\frac{v_a}{d}(Ar\varepsilon^{1.6})^{0.5206} \tag{35}$$

where $Ar = gd^3(\rho_p - \rho_a)\,{}^{\rho_a}/_{\mu_a^2}$ is the Archimedes number, g is the gravity acceleration, ε is a particle shape factor (sphericity to circularity ratio), μ_a is the dynamic viscosity, d is the particle equivalent diameter, and ρ_a and ρ_p are the air and particle density, respectively.

2.2.3.3.2 Dry deposition

Dry deposition, acting at the bottom layer of the model, is a complex process depending on physical and chemical properties of the particle, the underlying surface characteristics and micro-meteorological conditions. Dry deposition in the model is based on that originally proposed by Zhang et al. (2001). This parameterization has been updated to account for the different settling velocities available for volcanic particles - Eq. (29). The dry deposition velocity in the model, v_d ($m\ s^{-1}$), is given by:

$$v_d = v_s + \frac{1}{(R_a + R_s)} \tag{36}$$

where R_a is the aerodynamic resistance of the particle, and R_s is the surface resistance (both in $s\ m^{-1}$). These terms take into account all the effects of the lowermost layer of the atmosphere, such as turbulence (R_a) and Brownian diffusion, impaction and interception (R_s). It is worth mentioning that, for most of its resident time, airborne volcanic ash lies above the near-surface atmospheric layers, where gravitational settling dominates. This fact implies that, in most cases, dry deposition has little influence on model results for volcanic ash.

2.2.3.4 Mass conservation

Mass conservation is a critical requirement for any atmospheric transport algorithm. Non-conservative schemes can significantly underestimate or overestimate concentrations, especially for long time integrations, in which it is critical that the tracer advection scheme is consistent with the mass continuity equation (Jöckel et al., 2001). Most mesoscale meteorological models use observation/analyzed fields or global model results as initial conditions, and therefore they are not very sensitive to slowly accumulated mass inconsistencies as re-initializations remove accumulations. However, dispersal models are usually very sensitive to mass inconsistencies set in previous simulations or spin-up fields as initial conditions, thereby accumulating mass inconsistencies.

In addition to mass conservation, monotonicity and prevention of non-physical under and overshoots in the solution are also a highly desirable characteristics in transport schemes (Rood, 1987). For these reasons, the model includes a conservative, positive definite (i.e. tracer is a positive scalar) and monotone (i.e. entirely increasing) Eulerian scheme for advection. The positive definiteness in the model is guaranteed by advecting the square root of the tracer using a modified Adams-Bashforth scheme for the

horizontal direction and a Crank-Nicolson scheme for the vertical direction. The conservation of the tracer is achieved as a result of the preservation of quadratic quantities by the advection scheme. Monotonization is applied *a posteriori* to eliminate new extrema (Janjic et al., 2009). The conservative nature of NMMB-MONARCH-ASH is evaluated by calculating the mass flux at the boundaries (for regional domains) of the computational domain, the airborne mass, and the mass deposited on the ground to verify mass conservation at each time-step (e.g. < 0.5% mass creation for a 30 day simulation).

2.3 Model evaluation

The forecast skills of NMMB-MONARCH-ASH have been tested for several well-characterized eruptions, including the 39ka Campanian Ignimbrite (Italy), Decepcion Island 1970 (Antarctica), Pinatubo 1991 (Philippines), Etna 2001 (Italy), Chaitén 2008 (Chile), Eyjafjallajökull 2010 (Iceland), and Cordón Caulle 2011 (Chile) eruptions (e.g. Marti et al., 2013, 2014, 2015, 2016, 2017). This section presents two applications of the model for the ash dispersal forecast of weak and strong long lasting eruptions. Section 2.3.1 summarizes the results of the regional and global simulations for the first days of the 2011 Cordón Caulle eruption. This event represents a suitable case study of strong long-lasting eruptions with changing winds, which is useful to evaluate the advantages of the on-line approach for operational forecast. In a parallel effort, Sect. 2.3.2 summarizes the results from the regional configuration of the model for the 2001 Etna eruption. This eruption is a good example of a weak, long-lasting eruption, useful when evaluating the sedimentation mechanisms of the model against well-characterized tephra deposits.

2.3.1 The 2011 Cordón Caulle eruption

The 2011 Cordón Caulle eruption was a typical mid-latitude Central and South Andean eruption, where dominating winds carried ash clouds over the Andes causing abundant ash fallout across the Argentine Patagonia. Besides the significant regional impacts on agriculture, livestock and water distribution systems, this eruption stranded thousands of passengers due to air traffic disruptions in the southern hemisphere, thereby causing important economic losses to airlines and society (e.g. Raga et al., 2013; Wilson et al., 2013). This event evidenced the global nature of the volcanic ash dispersion phenomena and highlights the need for accurate real-time forecasts of ash clouds.

The Cordón Caulle volcanic complex (Chile, 40.5º S, 72.2º W, vent height 1420 m a.s.l.) reawakened on 4 June 2011 around 18:30 UTC after decades of quiescence. The initial explosive phase spanned more than two weeks, generating ash clouds that dispersed over the Andes. The climactic phase (~27 h) (Jay et

al., 2014) was associated with a ~9 km (a.s.l.) high column (Osores et al., 2014). For the period between 4 - 14 June, numerous flights were disrupted in Paraguay, Uruguay, Chile, southern Argentina and Brazil. The two major airports serving Buenos Aires and the international airport of Montevideo, Uruguay, were closed for several days, along with airports in Patagonia (Wilson et al., 2013). A detailed chronology of the eruption can be found in Collini et al. (2013) and Elissondo et al. (2016), the stratigraphy and characteristics of the resulting fallout deposit are described in Pistolesi et al. (2015) and Bonadonna et al., (2015b), and a summary of the environmental impacts of the eruption is discussed in Raga et al. (2013) and Wilson et al. (2013). This section describes the synoptic meteorological situation during the first two weeks of eruptive activity (Fig. 9), and gives a brief chronology of the events in order to compare them with the predictions of the model.

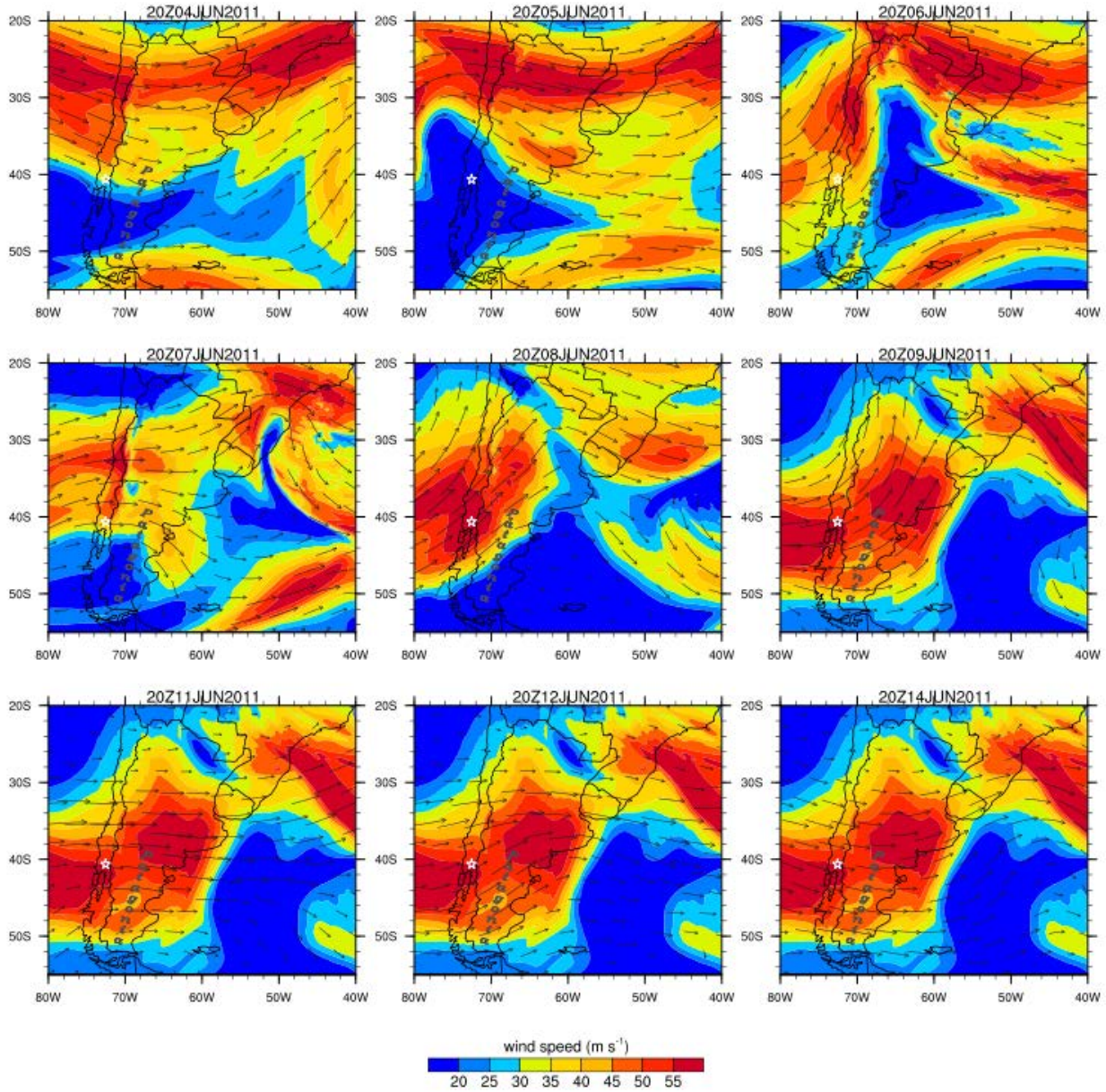

Figure 9. Meteorological synoptic situation during the first two weeks (4-14 June) of the 2011 Caulle (white star) activity over South America. Plots show the direction (vector) and velocity (contours m s^{-1}) of the wind at 9100 m above ground level (300 hPa circa). Meteorological data obtained from the NMMB meteorological forecast driven with ERA-Interim reanalysis at 0.75º horizontal resolution (extracted from Marti et al., 2017).

The eruption developed as a long-lasting rhyolitic activity with plume heights above the vent between 9-10 km high a.s.l. (4-6 June), 4 and 9 km during the following week (7-14 June) and < 6 km after 14 June (Global Volcanism Program, GVP, http://www.volcano.si.edu). The first major episode, on 4 June (18:45 UTC), resulted in an ash cloud (9-10 km) that reached the Chile-Argentina border within the hour of the eruption. On June 5, E-SE winds drove the plume to the Atlantic Ocean (1800 km away from the source), leaving a large area of Argentina territory affected by ash fall. On June 6, the plume changed its direction abruptly toward N-NE, reaching the northern regions of the Argentine Patagonia, and then shifted direction again towards SE, threating the Buenos Aires air space. On June 7, a second episode resulted in a plume (4-9 km) dispersing ash further to the north of Argentina leading to a more recognizable shift of winds over the E-SE. On June 8, the volcanic cloud (9-10 km a.s.l.) dispersed towards NE with a bend toward SE 400 km from the source. On June 9, the plume had a NE direction reaching the city of Buenos Aires and the northern boundary of Paraguay following a frontal zone passing through Patagonia. This resulted in major air traffic disruption at the two airports that service the city: Aeroparque (AEP) and Ezeiza (EZE), which remained closed intermittently during the following 15 days. Later during the day, the wind turned SE dispersing ash over Uruguay, Brazil and Paraguay. Ash cloud continued to change in direction over the next 6 days, with clouds following the ridge structure to the NE and SE, respectively.

2.3.1.1 Regional simulation

2.3.1.1.1 Model set-up

The model domain for the regional run is presented in Table 6 and consists of 268x268x60 grid points covering the northern regions of Chile and Argentina using a rotated latitude–longitude grid with a horizontal resolution of 0.15º x 0.15º. The top pressure of the model was set to 21 hPa (~34 km) with a mesh refinement near the top (to capture the dispersion of ash) and the ground (to capture the characteristics of the atmospheric boundary layer). The computational domain spans in longitude from 41º W to 81º W and in latitude from 18º S to 58º S. Runs were performed with the on-line version of NMMB-MONARCH-ASH from 3 June 2011 at 00:00 UTC to 21 June 2011 at 00:00 UTC. The integration time-step for the meteorological core and aerosol transport was set to 30 seconds. The dynamic time-steps for the long and short wave radiations were computed every 120 time-steps. Feedback effects of ash particles on meteorology and radiation were not included in this run. The meteorological driver was initialized with wind fields from the Era-Interim reanalysis at 0.75º x 0.75º resolution as initial and 6-h boundary conditions. In order to reduce the errors in meteorological conditions, they were reinitialized every 24 h with a spin-up of 12 h.

Daily eruption source parameters (ESP) were obtained from Osores et al. (2014), who estimated column heights for each eruptive pulse using the Imager Sensor data from the GOES-13 satellite, applying the

cloud-top IR image technique (Kidder and VonderHaar, 1995). Mass flow rate released along the column was derived from column heights based on Mastin et al. (2009), assuming a Suzuki vertical distribution of mass typical of explosive Plinian eruptions (A=4 ; λ=5). Grain size distribution was obtained from Collini et al. (2013) and discretized in 10 bins ranging from -1Φ (2 mm) to 8Φ (4 μm) with a linear dependency of particle density on diameter ranging from 1.000 to 2.200 kg m^{-3}. Particle sphericity was set to a constant standard value of 0.9 for all bins. The P*ercentage* aggregation model was used to update the TGSD with a new bin for aggregates, resulting in a total of 11 bins.

MODEL CONFIGURATION

Dynamics	NMMB (30s/180s time-step)
Physics	Ferrier microphysics BMJ cumulus scheme MYJ PBL scheme LISS land surface model
Aerosols	11 ash bins (30s/180s time-step)
Source Term (emissions)	
Duration	20 days
Vertical distribution	Suzuki distribution
MER formulation	Mastin et al. (2009)
Aggregation model	Percentage
Sedimentation model	Ganser (1993)
Run Set-up	
Number of processors	512
Domain	Regional/Global
Horizontal resolution	0.15º x 0.15º / 1º x 0.75º
Vertical layers	60
Top of the atmosphere	21 hPa
Meteorology Boundary conditions (spatial resolutions)	ECMWF EraInterim Reanalysis (0.75º x 0.75º)

Table 6. Model configuration for the 2011 Cordón Caulle regional and global runs. The regional run used a horizontal resolution of 0.15º x 0.15º with a 30s dynamic time-step, while the global domain used a horizontal resolution of 1º x 0.75º with a 180s dynamic time-step.

2.3.1.1.2 Validation of results against satellite imagery

Model results for the airborne mass concentration of ash were validated using qualitative and quantitative comparisons with data obtained using two different techniques. On one end, a qualitative comparison is performed between the simulated column mass (g m^{-2}) from the model and the NOAA-AVHRR satellite imagery provided by the high-resolution picture transmission (HRPT) division of the Argentinian National Meteorological Service. Figure 10 shows how the model forecasts for cloud trajectory and arrival times are in agreement with observations, capturing the three major dispersion episodes. It should

be noted that these types of images are not directly comparable because the MODIS ash detection threshold and the reflectivity coefficients of volcanic ash are not well constrained. However, the figure illustrates the capability of the model to predict the variation of the cloud position with time.

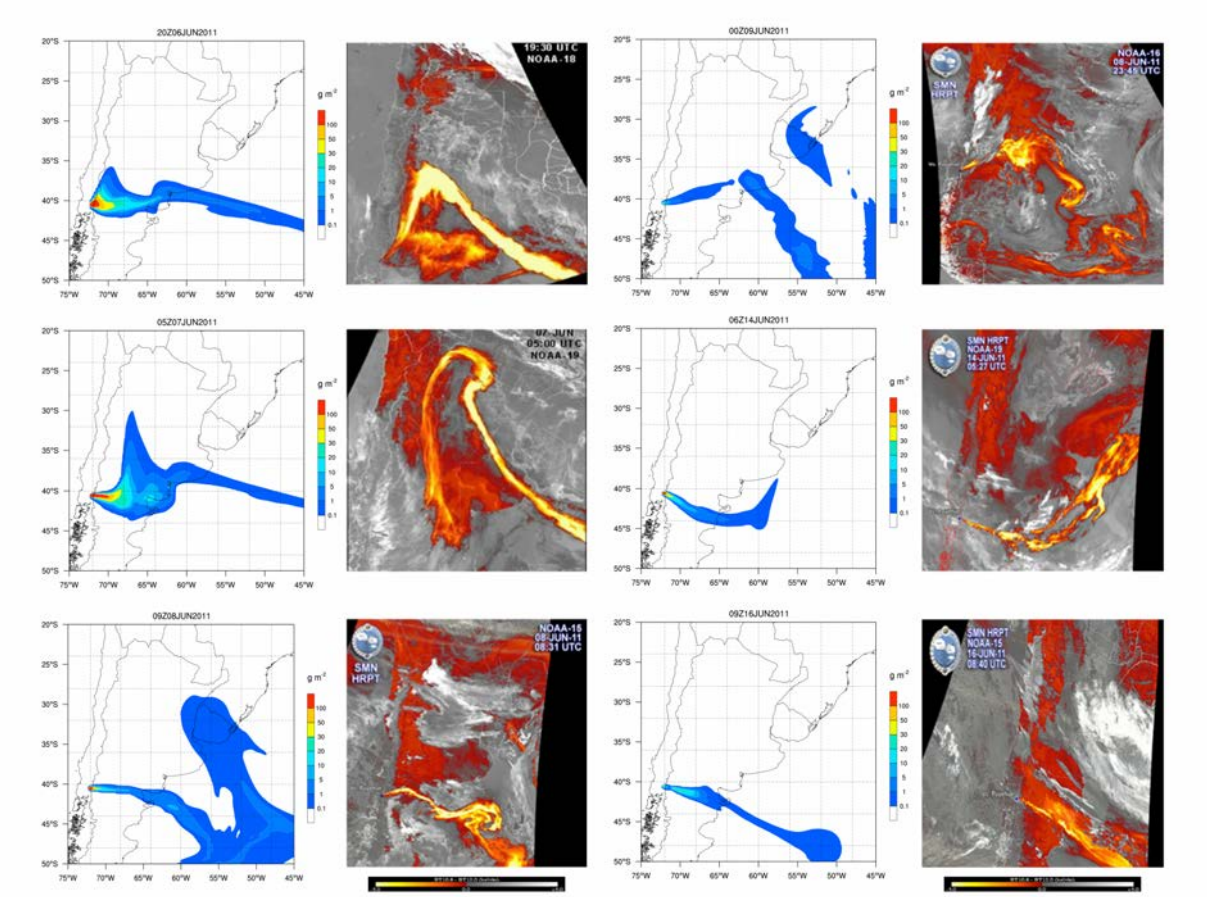

Figure 10. Composite image of NMMB-MONARCH-ASH results for dispersion of ash for the 2011 Caulle eruption at different time slices. Simulation results are compared against split window algorithm NOAA-AVHRR satellite images (bands 11-12 microns). Contours indicate ash column load (g m^{-2}) resulting from integrating the mass of the ash cloud along the atmospheric vertical levels (extracted from Marti et al., 2017).

Column mass simulations were also validated against ash mass loadings presented by Osores et al. (2015), who retrieved ash-contaminated pixels detected on the basis of the concept of reverse absorption (Prata, 1989a, 1989b), i.e. those pixels with brightness temperature differences between 11 and 12 μm (BTD11-12 μm) that are lower than 0 K. To minimize the presence of false positives, pixels with a BTD11-12 μm > -0.6 K and clear sky pixels were removed. Mass loadings were mapped up to 15 g m^{-2} based on an approach which combines the satellite data with look-up tables of brightness temperatures obtained with a radiative transfer model and optical properties of andesite volcanic rocks (Prata, 2011).

Figure 11 shows a good quantitative agreement between the model results and the airborne ash mass loadings described above.

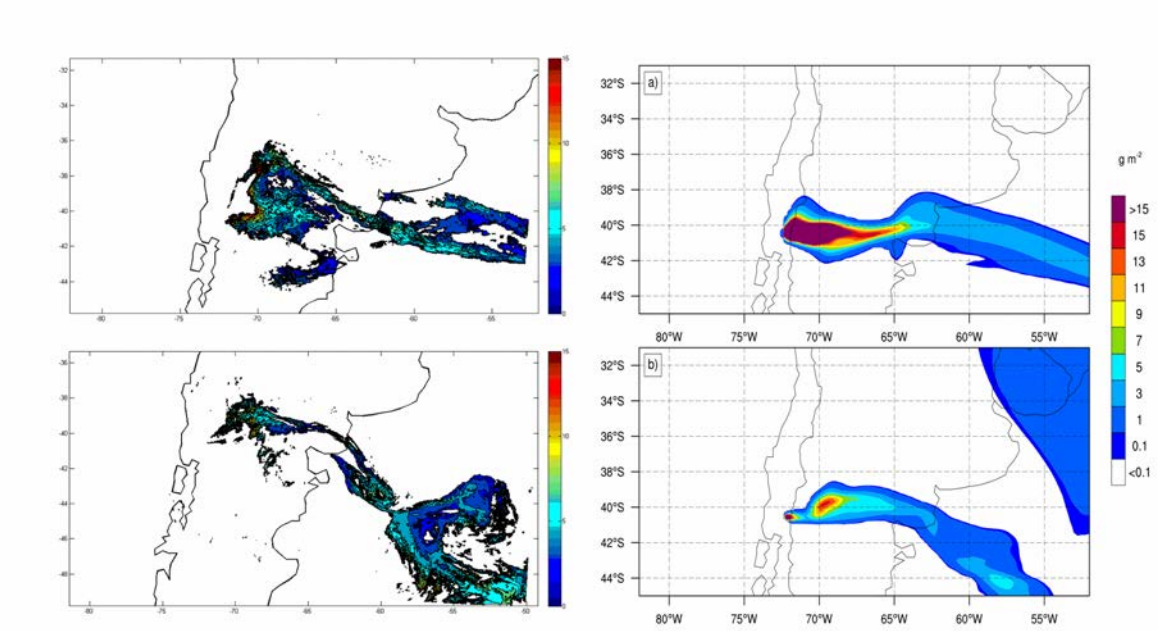

Figure 11. Left: Mass loadings (g m^{-2}) of the 2011 Caulle volcanic ash cloud from the MODIS-based retrievals (Osores et al., 2015). Right: Predicted column mass (g m^{-2}) with NMMB-MONARCH-ASH for a) 6 June at 14:25 UTC and, b) 8 June at 14:15 UTC (extracted from Marti et al., 2017).

2.3.1.1.3 Validation of results against fallout deposit

Tephra was mostly deposited eastward from the source during the first 72 h of the event within an elongated area between 40-42º S and 64-72º W. Results from the ash deposition forecast were validated against: i) a detailed characterization of the proximal deposit for the first 72 h of the eruption, and ii) an isopach map derived from measurements taken for the period beginning on 4 June until 30 June (Collini et al., 2013).

To evaluate the simulated computed thicknesses (cm) by the model near the vent during the first 72 h of the event, model results were compared against a comprehensive classification of the proximal deposit presented by Pistolesi et al. (2015b), who constrained the stratigraphic sequence of the deposit in different units (phases). In here, the deposit is constrained to the first three units of their work, corresponding to the first 72 h of the eruptive even and including: i) Unit I, containing coarser-grained layers A-B, representing the very first stage of the eruption within the first 50 km from the vent, and layers A–F associated to the first 24-30 h of the eruption (afternoon of 4 to morning of 5 June); ii) Unit II, containing layer H, a fine pumice lapilli layer which was emplaced starting on the night of 6 June; iii) Unit III, enclosing layer K2, the easiest to identify from several coarser (fine-lapilli) grain-size layers, and being associated to the morning of 7 June. Figure 12 shows that NMMB-MONARCH-ASH can reproduce the deposit presented by Pistolesi et al. (2015b) both in time and space. Key sections located along the dispersal area (e.g. San Carlos de Bariloche – SCB, 90 km from the vent; Ingeniero Jacobacci – IJ, 240 km east of the vent) were used as geographic references.

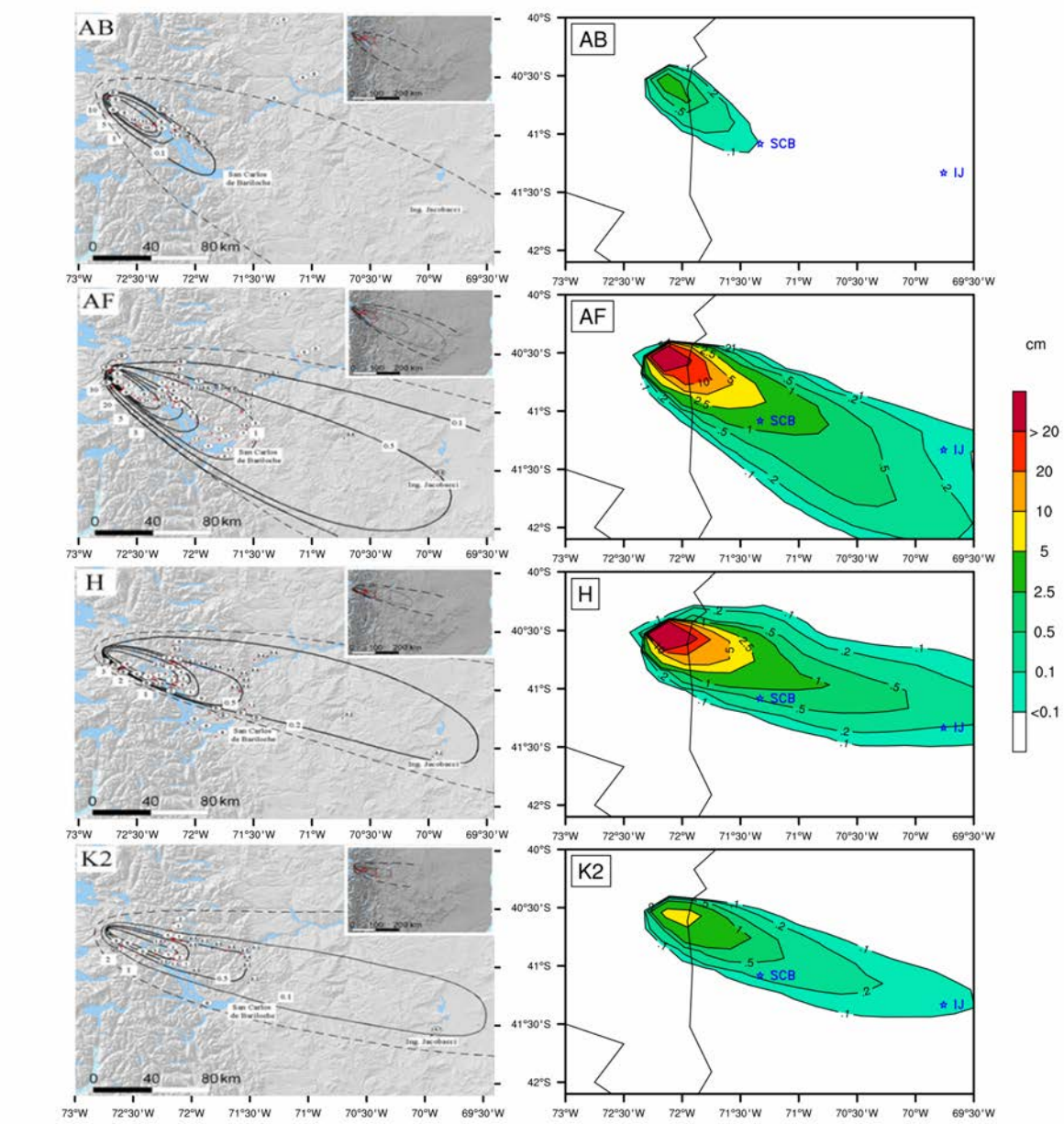

Figure 12. Left: Isopach maps in centimeter of layers A-B, A–F, H, and K2. Dashed lines infer the limit of the deposits presented in Pistolesi et al. (2015b). Right: Corresponding NMMB-MONARCH-ASH computed thicknesses (cm). Key locations in blue include San Carlos de Bariloche (SCB) and Ingeniero Jacobacci (IJ), 90 and 240 km east of the vent); (extracted from Marti et al., 2017).

To evaluate the model performance at the end of our simulation, model results were also validated against an isopach map derived from measurements taken from the 4 to 30 June presented by Collini et al. (2013). Deposit load variations produced by remobilization were not considered in this analysis. Figure 13 shows good agreement between the modeled deposit load (kg m^{-2}) at the end of the simulation and the measured ground deposit isopachs (kg m^{-2}) at 30 June from Collini et al. (2013). The model resulted in a cumulative mass of $\sim 4.2 \times 10^{11}$ kg. This value is in agreement with previous works, where total mass was either modeled (Collini et al., 2013) or estimated by empirical fits (Bonadonna et al., 2015b). Ashfall

forecast with the NMMB-MONARCH-ASH model represented well the overall deposit load for the 2011 Caulle eruption.

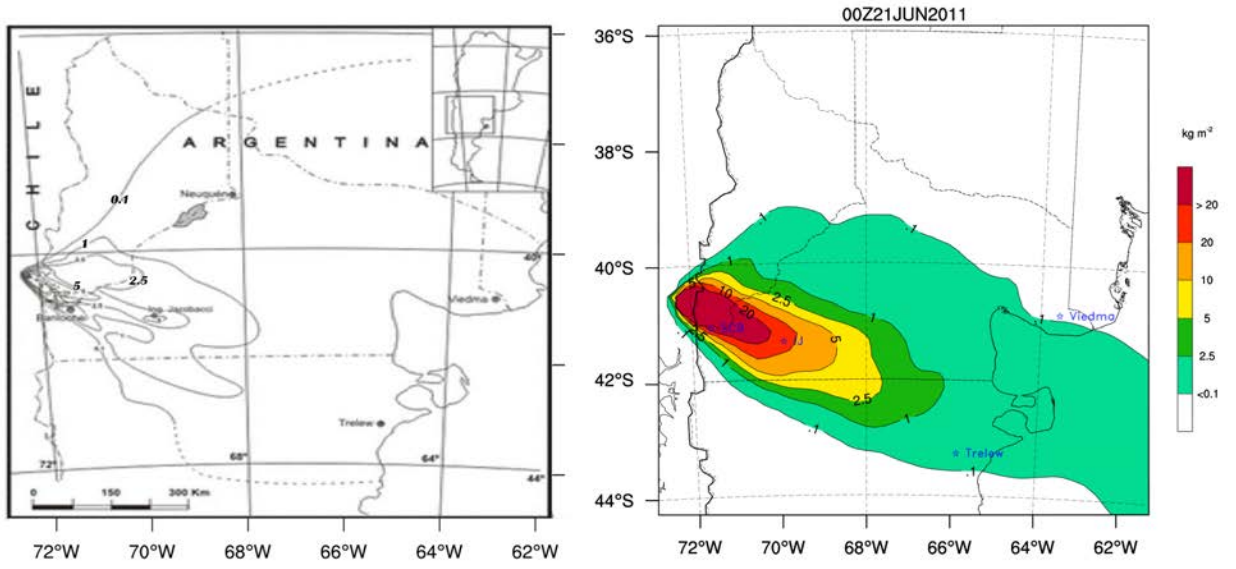

Figure 13. Left: measured ground deposit isopachs (kg m^{-2}) for the period beginning on 4 June until 30 June. Dashed lines infer the limit of the deposits (modified from Collini et al., 2013). Right: Predicted deposit load (kg m^{-2}) with NMMB-MONARCH-ASH at the end of the simulation. Key locations in blue include San Carlos de Bariloche (SCB; 90 km from the vent), Ingeniero Jacobacci (IJ; 240 km east of the vent), and Trelew and Viedma (~ 600 km SE and NE of the vent, respectively); (extracted from Marti et al., 2017).

2.3.1.2 Global simulation

For this simulation, the global domain was configured using a regular latitude–longitude grid with a horizontal resolution of 0.75º × 1º and 60 vertical layers. The ash distribution is simulated between 3-21 June 2011 using the Era-Interim reanalysis at 0.75º x 0.75º resolution as initial conditions. Meteorological conditions for the global runs were also reinitialized every 24h. The atmospheric model's fundamental time-step was set to 180 s, while the rest of the model variables and grain size distribution remained the same as in the regional simulation. Figure 14 shows the global dispersal of ash for the 2011 Cordón Caulle eruption at different times of the simulation. As it can be inferred from this figure, by 10 June, the plume entered the Australian and New Zealand airspace (Fig 14b) covering more than half of the southern hemisphere. At that point, the Civil Aviation Authority of New Zealand warned pilots that the ash cloud was between 20,000 and 35,000 feet (6 to 11 kilometers), the average cruising level for many aircraft (Sommer, 2011). Before the end of our simulation, on 13 June the ash cloud had completed its first circle around the globe. This is in agreement to satellite images reported by the Darwin Volcanic Ash Advisory Centre (Darwin VAAC, 2011). Finally, results from the global simulation are also in agreement with those from our regional run.

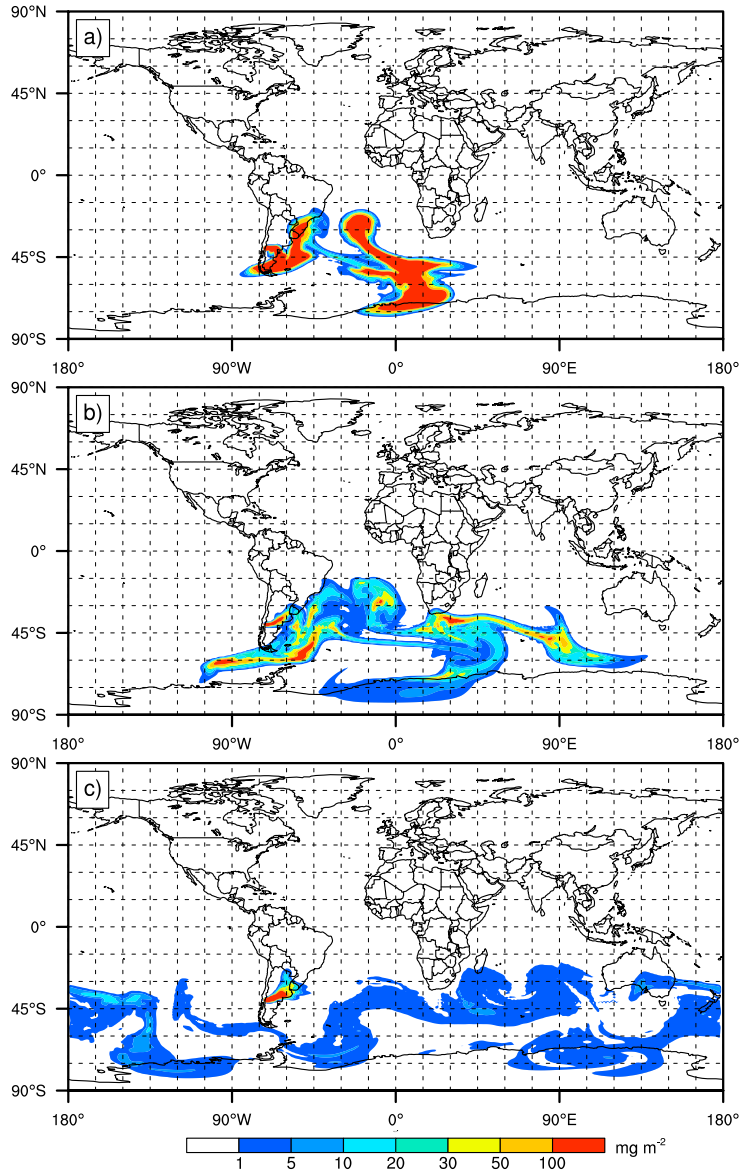

Figure 14. NMMB-MONARCH-ASH total column concentration (mass loading; mg m^{-2}) from our global simulation. Results for a) 8 June at 09:00 UTC, b) 10 June at 04:00 UTC, and c) 14 June at 06:00 UTC (modified from Marti et al., 2017).

2.3.1.3 Forecasting impacts on civil aviation

NMMB-MONARCH-ASH can furnish values of airborne concentration at relevant flight levels (FL), defined as a surface of constant atmosphere pressure (expressed in hundred of feet) separated from other such surfaces by specific pressure intervals, and for which ash concentration is forecasted. This information is particularly important for air traffic management and can be used to decide alternative routes to avoid an encounter with a volcanic cloud. Airborne concentration at FL050 (5,000 feet of nominal pressure) is relevant for the determination of flight cancellations and airports closures, while concentrations at FL300 (30,000 feet) are critical to assist flight dispatchers while planning flight paths and designing alternative routes in the presence of a volcanic eruption. The model runs as if responding to an eruptive event, i.e. only used the semi-quantitative data available at that time as volcanological inputs.

Figure 15 shows the airspace contamination forecasted by the model during the 6-7 June at flight levels FL050 and FL300, within a latitude band between 20º S and 55º S.

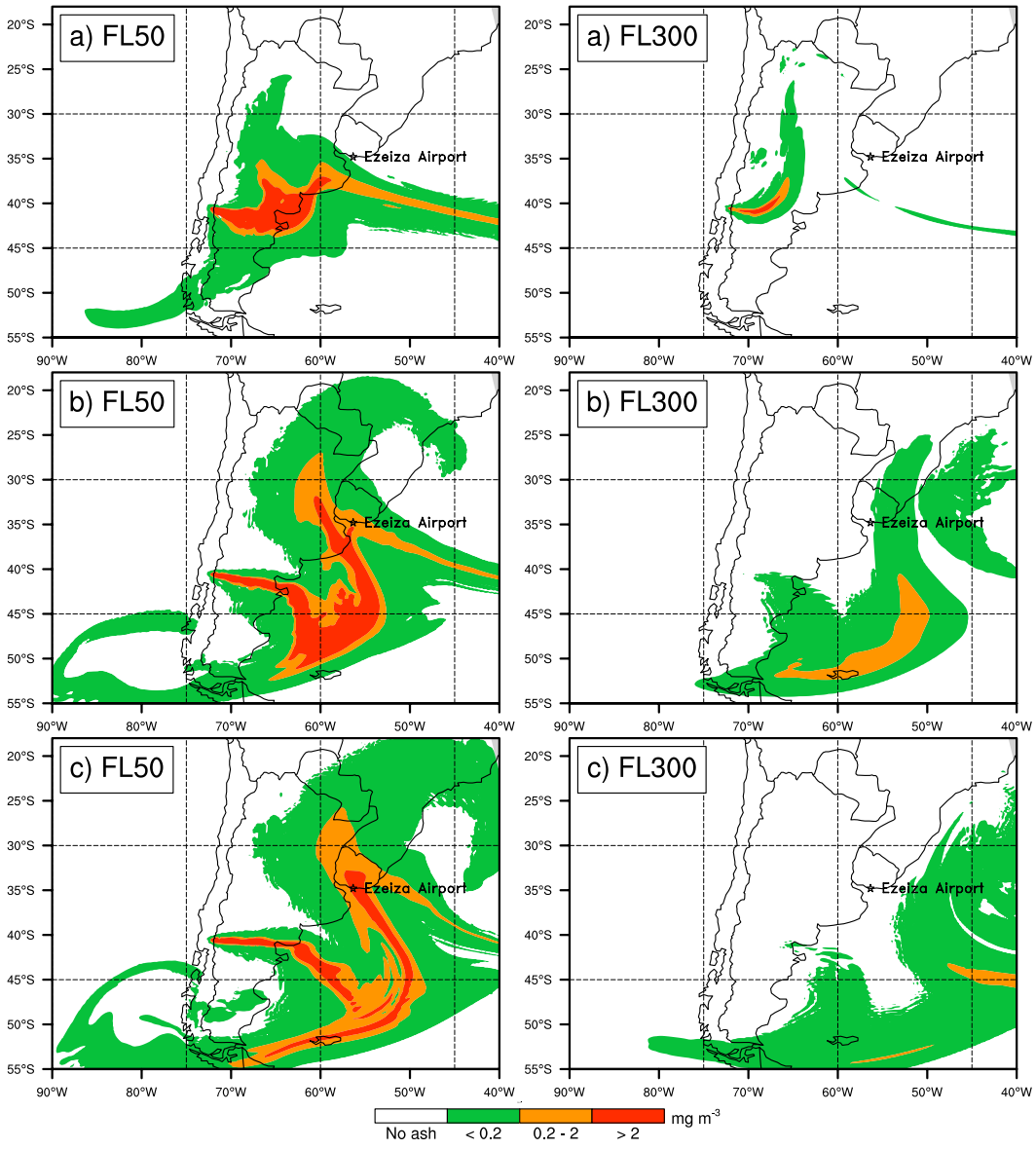

Figure 15. NMMB-MONARCH-ASH Flight level ash concentrations (mg m^{-3}) before and after closure of the Buenos Aires (Ezeiza) airport and air space. Results for FL050 (left) and FL300 (right) for a) 6 June at 11:00 UTC, b) 7 June at 04:00 UTC, and c) 7 June at 12:00 UTC. Safe ash concentration thresholds are shown (red contours illustrate "No Flying" zones); (extracted from Marti et al., 2017).

Model results show the volcanic cloud twisting in different directions during that period of time, achieving critical concentration values within a wide area east of the Andes range. On 6 June, simulation results show the volcanic cloud at high atmospheric pressure (~ 30,000 feet or 300 hPa) moving northwards, and the one at lower atmospheric pressure (~ 5,000 ft or 850 hPa) threatening the main international airports that service the region of Buenos Aires (Fig. 15a). In the morning of 7 June, the ash

cloud present at lower atmospheric pressure (~ 5,000 ft) changed its direction towards the SW, ultimately affecting part of the Patagonia and Chile (Fig. 15b), while higher ash clouds started their course around the globe (Fig. 15c). These results suggest that the cancellation of multiple flights in several Argentinean airports during this time was justified. It is important to point out that, for this section, our objective is not to perform a detailed study of the Caulle eruption but to use it as a blind test to confront short-term model predictions and semi-quantitative syn-eruptive observations.

2.3.2 The 2001 Mt. Etna eruption

Mt. Etna is the most active volcano in Europe and constitutes a continuous hazard for eastern Sicily. Since 1980, Mt. Etna has injected large volumes of pyroclasts into the atmosphere (between 10^4 and 10^7 m^3 per event) over more than 160 eruptive episodes (Scollo et al., 2012). The explosive activity of Mt. Etna reached its climax in 2001 and 2002–03 when two major flank eruptions occurred; both characterized by long-lasting explosive activity (Branca and Del Carlo, 2005). The 2001 event represents a good case to evaluate the deposition mechanisms of the model against the well-characterized tephra deposit reported in Scollo et al. (2007). The explosive activity at the 2570 m vent had three main phases characterized by phreatomagmatic, magmatic and vulcanian explosions. The eruption started with a series of phreatomagmatic explosions during the first days of the eruption. These explosions were followed by a second eruptive phase characterized by strombolian and Hawaiian style explosions during 19-24 July. The explosive activity continued until 6 August with a series of vulcanian explosions. Tephra fallout associated to the explosive activity during 21-24 July represented a major source of hazard for eastern Sicily. Flight operations were cancelled at the Catania and Reggio Calabria airports during the 22 and 23 July. A detailed chronology of the eruption can be found in Scollo et al. (2007). Volcanic plumes were detected by the Multiangle Imaging Spectro Radiometer (MISR) on board NASA's Terra spacecraft, and analyzed with stereo matching techniques to evaluate the height of the volcanic aerosol with a precision of a few hundred meters (Scollo et al., 2012). This section validates NMMB-MONARCH-ASH against the tephra deposit produced from the 2570 m vent for that period of time, and compares the model performance against simulations results from the FALL3D model (see section 1.3.3.1) for the same event.

2.3.2.1 Regional simulation

2.3.2.1.1 Model set-up

Two regional domains were used to simulate the first phase of the 2001 eruption of Mt. Etna (Table 7). The first domain (Regional 1), used to reconstruct the tephra deposit, consists of 101x101x60 grid points covering the SE flank using a rotated latitude–longitude grid with a horizontal resolution of 0.05º x 0.05º. Similarly to the Cordón Caulle simulations, the top pressure of the model was set to 21 hPa (~34 km) with a mesh refinement near the top and ground. The computational domain spans in longitude from 12.5º

E to 17.5º E, in latitude from 35.25º N to 40.25º N. Simulation runs were performed with the on-line version of NMMB-MONARCH-ASH from 21 July 2001 at 00:00 UTC to 25 July 2001 at 00:00 UTC. The integration time-step for the meteorological core was set to 10 seconds. The meteorological driver was initialized with Era-Interim reanalysis meteorological data at 0.75º x 0.75º resolution as initial and 6-h boundary conditions. A spin-up of 12 h was used to prepare each daily model run, reinitialized with the corresponding reanalysis of the model tracers' output from the previous day, and the associated eruption source parameters. Meteorological conditions were reinitialized every 24 h. The grain size distribution and eruption source parameters were obtained from Scollo et al. (2007), who assumed a Suzuki vertical mass distribution located at the middle of the eruption column (A=2; λ=1), and employed the Mastin et al. (2009) empirical relationship to characterize the MER and the Voronoi tessellation method to obtain the grain size distribution. Finally, sensitivity analyses were performed against the different aggregation schemes available in the model. In all cases, the TGSD was updated with a new bin for aggregates, resulting in a total of 8 bins.

A second regional domain (Regional 2) was used to evaluate tephra dispersal between 21 and 25 of July. In this case, the domain consisted of 201x201x60 grid points covering a computational domain spanning in longitude from 41º E to 81º E, in latitude from 18º S to 58º S. This domain used a coarser horizontal resolution of 0.1º x 0.1º. The integration time-step for the meteorological core was set to 30 seconds. The rest of model set-up was kept the same as in the first regional domain (Regional 1).

MODEL CONFIGURATION

Source Term (emissions)	
Duration	3 days
Vertical distribution	Suzuki distribution
MER formulation	Mastin et al. (2009)
Column height above the vent	2570 m
Ash bins	8
Aggregation model	Cornell et al. (1983)
Sedimentation model	Ganser (1993)
Run Set-up	
Number of processors	256
Domain	Regional 1/ Regional 2
Horizontal resolution	0.1º x 0.1º / 0.05º x 0.05º
Vertical layers	60
Top of the atmosphere	21 hPa
Meteorology Boundary conditions	ECMWF EraInterim Reanalysis (0.75º x 0.75º)

Table 7. Model configuration for the 2001 Mt. Etna regional simulations. Regional Run1 used a horizontal resolution of 0.1º x 0.1º with a 30s dynamic time-step, while Run2 used a finer horizontal resolution of 0.05º x 0.05º with a 10s dynamic time-step.

2.3.2.1.2 Validation of results against fallout deposit

At the end of the second explosive phase, a continuous tephra layer covered Etna's flanks between Giarre and Catania (from E to S). Ash deposition results from the model were validated against 47 samples collected between 25 and 26 July from measured areas on flat open spaces, where the deposit did not show any reworking. The computed tephra dispersal and deposition from NMMB-MONARCH-ASH was able to reproduce the bilobate shape of the real deposit with the two axes oriented toward Acireale and Acicastello towns. Figure 16 compares the simulated deposit load (kg m^{-2}) at the end of the run against the isopachs map derived from measurements taken from the 21-24 July (Scollo et al., 2007). The model resulted in a cumulative mass of $\sim 1.18 \times 10^9$ kg. This value is in agreement with the results obtained from Scollo et al. (2007)

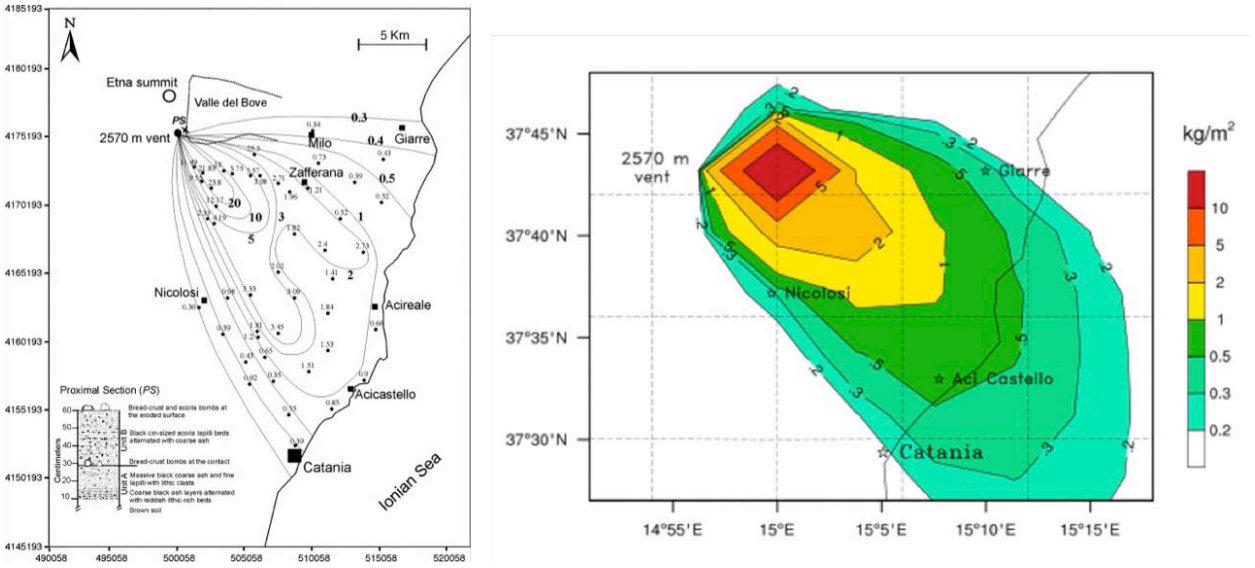

Figure 16. Left: Isomass map of the tephra deposit formed between 21 and 24 July 2001. Curves are given in kg m^{-2}. Coordinates are given in UTM-Datum ED50 (Scollo et al., 2007). Right: Modeled deposit load (kg m^{-2}) with NMMB-MONARCH-ASH at the end of the event (extracted from Marti et al., 2017).

2.3.2.2 Model intercomparison: NMMB-MONARCH-ASH vs. FALL3D

To validate the model performance of NMMB-MONARCH-ASH for its operational implementation, the tephra deposition results of the model are compared against those of the FALL3D model for the reconstruction of the 2001 Mt. Etna eruption. For this comparison both models are run using the same meteorological and volcanological initial conditions (Table 7). Figure 17 shows the simulated thicknesses (vertical axis) for both transport models against the observations (horizontal axis) presented in Scollo et al. (2007). The model improved the tephra distribution results from FALL3D simulations for the same event (R^2; 0.80/0.62), reducing the RMSE (0.014/0.24) and bias (0.02/0.6). In particular, all values simulated with NMMB-MONARCH-ASH plot inside the region between 5 and 1/5 (dashed orange line) times the observed mass at each station. The greatest differences perceived against the observations for both models belong to those points located at distances less than 15 km from the vent. The mean value of the relative error between the computed values and observed data is 64%, which improves those from

FALL3D (91%), and are comparable with those of Scollo et al. (2007), who obtained a 57% by deposit best-fitting using the HAZMAP dispersion model.

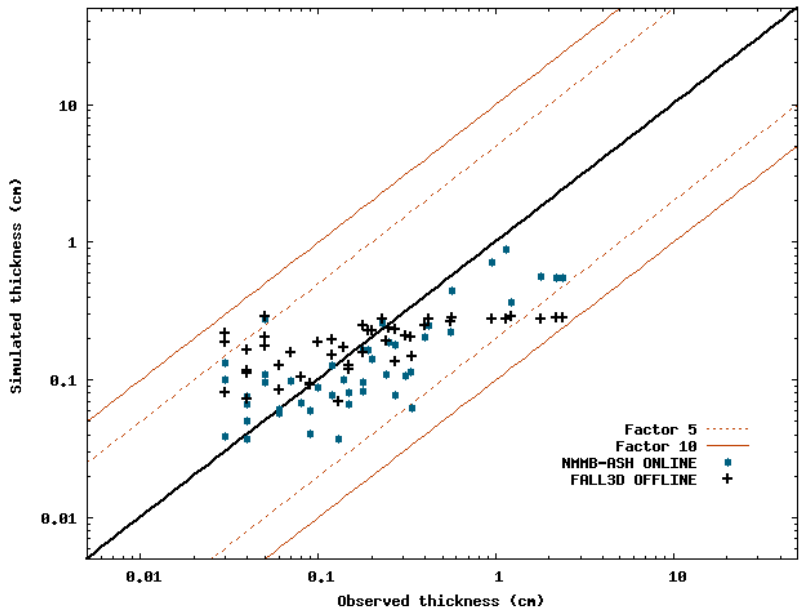

Figure 17. Simulated versus observed thicknesses at 47 locations of the 2011 Etna eruption with NMMB-MONARCH-ASH (circles) and FALL3D (crosses). The solid bold line represents a perfect agreement, while the dashed and solid thin orange lines mark the region that is different from observed thicknesses by a factor 5 (1/5) and 10 (1/10), respectively (extracted from Marti et al., 2017).

2.4 Numerical performance

The high computational efficiency of the NMMB meteorological driver allows for the application of nonhydrostatic dynamics at a global scale (Janjic et al., 2009), and supports that NMMB-MONARCH-ASH could be used in an operational forecast of volcanic ash clouds. Model parallelization is based on the Message Passing Interface (MPI) library. The computational domain is decomposed into sub-domains of nearly equal size in order to balance the computational load, where each processor is in charge to solve the model equations in one sub-domain. The Eulerian schemes in the model require relatively narrow and constant width halos (i.e. data points from the computational domain of neighboring sub-domains that are replicated locally for exchange), which simplify and reduce communications.

To optimize a future operational implementation of the model, we aim to minimize the time-to-solution required avoiding communication overhead. To measure this, the parallel speed-up (computation speed) of the model is analyzed; that is, the performance gains of parallel processing in comparison to serial processing:

$$S_{(P)} = \frac{t_{(P=1)}}{t_{(P)}} \tag{37}$$

where S is the computed speed-up value, and t is the simulation run-time employing P processors instead of running it serially ($P = 1$). Figure 18 shows the parallel speed-up of the modeling system for a global

simulation of the climactic phase for the 2011 Cordón Caulle (Table 6). On the MareNostrum-III supercomputer, maximum efficiency for the global simulation described in Table 6 is reached between 32-40 nodes (16 CPUs each).

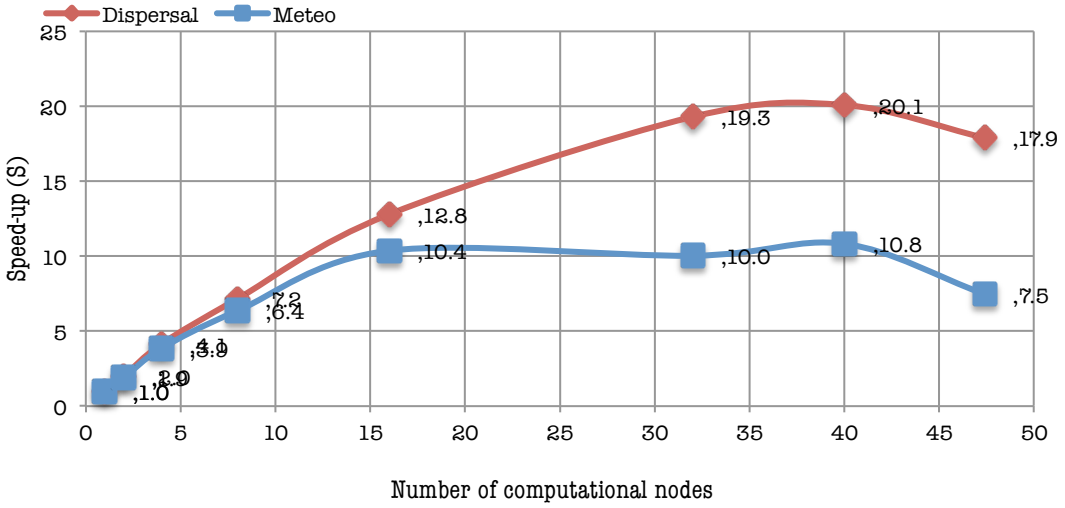

Figure 18. NMMB-MONARCH-ASH parallel speed-up results (S; computational speed) for meteorology only (blue) and for meteorology and dispersal combined (red); (modified from Marti et al., 2017).

In this same context, the model scalability (scaling efficiency) was evaluated for NMMB-MONARCH-ASH regional and global configurations by performing a strong scalability test. For this test, the problem size of our simulation (e.g., model domain and resolution) remains fixed while increasing the number of processing cores. This is measured by the parallel efficiency of the model, which computes the ratio between the parallel speed-up over the number of processors employed:

$$E_{(P)} = \frac{S_{(P)}}{P} \tag{38}$$

Parallel efficiency is used as a metric to determine how far the model's speed-up is from the ideal. If the speed-up is ideal, the efficiency is 1, regardless of how many cores the program is running on. If the speed-up is less than ideal, the efficiency is less than 1. Figure 19 shows the parallel efficiency of the modeling system. A parallel maximum efficiency of 0.6 is found for the global simulation under the same computational conditions than the parallel speed-up.

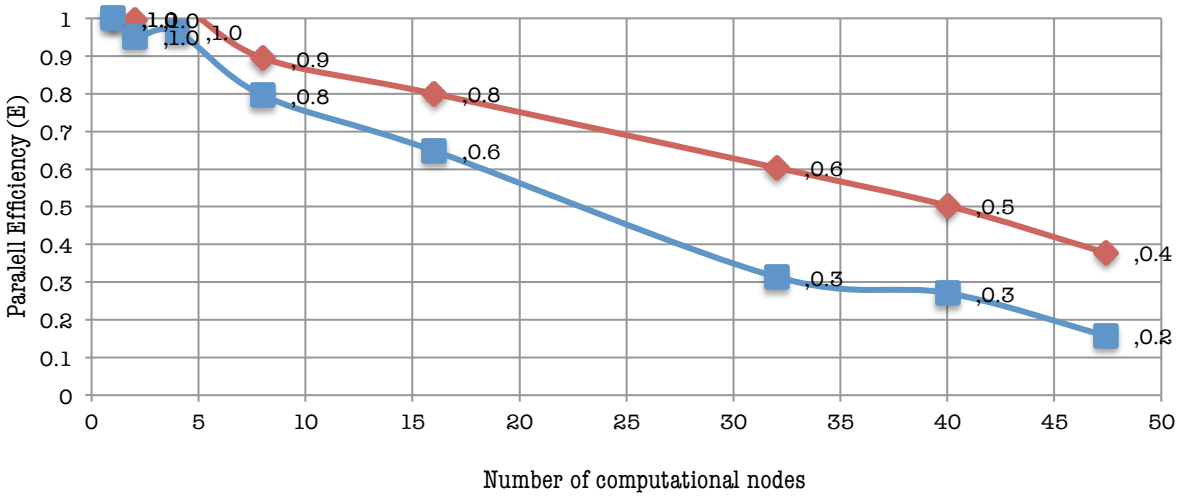

Figure 19. NMMB-MONARCH-ASH parallel efficiency (E) for meteorology only (blue) and for meteorology and dispersal combined (red); (modified from Marti et al., 2017).

In addition, scalability analyses were performed on all the available source term and sedimentation schemes in the model. The relative computational cost associated with the main processes in NMMB-MONARCH-ASH is presented in Fig. 20. Processes represented include: meteorological driver, volcanic ash transport and sedimentation forecast, aggregation of particles, gravity current effects, and the restart phase. The restart phase represents the CPU time employed to rerun the preprocess system (see section 2.5.1) every 24h of simulation. This figure suggests that the computational increase (CPU time) associated to the ash module can vary from 5 to 55%, depending on the number of computational nodes employed. It is important to note that, depending on the settling velocity model employed, up to 60% of the time allocated to the ash module is assigned to the sedimentation term.

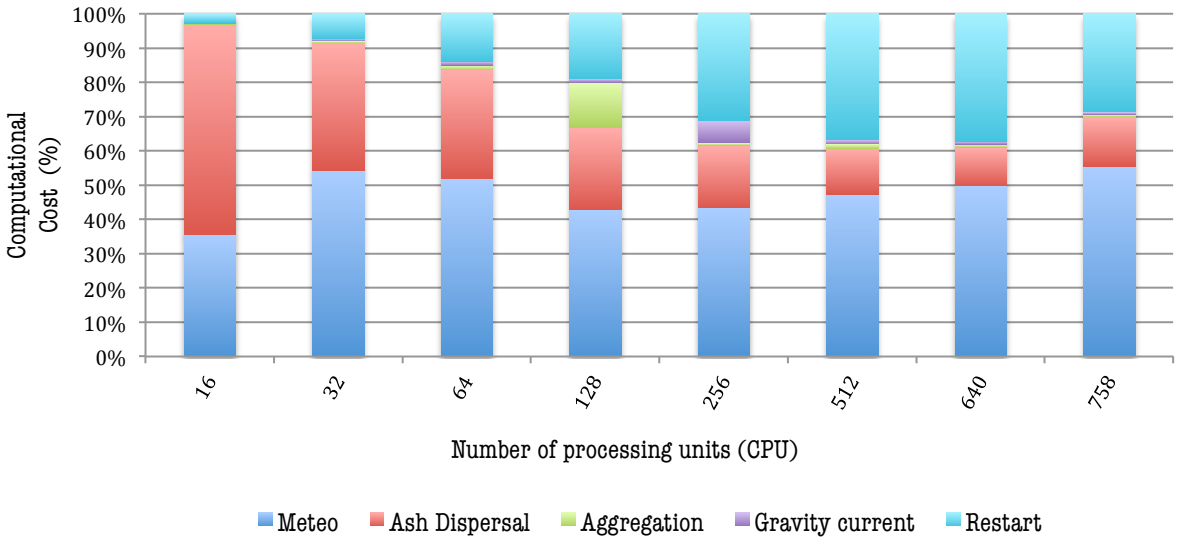

Figure 20. NMMB-MONARCH-ASH relative computational cost (%) with increasing CPUs. Represented processes include: Meteorology (blue); Ash dispersal for 10 bins (red); Aggregation (green); Gravity current (purple) and; Restart phase (light blue); (extracted from Marti et al., 2017).

Results from the scalability analysis show that the model performance (in terms of speed-up) depends on the problem size as well as on the domain partitioning topology. In that context, the relative computational cost of the model's meteorological core (NMMB) is evaluated as a function of its domain decomposition (e.g., distribution of processing units for the horizontal domains – nodes *i* and *j*). For this analysis the bin-performance dependency of the model is considered, therefore evaluating only the cost of one bin of ash. Figure 21 suggest that, for an optimal simulation using 32 nodes, the computational cost of the meteorological core decreases over 10 % when the weight of the decomposition is focused on the *j* nodes (e.g., more computational resources assigned for the Fast Fourier Transformation algorithm). The best domain decomposition resulted in 6(*i*)x84(*j*)+8(*w*); where *i* and *j*, are the number of processors employed in the horizontal and vertical dimensions respectively, and *w*, the number of writing processors.

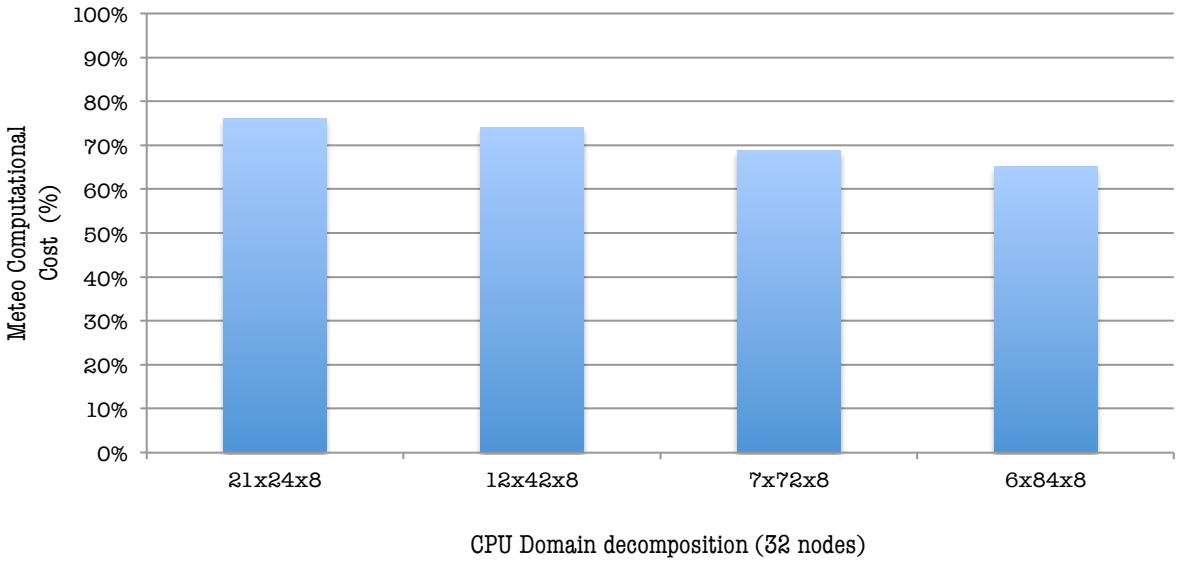

Figure 21. NMMB-MONARCH-ASH meteorological core cost (%) for the best (32 node) domain decomposition (AxBxC). A and B indicate the number of CPU employed for the horizontal *(i)* and vertical *(j)* dimensions, respectively; while C refers to the writing number of processing units employed.

For operational purposes, the computational time employed to provide ash dispersal forecast using NMMB-MONARCH-ASH is evaluated for the global simulation with 1 bin of ash. Figure 22 shows that the maximum time required by the model to perform a 24 h forecast, running all the physical processes (e.g., advection, diffusion, sedimentation, etc.) every time-step (180 seconds) is less than 5 minutes when using the best domain decomposition presented before (6x84+8). This time can be further optimized for operational purposes, e.g., calling the model physics less frequently in order to save computational time. As a general rule of thumb, the adjustment time-step in seconds for the meteorological core can be taken as 2.25 times the grid spacing in kilometers. For higher resolution model runs made without parameterized convection, a time-step in seconds of about 1.9 to 2.0 times the grid spacing may be more appropriate (Janjic and Gall, 2012).

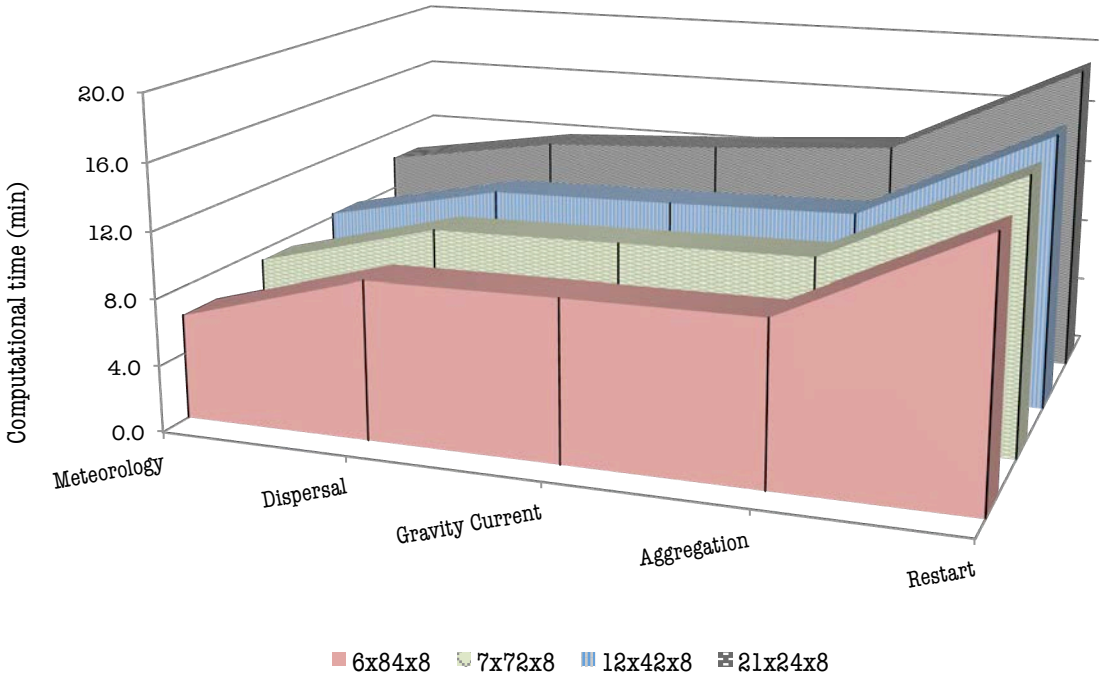

Figure 22. NMMB-MONARCH-ASH computational time for a 24h global forecast. Different domain decompositions options are shown.

2.5 Operational implementation

The Barcelona Supercomputing Center is currently considering a modeling integrated system to provide operational forecast of volcanic ash with NMMB-MONARCH-ASH. The system includes a preprocessing tool (prepares the model for real-data simulations), an executable file to run the model, and a user-based postprocessing utility tool. Figure 23 shows a simple schematic representation of the operational implementation of the model. The outcome of this modeling system is currently being evaluated against the FALL3D operational model. This section introduces the structure of the operational NMMB-MONARCH-ASH system. Preliminary results for the model intercomparison against FALL3D are described in Sect. 2.3.2.2.

2.5.1 The preprocessing system

The preprocessing utility system consists of a set of programs whose collective role is to prepare the model for real-data simulations. Programs are grouped to preprocess geographical, meteorological and climatological inputs and interpolate those to the model grid(s). The preprocessing system employed in this version of the NMMB model (v.2.0.1) uses three main programs: *runfix*, *degrib* and *runvariable*.

- *Runfix* defines the model domain(s) and interpolates static geographical data to the model grid(s). In addition to computing the latitude and longitude of the rotated grid points, this program

interpolates soil categories, land use types, terrain height, annual mean deep soil temperature, monthly albedo, maximum snow albedo, and slope category.

- *Degrib* extracts the necessary meteorological fields from GRIB-formatted files, used as initial condition for global simulations and as initial and boundary conditions for single regional domains (i.e. not nested with a global domain). GRIB files contain time-varying meteorological fields obtained from another regional or global NWPM. In addition to the available NCEP's North American Model (NAM) or Global Forecast System (GFS) model, the program has been updated to include European Centre for Medium-Range Weather Forecasts (ECMWF) ERA-Interim reanalysis data as forcing.

- *Runvariable* interpolates the meteorological fields extracted by *debgrib* to the model grid(s) defined by *runfix* and prepares the climatological schemes. This program generates the initial and boundary conditions that are ingested by NMMB using the NOAA Environmental Modeling System (NEMS; Janjic, 2005; Janjic and Black, 2007), a high performance software superstructure and infrastructure based on the Earth System Modeling Framework (ESMF) for use in operational prediction models at NCEP.

2.5.2 The ash module I/O files

The model takes three run-specific input files:

- The model input file (*nmmb.inp*), which defines the computational and physical schemes needed by the meteorological core, the atmospheric model's fundamental time-step, and the parameterization for chemical processes and radiative schemes for aerosol tracers (including ash), amongst other properties of the model. For long-lasting eruptions, the model performs restart runs initializing the tracers from the previous day's history file.

- The ash input file (*ash.inp*), which defines those parameters employed in the ash module. The user-defined parameters include: i) the characterization of the source term: eruption source type, column height and determination of the mass eruption rate, eruption duration, aggregation processes, and particle settling velocity model. In the event of various eruptive phases, the respective ESPs for each phase can be defined; ii) the settings to turn on/off the gravity current model altering the particle transport in the umbrella cloud; and iii) the definition of the coupling strategy (on vs. off-line) employed by the model.

- The granulometry input file (*ash.tgsd*), which specifies the diameter, density, sphericity, and relative mass fraction of each particle bin. This information is typically obtained from field data or created by external utility programs for idealized grain size distributions.

Once a simulation is concluded, NMMB-MONARCH-ASH writes the following output files (includes outcomes from postprocess system):

- A log file (*ash.log*), containing information about the run, including a summary of the computed volcanic ash source and mass balance statistics for each time-step, and errors and warnings if any.

- A granulometry log file (*ash.grn*) with the final granulometry used for the simulation. If aggregation was active, a new bin class for aggregates was added to the original *ash.tgsd*.

2.5.3 The Postprocess system

The postprocess utility tools are designed to interpolate outputs from the NMMB-MONARCH-ASH native grid(s) to National Weather Service (NWS) standard levels (pressure, height, etc.) and standard output grids (Lambert Conformal, polar-stereographic, etc.) in NetCDF format. The system also includes the *NMMB2GMT* program, which uses the Generic Mapping Tools (GMT) software (Wessel and Smith, 1991) to produce similar plots to the Volcanic Ash Graphics (VAG) used by Volcanic Ash Advisory Centers in operational forecasts.

The postprocess writes the following files:

- A forecast results file (*problemname.nc*) in NetCDF format containing, amongst other variables, the total column mass concentration (g m^{-2}) and ground deposition (kg m^{-2}) for all bins, the concentration at different Flight Levels (g m^{-3}) and the Aerosol Optical Depth. This information can be processed using several open-source programs to generate plots and animations. Alternatively, the post-process utility program *NMMB2GMT* has been developed to generate basic GMT scripts automatically.

- A restart file (*nmmb.hst*) used to initiate a new run using the ash concentrations from a previous simulation.

- A log file (*nmmb_post.out*), containing information basic information about the postprocess outcome (e.g. files read, NetCFD definition and output location, etc.).

2.6 Summary and conclusions

This chapter presents NMMB-MONARCH-ASH, a new on-line multiscale meteorological and transport model developed at the Barcelona Supercomputing Center (BSC) to forecast the dispersal and deposition of volcanic aerosols. The objective of this model is to improve the current state-of-the-art of tephra dispersal models, especially in situations where meteorological conditions are fluctuating rapidly in time, two-way feedbacks are significant, or long-range ash cloud dispersal predictions are necessary. To date, no operational on-line coupled dispersal model is available to forecast volcanic ash. NMMB-MONARCH-ASH is the first on-line system specifically designed to predict ash cloud trajectories, concentration of ash at relevant flight levels, and the expected deposit thickness for both regional and global domains in research and operational set-ups. The model solves the mass balance equation for volcanic ash by means of a new ash module embedded in the BSC's operational system for short/mid-term chemical weather forecast (NMMB-MONARCH). In addition to volcanic ash, the system is also capable to forecast the dispersion of other atmospheric aerosols (e.g. dust, sea salt, black carbon, organic aerosol, sulfates, etc.). Its multiscale capability allows for nested global-regional atmospheric transport simulations, taking into account the characterization of the source term (emissions), the transport of volcanic particles (advection/diffusion), and the particle removal mechanisms (sedimentation/deposition). The model has been shown to be robust and scalable to arbitrary domain sizes (regional to global) and numbers of processors (e.g. 50% up to 640 processors).

The forecast skills of NMMB-MONARCH-ASH have been validated against two well-characterized eruptions. On one end, the regional and global configurations of the model have been evaluated to forecast the dispersal of ash for the first days of the 2011 Cordón Caulle eruption (strong long-lasting eruption with rapid wind changes). On the other end, the sedimentation mechanisms of the model have been evaluated employing different regional configurations for the first phase of the 2001 Etna eruption (a good case study of weak long-lasting eruption with well-characterized tephra deposits). In general, simulation results demonstrate that NMMB-MONARCH-ASH is capable to reproduce the spatial and temporal dispersal variability of the ash cloud and tephra deposits.

The performance of the novel on-line approach in NMMB-MONARCH-ASH has been compared against FALL3D, a well-known off-line dispersal model traditionally employed in several operational settings at the Buenos Aires and Darwin VAACs. Results from this model intercomparison show that NMMB-MONARCH-ASH improves the tephra distribution results from FALL3D simulations for the same event (R^2; 0.80/0.62), reducing the RMSE (0.014/0.24) and bias (0.02/0.6) by an order of magnitude.

The numerical performance of NMMB-MONARCH-ASH has been evaluated in terms of its parallel speed-up (computational speed) and its scaling efficiency. Scalability analyses for the computational domain described in Table 6 show a parallel efficiency of 0.6 when employing 512-640 processors. The relative computational cost associated with the main processes in the model suggest that the

computational increase (CPU time) associated to the ash module can vary from 5 to 55%, depending on the number of computational nodes employed. The relative computational cost of the model's meteorological core (NMMB) depends on the selected domain decomposition. In that context, the computational cost of the meteorological core decreases over 10 % when the weight of the decomposition is focused on the *j* nodes. For the specific model configuration presented in Table 6, the best domain decomposition to transport 1 ashbin resulted in 6(*i*)x84(*j*)+8(*w*); where *i* and *j*, are the number of processors employed in the horizontal and vertical domains respectively, and *w,* the number of writing processors. For operational purposes, the computational time employed to provide ash dispersal forecast using NMMB-MONARCH-ASH for a 24h forecast is less than 5 minutes when using the best domain decomposition. The current version of the modeling system includes a preprocessing tool (prepares the model for real-data simulations), an executable file to run the model, and a user-based postprocessing utility tool. The work described in this chapter is based on NMMB-MONARCH-ASH version 1.0 (released in 23 November 2016). The code, written in FORTRAN-90, is portable and efficient on different parallel computing platforms.

Chapter 3

3 Quantification of off-line modeling errors with the NMMB-MONARCH-ASH v1.0 model

3.1 Introduction

Volcanic ash modeling systems are used to simulate the atmospheric dispersion of volcanic ash and to generate operational short-term forecasts to support civil aviation and emergency management. These systems are vital in efforts to prevent aircraft flying into ash clouds, which could result in catastrophic impacts (e.g. Miller and Casadevall, 2000; Prata and Tupper, 2009). The aviation community is concerned about the detection and tracking of volcanic ash clouds to provide timely warnings to aircrafts and airports. In the event of an eruption, the individual Volcanic Ash Advisory Center (VAAC) responsible for the affected region combines ash cloud satellite observations and dispersal simulations to issue periodic Volcanic Ash Advisories (VAAs). These are text and graphical products informing on the extent of the ash clouds at relevant flight levels and their forecasted trajectories at 6, 12 and 18 hours ahead that are updated periodically or whenever significant changes occur in the eruption source term. All this information is used to ensure flight safety by supporting critical decisions such as closure of ash-contaminated air space and airports or diversion of aircraft flight paths to prevent encounters. The noteworthy economic impact and social disruption of these air traffic restrictions are, therefore, directly associated to the accuracy of the volcanic ash cloud detection and modeling systems.

The objective of this chapter is to quantify the model shortcomings and systematic errors associated with traditional off-line forecasts. In that context, the strategies available in the NMMB-MONARCH-ASH model (Marti et al., 2017) are employed to evaluate the predictability limitations of the off-line coupling approach against those from an on-line forecast considered to be the best estimate of the true outcome. Section 3.2 in this chapter describes the methodology used to quantify the coupling model errors; Section 3.3 presents the results from a synthetic case study with constant ESPs and focused to quantify the systematic errors attributed to the meteorological coupling intervals. Section 3.4 evaluates the results from two real cases that suitably illustrate the severe disruptive effects of European (2010 Eyjafjallajökull) and South-American (2011 Cordón Caulle) volcanic eruptions. Section 3.5 discusses the magnitude of the model forecast errors implicit in the off-line approach by comparing it with other better-constrained sources of forecast error, e.g. uncertainties in eruption source parameters. Finally, Sect. 3.6 provides the conclusive remarks of this work.

3.2 Methods

3.2.1 Modeling background

NMMB-MONARCH-ASH (Marti et al., 2017) is a novel on-line meteorological and atmospheric transport model to simulate the emission, transport and deposition of tephra (ash) and aerosol particles

released during a volcanic eruption. The model predicts ash cloud trajectories, concentration of ash at relevant flight levels, and the expected ground deposit for both regional and global domains. The on-line coupling in NMMB-MONARCH-ASH allows for solving both meteorology and tephra/aerosol transport concurrently and interactively at every time-step. The computational efficiency of its meteorological core suggests that NMMB-MONARCH-ASH could be used in an operational setting to forecast volcanic ash (Marti et al., 2017). A full description of the model can be found in Chapter 2 (Sect. 2.2).

The model allows for two different coupling strategies: on-line and off-line. The on-line version of the model runs the NWPM and VATDM modules synchronously, updating the transport of ash at each NWPM model time step. This coupling strategy offers a more realistic representation of the meteorological conditions, improving the current state-of-the-art of volcanic ash dispersal models, especially in situations where meteorological conditions are changing rapidly in time, two-way feedbacks are significant, or distal ash cloud dispersal simulations are required. In contrast, in the off-line version, the model uses “effective wind fields” in which, meteorological conditions (e.g. wind velocity, mid-layer pressure, etc.) are set to constant, and are only updated at the user-defined coupling interval. This strategy aims to replicate the decoupling effect of traditional VATDM dispersal models used at operational level.

3.2.2 Forecasts

The skills of an atmospheric dispersal model are known to vary in space and time. In that context, NMMB-MONARCH-ASH simulations were performed to study the sensibility of the off-line modeling approach towards the coupling interval and the dispersal distance of the forecast. On-line forecasts were evaluated against simulations from four different off-line coupling intervals (i.e. 1, 3, 6 and 12h) to compare the skills of each off-line coupling strategy. To this purpose, model comparisons were performed for: i) a synthetic case study with constant ESPs to focus exclusively on the effect of the off-line coupling interval; and ii) two historical cases accounting for the effects of changing the ESPs, including a case where meteorological conditions change rapidly in time (first phase 2011 Cordón Caulle eruption), and a case where these changes are less abrupt (first phase 2010 Eyjafjallajökull eruption). Finally, in order to assess the order of magnitude of the error associated to the off-line forecasts, errors were compared with the better-constrained source of forecast error attributed to the source term (i.e. uncertainties in column height and related mass eruption rate), known to be one of the main reasons (first order) for VATDM output variability (e.g. Bonadonna et al., 2010).

Forecasts (off and on-line) for each application use the same computational domain and share the same spatial and temporal scales, allowing for a gridded (point-to-point) evaluation. The standard NMMB-MONARCH-ASH parameterization is employed for all simulations (Marti et al., 2017). The meteorological driver is initialized with wind fields from the Era-Interim reanalysis at 0.75º x 0.75º resolution and, for regional domains, the reanalysis also furnishes 6-h boundary conditions. For the purpose of this study, forecasts predict ash cloud trajectories and concentration of ash at relevant flight

levels for a period up to 48 hours. This approach is consistent with most volcanic ash forecasts operational systems.

3.2.3 Evaluation methods

In general terms, forecast evaluation is the process of assessing the goodness of a model prediction. The forecast is compared, or verified, against a corresponding observation of what actually occurred or some good estimate of the true outcome. For the purpose of this work, the output from the on-line forecast is considered to be the model "observations" (i.e. best-estimate of the true outcome) and is compared against those results from the different off-line forecasts. However, it is important to highlight that the aim of these simulations is not to reconstruct the actual eruptive events but to compare the skills of the off-line forecasts against the on-line in order to quantify their differences.

The accuracy of a volcanic ash forecast can be measured by means of different evaluation scores, as no single metric is adequate to fully determine the goodness of a VATDM prediction. Consequently, a detailed assessment of the strengths and weaknesses of a set of forecasts normally requires more than one or two scores (Jolliffe and Stephenson, 2012). This chapter evaluates the skills of the off-line versus on-line NMMB-MONARCH-ASH forecasts in terms of their ash column loading (ACL) using different quantitative and categorical evaluation scores. These scores are often grid-point-based; they compare observations and predictions per grid cell and compute various metrics for the entire set or a subset of grid-points. Objects from both on-line and off-line ACL fields must be identified for each evaluation score. An object is a group of adjacent grid cells that have an ash cloud loading value above a given threshold. Here, the threshold is defined as the typical ash detection limit for most satellite ACL retrievals (~ 0.2 g m^{-2} - Prata and Prata, 2012). Modeled ACL values below this threshold are omitted from all evaluation metrics.

3.2.3.1 Quantitative evaluation scores

Quantitative evaluation scores are useful to determine the degree to which a forecast differs from the best estimate of the true outcome (i.e. the on-line simulation). Quantitative measures such as correlation coefficients, root-mean-square error (RMSE), or bias, are simple in implementation and thus are regularly used to compare and monitor the quality of a forecast. Here, RMSE is used to assess the average magnitude of forecast errors; bias to assesses the difference between the on-line and off-line forecast means; and the Pearson's correlation coefficient to reflect their linear association. Due to their invariance properties, these measures are considered to be suitable in many predictive sciences, and in particular in weather and climate forecasting (Jolliffe and Stephenson, 2012).

However, the skill of a dispersion forecast is known to vary in space and time, making these commonly

used evaluation scores problematic for grid-point-based measures. A classical example to illustrate these limitations is the "double penalty problem" (Wernli et al., 2008), where a forecast is correct in terms of amplitude, size and timing, but slightly incorrect concerning location, resulting, for example, in very poorly rated correlation and RMSE scores. To overcome these limitations, previous scores are complemented with the quantitative object-based metric SAL (Wernli et al., 2008). This metric individually considers aspects of the structure (S), amplitude (A), and location (L) of a forecast, revealing meaningful information about the systematic differences between forecasts. This diagnostic metric has been previously used to measure the skill of volcanic ash forecast using data insertion from satellite observations (Wilkins et al., 2016) and has been adapted here to compare the differences between on-line and off-line coupled NMMB-MONARCH-ASH forecasts. Figure 23 provides a schematic representation of different metric combinations and scores in SAL.

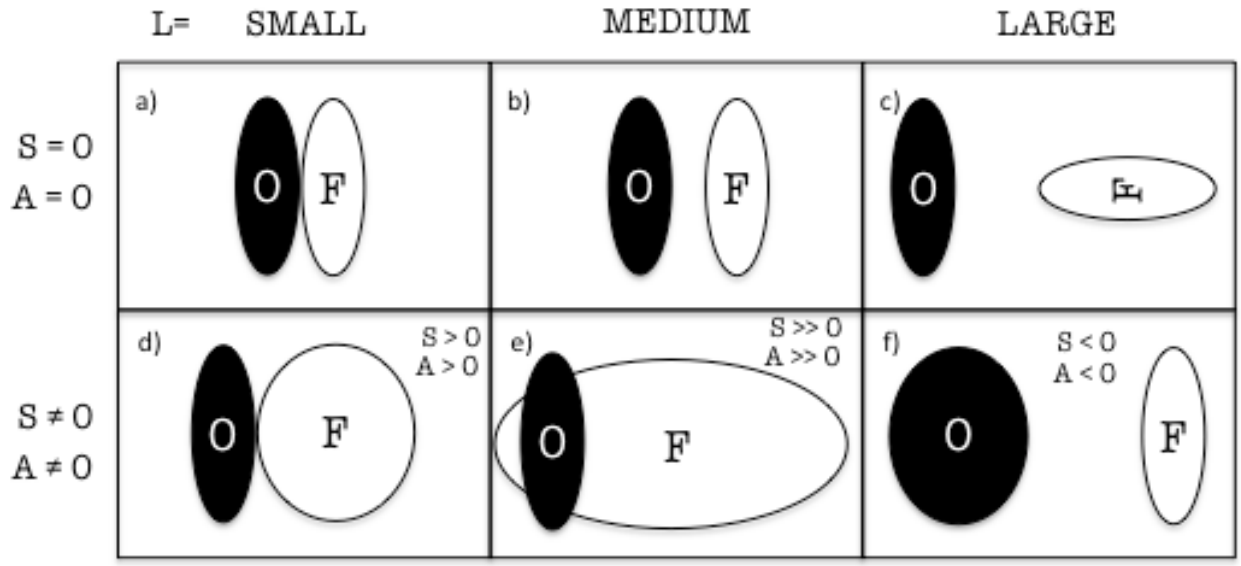

Figure 23. Schematic representation of the possible on-line (O; representing the "observations") and off-line forecasts (F) combinations of the different components for the quantitative object-based metric SAL: Structure (S), Amplitude (A) and Location (L). Modified from *Wernli et al.* (2008).

The structure [S, Eq. (39)] component in SAL captures information about the size and shape of ACL objects by computing the normalized weighted mean mass difference [V, Eq. (40)] for the on-line and off-line forecasts:

$$S = \frac{V_{off} - V_{on}}{0.5\left|V_{off} + V_{on}\right|} \tag{39}$$

Weighted means (V) of the ash column load fields are estimated considering the mass (R_n) and the scaled mass [V_n, Eq. (41)] for the number of objects in the domain (M):

$$V = \frac{\sum_{n=1}^{M} R_n V_n}{\sum_{n=1}^{M} R_n} \tag{40}$$

Scaled masses (V_n) for all objects are calculated separately for each object, as follows:

$$V_n = \sum_{(xy)\in O_n} {R_{xy}}/{R_n^{max}} \tag{41}$$

where xy is the grid cell location within forecasted field, R_{xy} is the area-integrated concentration field (i.e., ash mass) in grid cell xy, and R_n^{max} is the maximum grid cell ash mass in object O_n. Note that, in the case of a single object, $V = V_n$. Structure scores range between [-2,2], with positive values indicating more objects in the off-line forecast and ACL values are too spread out and/or flat. A negative S score occurs when the off-line forecast ACL objects cover too small of an area or are too peaked (or a combination of both).

The amplitude (A) component of SAL corresponds to the normalized difference of the domain-average ash mass values (R). This provides a simple measure of the quantitative accuracy of the total mass of ash in the domain ignoring the field's subregional structure:

$$A = \frac{\bar{R}_{off} - \bar{R}_{on}}{0.5\left|\bar{R}_{off} + \bar{R}_{on}\right|} \tag{42}$$

where $\bar{R}_{off}$ and $\bar{R}_{on}$ are the ash masses averaged over all grid cells in the domain (D), i.e., $\bar{R}_n = \sum_{(xy)\in O_n} {R_{xy}}/{D}$. Amplitude scores range between [-2,2] with 0 denoting no difference between off-line and on-line forecasts. An amplitude score of +1/-1 indicates that off-line forecasts overestimate/underestimate the domain-averaged ACL by a factor of 3. Scores of $A = 0.4$ and 0.67 correspond to factors of 1.5 and 2, respectively (Wernli et al., 2008).

The location (L) component of SAL compares the mass distribution between forecasts. The L component is composed by two parts:

$$L = L_1 + L_2 \tag{43}$$

The first one [L_1, Eq. (44)] compares the normalized distance between the center of mass (C) of the off-line and on-line ACL fields over the maximum distance within the entire domain (d):

$$L_1 = \frac{|C_{off} - C_{on}|}{d} \tag{44}$$

The values of L_1 are in the range of [-1,1], with $L_1 = 0$ suggesting identical centers of mass for both forecasts. However, separated ash clouds could also have the same center of mass, and therefore $L_1 = 0$ would not necessary indicate a perfect match. The second part of the location component [L_2, Eq. (45)] aims at distinguish such situations by measuring the weighted average difference [H, Eq. (46)] between the center of mass of the total ash load and the center of mass for each object (C_n):

$$L_2 = 2\frac{|H_{off} + H_{on}|}{d} \tag{45}$$

$$H = \frac{\sum_{n=1}^{M} R_n |C_{off} + C_{on}|}{\sum_{n=1}^{M} R_n} \tag{46}$$

In the event that both on-line and off-line ACL fields have only one object, then $L_2 = 0$. Note that a factor of 2 is used to scale L_2 to the range of L_1. Hence, the total location component of L can reach values between [0,2], and can only be possibly for an off-line forecast where both the distance between objects and the center of mass agree with the on-line forecast. It is important to mention that since both off-line and on-line computational domains are the same, the magnitude dependency of L to the size of the domain does not affect our interpretation of this SAL component.

Absolute SAL scores range from 0 to 6, with scores closest to 0 denoting the best agreement between forecasts. The computation of the structure and location components of SAL requires to group adjacent grid cells into objects with a value above a given threshold for the forecasted variable. For this study, objects are given as $O_n, n = 1, \dots, M$, where M is the number of objects in the model domain. Each object combines at least two grid cells to avoid unrealistic single ash-containing grid cells. As defined previously, the object identification threshold for the ash cloud loading is set to 0.2 g m^{-2}. Modeled ACL values below this threshold are omitted from all components of SAL.

3.2.3.2 Categorical evaluation scores

From an operational perspective, it is also important to know whether the presence of volcanic ash constitutes an airspace threat or not. In that context, the significance of quantitative volcanic ash forecasts can be measured in terms of categorical evaluation scores (Jolliffe and Stephenson, 2012). These scores are less sensitive to larger errors than quantitative evaluations scores. This is particularly important for extremely skewed data such as ACL, providing the degree to which the forecast supports a decision maker during an emergency event (i.e. closure of airspace). Consequently, ash loads can be viewed categorically (or binary for “yes” or “no” events) according to whether that value exceeds a threshold

(event) or not (non-event). This section computes a series of categorical evaluation scores based on a contingency table (Table 8), which describes the combined distribution of forecast events and non-events for each coupling strategy.

Off-line forecast exceeding threshold	On-line forecast exceeding threshold	
	Yes	No
Yes	$Hits$	$False\ Alarm$
No	$Misses$	$Correct\ Negatives$

Table 8: Contingency table of binary events for categorical verifications scores at each grid-point.

In Table 8, "Hits" represents the number of grid-points for which both forecasts (off-line and on-line) exceed the threshold previously established (0.2 g m^{-2}); "Misses" represents the number of points for which only on-line forecasts exceed this threshold; "False Alarms", indicates the number of points for which only off-line forecasts exceeded the threshold; Finally, "Correct Negatives", represents the number of points for which neither off-line nor on-line forecasts exceeded the threshold value. This chapter uses these binary skill metrics to calculate four categorical evaluation scores:

a) *Probability of detection (POD):* Measures the fraction of ash points observed in the on-line forecast and that were correctly predicted by the off-line forecast. This score is good for rare events, should be used together with the FAR score [FAR, Eq. (48)], and is insensitive to false alarms. The POD score can reach values between [0,1]:

$$POD = \frac{Hits}{(Hits\ +\ Misses)}\ ;\ [0,1] \tag{47}$$

b) *False alarm ratio (FAR):* Measures the fraction of ash points predicted by the off-line forecast that were observed to be non-events (i.e. non exceeding the threshold) in the on-line forecast. This score should be used together with the previous POD score and ignores the misses. The FAR score can reach values between [0,1]:

$$FAR = \frac{False\ Alarm}{(Hits\ +\ False\ Alarm)}\ ;\ [0,1] \tag{48}$$

c) *Frequency bias (FBI):* Measures the ratio of frequency of off-line forecast points to the frequency of observed ash points in the on-line forecast. This score indicates whether the forecast system has a tendency to under-forecast (FBI<1) or over-forecast (FBI>1) events. However, it does not measure how well the off-line forecast corresponds to the on-line simulation, only measures relative frequencies. The FBI score can reach values between [0,∞]:

$$FBI = \frac{(Hits\ +\ False\ Alarm)}{(Hits\ +\ Misses)}\ ;\ [0, \infty] \tag{49}$$

d) *Critical success rate (CSI):* Measures the fraction of all off-line and on-line forecast points that were correctly diagnosed and does consider both misses and false alarms. The *CSI* score can reach values between [0,1]:

$$CSI = \frac{Hits}{(Hits\ +\ Misses\ +\ False\ Alarms)}\ ;\ [0,1] \tag{50}$$

Similar metrics, such as the Figure of Merit in Space (FMS; Galmarini et al., 2010), have been used in previous works (e.g. Wilkins et al., 2016) to complement the SAL score for the evaluation of the spatial coverage between forecasts:

$$FMS = \frac{B_{off} \cap B_{on}}{B_{off} \cup B_{on}}\ ;\ [0,1] \tag{51}$$

In both cases, a score of 1 suggests a complete spatial overlap of the evaluated forecasts. Alternatively, the spatial overlap will decrease as these scores reach values close to 0. This work employs the Figure of Merit in Space (FMS) metric to evaluate the spatial coverage of the forecasts and to complement a missing spatial coverage component in SAL. To be consistent with our implementation of SAL, the spatial ash coverage is computed only for forecast ACL fields exceeding a threshold of 0.2 g m^{-2}. However, it is worth mentioning that a low FMS score could also suggest two similar shapes shifted in space (Mosca et al., 1998) and, therefore, should be used together with the SAL score.

3.3 Synthetic case study

The first step of our evaluation consists in isolating the model's shortcomings and systematic errors that are exclusively associated to the off-line coupling strategy employed in traditional volcanic ash forecasts. To this purpose, a preliminary synthetic case is constructed based on the first 48h of the 2011 Caulle eruption with constant Eruption Source Parameters (ESPs). This synthetic application reduces the differences associated to the source term (i.e. different source term quantification because of different wind fields) and allows us to isolate the systematic errors corresponding to the off-line coupling approach. Within this framework, the eruption duration is limited to 12h, using a constant column height, and employing the Mastin et al. (2009) relationship (mass eruption rate vs. column height: see section 2.2.3.1.1), for the dispersion evaluation of a single bin of ash (1 particle class) during the first 48h of the

event. Multiple regional simulations with NMMB-MONARCH-ASH were performed to produce four different off-line coupled forecasts (i.e. 1, 3, 6 and 12h). Details about the 2011 Caulle eruption, accompanying meteorological conditions, and the computational domain are described in detail in Sect. 3.5. Table 9 provides a summary of the ESPs used for this application.

Source term	Synthetic	2010 Eyjafjallajökull	2011 Cordón Caulle
Run duration	12h	96h	72h
Vertical distribution of mass in the column	Suzuki (1983) distribution	Suzuki (1983) distribution	Suzuki (1983) distribution
MER vs. column height relationship	Mastin et al. (2009)	Degruyter and Bonadonna (2012) (Fig. 5b)	Degruyter and Bonadonna (2012) (Fig. 10a)
Column height	8500m	Fig. 5c	Fig. 10b
TGSD	1 bin (Φ=6)	(Bonadonna et al., 2011)	Bonadonna et al., (2015b)
Sedimentation model	(Ganser, 1993)	(Ganser, 1993)	(Ganser, 1993)

Table 9: Summary of Eruption Source Parameters (ESPs) used in NMMB-MONARCH-ASH for the synthetic case, and the 2010 Eyjafjallajökull and 2011 Cordón Caulle applications.

The skills of these forecasts were compared against the on-line coupled simulation employing the quantitative and categorical evaluation scores described in Sect. 3.2. Scores at the end of the simulation (48h) are shown in Table 10. This chapter focuses on describing the scores for the 6h off-line coupled forecast, representative of an operational forecast driven by reanalysis data.

Coupling/Score	R	RMSE	BIAS	S	A	L	|SAL|	POD	FAR	FBI	FMS
1h	0.849	0.107	-1.090	-0.026	-0.007	0.006	0.039	0.897	0.039	0.934	0.855
3h	0.631	0.167	-2.589	-0.077	-0.008	0.012	0.097	0.752	0.108	0.843	0.669
6h	0.357	0.220	-3.362	-0.143	0.008	0.027	0.178	0.603	0.243	0.796	0.477
12h	0.039	0.269	-5.239	-0.077	-0.003	0.027	0.107	0.400	0.413	0.682	0.281

Table 10. Evaluation scores for the synthetic case at the end of the 48h forecast with NMMB-MONARCH-ASH.

Figure 24 shows the results of the quantitative evaluation scores: RMSE (Fig. 24a), correlation coefficient (Fig. 24b) and bias (Fig. 24c); as a function of the forecast's length for each coupling interval in the synthetic case. These scores assist in determining the degree to which off-line forecasts correspond to the best estimate of the true outcome (on-line forecast). In general terms, and as expected a priori, all scores indicate that the quality of the forecast decreases with decreasing coupling frequency (i.e. 1, 3, 6 and 12h) and length of the forecast. The RMSE score is presented in Fig. 24a, and is used to assess the average magnitude of the off-line forecast errors. Figure 24b shows how the linear association between the on-line and off-line forecasts (Pearson's correlation coefficient) significantly decreases with decreasing coupling frequency, reaching noticeably low correlations. For example, the resulting coefficient for the 6h-coupled forecast after 24h of simulation is below 0.5, and below 0.4 after 48h.

These scores indicate that 6h coupling off-line forecasts are not capable to reproduce more than half of the true outcome, suggesting that the coupling frequency in tephra dispersal modeling could be a critical source of error. This result is relevant considering that 6h-coupled forecasts are used by some emergency-response model setups. Finally, Figure 24c depicts the forecasts bias over those from the on-line simulation. In general terms, all off-line forecasts underestimate ACL, reaching values between -1 and -5 g m^2 at the end of the forecast for the 1h and 12h coupling intervals, respectively (Table 10).

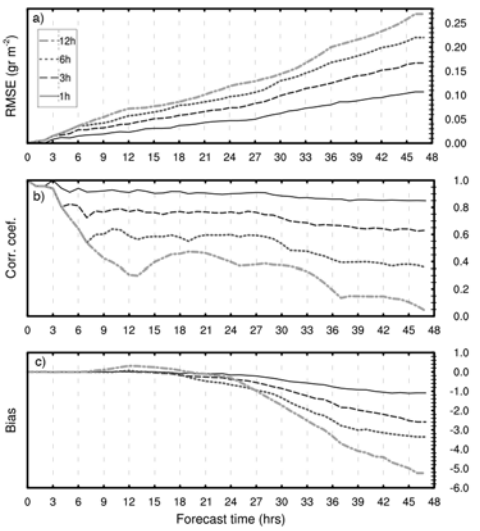

Figure 24. Quantitative evaluation scores for NMMB-MONARCH-ASH synthetic application: a) root mean square error; b) Pearson's correlation coefficient; c) error bias.

Figure 25 illustrates the results from the quantitative object-based metric SAL, aimed to evaluate the variation in space and time of the forecasts. As with previous scores, the error associated to the SAL score also increases with the length of the coupling frequency. For all off-line simulations within the synthetic case, the structure component of the metric (Fig 25a) explains most of the discrepancy with the on-line forecast. Negative values of *S* indicate that off-line forecasts predict fields that cover too small of an area and/or are too peaked. In addition, results from the amplitude and location components indicate a slight overestimation of the domain-averaged ACL for all off-line forecasts, employing comparable centers of mass with the on-line reference. In general terms, systematic differences in the off-line forecast are 4 times higher for a coupling frequency of 6h than those of 1h interval (Table 10).

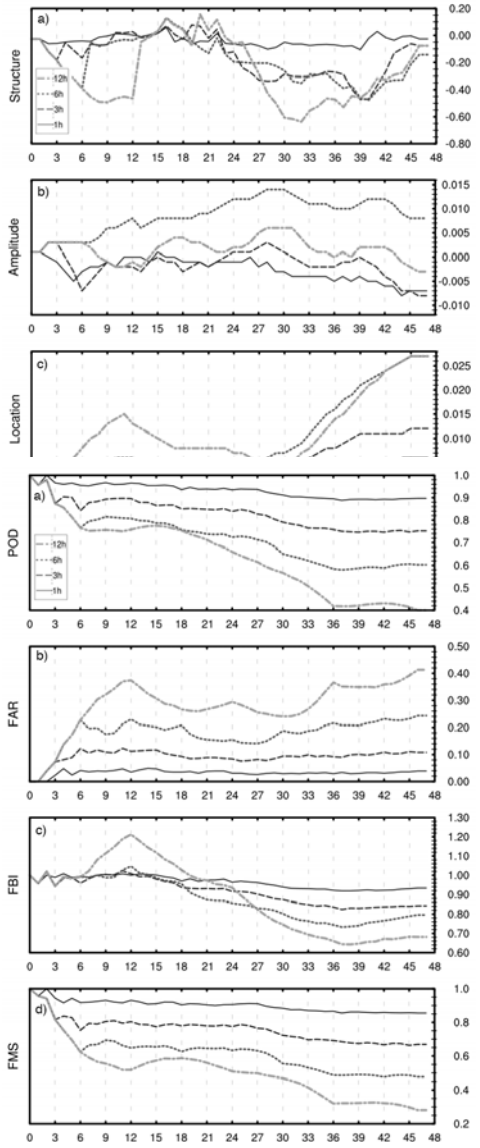

Figure 25. SAL evaluation scores for NMMB-MONARCH-ASH synthetic case: a) Structure; b) Amplitude; c) Location; d) combined SAL.

Categorical scores resulting from the evaluating of the synthetic case are summarized in Fig. 26. As in the previous scores, a threshold value of 0.2 g m^{-2} is considered to define the ash-contaminated objects, categorizing these as "yes" or "no" events depending if they exceed or not this threshold. These

Figure 26. Categorical evaluation scores for NMMB-MONARCH-ASH synthetic case including: a) Probability of detection (POD); b) False alarm ratio (*FAR*); c) Frequency bias (FBI), and; d) Figure of Merit in Space (FMS).

scores are critical for the aviation industry during a volcanic crisis since they can determine the closure of the airspace or the cancellation of flights. Figure 26a illustrates the probability of detection (POD) for each forecast. As expected, this metric clearly shows how the probability of detecting ash-contaminated points in the off-line forecasts decreases with decreasing coupling frequency and the forecast length. In addition, this figure also suggests that POD scores decrease considerably during the first hours of the forecast, matching the time for which the source was active. This trend is applicable to all categorical evaluation scores. After 48h, the POD scores for the 3h and 6h coupled forecasts are 0.752 and 0.603, respectively. For coupling frequencies above 6h, the probability of detecting an ash-contaminated areas drops below 50% (e.g. 12h couple forecast in Table 3). POD scores are complemented by the results from the False Alarm Ratio (FAR) metric, which measures the fraction of ash events predicted by the off-line forecasts that were observed to be non-events.

Figure 26b shows FAR scores to be consistent with POD scores and predict a 25% of false ash-contaminated object for the given domain after 48h of the 6h-coupled simulation. The equivalent plot for the Frequency Bias (FBI) metric as a function of forecast length is shown in Fig. 26c. This metric indicates that all forecasts tend to overestimate the ACL, especially while the eruption is active. After that time, FBI scores stabilize between values ranging from 0.7 to 1.0. Finally, Fig. 26d illustrates the spatial overlap between off-line and on-line forecasts defined by the Figure of Merit in Space (FMS). This metric provides similar results to the POD metric. However, in this case, false alarms (Table 8) are also considered in the metric leading to FMS scores lower than those for the POD metric. Considering this, FMS scores indicate that the spatial overlap (i.e. probability of hits over hits, misses and false alarms) between the on-line and the 6h coupled offline forecasts after 48h of simulation is below 50% (Table 10).

3.4 Historical cases

In addition to the synthetic case, this chapter presents two applications of NMMB-MONARCH-ASH for the simulation of the initial phases of the 2010 Eyjafjallajökull and 2011 Cordón Caulle eruptions. In these cases, off-line forecasts are evaluated taking into account the effects of the coupling interval and the actual changes in the ESPs (i.e. MER depending on wind field) for each event. A summary of the ESPs used for each application is presented in Table 9. These two events have shed light onto the importance of ash dispersal in the context of aviation safety (Bonadonna et al., 2012), and they suitably illustrate the severe disruptive effects of European and South-American eruptions. Similar to the synthetic case: on-line and off-line forecasts were compared on the same temporal scales and spatial grid; a gridded (point-to-point) evaluation was performed between forecasts following the criteria presented in the contingency Table 8; the output of the on-line forecast was considered as the "observed" (best estimation of true outcome) field; and a threshold of 0.2 g m^{-2} was employed as the ash cloud loading detection limit.

Each application includes: i) a brief description of the eruptive event; ii) a summary of the modeling set-up to simulate the eruption and; iii) a comprehensive evaluation of the plume dispersal forecast including qualitative, quantitative and categorical evaluations and metrics.

3.4.1 The 2010 Eyjafjallajökull eruption

The April 2010 eruption of Eyjafjallajökull volcano (63.6Nº, 19.6Wº, vent height 1666 m a.s.l.) in southern Iceland, created unprecedented disruptions to European air traffic during 15–20 April. On 14 April a major outbreak of the central crater under the covering ice cap lead to a submittal activity causing phreatomagmatic explosions, generation of volcanic ash, and eruption columns rising up to 9 km (a.s.l) (Institute of Earth Sciences, 2010). The initial ash clouds travelled rapidly across the North Atlantic and North Sea, reaching southern Norway on 15 April and then traveling southwards as a frontal cloud crossing over to north-European countries. In turn, the London VAAC dispatched immediate warnings to European aviation authorities and other VAAC centers every 3-6 hours. The southern part of the ash cloud finally diluted and grounded in the northern parts of the Alps. On 20 April new aviation guidelines based on safe ash concentration thresholds were adopted, allowing for the ability to resume operations in large areas previously banned. In addition, several other ash cloud episodes occurred during late April and May, disrupting the European airspace for a total of 13 days (over 4 million passengers stranded due to cancellation or delay of over 100,000 flights), affecting 25 countries, and costing the aviation industry billions of Euros (Oxford Economics, 2010). These impacts brought into focus how significantly volcanoes can affect communities and economies far away from the source, and the critical importance of accurate volcanic ash forecasts.

3.4.1.1 Modeling set-up

For the purpose of simulating this eruption, NMMB-MONARCH-ASH employed a model domain consisting of 401x428x60 grid points, covering the northern and western regions of Europe and using a grid with a horizontal resolution of 0.15º x 0.15º. The top pressure of the model was set to 10 hPa (~26 km) with a mesh refinement near the top (to capture the dispersion of ash) and the ground (to capture the characteristics of the atmospheric boundary layer). The computational domain spans in longitude from 30º W to 30º E and in latitude from 34º S to 84º N. The Eruption Source Parameters (ESPs) characterizing the event are described in Table 9 and presented in Fig. 27. Figure 27a shows the variations in column height for the duration of the forecast (Arason et al., 2011). Figure 27b illustrates the results from estimating the Mass Eruption Rate (MER) using the different formulations available in NMMB-MONARCH-ASH (see section 2.2.3.1.1). For those simulations employing empirical correlations to estimate MER based on fits accounting for wind bent-over effects (e.g. Degruyter and Bonadonna, 2012), it is important to see what are the differences in MER associated to the different off-

line coupling intervals with the NWPM. Figure 27c shows these variations in MER and compares them with the fully coupled on-line forecast.

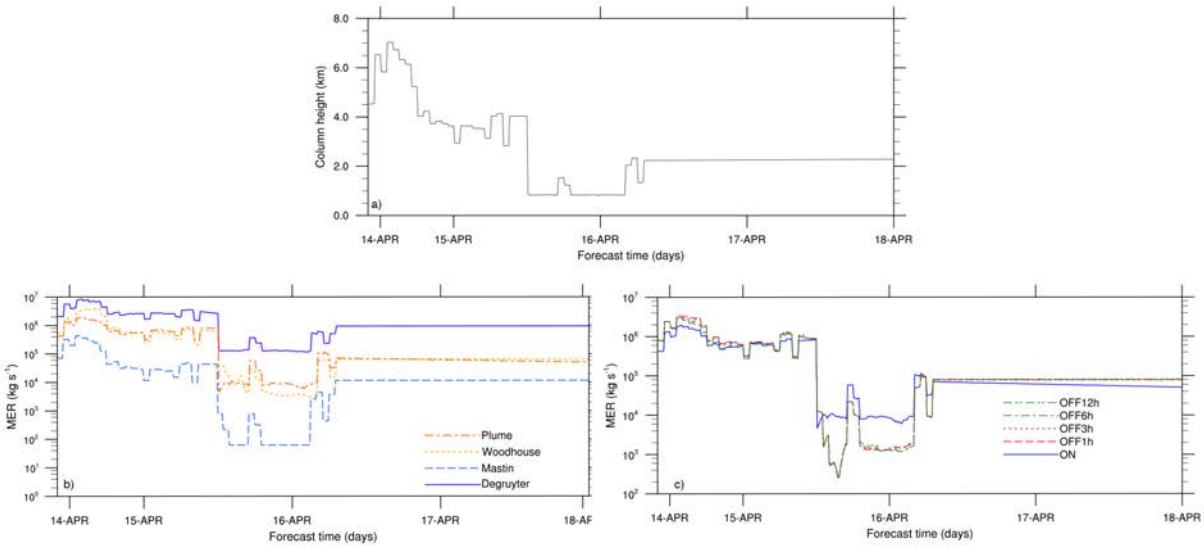

Figure 27. Eruption Source Parameters for the 2010 Eyjafjallajökull application: a) Column height change over time (Arason et al., 2011); b) Resulting MER over time considering different parameterizations (Degruyter and Bonadonna, 2012; Folch et al., 2016a; Mastin et al., 2009; Woodhouse et al., 2013); c) Resulting MER for each coupling strategy (Degruyter and Bonadonna (2012) only).

3.4.1.2 Qualitative evaluation

Figure 28 shows the plume dispersal (ash column loading; ACL) from the on-line forecast corresponding to the first explosive phase (14–18 April) of the Eyjafjallajökull eruption (Gudmundsson et al., 2012). This phase is conveniently divided into 14–16 April, when the volcanic plume produced a well-defined sector towards the east, and 17 to early 18 April, when northerly winds drove the plume to the south.

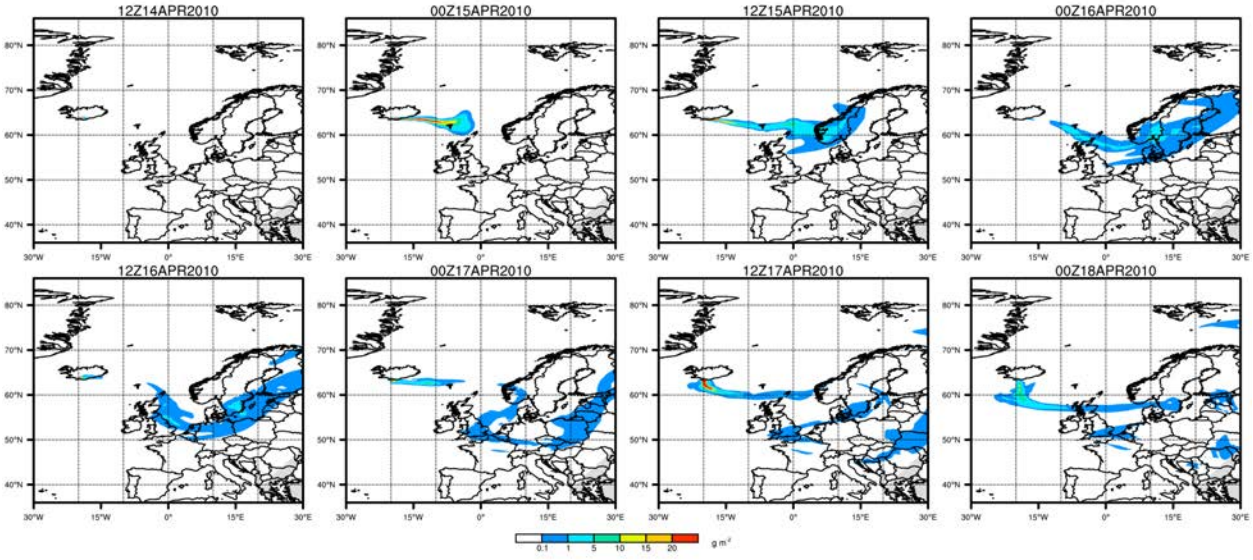

Figure 28. NMMB-MONARCH-ASH total ACL (mass loading; g m^{-2}) for the 2010 Eyjafjallajökull application.

Complementary to this figure, Figure 29 illustrates the airspace contamination forecasted by the model during the first phase of the eruption at flight levels FL050 and FL200. This figure illustrates the ash hazard aviation guidelines, which distinguish zones of low (green; ash concentration less than 0.2 mg m^{-3}), moderate (orange; ash concentration between 0.2 and 2 mg m^{-3}) and high (red; ash concentration above 2 mg m^{-3}) concentration of ash employed to regulate No Fly zones. This information is critical for air traffic management to assist flight dispatchers while planning flight paths and designing alternative routes in the presence of a volcanic eruption. Model results show the volcanic cloud traveling E-NE, achieving critical concentration values in northern Europe during 15-17 June, and suggesting severe disruptions in the European airspace.

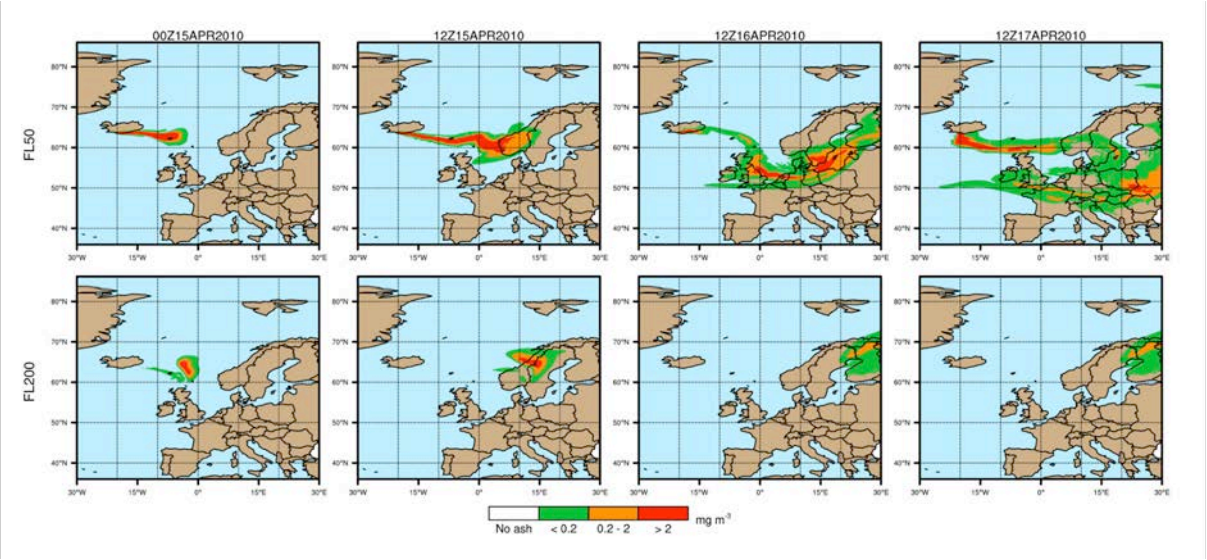

Figure 29. Ash hazard aviation guidelines applied for 2010 Eyjafjallajökull application over time. Zones of low (green; ash concentration <0.2 mg m^{-3}), moderate (orange; ash concentration between 0.2 and 2 mg m^{-3}) and high (red; ash concentration above 2 mg m^{-3}) concentration are displayed for FL050 (top) and FL200 (bottom).

Figure 30 shows a qualitative comparison between the on-line and the different off-line coupled forecasts for Eyjafjallajökull application. Qualitative comparisons are presented for each coupling interval in different rows (i.e. 1st row = 1h; 2nd row = 3h; 3rd row = 6h; 4th row= 12h coupling). Areas in grey ("Hits") represent grid points for which both forecasts (off-line and on-line) exceed the established threshold. Red areas ("Misses") indicate those regions where the off-line forecast fails to predict existing ash (underprediction). Finally, blue areas ("False Alarms") illustrate those domain areas for which only off-line forecasts exceed the threshold, implying a false prediction of ash (overprediction). In general terms, off-line forecasts for the Eyjafjallajökull event tend to overpredict towards the north of the plume and to underpredict towards the south. While results of the 1h off-line forecast indicate mostly Hits (H), Fig. 8 clearly shows how the number of Missed (M) and False Alarm (FA) points increase with the coupling frequency and the length of the forecast. This is consistent with those results presented previously in the synthetic case.

As a consequence, these forecasts would miss, for example, the arrival of volcanic ash over northern Germany in the late afternoon of 16 April as indicated by the DWD ceilometer network at the time of the eruption (Flentje et al., 2010). As a general approximation, Fig. 30 suggests that for the Eyjafjallajökull eruption, off-line forecasts with coupling intervals of 3h and above could result in significant inconsistent predictions (M + FA areas).

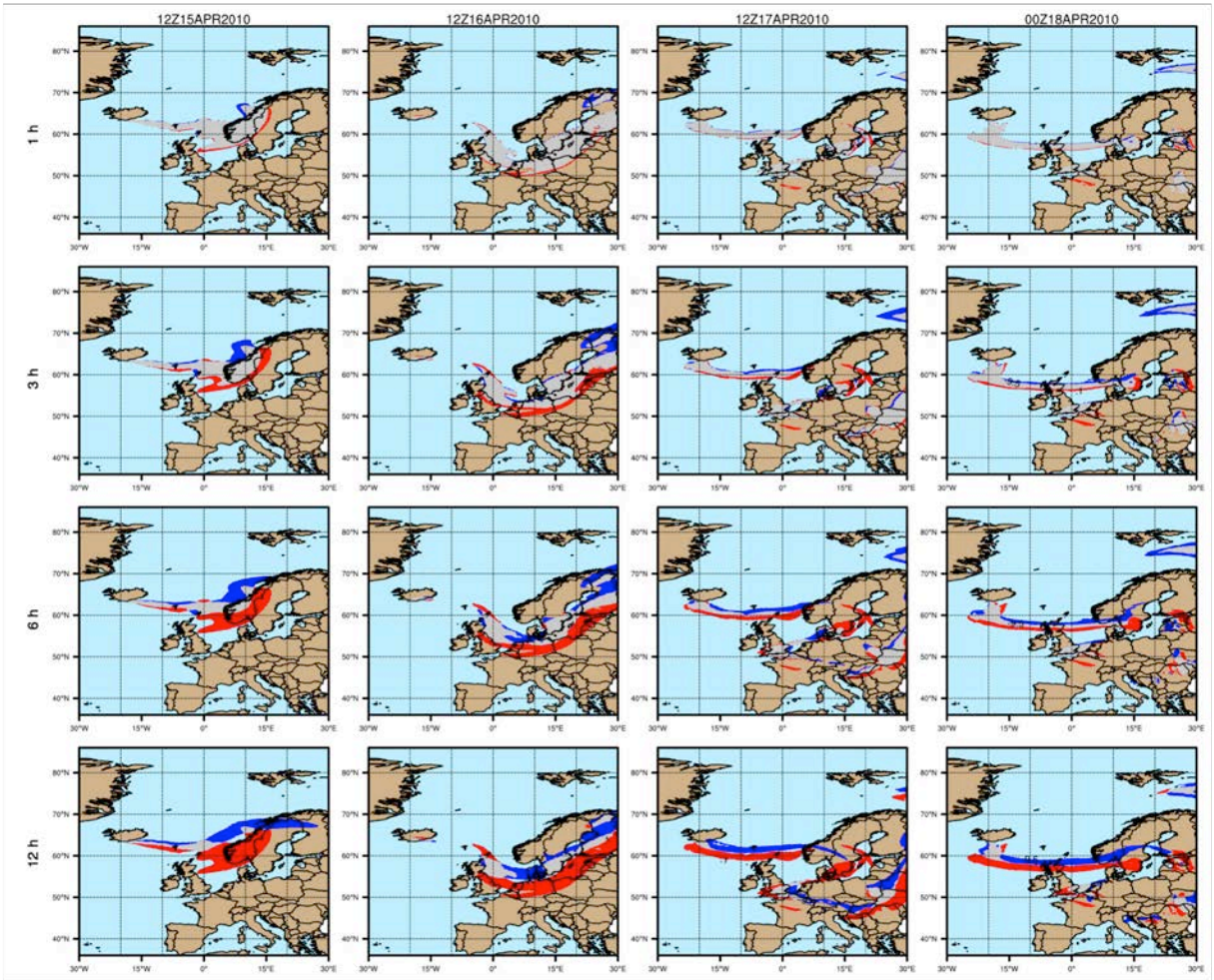

Figure 30. Qualitative comparison between the on-line and off-line forecasts with 1h (row 1), 3h (row 2), 6h (row 3) and 12h (row 4) coupling intervals. Gridded evaluation is performed following the criteria presented in the contingency Table 1. Hit (grey), Missed (red) and False Alarm (blue) predictions are shown for the 2010 Eyjafjallajökull case over time.

3.4.1.3 Quantitative and Categorical evaluation

Figure 31 shows the results of the quantitative and categorical evaluation for the ACL off-line forecasts for the 2010 Eyjafjallajökull application. Complementing this figure, Table 11 shows the scores for all coupled forecasts after 48h from the eruption starting time. As found in the synthetic case, quantitative and categorical metrics lessen their scores for longer coupling intervals and forecast lengths.

Quantitative evaluation scores RMSE (Fig. 31a), correlation coefficient (Fig. 31b) and bias (Fig. 31c) show comparable trends than those reported for the synthetic case. After 48h of simulation, the 6h-

coupled forecast scores show barely any correlation with the on-line forecast and a RMSE of 0.149 g m^{-2}. Bias scores suggest that all off-line forecasts tend to underestimate ACL between -0.33 and -2.5 g m^2 at the end of the forecast. Figures 31d through 31g illustrate the results from the quantitative object-based metric SAL, quantifying the variation in space and time of the forecasts. For the Eyjafjallajökull application, both the structure (Fig. 31d) and amplitude (Fig. 31e) from the off-line forecasts explain most of the discrepancy with the on-line forecast. Contrary to the synthetic case, where the amplitude component (A) had a residual effect towards the total SAL, in this application the off-line forecasts tend to underestimate the total concentration of ash in the domain by a factor of 1.5 for coupling intervals equal to or above 6h. This is anticipated since meteorological conditions are kept constant for the given interval and no additional ash-contaminated objects are found in the domain. After the first coupling with the NWPM takes place, scores start to stabilize. Location scores (Fig. 31f) suggest a comparable mass distribution of the ACL fields for the on-line and off-line forecasts. Finally, absolute SAL scores after 48h of simulations (Table 11) indicate that systematic differences in the off-line forecast are approximately 2 times higher for a coupling frequency of 6h than those of 1h interval.

Categorical scores for the Eyjafjallajökull application are summarized in Fig. 31h through Fig. 31k. Results from the POD metric (Fig. 31h) show that the probability of detecting ash-contaminated events in the off-line forecasts decreases with decreasing coupling frequency, especially during the time the first coupling with the NWPM occurs. After 48h, POD scores for the 6h-coupled forecast are below 50% (i.e. 0.46). Conversely, results from the False Alarm Ratio (FAR) metric follow an increasing trend (Fig. 31i), misrepresenting near 45% objects in the domain. Results from the Frequency Bias (FBI) metric (Fig. 31j) indicate that all off-line forecasts tend to overestimate the ACL. Finally, FMS scores suggest that the spatial overlap between the on-line and the 6h coupled offline forecasts after 48h of simulation is below 50% for those simulations with coupling intervals of 3h or more.

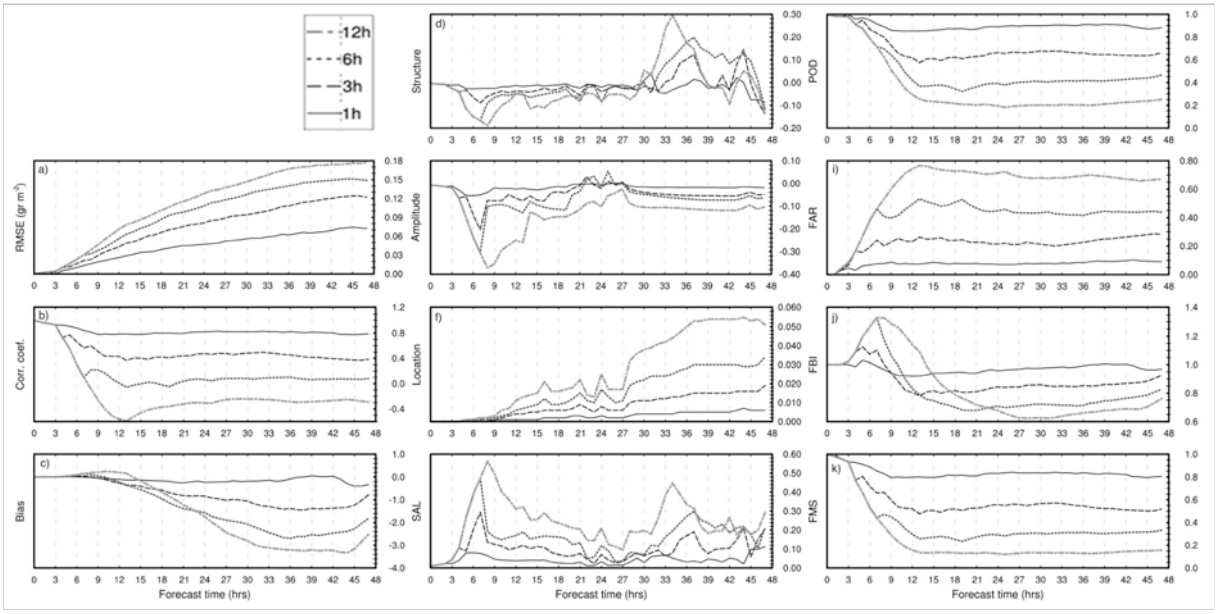

Figure 31. On-line vs. off-line evaluation scores for the 2010 Eyjafjallajökull case.

Coupling/Score	R	RMSE	BIAS	S	A	L	|SAL|	POD	FAR	FBI	FMS
1h	0.787	0.072	-0.327	-0.087	-0.019	0.006	0.112	0.881	0.091	0.969	0.805
3h	0.386	0.122	-0.783	-0.138	-0.049	0.019	0.206	0.664	0.283	0.926	0.499
6h	0.08	0.149	-1.82	-0.116	-0.063	0.034	0.213	0.465	0.438	0.828	0.332
12h	-0.292	0.177	-2.521	-0.136	-0.105	0.051	0.292	0.251	0.671	0.762	0.156

Table 11. Evaluation scores for the 2010 Eyjafjallajökull eruption application at the end of the 48h forecast with NMMB-MONARCH-ASH.

3.4.2 The 2011 Cordón Caulle eruption

The 2011 Cordón Caulle eruption exemplifies a typical mid-latitude Central and South Andean eruption. The Cordón Caulle volcanic complex (Chile, 40.5º S, 72.2º W, vent height 1420 m a.s.l.) reawakened on 4 June 2011 around 18:30 UTC after decades of quiescence. The initial explosive phase spanned over more than two weeks, generating ash clouds that dispersed over the Andes (Collini et al., 2013). The climatic phase (~27 h) (Jay et al., 2014) was associated with a ~9 km (a.s.l.) high column (Osores et al., 2014). For the period between 4-14 June, numerous flights and airports were disrupted in Paraguay, Uruguay, Chile, southern Argentina and Brazil (Wilson et al., 2013). A thorough description of this eruptive event can be found in Sect. 2.3.1.

3.4.2.1 Modeling set-up

The model domain for this application consists of 268x268x60 grid points covering the northern regions of Chile and Argentina using a horizontal resolution of 0.15º x 0.15º. The top pressure of the model was set to 10 hPa (~26 km). The computational domain spans in longitude from 41º W to 81º W and in

latitude from 18º S to 58º S. The Eruption Source Parameters (ESPs) characterizing the Caulle event are described in Table 9. Figure 32a shows the slight MER variation in column height for the duration of the forecast. Figure 32b illustrates the results from simulating the MER over time considering different plume models.

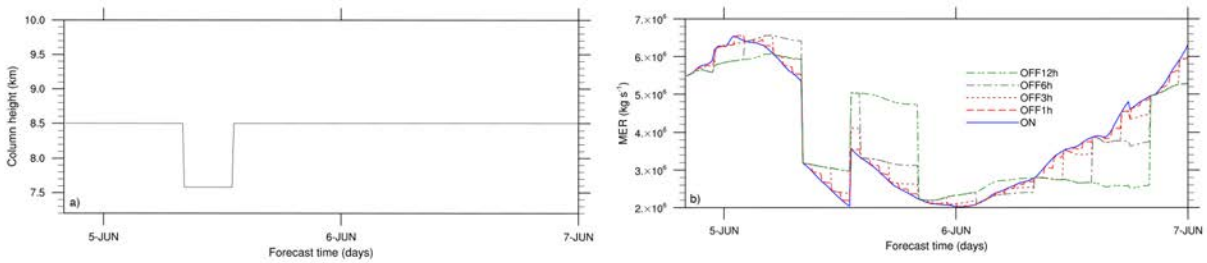

Figure 32. Eruption source parameters for the 2011 Cordón Caulle case: a) Column height fluctuation over time (Osores et al., 2014); b) Resulting MER over time for each coupling strategy.

3.4.2.2 Qualitative evaluation

Figure 33 illustrates the plume dispersion from the on-line forecast associated to the early Plinian phase (4-7 June) of the Cordón Caulle eruption. The initial ash cloud reached the Atlantic coast on 4 June late afternoon, just before turning to the northeast to reach the northern part of Argentina during the 6 June and the city of Buenos Aires the days after.

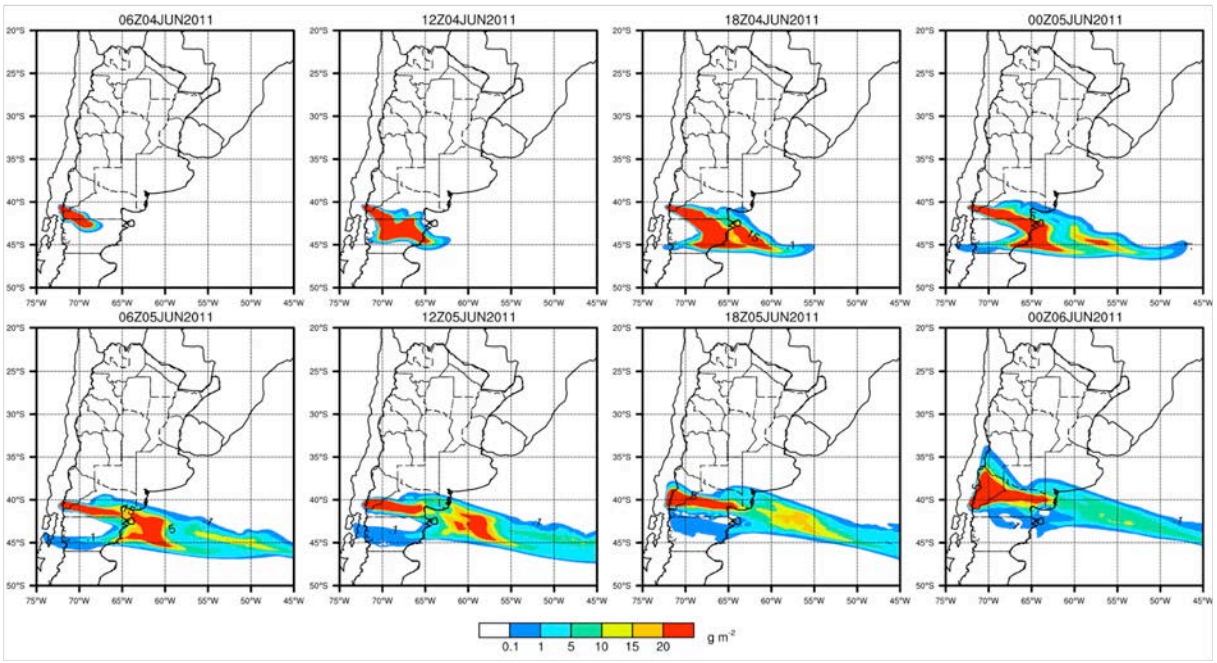

Figure 33. NMMB-MONARCH-ASH total column load (mass loading; g m^{-2}) for the 2011 Cordón Caulle case.

The effect of the plume dispersion on air-traffic management is shown in Figure 34. This figure shows the airspace contamination forecasted by the model during 4–6 June at Flight Levels FL050 and FL200. Model results show the volcanic cloud achieving critical concentration values within a wide area east of the Andes range.

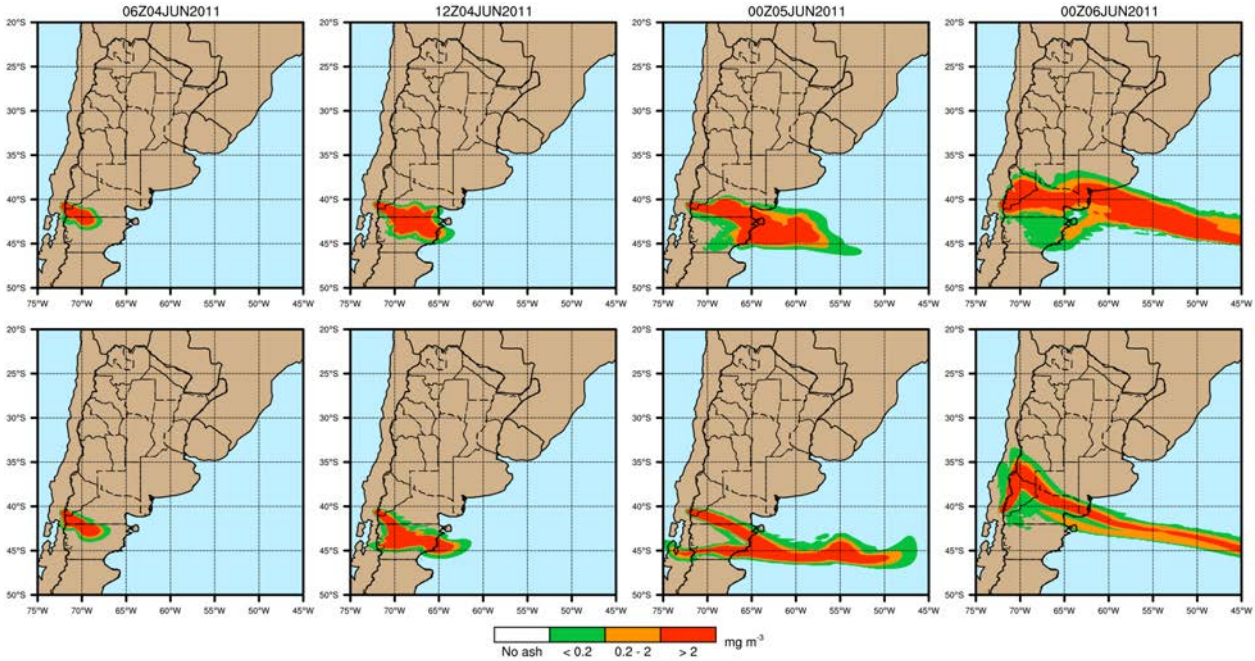

Figure 34. Ash hazard aviation guidelines applied for the 2011 Cordón Caulle application over time. Zones of low (green; ash concentration <0.2 mg m^{-3}), moderate (orange; ash concentration between 0.2 and 2 mg m^{-3}) and high (red; ash concentration above 2 mg m^{-3}) concentration are displayed for FL050 (top) and FL200 (bottom).

Figure 35 shows the qualitative comparison between the on-line and off-line coupled forecasts for the first days of 2011 Cordón Caulle eruption. In this case, given that the plume height during the first hours of the eruption was more constant (no significant changes in wind speed and direction) than for the Eyjafjallajökull application, the difference between forecasts is less suggestive, although still remarkable. Contrary to the Eyjafjallajökull application, off-line forecasts tended to underestimate to the north of the plume and slightly overestimate to the south. The resulting evaluation from these inconsistencies indicates that off-line forecast with longer coupling intervals missed the abrupt shift in the plume course known to be associated to early June 6. This alteration was due to the change in the wind direction toward N-NE first and then again towards SE (e.g. Elissondo et al., 2016). As a consequence, these results suggest that off-line forecasts would miss the correct arrival time of volcanic ash to the main airports in Buenos Aires (i.e. Ezeiza and Aeroparque Jorge Newbery airports).

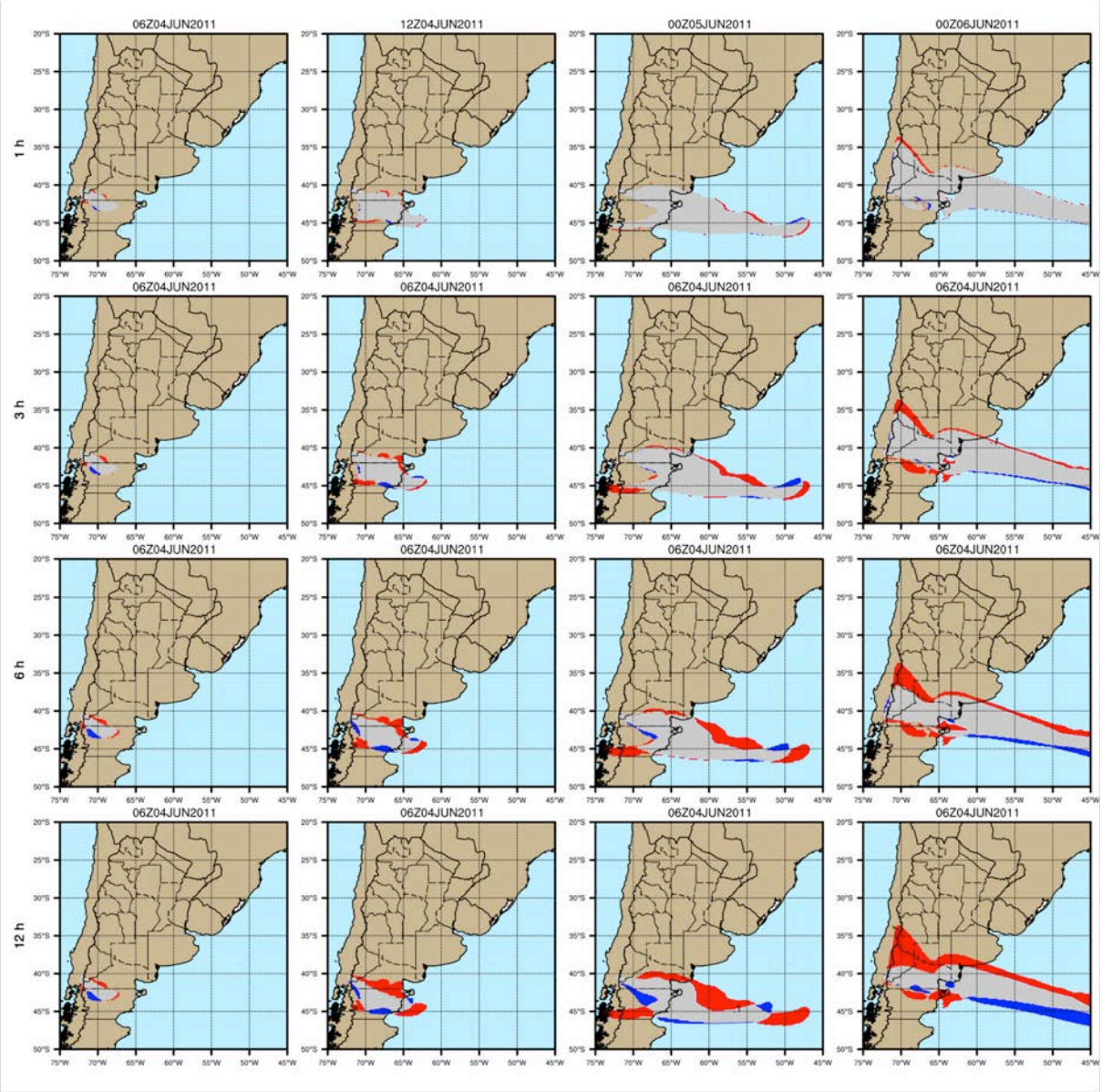

Figure 35. Qualitative off-line vs. on-line forecast comparison for 1h (row 1), 3h (row 2), 6h (row 3) and 12h (row 4) coupling intervals. Gridded evaluation is performed following the criteria presented in the contingency Table 8. Hit (grey), Missed (red) and False Alarm (blue) predictions are shown for the 2011 Cordón Caulle application over time.

3.4.2.3 Quantitative and Categorical evaluation

Figure 36 summarizes the results for the quantitative and categorical metrics for the 2011 Caulle application. Metric scores at the end of the simulation are presented in Table 12. Results for the Cordón Caulle application are consistent with those from the synthetic case and the Eyjafjallajökull application in that the uncertainty of the forecast increases significantly with the length of the coupling frequency employed. Quantitative evaluation scores RMSE (Fig. 36a), correlation coefficient (Fig. 36b) and bias (Fig. 36c) show comparable trends to those from the Eyjafjallajökull application. Despite this similarity, linear correlation coefficients between off-line and on-line forecasts for the Caulle application are higher than those from the Eyjafjallajökull simulation. This result is explained by the fewer changes in the source term (e.g. variations in the column height) during the Caulle event. After 48h of simulation, the

6h-coupled forecast scores a correlation coefficient of 0.60 with a RMSE of 0.16 g m^{-2}. Bias scores suggest that all off-line forecasts tend to underestimate ACL between -0.13 and -4.75 g m^{-2} at the end of the forecast.

Figures 36d through 36g illustrate the results from the quantitative object-based metric SAL for the Cordón Caulle event. SAL scores (Fig. 36g) suggest that differences between on-line and off-line strategies for the Cordón Caulle application are considerably higher than those for the Eyjafjallajökull application. This is due to the changing meteorological conditions during to the Cordón Caulle event, and confirms that inconsistences associated to off-line forecasts are more relevant in scenarios where the meteorological conditions (mainly wind speed and direction) vary rapidly in time. In terms of the individual components of SAL, Structure (Fig. 36d) and Amplitude (Fig, 36e) scores explain most of the discrepancy with the on-line forecast. Structure scores indicate that more objects occur in the off-line forecast and ACL values are too spread out and/or flat, while Amplitude scores suggest that off-line forecasts tend to overestimate the total concentration of ash in the domain up to a 1.5 factor. The systematic error associated to the off-line forecasts is clearly demonstrated after 18h of simulation (Fig. 36g), time during which changes in wind speed and direction start to be noteworthy (Fig. 33). Location scores (Fig. 36f) suggest a consistent mass distribution of the ACL fields amongst forecasts. The Cordón Caulle application is a perfect example to illustrate the importance of complementing traditional quantitative metrics with the quantitative object-based metric SAL. For this particular case, SAL scores are capable to capture the inconsistences of the off-line dispersion forecast due to the changing meteorological conditions that other quantitative metrics (i.e. RMSE, correlation coefficient, bias) cannot account for.

Finally, categorical scores for the Cordón Caulle application are presented in Fig. 36h through Fig. 36k. Results suggest that the skill of the forecast decreases with decreasing coupling frequency, following similar trends than those found in the Eyjafjallajökull application. After 48h, FMS scores suggest that the spatial overlap between the on-line and the 6h coupled offline forecasts is below 65% (Table 12; Fig 36k), with a probability of misrepresenting ash-contaminated objects above 10% (FAR; Fig. 36i). Results from the Frequency Bias (FBI) metric (Fig. 36j) indicate that all off-line forecasts tend to overestimate the ACL.

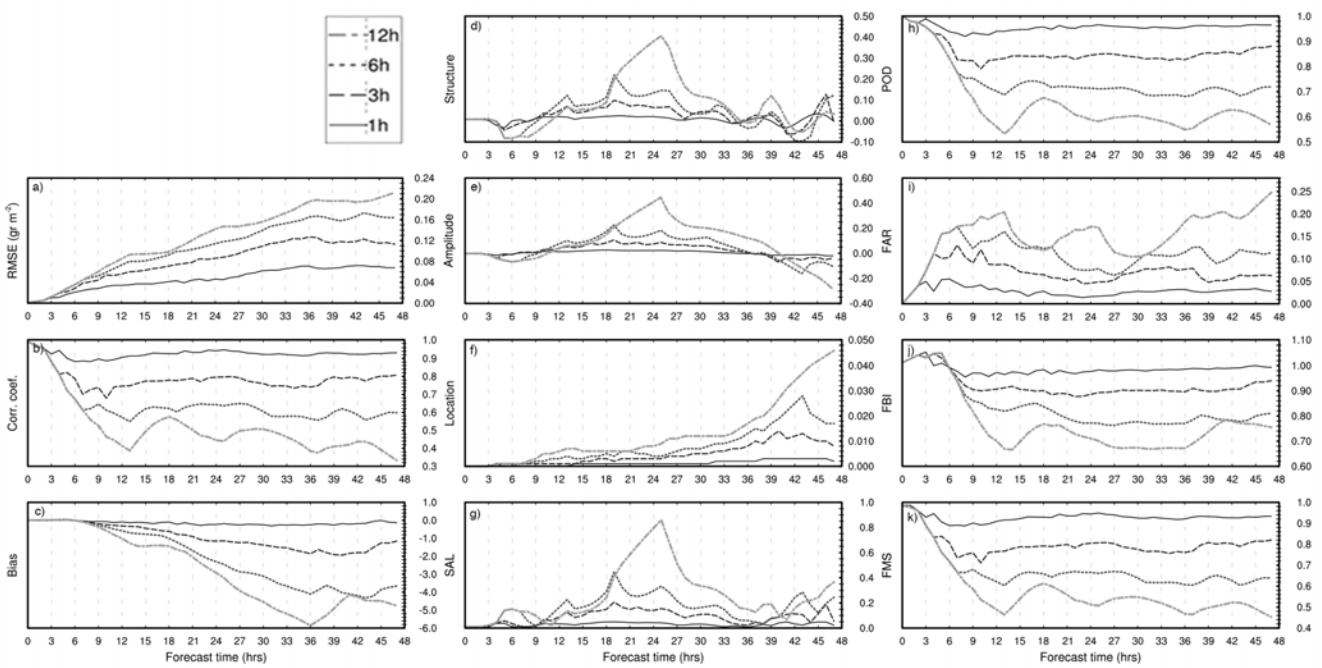

Figure 36. On-line vs. off-line evaluation scores for the 2011 Cordón Caulle application.

Coupling/Score	R	RMSE	BIAS	S	A	L	|SAL|	POD	FAR	FBI	FMS
1h	0.932	0.068	-0.131	-0.001	-0.02	0.002	0.023	0.965	0.028	0.993	0.934
3h	0.808	0.113	-1.16	-0.008	-0.038	0.008	0.054	0.881	0.063	0.94	0.82
6h	0.598	0.164	-3.657	0.123	-0.105	0.017	0.245	0.719	0.114	0.811	0.639
12h	0.333	0.212	-4.754	0.033	-0.287	0.046	0.366	0.568	0.248	0.755	0.453

Table 12. Evaluation scores for the 2011 Cordón Caulle eruption application at the end of the 48h forecast with NMMB-MONARCH-ASH.

3.5 Discussion

Volcanic ash modeling systems are used to simulate the atmospheric dispersion of volcanic ash and to generate forecasts to quantify the impacts from volcanic eruptions on air quality, aviation, and climate. However, volcanic ash forecasts require the consideration of numerous and complex uncertainties. The 2010 Eyjafjallajökull eruption clearly demonstrated the need for a better understanding of the uncertainties associated to the dispersal model employed in operational volcanic ash forecasting. Since then, the scientific community has focused on identifying and improving uncertainties primarily associated to the characterization of the source term (e.g. MER, column height, etc.). However and surprisingly, the quantification of systematic errors and shortcomings associated to the meteorological data driving the dispersion model has received little attention. Traditionally, operational volcanic ash forecasts employ off-line coupling strategies to produce the required meteorological fields at regular time intervals, e.g. every 1 or 6 hours for typical mesoscale and global operational NWPM outputs and reanalysis data, respectively. This chapter has shown the meaningful negative impact of employing off-line coupling intervals on the accuracy of the ash-cloud simulations as compared to on-line coupled forecasts. In particular, Section 3.3 showed the scores from evaluating a synthetic case focusing

exclusively on the effect of the coupling approach. Evaluation scores reveal that the uncertainty of the off-line forecasts increase significantly with the length at which the meteorological driver is coupled with the dispersion model (e.g. up to 4 times for the 6h-coupled forecast). However, the question on how does this compares to other better-constrained sources of forecast error remains still unanswered.

In order to answer this question, this chapter evaluated to which extend the magnitude of the model forecast errors implicit in the offline approach compare with that of the source term. To this purpose, four additional experimental simulations were performed under the synthetic case where ESP for the on-line forecast where modified by: i) employing a 2 MER factor (i.e. x2 and 1/2 times the original MER), and; ii) varying ± 20% the corresponding column height. As in previous applications, experimental forecasts were evaluated on the same temporal scales and spatial grid against on-line forecast employing a range of complementary quantitative and categorical metrics. Figure 37 illustrates the evaluation scores from these four simulations, and compares them with those of the 6h coupled off-line forecast. Overall, Fig. 37 reveals that systematic errors and shortcomings associated to the traditional off-line coupling strategies employed in operational volcanic ash forecast can be of the same other of magnitude than those uncertainties credited by the characterization of the source term. For example, correlation coefficients (Fig. 37b) and POD scores (Fig. 37h) suggest an additional 10-30% level of uncertainty attributed to the 6h coupled forecast than those associated to the source term. In that same context, at the end of the simulation, FMS scores (Fig. 37k) reveal that the spatial overlap between the on-line and the 6h coupled offline forecasts is ~ 20% lower than those from varying ± 20% the column height, and ~ 50% lower than those from altering the original MER. These results suppose a significant advance in the quantification of the uncertainty sources associated to traditional off-line volcanic ash forecasts.

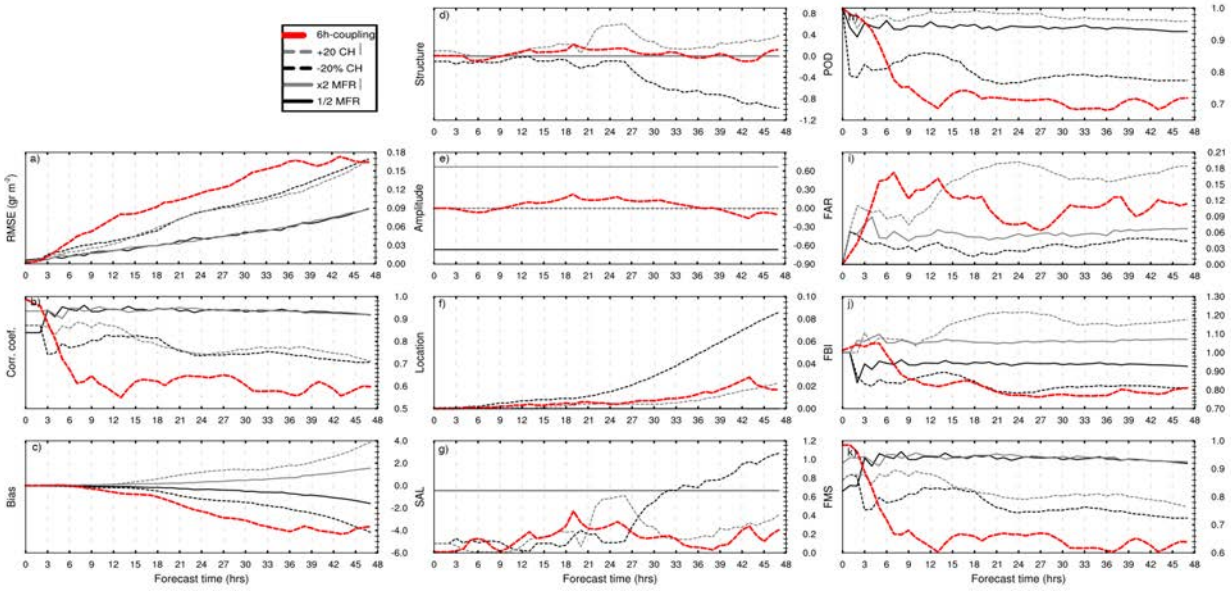

Figure 37. On-line vs. off-line evaluation scores evaluation scores for the NMMB-MONARCH-ASH synthetic application representing the uncertainty associated to the source term. ESPs were modified for the eruption column height (+/- 20%) and MER (x2 and ½). Scores are compared with those from the 6h off-line coupled forecasts (red line).

3.6 Summary and conclusions

This chapter quantifies the systematic errors inherent in off-line coupling strategies employed for operational volcanic ash forecasting. To this purpose, different coupling strategies available in the NMMB-MONARCH-ASH model (see Chapter 2 for model details) were employed to evaluate the predictability limitations of the off-line forecast against the on-line. Model comparison were performed for a synthetic case study focusing exclusively on the effect of the coupling approach, and for two historical cases accounting for changing meteorological conditions and ESPs. Evaluation scores indicate that systematic errors credited by off-line forecast (with more than 1h coupling interval) can be of the same order of magnitude that those better-constrained uncertainties associated to the source term. In particular, off-line forecasts in operational setups can result in significant errors in the dispersion of the ash plume for coupling intervals above 3h. The results of this study show that 6h coupling off-line forecasts fail to reproduce over 50% of the on-line forecast (best estimate of the true outcome) for a case with constant ESPs (synthetic case); close to 70% for the 2010 Eyjafjallajökull case and over 45% for the 2011 Cordón Caulle case. These inconsistencies are anticipated to be even more relevant in scenarios where the meteorological conditions change rapidly in time. The outcome of this chapter suppose a significant advance in the quantification of the uncertainty sources associated to traditional off-line volcanic ash forecasts, and advocates that operational groups responsible for real-time advisories for aviation consider employing computationally efficient on-line dispersal models.

Chapter 4

4 ON-LINE APPLICATION WITH NMMB-MONARCH-ASH. Antarctic volcanoes: A remote but significant hazard

4.1 Introduction

Explosive volcanic eruptions pose proximal hazards by tephra fallout and can disperse fine ash and volcanic aerosols over vast areas of the globe thereby generating a threat to human health and infrastructures and causing long-range air traffic disruptions. Several volcanic events occurred in recent years, including the 2010 Eyjafjallajökull, 2011 Grímsvötn and Cordón Caulle eruptions, led to large economic losses for the aviation industry and their stakeholders, and demonstrated the global extent of the phenomenon. From the tens of volcanoes located in Antarctica, at least nine are known to be active and five of them, all stratovolcanoes, have reported frequent volcanic activity in historical times (Fig. 38a)

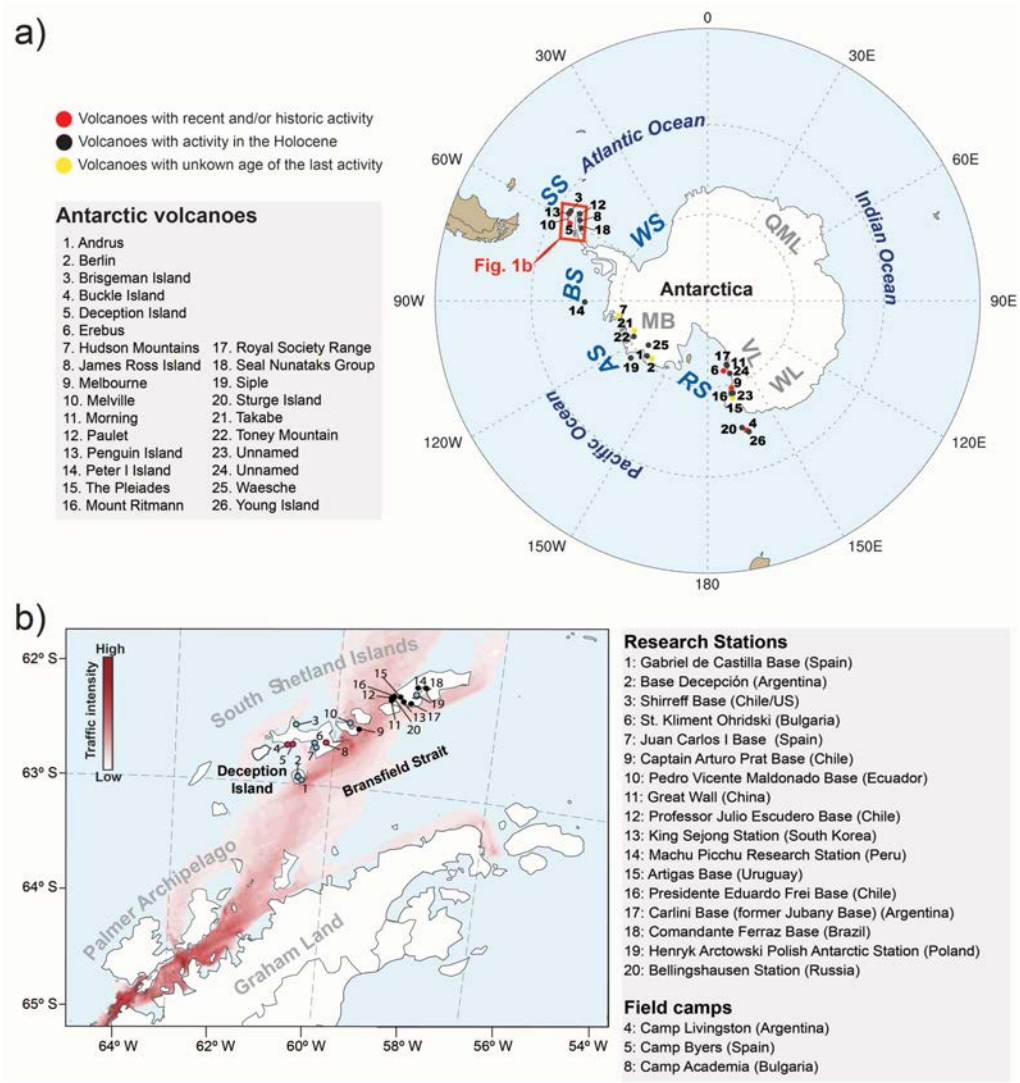

Figure 38. a) Location of Antarctic volcanoes listed in Table 13. AS: Amundsen Sea; BS: Bellinghausen Sea; MB: Marie Byrd Land; RS: Ross Sea; VL: Victoria Land; WS: Weddell Sea; WL: Wilkes Land. b) Location of year-round (black dots) and temporary (only austral summer)(blue dots) research stations nearby Deception Island. Red dots correspond to temporary field camps. The intensity of vessel traffic in the touristic season 2012/13 is also indicated (Bender et al., 2016).

Table 13 shows a list of volcanoes and last eruptions in Antarctica (Global Volcanism Program, http://www.volcano.si.edu).

Volcano name	Primary volcano type	Last eruption year	lat (º)	lon (º)
Andrus	Shield(s)	Unknown	-75.8	-132.33
Berlin	Shield(s)	-8350	-76.05	-136
Bridgeman Island	Stratovolcano	Unknown	-62.061	-56.717
Buckle Island	Stratovolcano	1899	-66.78	163.25
Deception Island	Caldera	1970	-63.001	-60.652
Erebus	Stratovolcano	2016	-77.53	167.17
Hudson Mountains	Stratovolcano(es)	-210	-74.33	-99.42
James Ross Island	Shield	Unknown	-64.15	-57.75
Melbourne	Stratovolcano	1892	-74.35	164.7
Melville	Stratovolcano	Unknown	-62.02	-57.67
Morning	Shield	Unknown	-78.5	163.53
Paulet	Pyroclastic cone	Unknown	-63.579	-55.78
Penguin Island	Stratovolcano	1905	-62.1	-57.93
Peter I Island	Shield	Unknown	-68.85	-90.58
Pleiades, The	Stratovolcano	-1050	-72.67	165.5
Rittmann, Mount	Shield	Unknown	-73.45	165.5
Royal Society Range	Pyroclastic cone(s)	Unknown	-78.25	163.33
Seal Nunataks Group	Pyroclastic cone(s)	Unknown	-65.03	-60.05
Siple	Shield	Unknown	-73.43	-126.67
Sturge Island	Stratovolcano	Unknown	-67.4	164.83
Takahe	Shield	-5550	-76.28	-112.08
Toney Mountain	Shield	Unknown	-75.8	-115.83
Unnamed	Pyroclastic cone(s)	Unknown	-73.45	164.58
Unnamed	Submarine	Unknown	-76.83	163
Waesche	Shield(s)	Unknown	-77.17	-126.88
Young Island	Stratovolcano	Unknown	-66.42	162.47

Table 13. List of Antarctic volcanoes and last eruptions according to the Global Volcanism Program (last accessed 02/05/2017).

To date, no study have assessed the potential regional and global scale risks associated to high latitude eruptions, albeit volcanic eruptions have damaged several Antarctic scientific stations repeatedly in the past (Roobol, 1982; Smellie, 2002). During the last decades, both scientific activity and tourism in the Antarctica have augmented notably, especially at the South Shetland Islands and the Antarctic Peninsula. This fact has significantly increased the exposure of population and infrastructures to volcanic

phenomena. For example, the islands of Deception and Livingston (South Shetland archipelago) host 5 research stations and 3 summer field camps, whereas Greenwich and King George islands, located in the same archipelago, are home to 10 all-year and 2 temporary research stations (Fig. 38b). In addition, the Palmer Archipelago and the northwestern coast of Graham Land have become important touristic destinations exceeding 30,000 visitors per year (IAATO, https://iaato.org/), drastically increasing the vessel traffic during the touristic season (e.g. traffic intensity; Fig. 38b). In light of the above, there is a real need to address the hazards posed by Antarctic eruptions.

The frequency of explosive ash-forming eruptions happening at high southern latitudes is uncertain. However, considering that *a priori* low energetic basaltic effusive activity may easily evolved into explosive if the raising magma interacts with sea water, snow or ice, the occurrence of moderate to highly explosive eruptions should not be disregarded (Pedrazzi et al., 2014). The objectives of this chapter are: i) analyze the potential impacts of ash dispersal and fallout from Antarctic volcanoes by focusing on Deception island as a case study, an active composite volcano with several tens of eruptions in the last 10,000 years (Bartolini et al., 2014; Smellie, 2002); ii) evaluate the ash dispersion dependency on the source location and magnitude for different eruptive scenarios in Antarctica; iii) investigate the seasonal climatic influence, by considering different meteorological situations typical for the Antarctic summer and winter periods.

The final objective of this chapter is to demonstrate that ash from high southern latitude volcanoes may pose a higher threat than previously believed. For this purpose, it is critical to employ a global model such NMMB-MONARCH-ASH (Marti et al., 2017) to understand ash circumpolar distribution patterns at high southern latitudes, which have obvious implications for tephrostratigraphic and chronologic studies that provide valuable isochrones to synchronize paleoclimate records. Section 4.2 in this chapter provides a description about Deception Island and its historical volcanism. Section 4.3 describes the methodology employed in this work. Section 4.4 presents the meteorological, ash dispersal and fallout simulations results. Section 4.5 discusses the potential impact of global aviation safety and climate associated to volcanic ash from Antarctic eruptions. Section 4.6 provides the conclusive remarks of this study.

4.2 Volcanism at Deception Island

Deception Island (DI), located at the spreading center of the Bransfield Strait marginal basin, consists of a horse-shoe-shaped composite volcanic system truncated by the formation of a collapse caldera represented as a sea-flooded depression known as Port Foster (Smellie, 2002). The tephra record from Deception and neighboring islands, reveals over 30 post-caldera Holocene eruptions, although a considerably higher number of eruptions are assumed to have occurred (Orheim, 1972). Indeed, over 50 relatively well-preserved craters and eruptive vents, scattered across the island, can be reconstructed and mapped (Fig. 39). The eruption record in Deception Island since the 19th century reveals periods of high

activity (1818–1828, 1906–1912) followed by decades of dormancy (e.g. 1912–1967) (e.g. Orheim, 1972; Roobol, 1982; Smellie, 2002). The unrest episodes recorded in 1992, 1999 (Ibáñez et al., 2003) and 2014-2015 (Almendros et al., 2015) demonstrate that the volcanic system is still active and may be cause of concern in the future. During the most recent explosive eruptions occurred in 1967, 1969 and 1970, ash fall and lahars destroyed or severely damaged the scientific bases operating on the island at that time (Roobol, 1982).

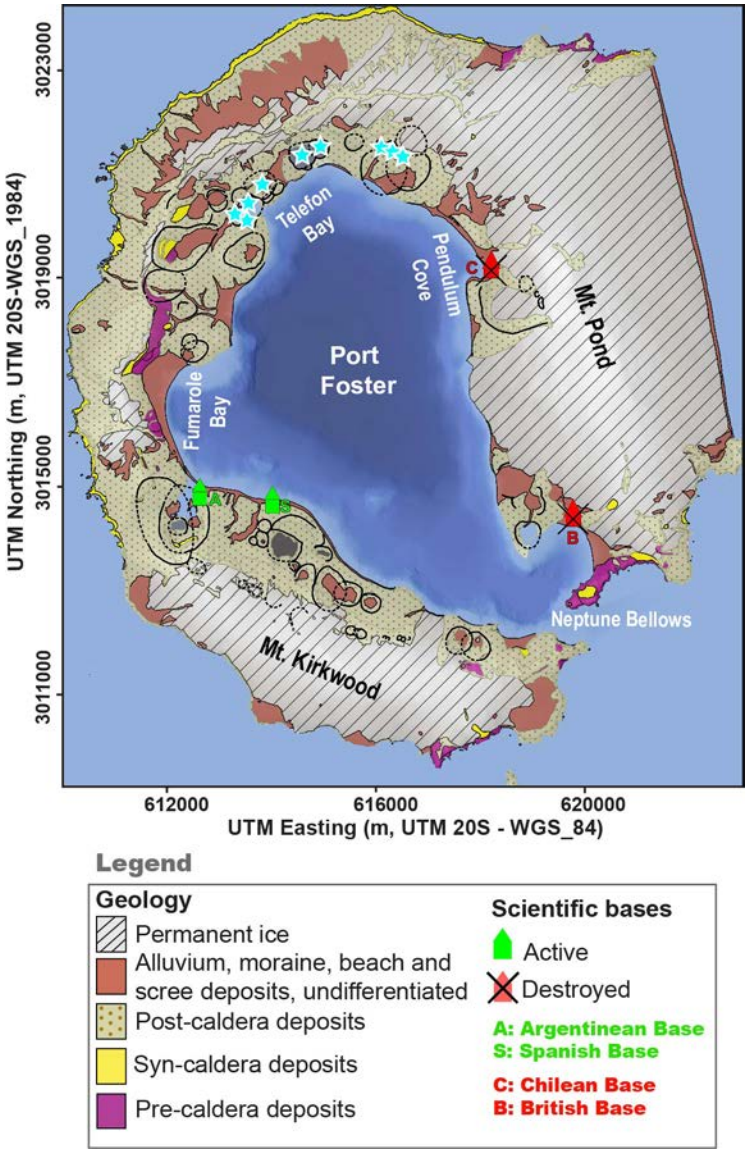

Figure 39. Simplified geological and tectonic map of DI (modified from Martí et al. (2013) and Smellie (2002). Blue stars show the sites of the 1970 volcanic event (data obtained from Spatial Data Infrastructure for Deception Island SIMAC, Torrecillas et al., 2006). Black solid and dashed lines delimit visible and inferred post-caldera volcanic craters.

Historical volcanism at DI, mostly classified as Volcanic Explosivity Index (VEI) 2-3, involves small to moderate-volume monogenetic eruptions (< 0.1 km^3) with eruptive columns up to 10km height (Bartolini et al., 2014; Pedrazzi et al., 2014; Smellie, 2002). Based on the analysis of past eruptions, the most disrupting hazard during a volcanic eruption on DI is ash fall. Due to the strong winds and the low altitude of the tropopause in the area (8-10 km; Smellie, 1999), ash fall deposits are rapidly dispersed

(Fretzdorff and Smellie, 2002; Liu et al., 2016; Pallàs et al., 2001). In fact, the common presence of DI tephra in lacustrine cores of neighboring islands, marine sediments of the Bransfield Strait and Scotia Sea (>800 km distance), and even in South Pole ice cores, suggests that some post-caldera eruptions may have been much more violent than those experienced in recent centuries. These eruptions would have involved eruptive columns exceeding 20 km in height and much larger volumes of magma (Liu et al., 2016; Moreton and Smellie, 1998; Smellie, 1999). In DI, variations in the degree of explosivity can be explained by eventual interactions of sea, underground aquifer, or glacier water with the rising or erupting magma (Pedrazzi et al., 2014).

4.3 Methods

This section presents the methodology to reconstruct, for the first time, the 1970-like eruptive scenario at DI to assess the potential impacts of ash dispersal evaluate the dispersion dependency on the source location and magnitude for different eruptive scenarios and seasonal periods.

4.3.1 Tephra dispersal modeling

Simulations with the on-line version of NMMB-MONARH-ASH (Marti et al., 2017) were performed to evaluate long-range dispersal of volcanic ash for a case of similar characteristics as the most recent eruption occurred in 1970 (Pedrazzi et al., 2014). The model predicts ash cloud trajectories, concentration at relevant flight levels, and deposit thickness for both regional and global domains. Regional-scale simulations serve to constrain the expected fallout ranges and deposit thicknesses whereas the global-scale ones aim at assessing potential long-range impacts on air traffic. Ash concentration values at FL050 (5,000 feet of nominal pressure) are relevant for airport closure whereas concentrations at FL250 and FL350 (25,000 and 35,000 feet) were used to evaluate the potential impacts from ash dispersal on aviation. Additionally, to evaluate the ash dispersion dependency on the source location and eruption magnitude (column height), dispersion results from the DI scenario were compared with: i) those with similar set-up but with the source located at higher latitudes, more specifically, at a position equivalent to Mt. Erebus volcano (77.5ºS and 167ºE); and ii) those from an eruptive event with ± 50% variation in the height of the eruptive column.

4.3.1.1 Model set-up and data

Table 14 summarizes the NMMB-MONARCH-ASH model configuration for the global and regional domains. The Eruption source parameters (ESP) for the 1970-like scenario were obtained from Pedrazzi et al. (2014), who inferred a column height of 10 km and a volume of 0.1 km^3. The model estimates the mass eruption rate from column height and atmospheric conditions above the vent based on the parameterization of Degruyter and Bonadonna (2012).

MODEL CONFIGURATION

Dynamics	NMMB (10s/180s time-step)
Physics	Ferrier microphysics BMJ cumulus scheme MYJ PBL scheme LISS land surface model
Aerosols	5 ash bins (30s/180s time-step)
Source Term (emissions)	
Duration	12h
Vertical distribution	Point source
MER formulation	Degruyter and Bonadonna (2012)
Aggregation model	None
Sedimentation model	Ganser (1993)
Run Set-up	
Duration	9 days
Number of processors	256/512
Domain	Regional/Global
Horizontal resolution	0.052º x 0.037º / 1º x 0.75º
Vertical layers	60
Top of the atmosphere	21 hPa
Meteorology global conditions (spatial resolutions)	ECMWF EraInterim Reanalysis (0.75º x 0.75º)

Table 14. Model configuration for the regional and global runs for a 1970-like eruptive scenario at Deception Island.

The particle Total Grain Size Distribution (TGSD) was reconstructed from tephra deposits measured at Livingstone island and discretized in 5 bins ranging from 2Φ (0.5 mm) to 6Φ (16μm) with a linear dependency of particle density on diameter ranging from 1666 to 2800 kgm^{-3} (Table 15). It should be noted that, due to the lack of sampling in more proximal locations the resulting TGSD is fine-skewed. As a consequence, simulations are expected to slightly underestimate deposit load and overestimate far-range concentrations.

size (Φ)	diameter (mm)	density (kg m^{-3})	sphericity (-)	mass fraction (%)
2	0.5	1666	0.9	2.92
3	0.25	1950	0.9	30.20
4	0.125	2233	0.9	33.80
5	0.031	2516	0.9	30.02
6	0.016	2800	0.9	3.05

Table 15. TGSD employed in NMMB-MONARCH-ASH for all DI runs

4.3.2 Seasonal climate variability

The seasonal climate variability of Antarctica is mainly controled by the Southern Annular Mode (SAM). Changes in this mode explain up to 30% of the deseasonalized variability in both geopotential and winds (Bergmann and Dobslaw, 2012). For this reason, each set of simulations considers meteorological situations typical for the Antarctic summer and winter periods, selecting 1982 and 1995 as representative years, respectively. For each of these two periods (S-82/W-95), the specific days with season-mean upper-level winds were selected for simulations. In addition, two additional simulation sets were performed to give special emphasis to the summer situation in Antarctica, where there is a significant increase of tourists and scientific researchers. The additional summer dates were chosen in coincidence with the recent unrest episodes recorded in 1992 and 1999 (S-92/S-99) (Ibáñez et al., 2003).

4.4 Results

4.4.1 Meteorological conditions

Figure 40 shows the meteorological results over the South Pole during the two selected seasons (S-82/W-95). A persistent large-scale clock-wise circulation around an upper-level low-pressure zone located close to the Pole is clearly visible at any time. The polar vortex extends up to the stratosphere, with a global-scale circulation covering latitudes from 70º up to 50º depending on the period. At these stratospheric levels, the resulting polar jet stream is very intense (wind speeds over 60 m/s), widening notably during the winter (Fig. 40b) and narrowing during the summer (Fig. 40a).

In the particular case of the summer situation, the jet stream remains confined at around 65º latitude. This is also true close at the tropopause (Fig 42 - 10 km time series height plots), where Rossby waves start to form and large-scale wind meandering appears. Finally, at mid-tropospheric levels (Fig. 41 and 44: 5 km time series height plots), the meteorological situations show lesser seasonal dependency and are characterized by a breaking of the jet stream and a pronunciation of the meanders reaching much lower latitudes. These well-known synoptic situations have implications on tephra dispersal patterns and anticipate distinct behaviors depending on the volcano location and eruption column height. On the one hand, low plumes (<10 km) from high-latitude (>70º) volcanoes are likely to be confined within the less-intense-winds zone encircled by the jet stream, i.e. displaying no transcontinental dispersal. However, this may not be the case for higher plumes from these volcanoes (Fig. 43 and 46), which could be advected towards the continental periphery and then entrapped by the jet stream before ash settling on the ground. On the other hand, ash released at any height from lower-latitude volcanoes (e.g. Deception Island) is more likely to encircle the globe and reach sub-polar latitudes by meandering advection. Meteorological model results for all climatological periods are presented in detail in Figs. 41- 46.

4.4.2 Long-range ash dispersal

Global and regional-scale ash dispersal simulations were performed for the DI 1970-like scenario under the different "climatically-representative" meteorological situations. Figures 47 and 48 show global-scale model results from an eruptive column of 10 km height for the summer and winter seasons, respectively. Simulation results for the other summer scenarios (S-92/S-99) are presented for total column mass load (Figs. 49 - 54) and ash concentration at relevant flight levels (Figs 55 - 60). At global scale, moderate to high values of ash column load (>1 g m^{-2}) are found up to 4 days (96 h) after the eruption (see Figs. 49 - 54). In all simulations, the highest cloud column mass load values (>100 g m^{-2}) are limited to the first 48 h after the eruption start and are mainly found over the Atlantic Ocean, the Scotia and the Weddell Seas. However, a residual small amount of ash (0.1-1 g m^{-2}) is still present in the atmosphere up to 8 days after the eruption onset. Ash concentrations above the flight safety thresholds (0.2-2 mg m^{-3}, orange and red contours in Figs. 47 and 48, and Figs. 55 - 60) can be observed over South Africa and, in some cases, also over southern Australia or even over austral Patagonia, confirming the potential threat of this DI eruptive scenario to aviation. Depending on the specific wind conditions, some ash clouds re-enter back to the Antarctic Continent through the Queen's Maud Land during the first 48 h after the eruptions (e.g. Fig. 48) or through the Wilkes Land (with lower concentrations) after longer times (e.g. 72 h in Fig. 54). However, in most cases ash clouds circulate around (latitudes 70º-50º) and away (<50º) the continent, i.e. leaving no substantial fallout record on the main land, highlighting the possibility that many DI eruptions are not registered in the form of tephra layers in South Pole ice cores.

4.4.3 Ash fallout

Figure 61 shows the ash fallout deposits for the different meteorological conditions. Understandably, the precise orientations or the deposit axes depend on the regional winds during the selected days, which dispersed coarser particles predominantly to the southeast and southwest of DI. Deposits exceeding 1 cm in thickness can be found at distances as far as James Ross Island (> 190 km) or beyond Joinville Island (> 230 km). In any case, results highlight the potential for fallout to impact research stations and touristic destinations around Palmer Archipelago and Bransfield Strait locations. In addition, ash fallout could also have a disruption for touristic vessels operating in the region.

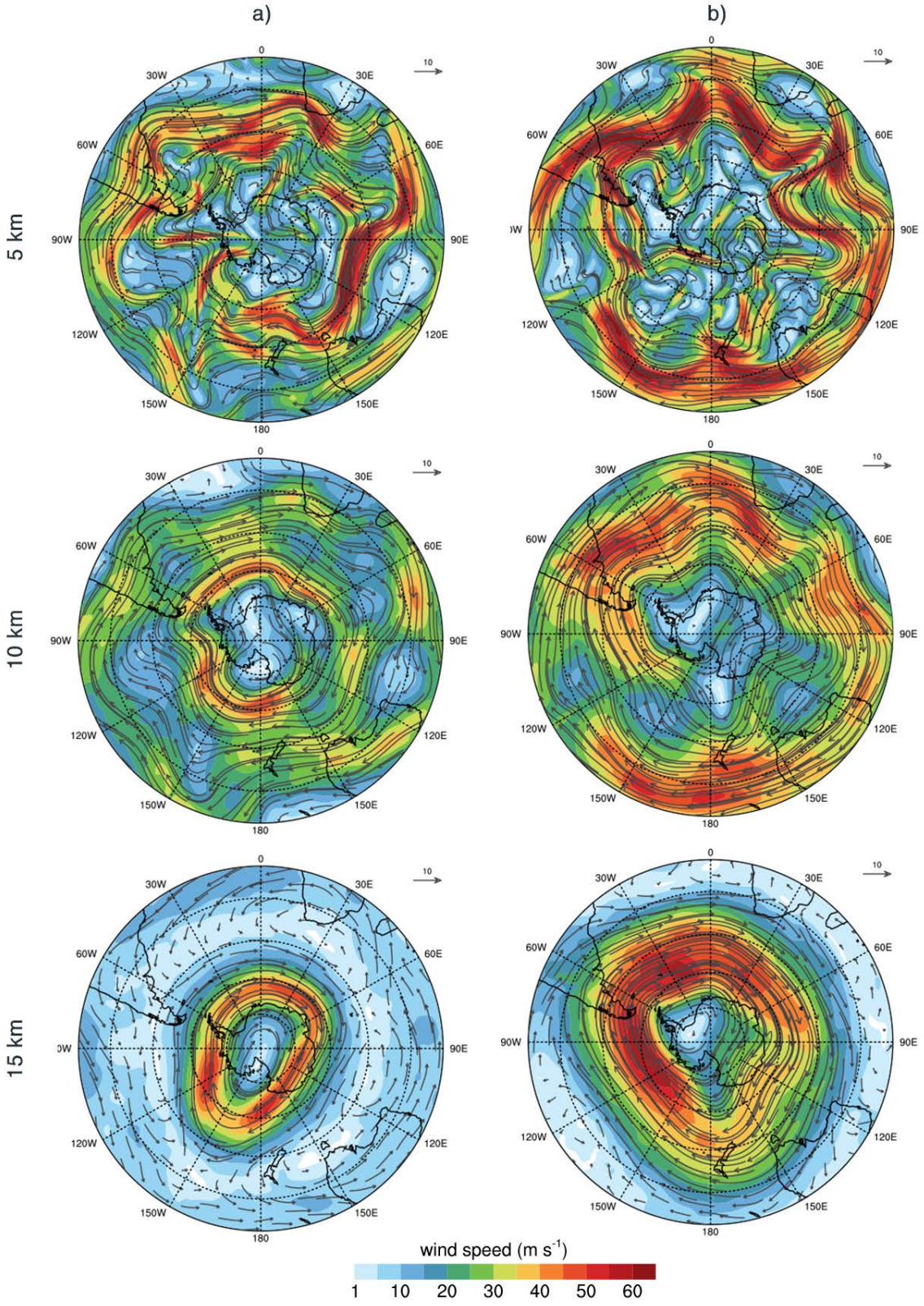

Figure 40. NMMB-MONARCH-ASH meteorological results over the South Pole during the selected (averaged) days of summer 1982 (a), and winter 1995 (b) seasons. Plots show wind vectors and velocity contours (m s^{-1}) at 5 (top), 10 (middle) and 15 (bottom) km a.s.l., roughly corresponding to mid-troposphere, tropopause and stratosphere respectively.

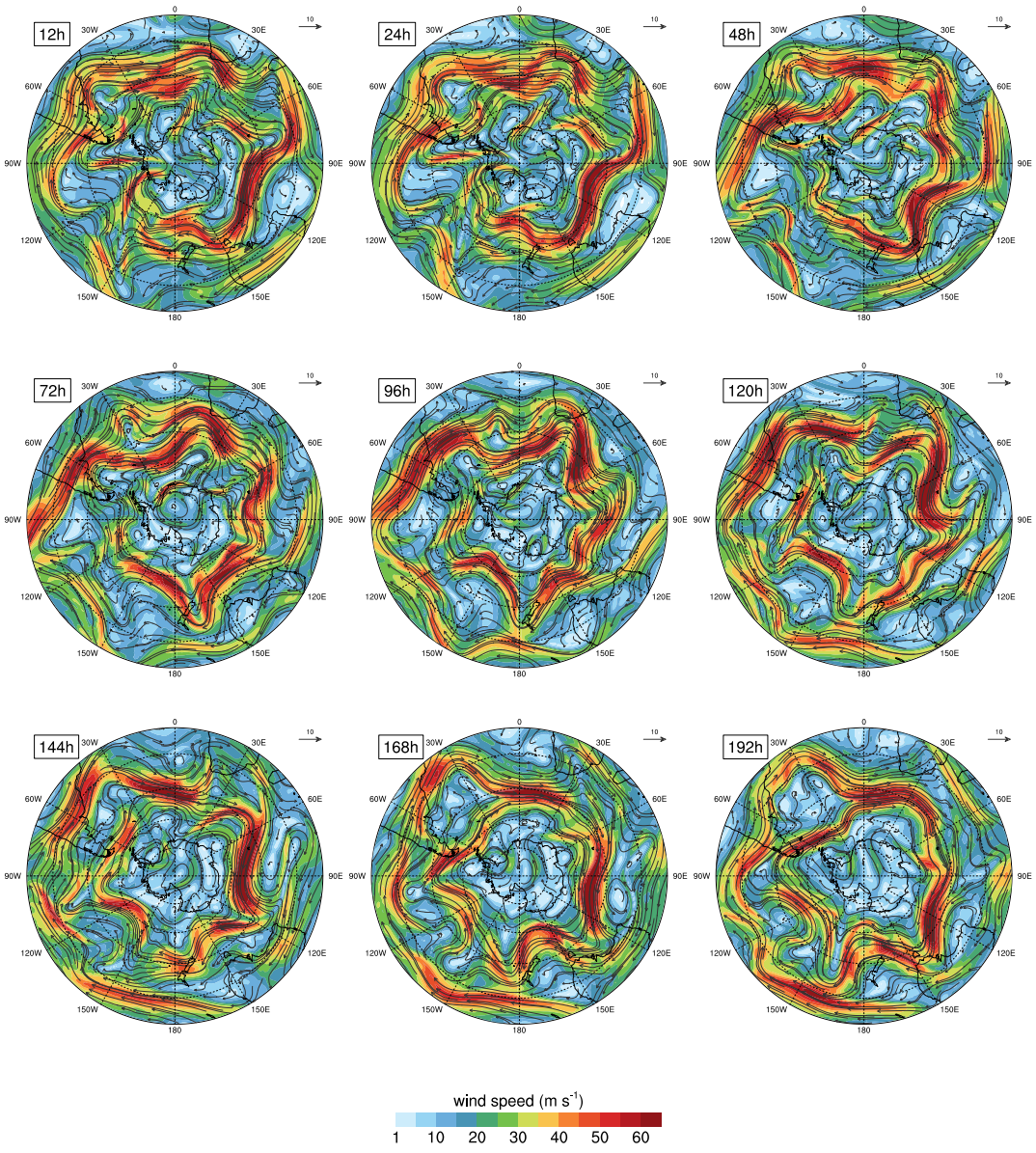

Figure 41. NMMB-MONARCH-ASH meteorological model results over the South Pole during the selected (averaged) days of the summer 1982 period. Plots show wind vectors and velocity contours (m s^{-1}) at 5 km height during 8 days (192h).

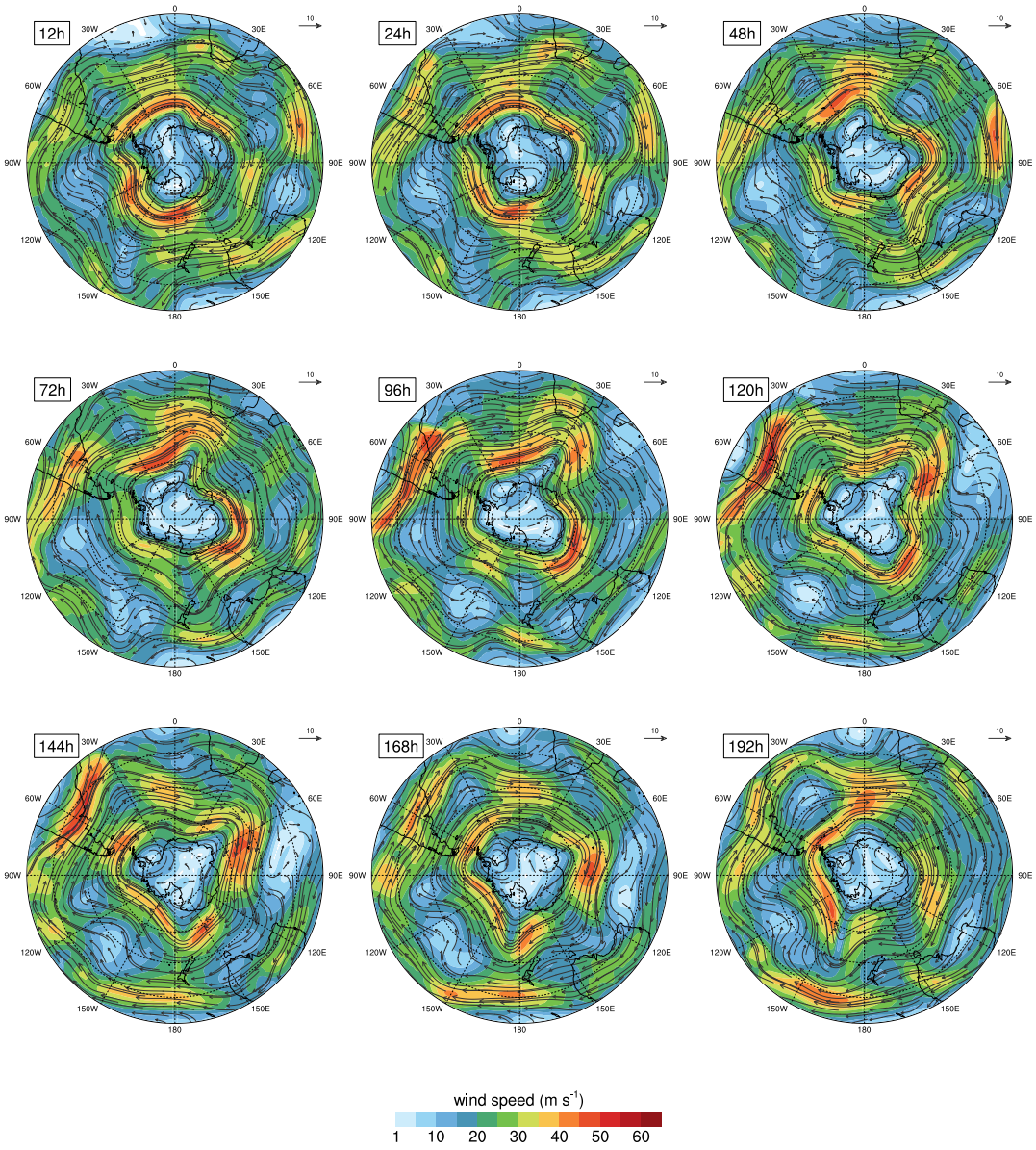

Figure 42. NMMB-MONARCH-ASH meteorological model results over the South Pole during the selected (averaged) days of the summer 1982 period. Plots show wind vectors and velocity contours (m s^{-1}) at 10 km height during 8 days (192h).

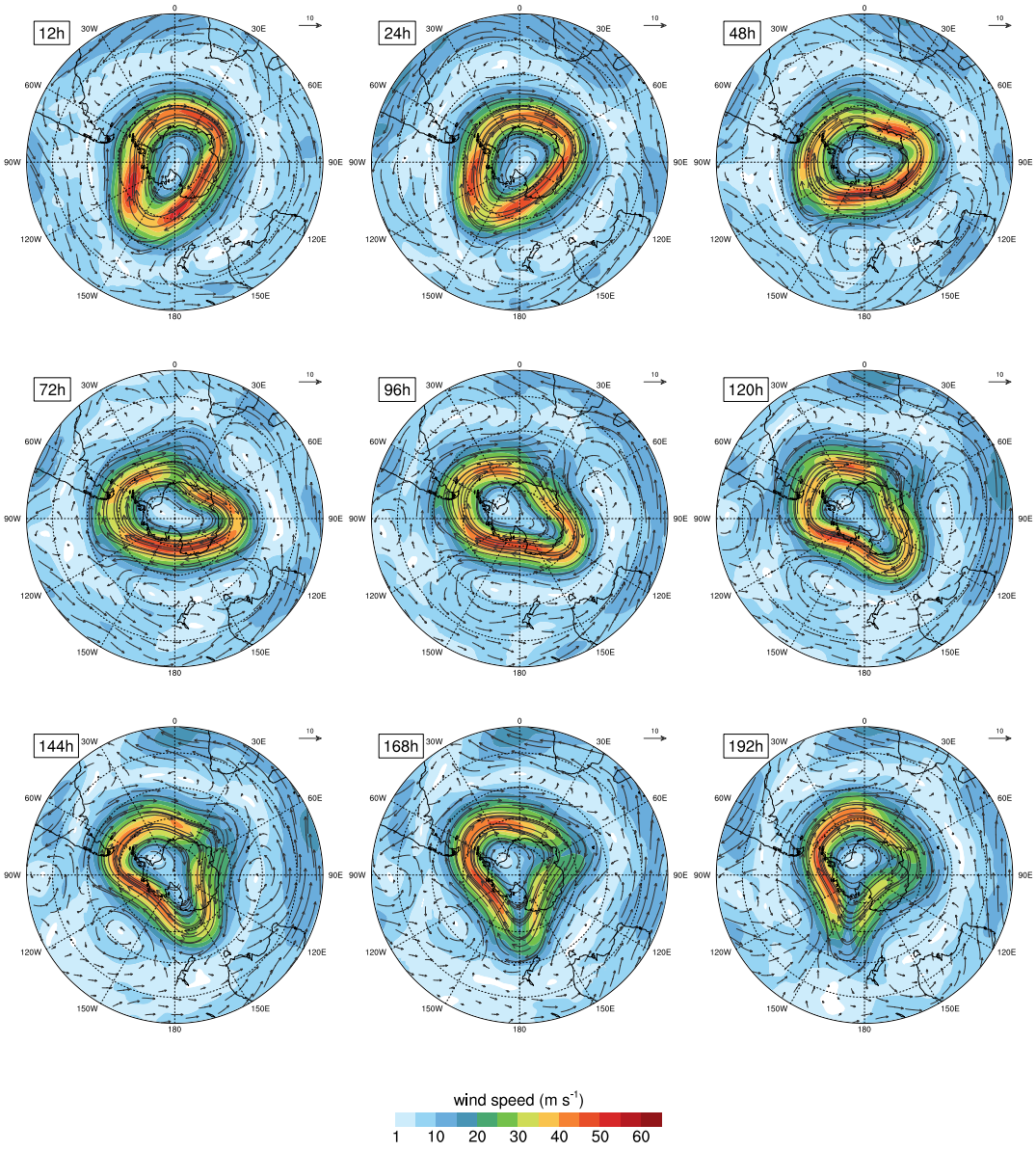

Figure 43. NMMB-MONARCH-ASH meteorological model results over the South Pole during the selected (averaged) days of the summer 1982 period. Plots show wind vectors and velocity contours (m s^{-1}) at 15 km height during 8 days (192h).

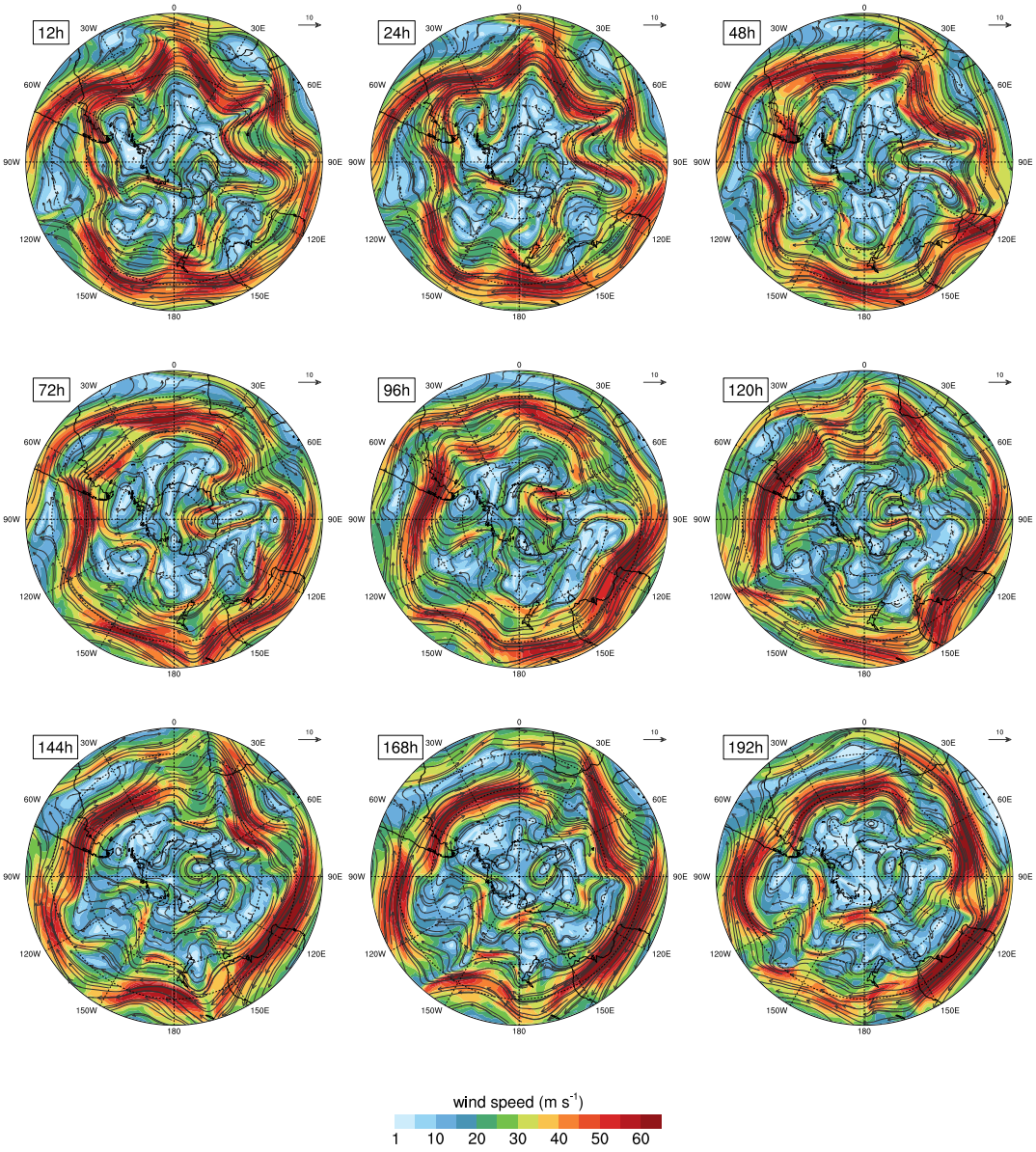

Figure 44. NMMB-MONARCH-ASH meteorological model results over the South Pole during the selected (averaged) days of the winter 1995 period. Plots show wind vectors and velocity contours (m s^{-1}) at 5 km height during 8 days (192h).

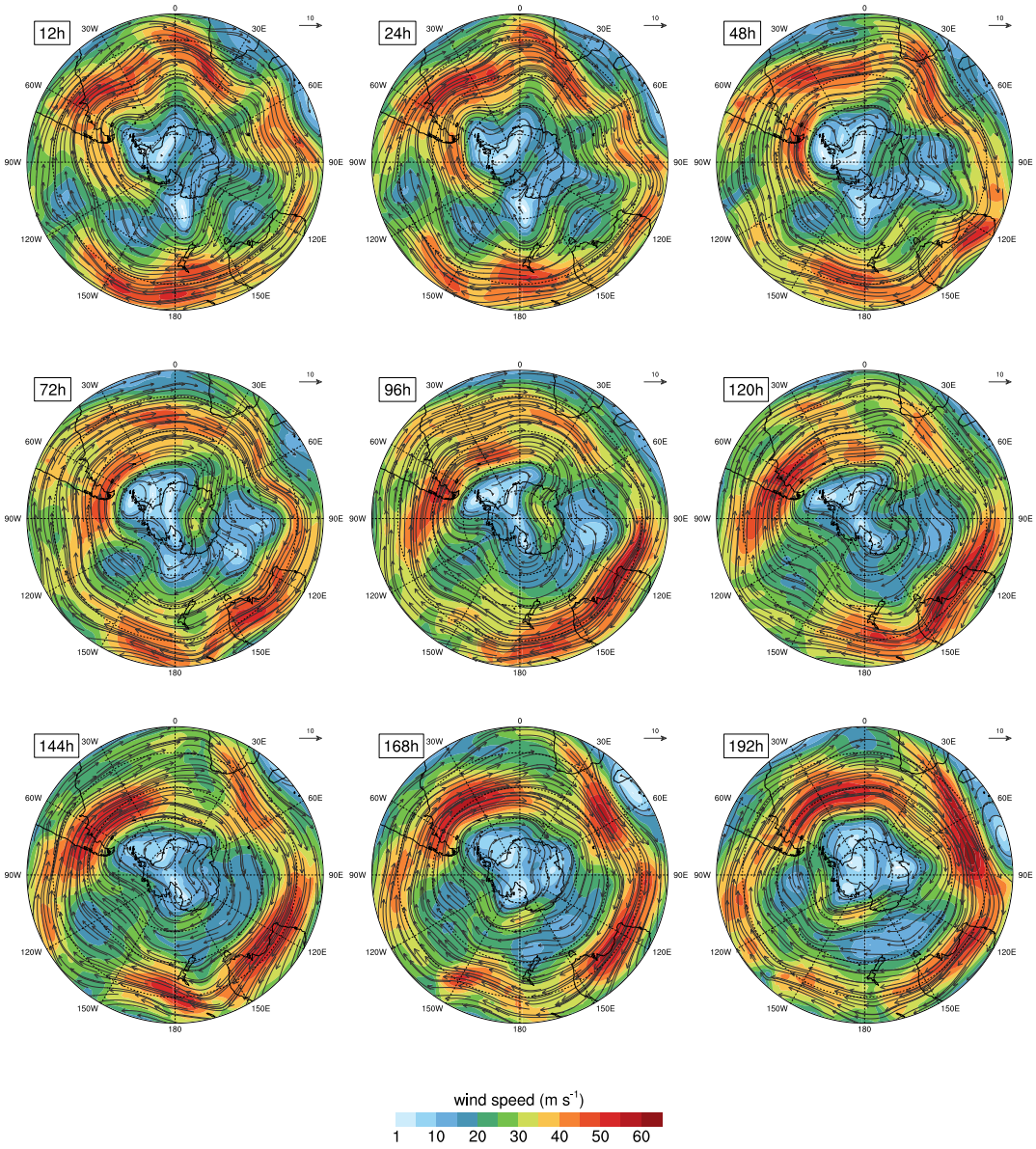

Figure 45. NMMB-MONARCH-ASH meteorological model results over the South Pole during the selected (averaged) days of the winter 1995 period. Plots show wind vectors and velocity contours (m s^{-1}) at 10 km height during 8 days (192h).

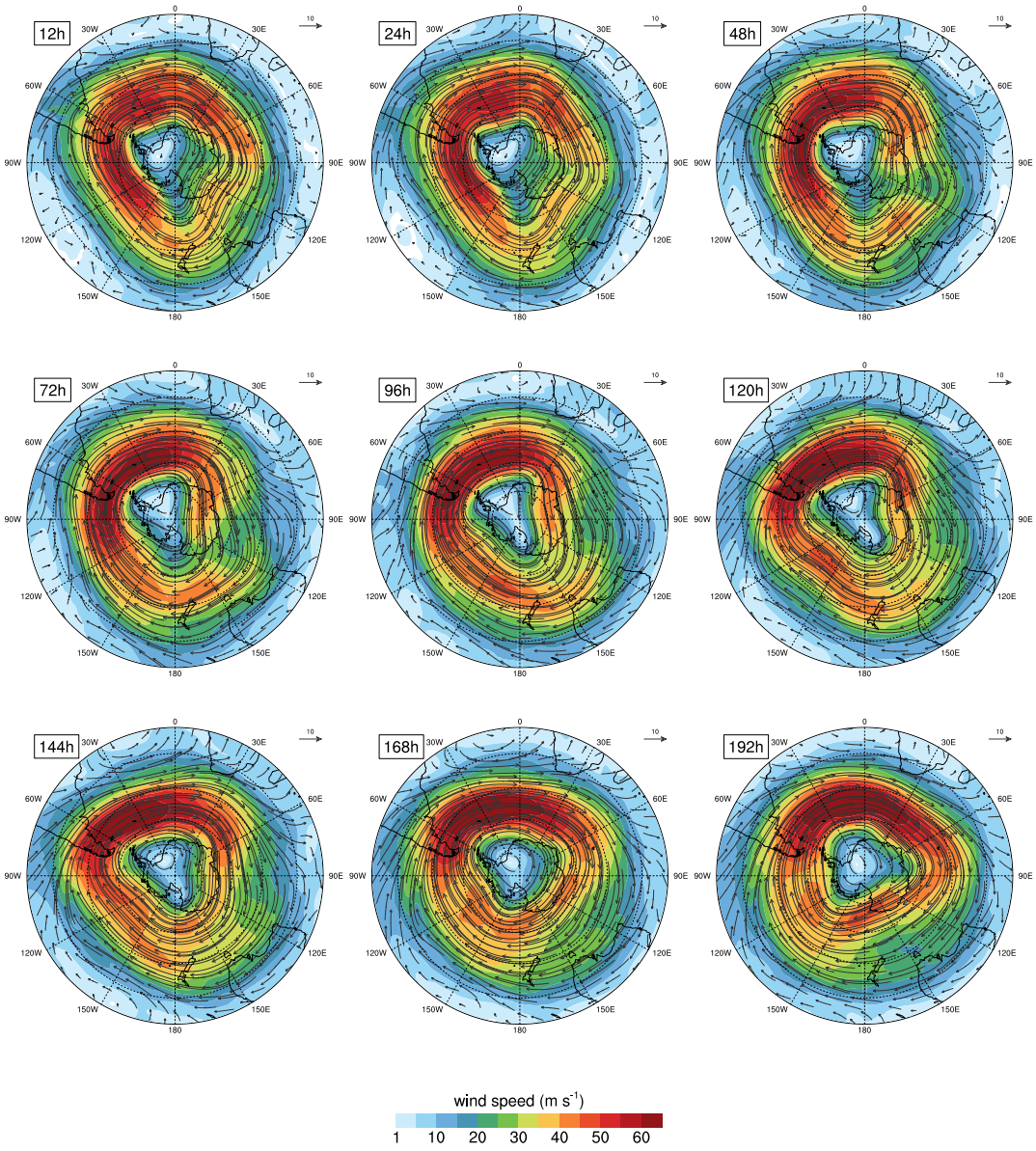

Figure 46. NMMB-MONARCH-ASH meteorological model results over the South Pole during the selected (averaged) days of the winter 1995 period. Plots show wind vectors and velocity contours (m s^{-1}) at 15 km height during 8 days (192h).

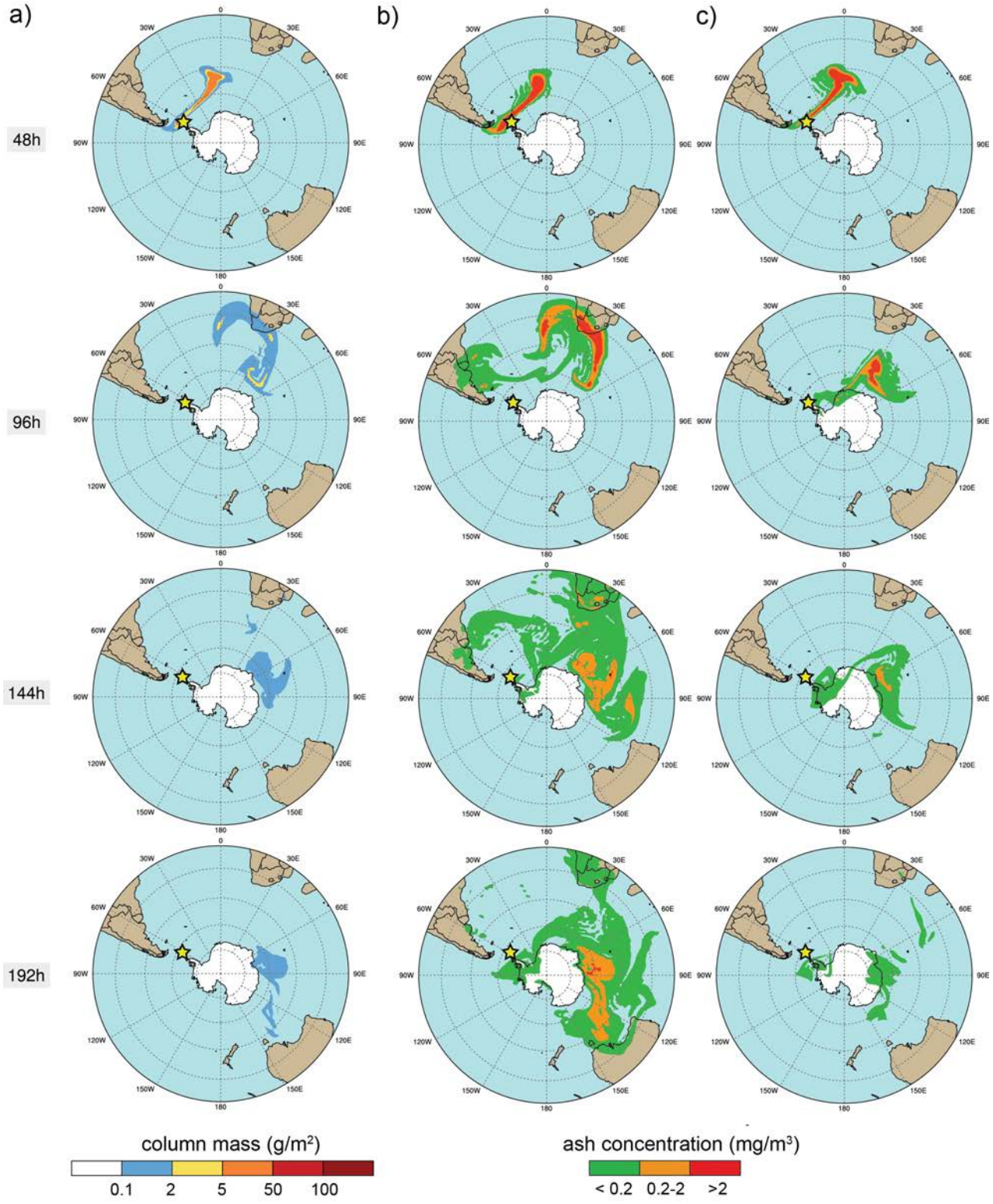

Figure 47. Global-scale NMMB-MONARCH-ASH model results for the summer 1982 period at different time instants (2, 4, 6, and 8 days after the eruption start from top to bottom respectively). An eruptive column of 10 km height was considered for the 1970-like scenario to simulate: a) the total column mass loading (g m^{-2}), b) the concentration of ash at Flight Level FL050 (mg m^{-3}), and c) the concentration at FL250 (mg m^{-3}). Safe ash concentration thresholds are shown (red concentration contours illustrate "No Flying" zones). The yellow star indicates the location of Deception Island.

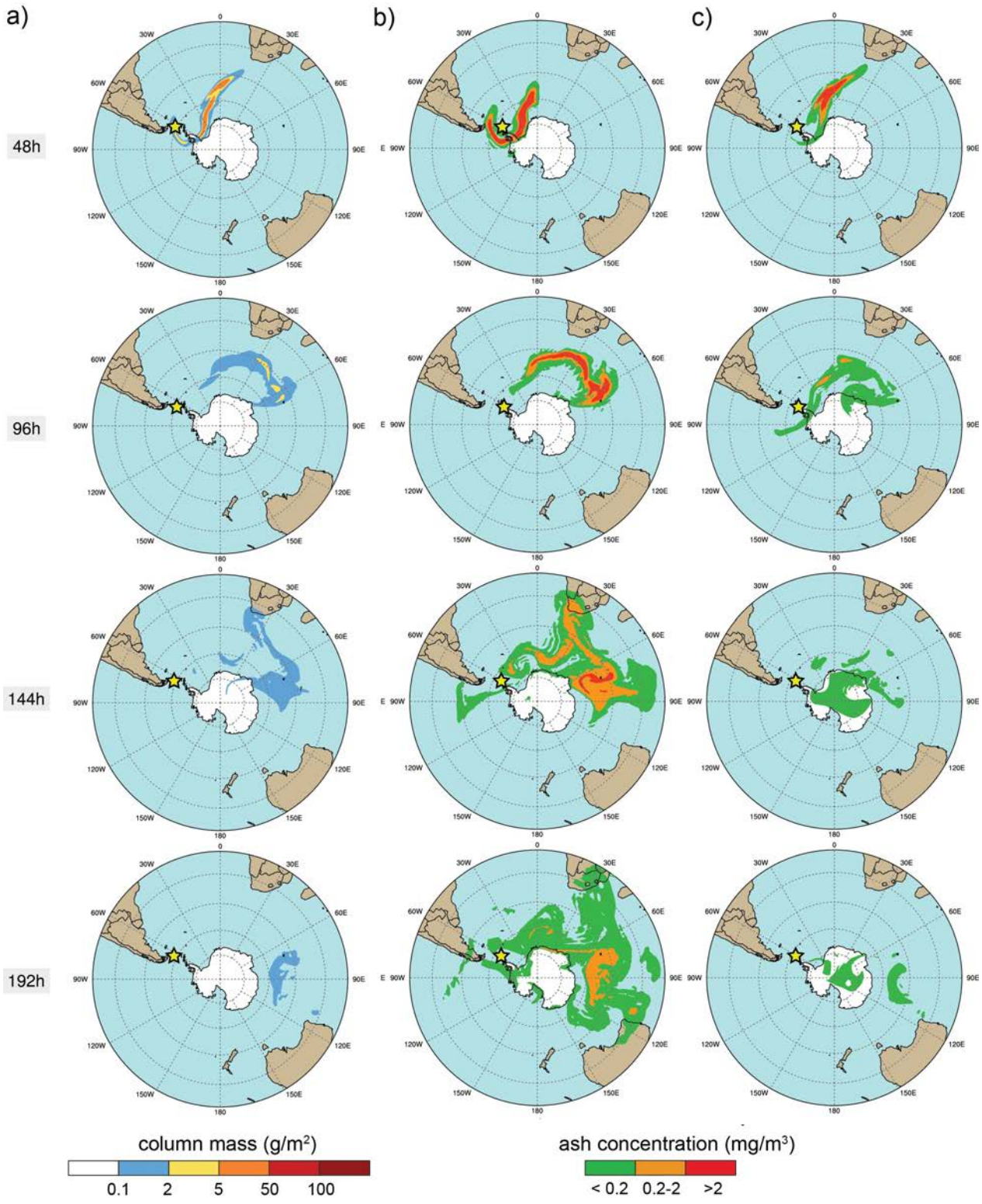

Figure 48. Global-scale NMMB-MONARCH-ASH model results for the winter 1995 period at different time instants (2, 4, 6, and 8 days after the eruption start from top to bottom respectively). An eruptive column of 10 km height was considered for the 1970-like scenario to simulate: a) the total column mass loading (g m^{-2}), b) the concentration of ash at Flight Level FL050 (mg m^{-3}), and c) the concentration at FL250 (mg m^{-3}). Safe ash concentration thresholds are shown (red concentration contours illustrate "No Flying" zones). The yellow star indicates the location of Deception Island.

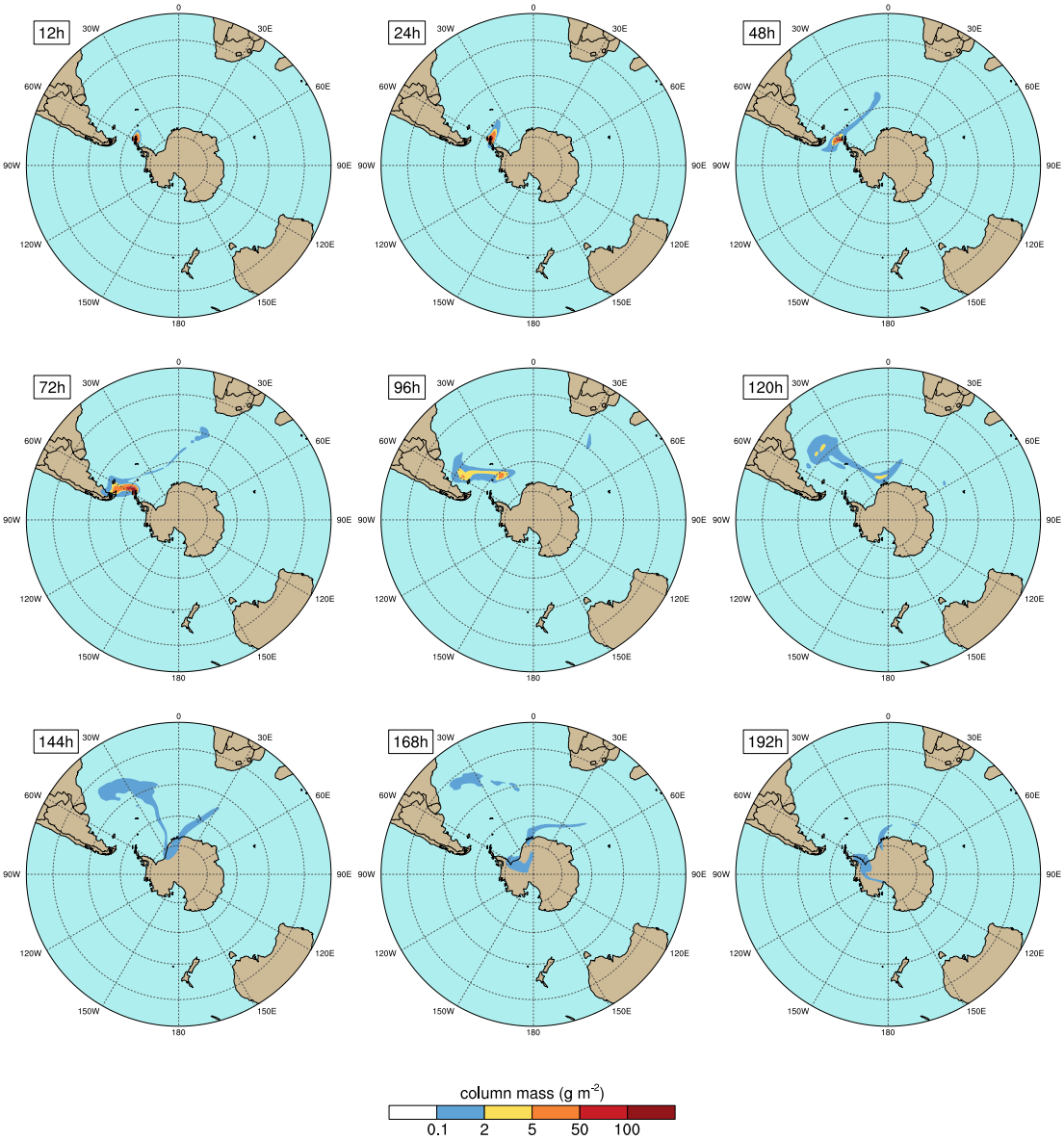

Figure 49. NMMB-MONARCH-ASH total ash column mass load (g m^{-2}) during the 1999 summer period at different time instants after the eruption start. Simulation considering an eruption column height of 5 km. The yellow star indicates the location of Deception Island.

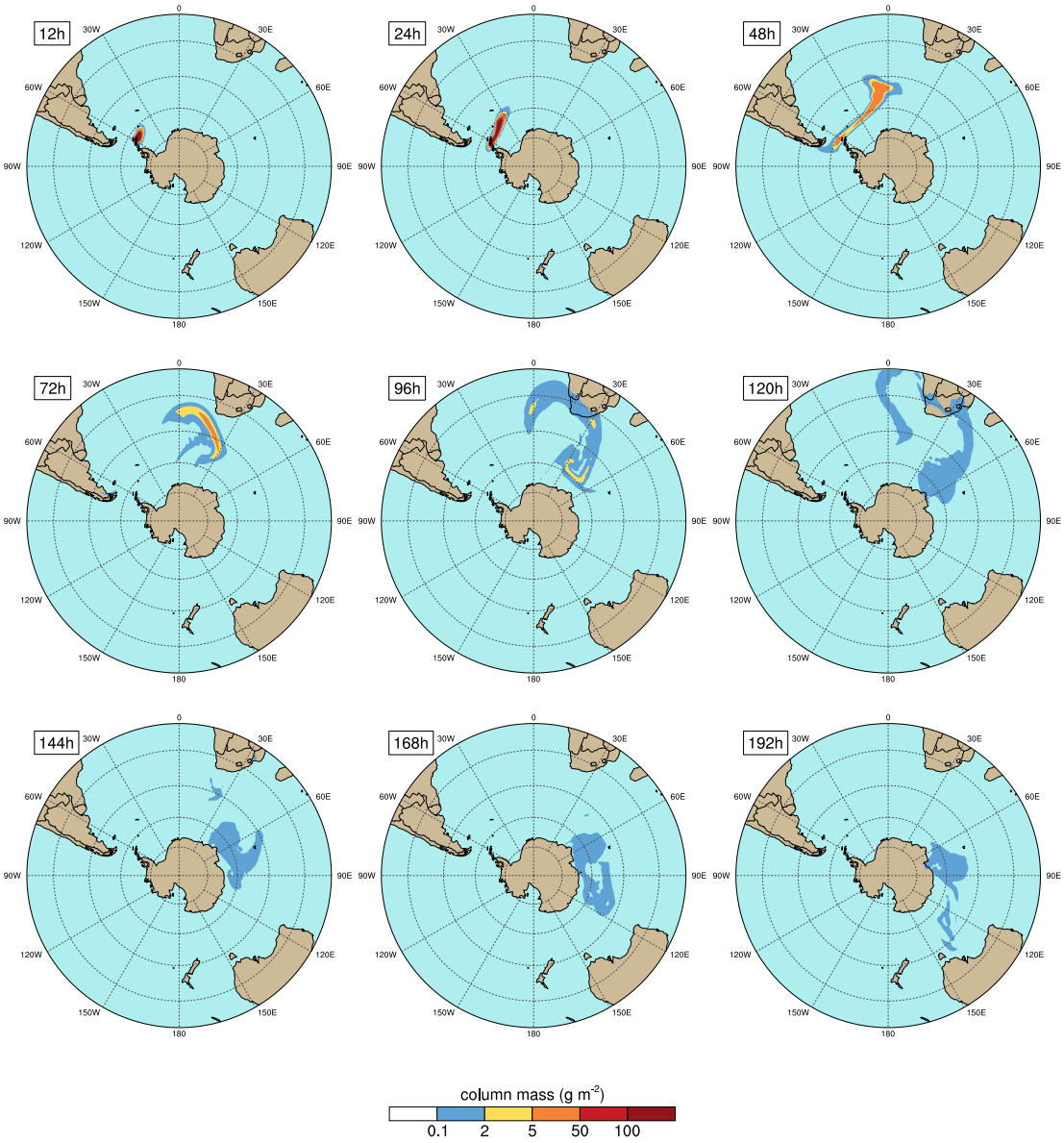

Figure 50. NMMB-MONARCH-ASH total ash column mass load (g m^{-2}) during the 1999 summer period at different time instants after the eruption start. Simulation considering an eruption column height of 10 km. The yellow star indicates the location of Deception Island.

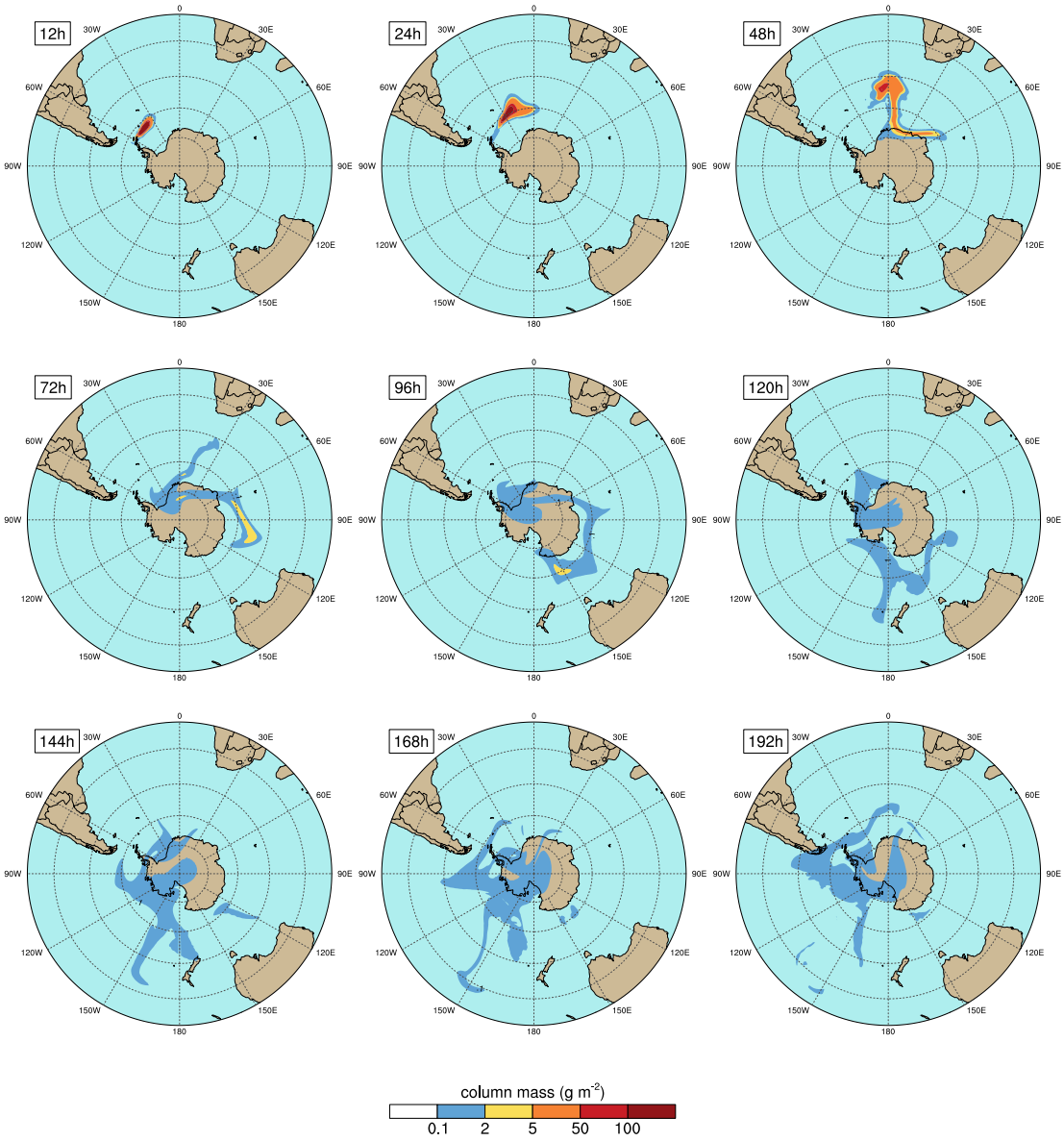

Figure 51. NMMB-MONARCH-ASH total ash column mass load (g m^{-2}) during the 1999 summer period at different time instants after the eruption start. Simulation considering an eruption column height of 15 km. The yellow star indicates the location of Deception Island.

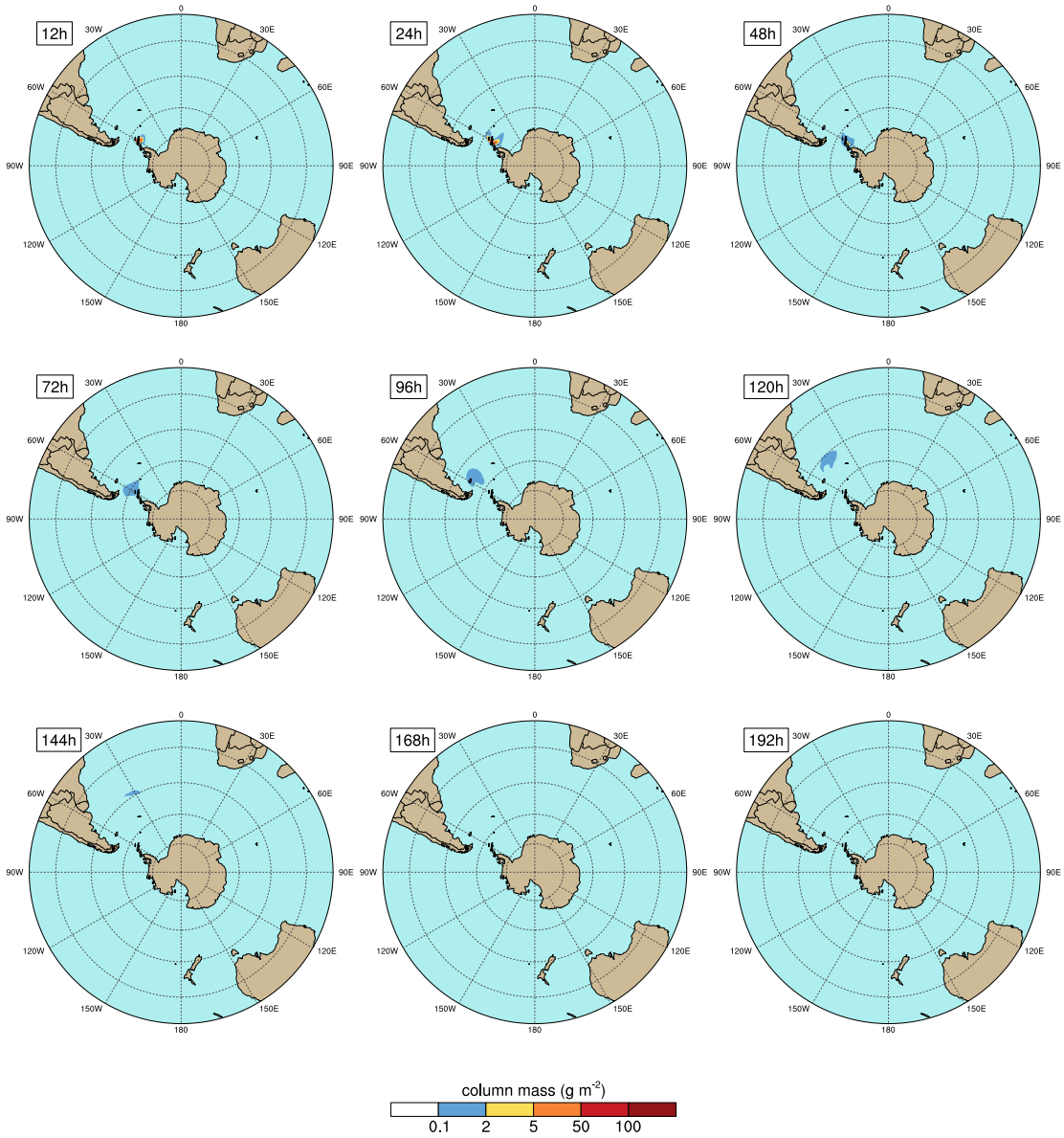

Figure 52. NMMB-MONARCH-ASH total ash column mass load (g m^{-2}) during the 1992 summer period at different time instants after the eruption start. Simulation considering an eruption column height of 5 km. The yellow star indicates the location of Deception Island.

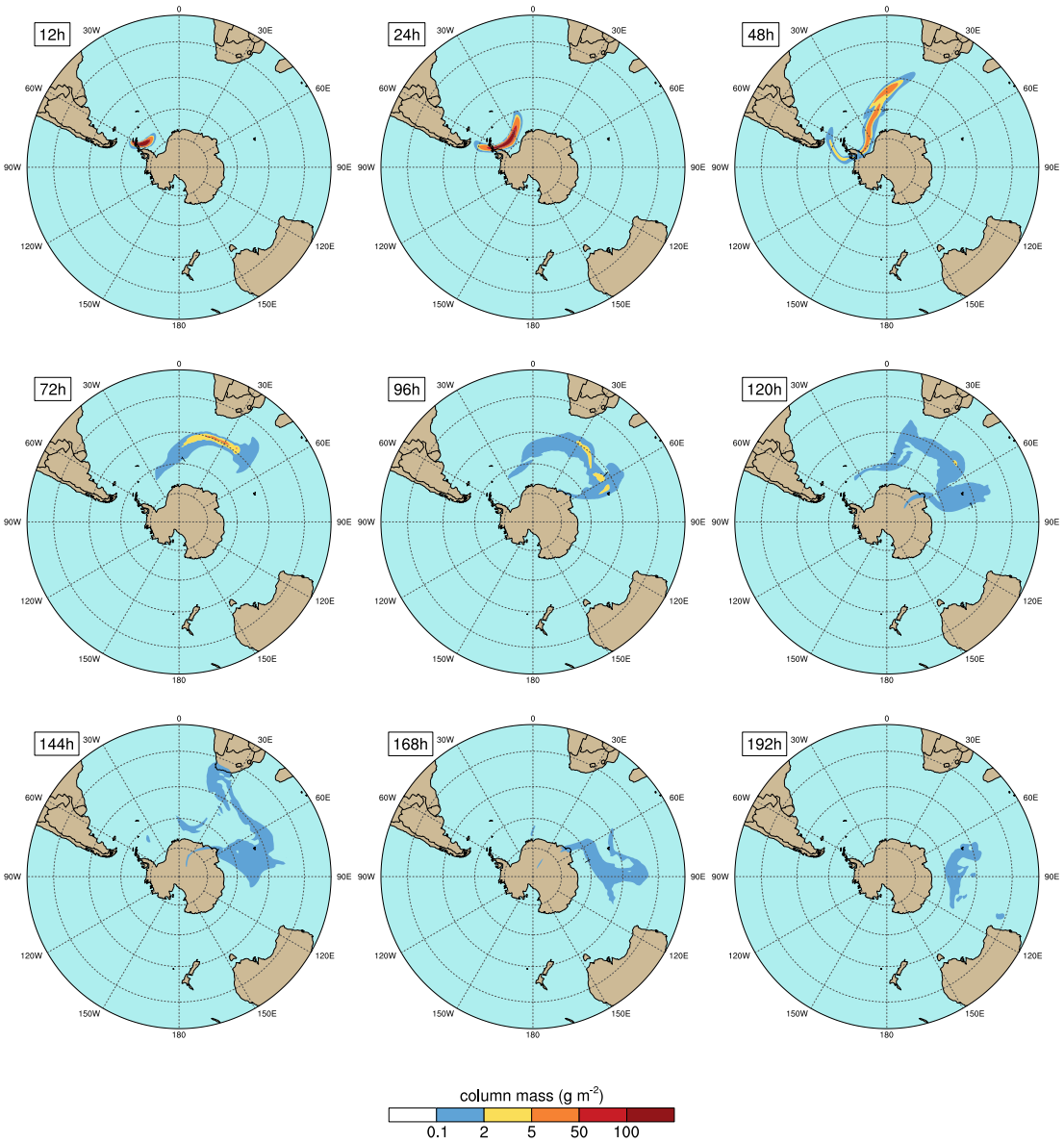

Figure 53. NMMB-MONARCH-ASH total ash column mass load (g m^{-2}) during the 1992 summer period at different time instants after the eruption start. Simulation considering an eruption column height of 10 km. The yellow star indicates the location of Deception Island.

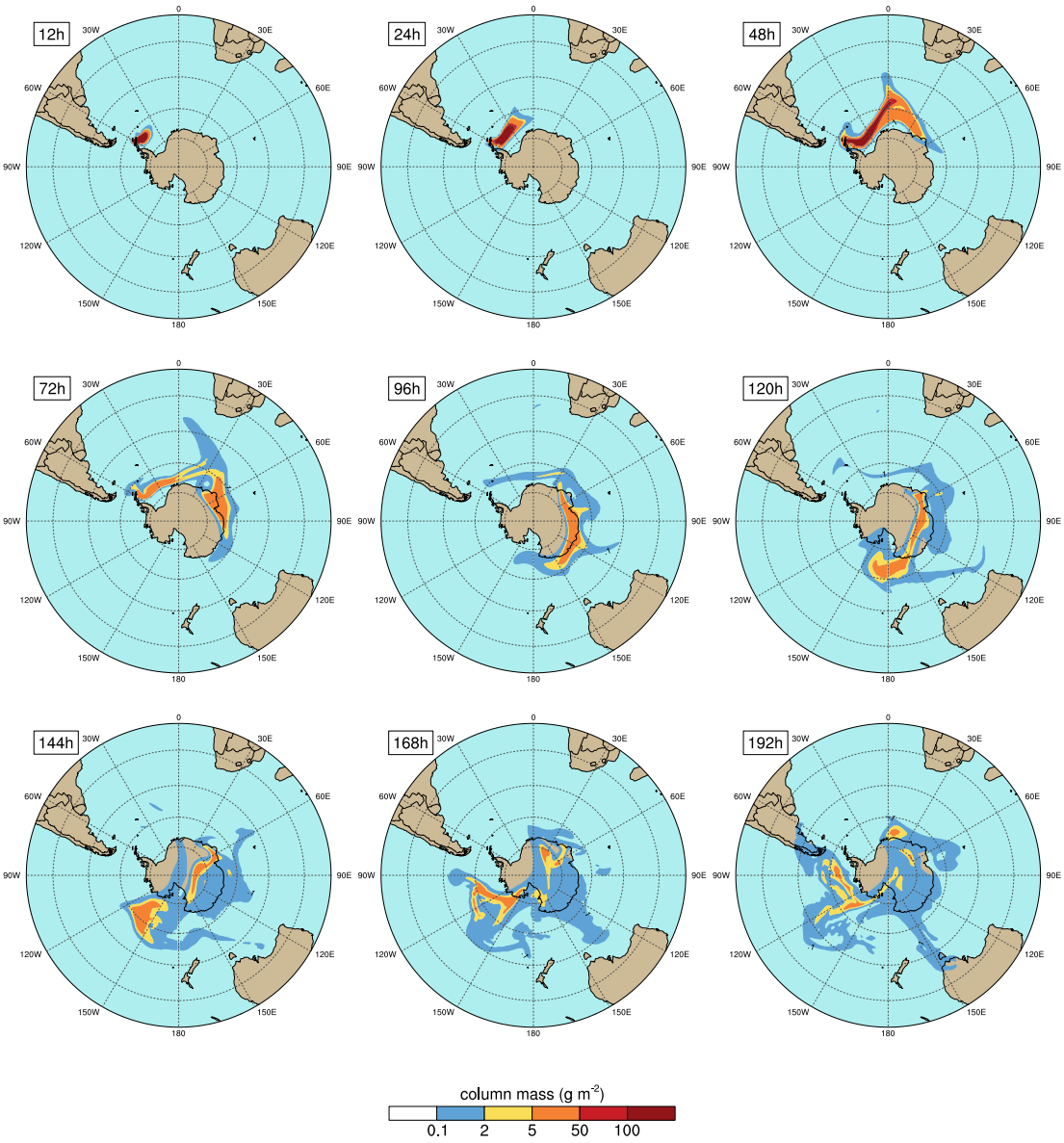

Figure 54. NMMB-MONARCH-ASH total ash column mass load (g m^{-2}) during the 1992 summer period at different time instants after the eruption start. Simulation considering an eruption column height of 15 km. The yellow star indicates the location of Deception Island.

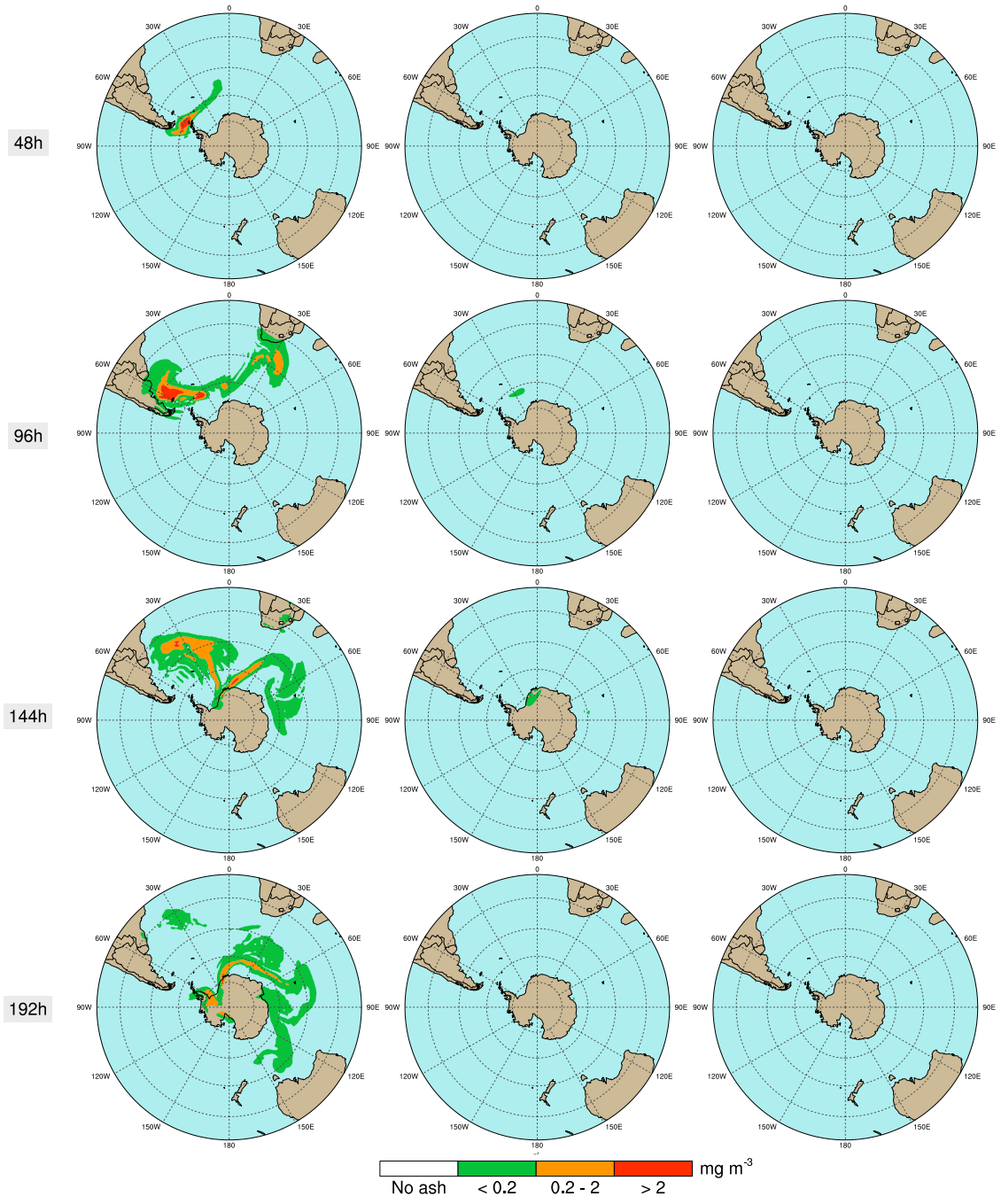

Figure 55. NMMB-MONARCH-ASH Flight Level ash concentrations (mg m^{-3}) at FL050 (left), FL250 (middle), and FL350 (right) at different time slices during the 1999 summer period. Safe ash concentration thresholds are shown (red contours illustrate "No Flying" zones). Simulation considering an eruption column height of 5 km. The yellow star indicates the location of Deception Island.

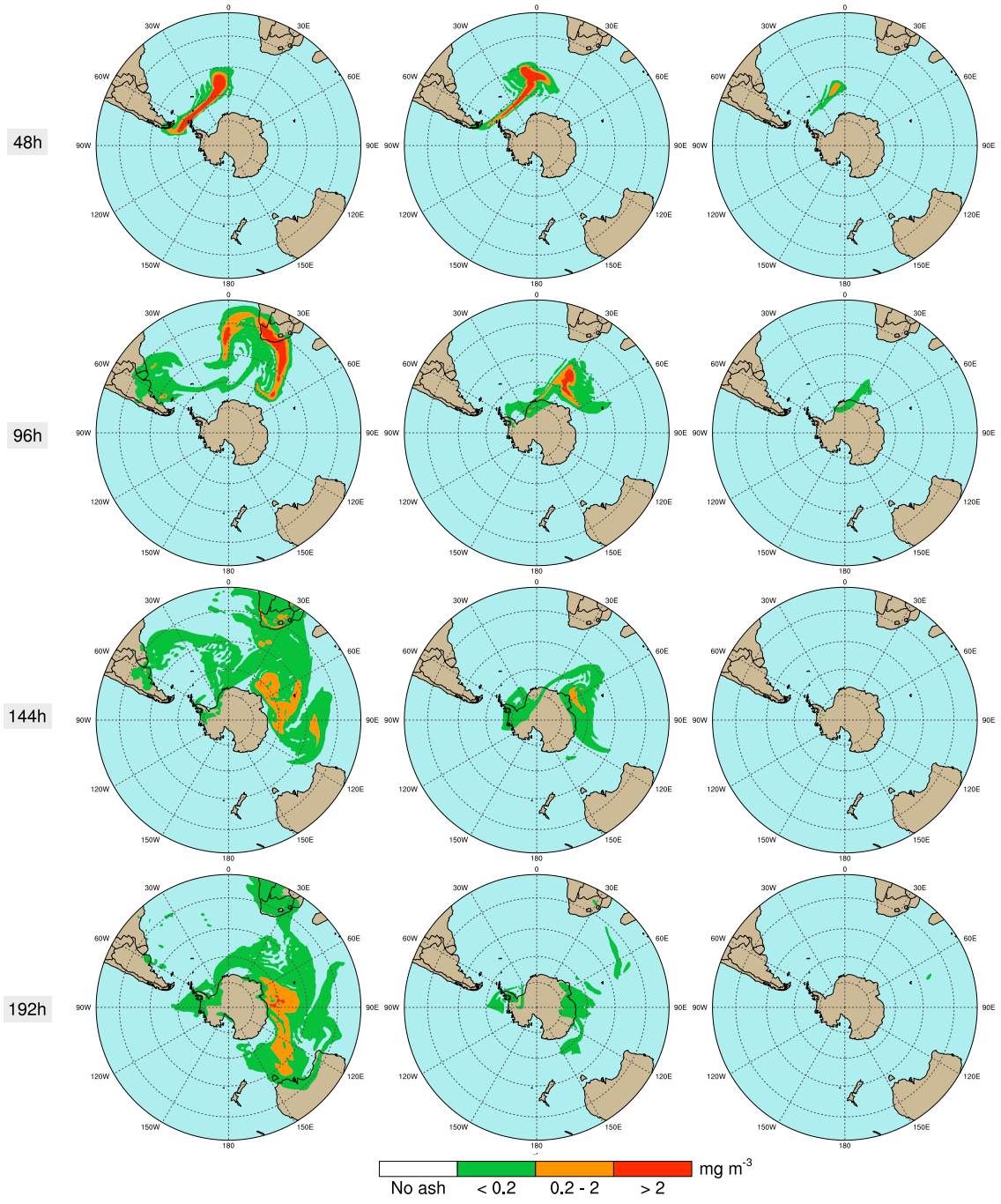

Figure 56. NMMB-MONARCH-ASH Flight Level ash concentrations (mg m^{-3}) at FL050 (left), FL250 (middle), and FL350 (right) at different time slices during the 1999 summer period. Safe ash concentration thresholds are shown (red contours illustrate "No Flying" zones). Simulation considering an eruption column height of 10 km. The yellow star indicates the location of Deception Island.

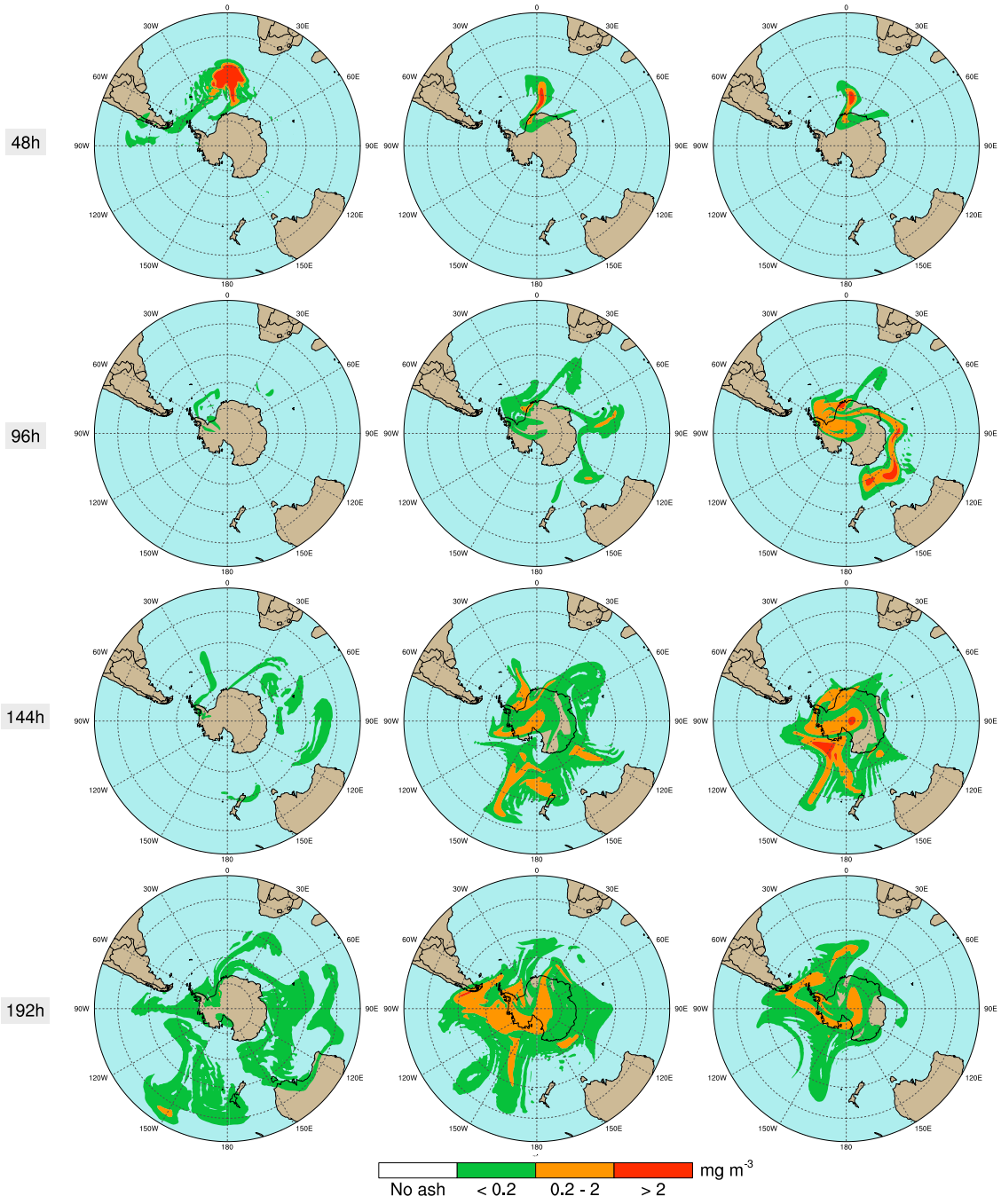

Figure 57. NMMB-MONARCH-ASH Flight Level ash concentrations (mg m^{-3}) at FL050 (left), FL250 (middle), and FL350 (right) at different time slices during the 1999 summer period. Safe ash concentration thresholds are shown (red contours illustrate "No Flying" zones). Simulation considering an eruption column height of 15 km. The yellow star indicates the location of Deception Island.

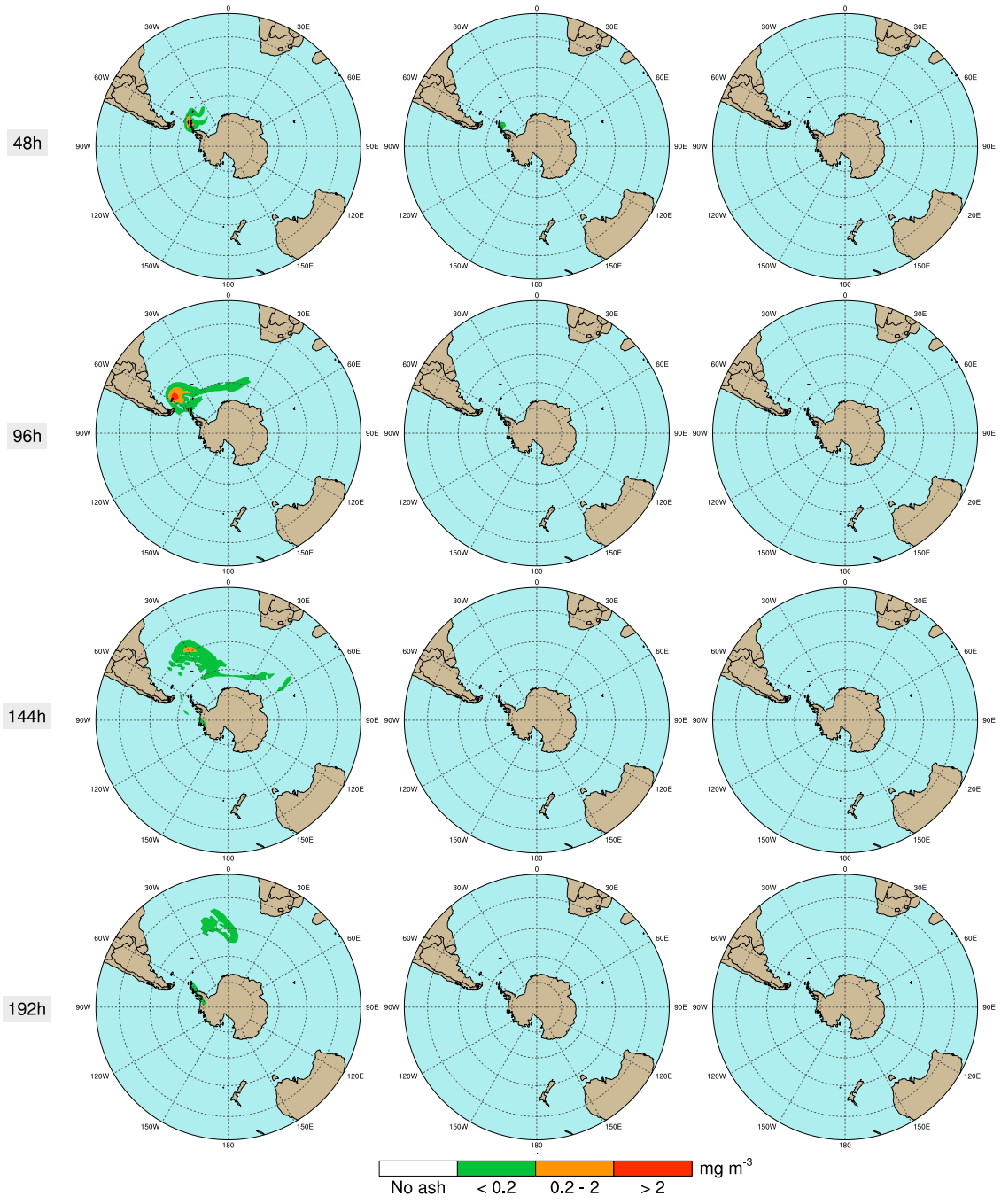

Figure 58. NMMB-MONARCH-ASH Flight Level ash concentrations (mg m^{-3}) at FL050 (left), FL250 (middle), and FL350 (right) at different time slices during the 1992 summer period. Safe ash concentration thresholds are shown (red contours illustrate "No Flying" zones). Simulation considering an eruption column height of 5 km. The yellow star indicates the location of Deception Island.

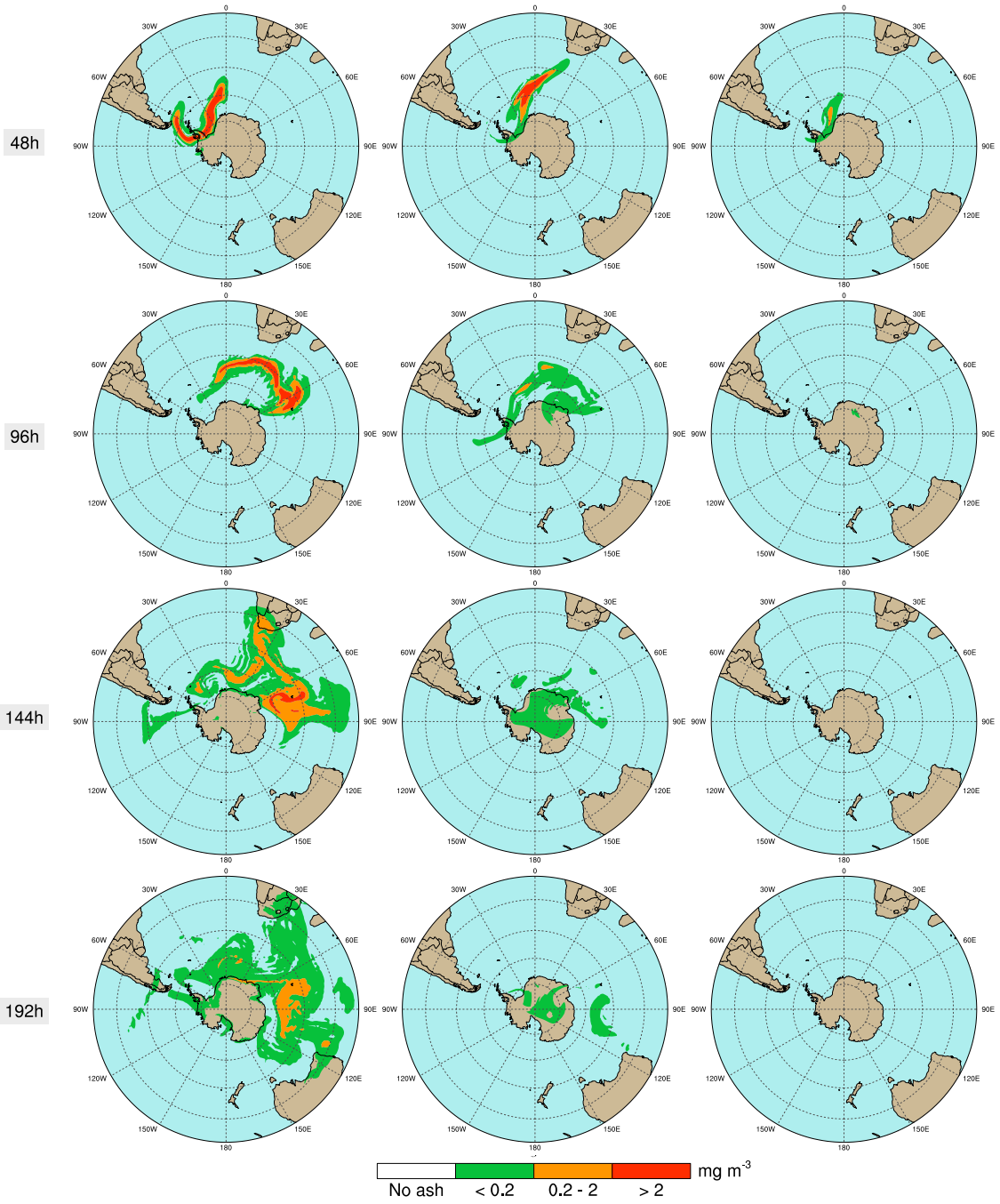

Figure 59. NMMB-MONARCH-ASH Flight Level ash concentrations (mg m^{-3}) at FL050 (left), FL250 (middle), and FL350 (right) at different time slices during the 1992 summer period. Safe ash concentration thresholds are shown (red contours illustrate "No Flying" zones). Simulation considering an eruption column height of 10 km. The yellow star indicates the location of Deception Island.

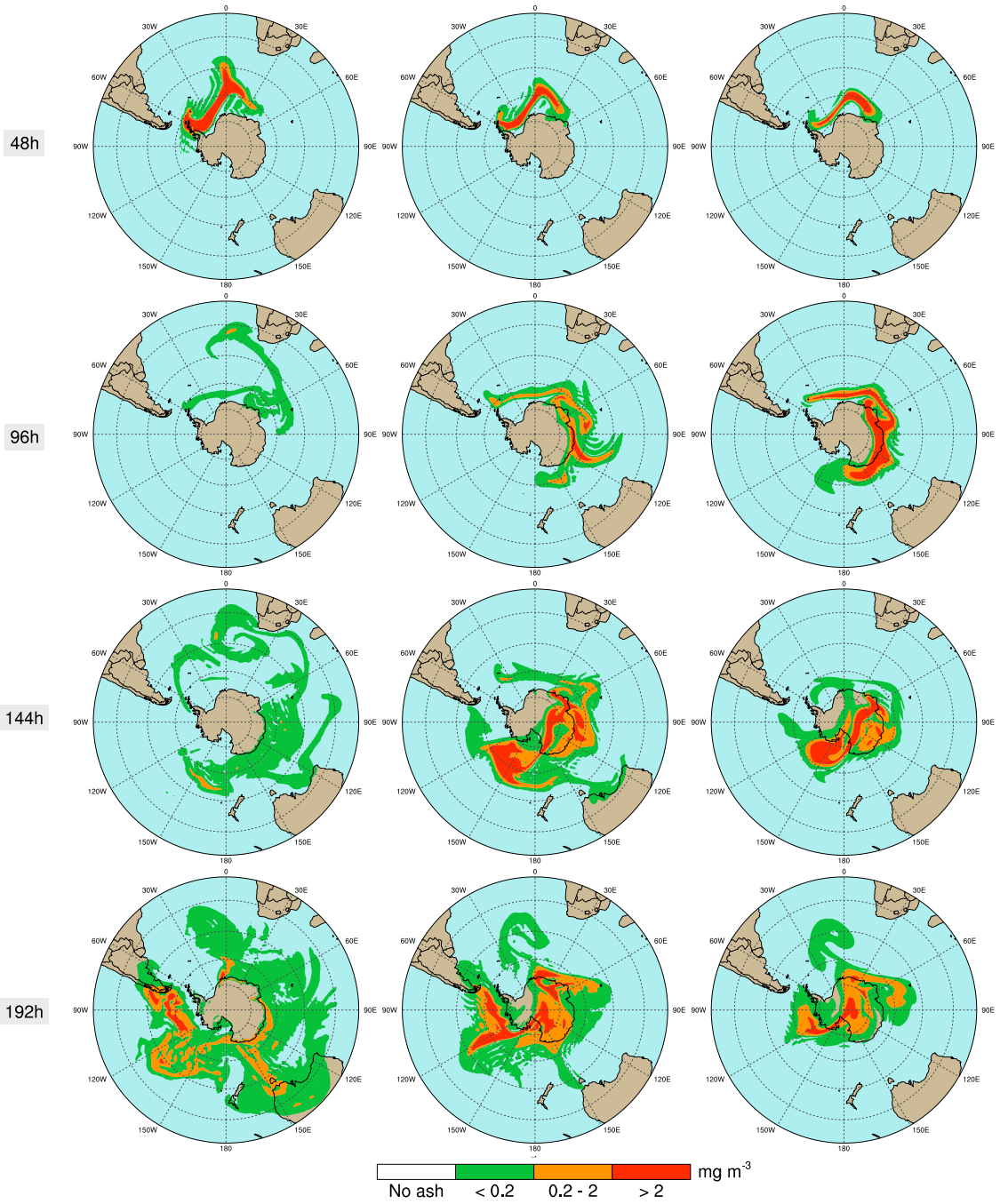

Figure 60. NMMB-MONARCH-ASH Flight Level ash concentrations (mg m^{-3}) at FL050 (left), FL250 (middle), and FL350 (right) at different time slices during the winter period. Safe ash concentration thresholds are shown (red contours illustrate "No Flying" zones). Simulation considering an eruption column height of 15 km. The yellow star indicates the location of Deception Island.

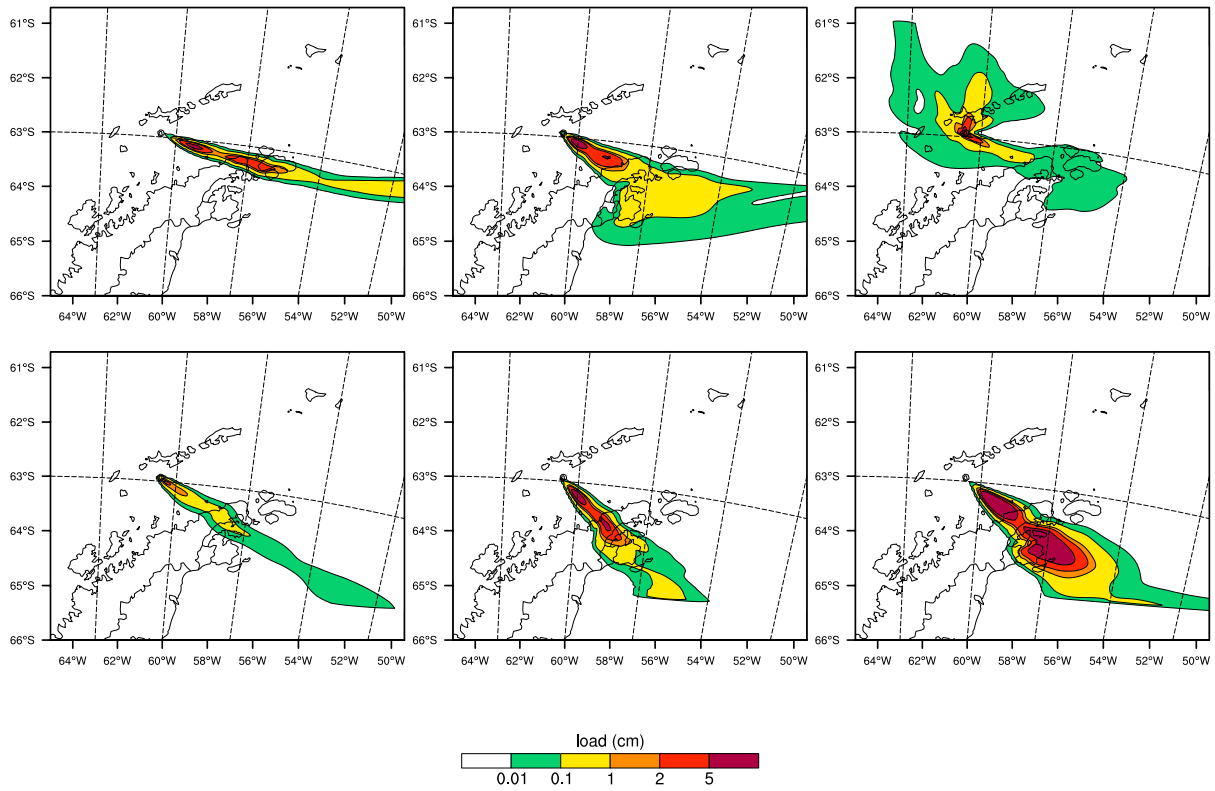

Figure 61. Regional-scale model ground deposit thickness (in cm) for the 1970-like scenario with different column heights of: 5km (left), 10km (middle), and 15km (right). Top and bottom panels show the corresponding ash deposition for the summer and winter periods, respectively.

4.5 Discussion

The potential impact associated to volcanic ash from Antarctic eruptions is mainly contingent on the volcano location and eruption column height (h). In that context, lower plumes (h<10 km) form high-latitude (>70º) eruptive events are likely to be confined close to the South Pole due to moderated wind zones encircled by the polar jet stream, while higher plumes have a higher potential for transcontinental ash dispersal. However, contrary to this situation, ash from lower-latitude Antarctic volcanoes (e.g. Deception Island) is more likely to encircle the globe, even for moderate size eruptions. In this case, volcanic ash clouds could reach up to tropical latitudes, a vast part of the Atlantic coast of South America, South Africa and/or Oceania. Thus, a wider dispersion of volcanic particles than previously believed may be originated resulting in significant consequences in the context of global aviation safety. For example, Flight level (FL) ash concentrations resulting from our NMMB-MONARCH-ASH simulations (Figs. 40 and 55 through 60) at FL050 (5,000 feet), FL250 (25,500 ft) and FL350 (35,000 ft), clearly show areas over which air traffic would be disrupted due to the presence of ash in the atmosphere (assuming "No Flying" zones with threshold of 2 mg m^{-3}). This is true not only in proximity to the South Shetland Islands, i.e. South American airports (over 1,000 km in distance) (e.g. Fig.41), but also in South Africa (over 6,400 km), affecting international and domestic flying routes, in addition to flights connecting Africa with South America and Australia (e.g. Fig. 42).

In a similar way, dispersal from events with smaller eruption columns (e.g. h=5 km), can result on "No Flying" areas affecting all flying routes towards international airports such as Buenos Aires and up to tropical latitudes (< 25º S, Tropic of Capricorn) (e.g. Fig. 49). For strong eruptive columns (e.g. h=15 km), ash takes longer to settle where and, including parts of West Antarctica, the Amundsen and Bellinghausen Seas and the South Pole, are still disrupted by the presence of volcanic ash, even eight days after the eruption on-set (Fig. 51). These results clearly recall the need for further research on the area to investigate the potential occurrence of an eruption on DI and to perform a proper hazard assessment for other active Antarctic volcanoes located on West Antarctica and along Victoria Land. Most importantly, considering that the eruption simulated here is by far not the largest that has been register neither in DI nor in Antarctica, future work is needed to evaluate the potential effects of a larger eruption (VEI >3) not only to air traffic but also to climate change.

4.6 Summary and conclusions

Ash emitted during explosive volcanic eruptions may disperse over vast areas of the globe posing a threat to human health and infrastructures and causing enormous disruption to air traffic. In Antarctica, at least five volcanoes have reported historic activity. However, no attention has been paid to the potential socio-economic and environmental consequences of an ash-forming eruption occurring at high southern latitudes. This chapter shows how ash from Antarctic volcanoes may pose a threat higher than previously believed. As a case study, this work evaluates the potential impacts of ash for a given eruption scenario from Deception Island, one of the most active volcanoes in Antarctica. Numerical simulations using the novel MMB-MONARCH-ASH model demonstrate that volcanic ash emitted from Antarctic volcanoes could potentially encircle the globe, leading to significant consequences to global aviation safety. Results obtained recall the need for performing proper hazard assessment on Antarctic volcanoes, and are crucial to understand the patterns of ash distribution at high southern latitudes with strong implications for tephrostratigraphy, pivotal to synchronize palaeoclimatic records.

Chapter 5

5 OFF-LINE APPLICATION WITH FALL3D. Reconstructing the Plinian and co-ignimbrite sources of large volcanic eruptions: A novel approach for the Campanian Ignimbrite

5.1 Introduction

Volcanic super-eruptions, those that eject magma in excess of 450 km^3 Dense Rock Equivalent (DRE) or ~1,000 km^3 of volcanic ash deposits (Self, 2006; Sparks et al., 2005), may have catastrophic long-term global impacts. Despite the low probability of occurrence in relation to human life-spans, the probability increases significantly when considering the time-scales of civilizations (Sparks et al., 2005). Many aspects of volcanic super-eruptions are not well understood due to a lack of historical precedents, and such eruptions must be reconstructed from their geological deposits (Self, 2006). Reconstructing the volume and tephra dispersal from volcanic super-eruptions is necessary to gain further insight into these catastrophic events and assess their widespread impact on humans, ecosystems and climate. Recent studies (Costa et al., 2012, 2014; Mastin et al., 2014) have demonstrated that the capability of numerical models to reconstruct tephra dispersal from these events has greatly improved in recent years.

Commonly associated with caldera-forming events, super-eruptions often include multiple eruptive sources with different styles of ash injection (Wilson, 2008). A common scenario begins with Plinian column destabilization and/or structural collapse of a caldera to produce a collapsing fountain that sheds pyroclastic flows. These high-density flows spread laterally along the ground at high-speeds (Sparks et al., 1978), eventually leading to formation of secondary, co-ignimbrite plumes (Fig. 62) (Woods and Wohletz, 1991).

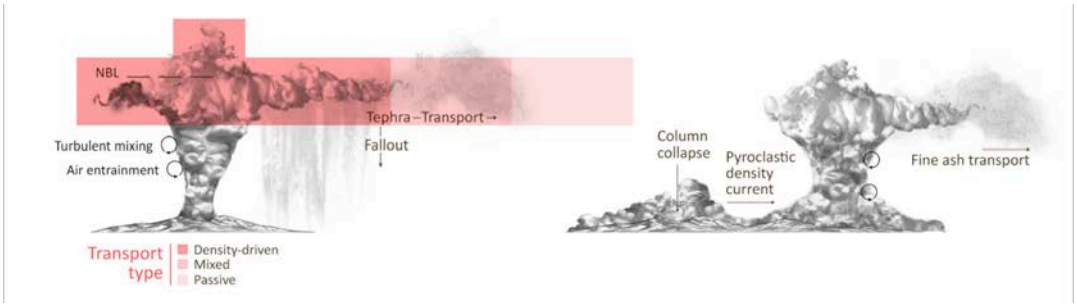

Figure 62. Schematic diagram (not to scale) of a super-eruption event with an initial (left) sustained Plinian phase followed by a column-collapse and large pyroclastic density currents eventually leading to co-ignimbrite plumes offset from the vent (right). Colored cells mark the extent of each transport regimes in the umbrella cloud (extracted from Marti et al., 2016).

Source conditions for co-ignimbrite plumes vary considerably from those of Plinian, with much larger source radii, lower initial ascent velocities and finer granulometry. However, previous numerical studies have simplified the characterization of volcanic super-eruptions to a single eruptive source, potentially leading to inaccurate estimations of their eruption dynamics. In order to evaluate the magnitude of each eruptive phase, it is critical to constrain their eruption dynamics and quantify optimal eruption source

parameters (ESPs; i.e. erupted mass, mass flow rate, eruption duration, plume height and total grain size distribution) that best represent each phase of the eruption.

In eruptions where both Plinian and co-ignimbrite sources (referred to as phases when separated in time during the eruption) have occurred, tephra deposits commonly have bimodal grain size distributions at individual sites (Sparks and Huang, 1980). A number of processes have been invoked to explain this bimodality, typically ascribed to depositional processes such as aggregation (Carey and Sigurdsson, 1989). However, such bimodality has also been interpreted as representing different eruptive phases, specifically Plinian versus co-ignimbrite (Engwell et al., 2014; Eychenne et al., 2012, 2015; Sparks and Huang, 1980). Inaccurate assessment of the proportion of co-ignimbrite ash in the deposit in distal areas can lead to an overestimation of the volume of the Plinian deposit (Perrotta and Scarpati, 2003).

Atmospheric transport of tephra released during this type of eruption is driven by the interaction of the volcanic plume and the atmospheric wind field (Costa et al., 2013). Plumes from high-intensity eruptions can be injected high into the stratosphere, reaching a maximum column height and intruding laterally at neutral buoyancy level (NBL) as a gravity current (Fig. 62). This current can spread at velocities exceeding those of the surrounding winds, affecting tephra transport and deposition near the source (Baines and Sparks, 2005; Costa et al., 2013). As particles are deposited and air is entrained, the plume density decreases and momentum reduces such that, at a certain distance, atmospheric turbulence and wind advection become the dominant atmospheric transport mechanisms (Baines and Sparks, 2005). Neglecting the gravitational spreading of the umbrella cloud in tephra dispersal simulations could misrepresent the interaction of the volcanic plume and the atmospheric wind field, especially for high-intensity eruptions and for proximal deposition of tephra (Mastin et al., 2014). For further details on the description of the gravity current transport, refer to Sect. 2.2.3.2.1.

In a recent work, Costa et al. (2012) combined FALL3D ash dispersion model simulations, analysis of an ensemble of wind fields, and thickness measurements of the tephra deposit to quantify volcanic ash dispersal of the Campanian Ignimbrite (CI) eruption. The dispersal model was used in conjunction with a downhill simplex inversion method (DSM; Connor and Connor, 2006) to investigate eruption dynamics. However, Costa et al. (2012) reconstructed the eruption as a single-phase event and neglected the gravitational spreading of the umbrella cloud in their tephra dispersal simulations, overlooking potentially important eruption processes. Reconstruction of the eruption as a two-phase event can provide a more realistic characterization of the eruption and allow for a better estimation of its duration.

The aim of this chapter is to further develop the Costa et al. (2012) computational approach to 1) reconstruct, for the first time, the duration and contribution of the two phases of the CI super-eruption and, 2) evaluate the effect of gravitational spreading of the umbrella cloud by coupling FALL3D with a

model that accounts for the gravity-driven transport in the umbrella cloud (Costa et al., 2013). In this particular case, the use of an off-system is preferred to constrain eruption source parameters (ESP) by means of inversion analysis. The off-line approach is convenient in terms of computational time and cost because different VATDM executions are possible without re-running the meteorological component, e.g. to refine the source term parameters during the inverse modeling. Section 5.2 in this chapter summarizes the eruptive event and presents the different datasets employed for the inversion and validation analyses. Section 5.3 describes the methodology used to perform the two-phase reconstruction of CI the super-eruption. Section 5.4 presents the results from reconstructing the eruption as a single and two-phase event, and summarizes the effect of the gravity current phenomena during the Plinian phase. Section 5.5 discusses the environmental and climate-forcing implications associated with the eruption to provide insight into its impact on the Middle to Upper Palaeolithic transition. Finally, Sect. 5.6 provides the conclusive remarks of this work.

5.2 The Campanian Ignimbrite: history and geological deposits

The trachytic-phonolitic Campanian Ignimbrite eruption (Barberi et al., 1978), the largest eruption of the last 200 ka in Europe, erupted from the Phlegrean Fields on the Bay of Naples (Italy) ~39,300 years ago (De Vivo et al., 2001). Geological evidence suggests that the eruption had two main phases; beginning with a sustained Plinian phase (Rosi and Vezzoli, 1999) followed by a secondary co-ignimbrite phase (Perrotta and Scarpati, 2003; Pyle et al., 2006). The upper portions of the Plinian deposits contain evidence for initiation of column collapse (generating a crater 13 km in diameter; Barberi et al., 1978) and are overlain by massive ignimbrite deposits (Rosi and Vezzoli, 1999), with local thicknesses exceeding 100 m. These deposits were emplaced by pyroclastic density currents that travelled in excess of 80 km from source (Fedele et al., 2003), and resulted in formation of the co-ignimbrite plume(s) (Perrotta and Scarpati, 2003). While the dynamics and physical characteristics of proximal deposits have been widely discussed in the literature (e.g. Barberi et al., 1978; Civetta et al., 1997; Engwell et al., 2014; Fisher et al., 1993) dispersal and volume estimates of the associated distal fallout deposit are still poorly constrained (Pyle et al., 2006), despite containing a significant portion of the erupted material.

According to recent studies, the resulting stratospheric aerosol cloud would have induced a “volcanic winter” (Rampino et al., 1988) with a cooling effect of ~ 6-9 ºC in Eastern Europe (Black et al., 2015). Additionally, it has been debated that the eruption, boosted by the impact of the broadly synchronous Heinrich Event 4 (Heinrich, 1988), contributed to the Middle to Upper Palaeolithic transition (Fedele et al., 2003; Zilhão, 2006).

5.2.1 Geological datasets

Two independent datasets containing deposit thickness were used for model inversion and validation. Dataset 1 contains 10 deposit thickness measurements with distinct bimodality from which a Total Grain Size Distribution (TGSD) was reconstructed. This is a more complete distribution than that used by Costa et al. (2012), who assumed an empirically parameterized TGSD bi-log-normal distribution. Dataset 2, contains

114 unimodal observations spanning across the dispersal area. Figure 63 shows the sampling locations for each dataset along with their reconstructed Total Grain Size Distribution (TGSD).

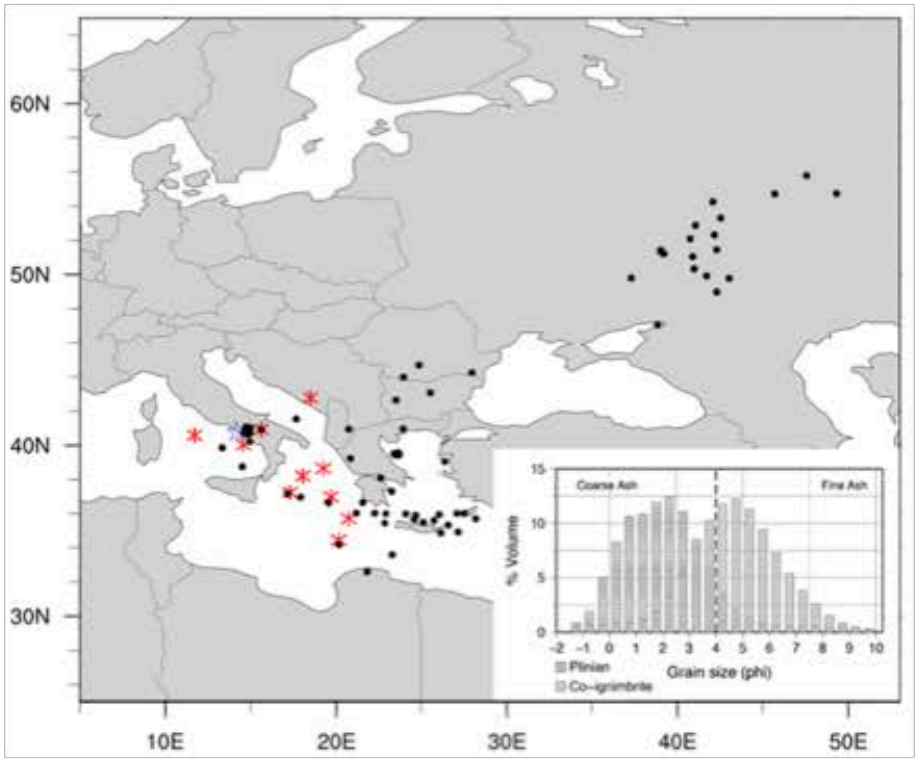

Figure 63. Map showing the location of the CI-caldera (blue star) and geological samples in dataset 1 (red asterisks) and 2 (black circles). The inset shows the reconstructed TGSD from dataset 1 (extracted from Marti et al., 2016).

5.2.1.1 Dataset 1 (two-phase inversion)

Dataset 1 was used for the two-phase inversion. The dataset was derived from analysis of more than 40 marine, lacustrine and land deposits across the dispersal area, originally presented in Engwell et al. (2014). The deposits range from 130 km from the source, at Lago Grande di Monticchio (LGdM), to distances of more than 2000 km, in Russia. Amongst these deposits, only the ten showing distinct bimodality were selected (Table 16). Within lake sediments at LGdM, the CI deposit was separated into a 16.5 cm thick coarse lapilli pumice fall overlain by a 13 cm thick vitric ash layer. This overlying ash layer, the co-ignimbrite layer, is fine grained with a median diameter of approximately 50 μmi, and is relatively homogenous, with little variation in median diameter and sorting coefficient within the deposit. While the lapilli deposit fines slightly towards the top of the deposit, the boundary with the overlying vitric ash layer is sharp. Similar trends have also been noted within deposits at greater distances from

source (Sparks and Huang, 1980), with the boundary between the two phases becoming more difficult to distinguish with distance. Deposits at greater distances were too thin for the two phases to be distinguished stratigraphically.

Sample	Lon (E)	Lat (N)	Depositional Environment	Water Depth (m)	Distance from source (km)	Thickness Plinian (cm)	Thickness Co-ignimbrite (cm)	% Co-ignimbrite Tephra
TR172-42	14.55	40.02	Deep Sea	728	118	11	4	27.7
LGM-10	15.61	40.93	Lake	NA	130	16.5	13	44.1
MONTEN	18.48	42.78	Cave	NA	430	5.1	2.9	36.2
RC9-191	18.03	38.20	Deep Sea	2,345	445	1.56	2.44	61.0
V10-69	17.28	37.23	Deep Sea	3,156	490	1.38	1.62	54.0
RC9-190	19.23	38.65	Deep Sea	1,712	497	1.4	2.6	65.0
RC9-189	19.68	36.98	Deep Sea	3,378	645	5.2	4.8	48.0
V10-67	20.72	35.70	Deep Sea	2,904	810	1.6	2.9	64.4
RC9-185	20.12	34.45	Deep Sea	2,858	890	0.75	2.25	75.0
TR171-21	20.13	34.45	Deep Sea	2,785	900	0.32	2.18	87.2

Table 16. Dataset 1 showing tephra layer thicknesses from Engwell et al. (2014) for Plinian and co-ignimbrite phases of the CI eruption with distance from the source. Note how the percentage of the co-ignimbrite contribution tends to increase with distance from source.

Deposits were chemically treated to remove any biological components, and grain size analysis was conducted using a combination of sieve and laser diffraction analysis (Engwell et al., 2014) using the Malvern Mastersizer 2000E. Deposits at LGdM are easily separated into Plinian and co-ignimbrite phases based on stratigraphy, with both deposits having a unimodal distribution. Grain size results for intermediate distances show the characteristic bimodality typical of deposits associated with multiple phases, and particularly those associated with Plinian and ignimbrite forming eruptions. Deposits at distances greater than 900 km from source are unimodal, and likely contain ash from both the Plinian and co-ignimbrite phase. However it was not possible to identify to what extent each component contributes (Engwell et al., 2014).

The total grain size distribution of the two main component phases (inset Fig.63) was calculated using the Voronoi Tessellation spatial statistical technique (Bonadonna and Houghton, 2005), whereby the identified deposit extent is divided into a number of territories according to the spacing and distribution of the measurements. In this case, the deposit extent of Pyle et al. (2006) was used as the tessellation limit. Uncertainties associated with estimation of TGSDs are typically related to the choice of deposit extent and to the number and distribution of analysed deposits (Bonadonna et al., 2015a; Bonadonna and Houghton, 2005). However, given the lack of variation in co-ignimbrite deposit grain size characteristics, regardless of direction and distance from source, the calculated TGSD is likely to be robust, and the resultant grain size is remarkably similar to co-ignimbrite deposits from other events (e.g. Montserrat; Bonadonna et al., 2002). In the case of the Plinian deposit, the fines from very distal deposits were not taken into account, and therefore the resultant grain size distribution is likely to underestimate the finest grain sizes.

5.2.1.2 Dataset 2 (single phase inversion and validation)

Dataset 2 was used for the single-phase inversion experiment and for validation purposes. The dataset consists of the 112 sample thicknesses previously used by Costa et al. (2012) plus two measurements in southeast Romania (Fitzsimmons et al., 2013). The location, thickness and distance from source of each geological sample is available in the Supplemental material (S2) in Marti et al. (2016).

5.3 Methods

This section presents a novel computational approach to infer ESP values that allow to reconstruct, for the first time, the duration and contribution of the two phases of the CI super-eruption, and to quantify the effect of the gravitational spreading of the umbrella cloud. This methodology employs four components: i) a meteorological dataset that statistically represents the meteorological conditions at the time of the eruptive event; ii) two independent datasets containing deposit thickness (see Sect. 5.2.1) used for inversion and validation purposes; iii) an off-line VATDM (i.e. FALL3D) to simulated the transport and deposition of tephra, and; iv) a downhill simplex inversion method that selects a solution that best reconstructs each phase of the eruption. Finally, this section also describes the methodology used to estimate the environmental emissions from the CI event to the atmosphere.

5.3.1 Wind fields

Costa et al. (2012) performed a five-step computational procedure to generate the set of 4D winds that statistically represents the (unknown) meteorological conditions at the time of the 39 ka CI eruption. To select dates, the authors performed forward simulations using a set of five hundred synoptic meteorological fields (using 15 years of European Centre for Medium-Range Weather Forecasts (ECMWF) ERA-40 reanalysis data). Costa et al. (2012) concluded wind fields from 5-12th of December 1991 best-represented the meteorological conditions at the time of the event (see online supplementary material in Costa et al., 2012). In this chapter, the methodology presented in Costa et al. (2012) is improved by using the ECMWF ERA-Interim reanalysis dataset at 0.25ºx0.25º resolution in the horizontal and 60 vertical levels from the surface up to 0.1 hPa. Meteorological fields from the ERA-Interim dataset were interpolated over the FALL3D computational mesh with a 1-hour interval. To improve the quality of the fit for the ultra-distal deposits, the wind field was rotated 7 degrees anti-clockwise around the vent. Considering these improvements, the wind fields from the 7th of December 1991 were found to statistically best represent those at the time of the eruption.

5.3.2 Tephra dispersal modeling

For this particular case, employing an off-line tephra dispersion model is convenient in terms of computational time and cost because different dispersal model executions are possible without re-running

the meteorological component, e.g. to refine the source term parameters during the inverse modeling. To this purpose, the stand-alone FALL3D Eulerian model for the transport and deposition of volcanic tephra (see Sect. 1.1.3.1) was employed (rather than NMMB-MONARCH-ASH) including the following parameterizations:

- To determine the vertical distribution of mass within the plume through inversion, the model assumes the Suzuki empirical parameterization (Pfeiffer et al., 2005; Suzuki, 1983) to control concentration of mass along the column.
- To account for aggregation processes, FALL3D uses the empirical aggregation model of Cornell et al. (1983), originally proposed for the CI eruption. For computational reasons, particle aggregation was assumed to occur within the eruption plume thereby affecting the original TGSD, which was modified considering a single aggregate class, depleting particle classes finer than the aggregate class itself.
- The horizontal diffusion coefficient was calculated using a large eddy parameterization such as the one used by the RAMS model (Pielke et al., 1992).
- The vertical diffusion coefficient was set to a constant value of 100 m^2s^{-1}.
- The particle settling velocity model of Ganser (1993) was used to predict settling rates of particles.
- Finally, to account for the gravity-driven transport, FALL3D is coupled with a parameterization that describes cloud spreading as a gravity current (see Sect.1.4.2.2). This model calculates an effective radial velocity of the umbrella spreading as a function of time, and combines it with the wind field centered above the vent in the umbrella region. To estimate the radial distance at which the critical transition between gravity-driven and passive transport occurs, the umbrella front velocity is compared with the mean wind velocity at the Neutral Buoyancy Level (NBL) estimating the Richardson number, Ri (gravity-driven regime when Ri > 1, passive transport regime for Ri < 0.25, and an intermediate regime in between these values).
- The computational domain contained 241x201x50 grid points resolution.

5.3.3 Inversion modeling and best-fitting criterion

To reconstruct the dynamics of an eruption, first it is necessary to understand the eruptive behavior of a given volcano. For prehistorically eruptions, were the volcanic dynamics cannot be directly or remotely observed, it is necessary to infer very basic parameters from the deposit (i.e. eruption column height, erupted mass, and the prevailing wind speed and direction). Given the meteorological and geological datasets previously obtained, this section introduces the (volcanological) inversion methodology used to

find the optional set of eruption parameters to characterize the Plinian and co-ignimbrite phases of the CI event. The inputs of the inversion method include the mass per unit area measurements (or thickness) of a tephra deposit and estimate parameters ranges (e.g. minimum and maximum values for plume height, total erupted mass, eruption duration, MER, total grain size distribution modes and variances, density of aggregates, etc.). Together via inversion, a downhill simplex inversion method (Connor and Connor, 2006) and the forward model FALL3D are used to determine optimal values for the estimated eruption parameter ranges. The basic steps employed by this inversion methodology include:

i. Define a range of values for the ESPs being modeled (see Table 17). The chosen number of eruption parameters defines an $N - dimensional$ solution space, N being the number of parameters to be optimized by inversion.

ii. Randomly initialize the parameter sets. Use FALL3D as the forward model for calculating initial tephra deposits using each randomly initialized parameter set.

iii. Compare model results against field observations from dataset 2 by employing two goodness-of-fit measures: i) the minimization criterion used in Folch et al. (2010), and; ii) the criterion originally proposed by Aida (1978) to measure the spatial variation between the recorded and computed tsunami heights. This measure has been previously adapted and proven to be suitable for best-fitting tephra deposits (Costa et al., 2014):

$$logK = \frac{1}{n}\sum_{i=1}^{n} \log K_i \quad \text{with} \quad K_i = {}^{M_i}/_{H_i} \tag{52}$$

$$\log k = \left[\frac{1}{n}\sum_{i=1}^{n} (logK_i)^2 - (logK)^2\right]^{1/2} \tag{53}$$

where n is the number of measurements, $K_i = {}^{M_i}/_{H_i}$ is the ratio of measured tephra thickness (load) to simulated thickness (load) at $i\text{-}th$ location. The first Aida index (K) is associated with the geometric average of the distribution and the second (k) is related to the geometric standard deviation of the distribution (expected to be 1.5-2 times larger for volcanic deposits than for tsunami heights). This approach was proven to be suitable for best-fitting tephra deposits (Costa et al., 2014).

iv. Select new parameter values using the downhill simplex method to minimize the difference between calculated values and observed measurements.

v. Iterate through this process to minimize the difference between calculated values and observed measurements. This iteration takes places until the goodness-of-fit measures fall within the tolerance limit selected:

$$0.95 < \mathrm{K} < 1.05 \quad \text{and the smallest } k \text{ coefficient (ideally k<1.45)} \tag{54}$$

5.3.4 Environmental and atmospheric emissions

The amount of volatiles released from the CI eruption is estimated using the volcanic emission approach originally described in Self (2004) for SO_2. This approach is updated here to estimate fluoride and chloride emissions during the CI eruption:

$$EM_n = f_w M_w \frac{(1 - W_{xls})(C_{incl} - C_{matrix})}{100} \tag{55}$$

where EM_n is the emission for each substance (in kg), M_w is the mass of erupted magma (in kg) obtained from the our best-fit results, W_{xls} is the mass fraction of crystals in the magma (Pappalardo et al., 2013; Signorelli et al., 2001), $(C_{incl} - C_{matrix})$ is the difference between the average chemical concentrations of the glass inclusions and the matrix in wt% (Civetta et al., 1997), and f_w is factor difference between the molecular weights (e.g. factor 2 for the SO_2 and S).

5.4 Results

5.4.1 Modeling the CI eruption as a two-phase event

Best-fit results from the inversion model (Table 17) indicate that the eruption began with a short (4h), high-intensity Plinian explosive phase that produced a column 44 km in height, and a mass eruption rate (MER) of 3.75×10^9 kg/s. Results also show that the vertical mass distribution can be characterized by a value of the Suzuki coefficient (Suzuki, 1983) commonly assumed for Plinian eruptive columns (A = 4). The Plinian phase deposited a total volume of 54 km^3 of tephra (~23 km^3 DRE), accounting for 26% of the total fallout deposit volume, and covered an area of ~1.3 million km^2 with deposits greater than 0.5 cm in thickness. Figure 64a shows that Plinian lapilli and coarse ash were predominantly deposited in southern Italy with deposit thickness decreasing with distance in concordance with data reported in

dataset 1. The correlation coefficient between the observed thicknesses in dataset 1 and the model results was 0.76 (Fig. 64e), with a relative root mean square error (RMSE) of 0.10.

Best-fit results for the second phase suggested the co-ignimbrite column(s) reached 37 km in height (with a Suzuki coefficient of A = 9), fed by an average MER of ~2.3×10^9 kg/s over approximately 19 h and produced deposits ~154 km^3 (~62 km^3 DRE) in volume. The fallout from the co-ignimbrite phase (Fig. 64b), much richer in fines than the Plinian phase, was spread over an area of ~3 million km^2 (thickness ≥ 0.5 cm), and would have represented almost 74% of the total bulk volume for the eruption. These results confirm the key role of the co-ignimbrite fallout in the total bulk volume (Engwell et al., 2014; Perrotta and Scarpati, 2003; Pyle et al., 2006;Engwell et al., 2014), and is consistent with fluid dynamics models indicating that co-ignimbrite plumes from very high-intensity eruptions (~10^9 kg/s) distribute a major proportion of fine grained particles into the stratosphere (Van Eaton et al., 2012b). Assuming that ~35-40% of the erupted material was elutriated from the pyroclastic density current (Sparks and Walker, 1977), the total MER for the ignimbrite phase would have been considerably higher than our estimates (up to ~5-6×10^9 kg/s). The correlation coefficient between observations (dataset 1) and simulation results was 0.83 (Fig. 64e), with a relative RMSE of 0.30.

The resulting optimal ESPs from the Plinian and co-ignimbrite phase inversions (Table 17) allows to simulate the total dispersal from the CI eruption (Fig. 64c), obtaining an eruption duration of 23h and a total deposit volume of ~208 km^3 (~84 km^3 DRE). Tephra fallout would have covered an area of over ~3 million km^2 (thickness ≥ 0.5 cm). Given volume estimations of 180 to 380 km^3 for the proximal pyroclastic density current deposits (Pyle et al., 2006), the total bulk volume would range from 388 to 588 km^3 (155–235 km^3 DRE). Finally, dataset 2 to validate results from the combined phases, obtaining a correlation coefficient of 0.81, a RMSE of 0.18 and a bias of 0.21.

5.4.2 Modeling the CI eruption as a single event

For the purpose of comparison, an additional single-phase inversion was performed using dataset 2. Best-fit results from (Table 17) suggested a column height of 38 km (with a Suzuki coefficient of A = 9), an average MER of 2.6×10^9 kg/s and a duration of 23 hours. The tephra volume deposited (Fig. 64d) would have totaled 211 km^3 (~84 km^3 DRE). This volume is consistent with the 208 km^3 obtained by the two-phase combined inversion. The correlation coefficient between the observed and the simulated thickness is 0.79, with a relative RMSE of 0.27 and bias of 0.47.

Table 17. Best-fit results obtained from reconstructing the CI super-eruption as a two-phase and single-phase event. The combined phase column is obtained by using the optimal ESPs resulting from the Plinian and co-ignimbrite phase inversions.

		TWO-PHASE			SINGLE-PHASE
Modelled dispersion parameters	Explored Range	Plinian phase	Co-ignimbrite phase	Combined phases	Single phase event
Tephra mass (kg)	Calculated	5.40×10^{13}	1.54×10^{14}	2.08×10^{14}	2.11×10^{14}

Average deposit density (kg/m^3) [a]	Assumed	1,000	1,000	1,000	1,000
Tephra volume (km^3)	Calculated	54	153.9	207.9	211.1
Tephra volume DRE (km^3)	Calculated	22.6	61.6	84.2	84.4
Duration (h)	12-48	4	19	23	23
Mass eruption rate (kg/s)	10^8-10^{10}	3.75×10^9	2.25×10^9	2.51×10^9 [b]	2.55×10^9
Column height (km)	20-50	44	37	38 [b]	38
TGSD modes (Φ) [c]	0-3/6-9	2.5 [d]	5 [d]	-	2.0/6.5 [c]
TGSD variances (Φ) [c]	1-3/1-3	1.16	1.22	-	2/2[c]
Suzuki coefficient A (–) [e]	2-9	4	9	8 [b]	9
Density of aggregates (kg/m^3) [f]	100-500	350	350	350	350
Diameter of aggregates (in Φ–unit) [f]	2-3	2.3	2.3	2.3	2.3
Pearson correlation coefficient (R) [h]	Calculated	0.76	0.83	0.81	0.79
Root-mean-square error (RMSE) [h]	Calculated	0.10	0.30	0.18	0.27
Aida indexes K/k (–)[i]	Calculated	1.01/1.05	1.03/1.07	1.02/1.14	1.02/1.15

[a] This value is used to convert mass loading to deposit thickness and thereby to calculate tephra volume from mass, whereas a bulk density of 2500 kg/m^3 was considered to convert into DRE volume.
[b] Weighted sum of input parameters for each phase.
[c] Total grain size distribution (TGSD) for the single phase reconstruction is assumed bi-Gaussian in Φ with maxima at μ_1 and μ_2 and corresponding variances σ_1 and σ_2.
[d] TGSD for the two-phase reconstruction was determined by Voronoi tessellation (Bonadonna and Houghton, 2005).
[e] The eruption source is described in a purely empirical way using the Suzuki distribution (Pfeiffer et al., 2005; Suzuki, 1983) for mass release along the column.
[f] Aggregation is accounted for using the empirical model of Cornell et al. (1983), assuming that 50% of the 63–44 μm ash, 75% of the 44–31 μm ash, and 95% of the less than 31 μm ash fell as aggregated particles, with diameter and density of aggregates found through the best-fit.
[h] Pearson correlation (R) and root-mean-square error (RMSE) based on the differences between log (measured thickness) and log (simulated thickness)
[i] Aida index for geometric average (*K*) and geometric standard deviation (*k*) of the distribution.

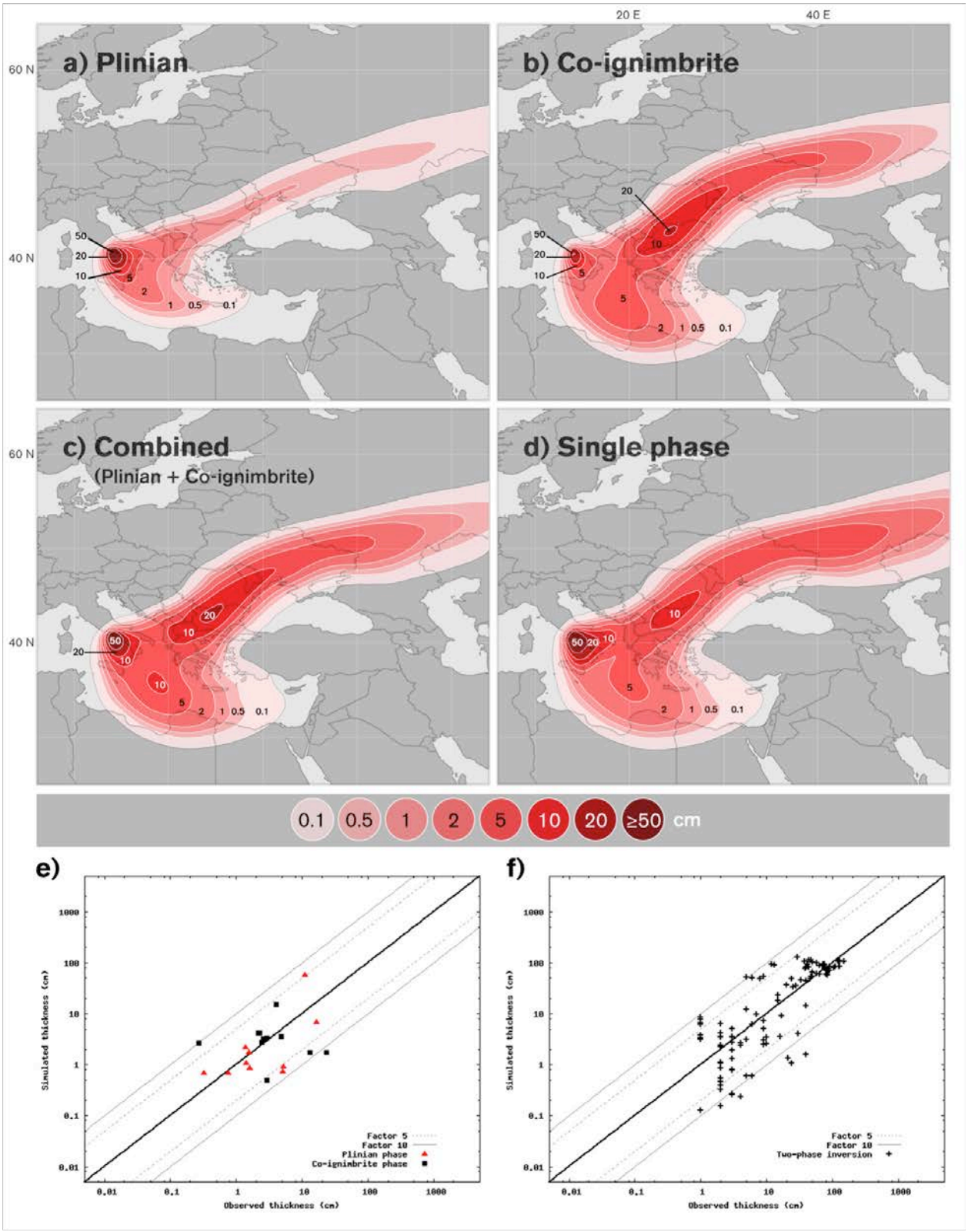

Figure 64. Isopach maps (cm) from inversion. (a) Plinian phase, (b) co-ignimbrite phase, (c) combined two-phase and, (d) single-phase inversion. Bottom plots show simulated versus observed thicknesses for (e) Plinian and co-ignimbrite phases and (f) two-phase approach. The solid bold line represents a perfect agreement, while the dashed and solid thin black lines mark the region that is different from observed thicknesses by a factor 5 (1/5) and 10 (1/10), respectively (extracted from Marti et al., 2016).

5.4.3 Atmospheric umbrella cloud spreading

Gravity-driven transport was found to be dominant for the first hour of the eruption with an effective radial velocity of ~130 m/s, resulting in an umbrella cloud radius of <100 km. Model results show the effect of atmospheric gravity-driven transport to be significant in proximal areas, increasing tephra deposition by 1.5-2 times NE from the source and decreasing up to 50% in the eastern Mediterranean region (Fig 65). The gravity-current model predicts a fully passive regime after ~ 3 hours, with a corresponding umbrella cloud radius of ~430 km. At this distance, atmospheric turbulence and wind advection would have dominated tephra transport for the CI eruption.

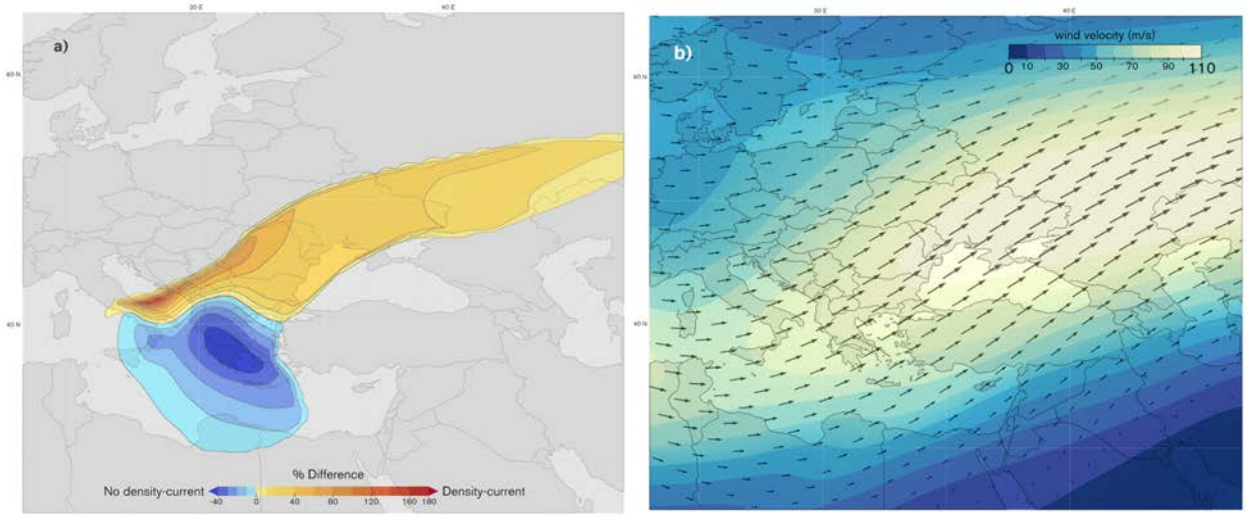

Figure 65. (a) Impact of gravity current on the deposit (variation in %). Positive values show areas where tephra deposition increases when accounting for gravity-current effects; negative indicate lesser tephra deposition. (b) Wind field at ~32 km elevation for the meteorological field that best represents the (unknown) meteorological conditions at the time of the CI eruption (7th December 1991).

5.5 Discussion

This chapter uncovers valuable new results and present new methods for reconstruction of the volume and tephra dispersal of the 39 ka CI super-eruption. The computational approach presented here infers ESP values for both phases, Plinian and co-ignimbrite, of the eruption accounting for the gravitational spreading of the umbrella cloud. This novel approach improves modeled tephra distribution across the dispersal area, and reduces the RMSE of the single-phase inversion by ~33% (0.18/0.27) and bias by ~52% (0.21/0.47). Total volumes, durations, phase-averaged MER, column height, and mass distributions (Suzuki coefficient *A*) for both (single and two-phase) inversions are consistent (i.e. total tephra volume differed by less than 1.5%), suggesting that results from the two-phase reconstruction are robust.

Results from the novel combined two-phase simulation were compared with those reported in the Costa et al. (2012) best-fit single-phase simulation (correlations coefficients of 0.81 and 0.77, respectively). The best-fit simulation for the two-phase approach uses a higher MER (75% increase), lower total volume

(15% decrease) and shorter duration (5 times) of the climatic phase of the eruption using dynamics that are more consistent with geological interpretations of the event. In addition, the two-phase reconstruction is in better agreement with the collapse conditions presented by Koyaguchi et al. (2010) (see Fig. 6 in their study), and the Woods and Wohletz (1991) column-height/MER relationship (see Fig. 3 in their study). Concerning the reconstruction of the deposit, the novel simulations suggest a slightly thinner tephra blanket in the East Black Sea than Costa et al. (2012). This is mainly due to the different TGSDs used in the two studies (the TGSD used here is reconstructed from field data limited to deposits within 900 km from source and is fines depleted with respect to Costa et al. 2012).

In general terms, the resulting proximal tephra fallout is consistent with previous studies (Civetta et al., 1997; Perrotta and Scarpati, 2003). Much of the dispersal area was covered by 1 – 10 cm of ash, including regions from the Mediterranean and Ionian Sea to the east European Plains. Dispersal results also predict a thick tephra deposit (10-20 cm) covering regions of present-day Macedonia, Bulgaria and Romania, which is consistent with tephra deposits in the south-eastern Romanian loess steppe (Fitzsimmons et al., 2013). Fine ash aggregation processes could explain this secondary maximum thickness. In order to account for ash aggregation this work uses the model of Cornell et al. (1983), who analysed the CI deposit (Y5 ash layer) and determined that 50, 75, and 100% of the 63–44, 44–31, and <31 μm ash could be considered as a single aggregated class. The model assumes a simplified distribution of aggregates in the eruption column with a single effective diameter and constant density. More sophisticated aggregation models could not be employed, as they are too computationally intensive for an inversion analysis. Ultra-distal dispersal simulations (>2500 km NE from source) is consistent with analyses of the CI ash layer identified in the Russian Plain (Pyle et al., 2006).

Reconstruction of the Plinian phase indicates that tephra volume from this phase is 2-3 times larger than previous studies (Pyle et al., 2006). However, the maximum height and mass distribution of the eruptive column in our simulations is consistent with the height estimated by field and laboratory analyses (Rosi and Vezzoli, 1999) of a sustained Plinian column with maximum mass distribution at 3/4 of the column height (Pfeiffer et al., 2005; Sparks, 1986). The resulting eastern dispersion trend is compatible with proximal Plinian fall products (Perrotta and Scarpati, 2003; Rosi and Vezzoli, 1999). On the other hand, tephra fallout from the co-ignimbrite phase is similar to higher-end estimates (73-140 km^3) from previous studies (Pyle et al., 2006). The relative proportion of the distal co-ignimbrite tephra (130 - 900 km from source) over the total bulk volume for the eruption is consistent with estimates reported Engwell et al. (2014) (74% versus 60 ± 6%). Deposits in Eastern Europe and North Africa in particular, are predominately composed of co-ignimbrite tephra. Figure 66 shows the contribution from the Plinian and co-ignimbrite tephra to the total bulk volume. At distances greater than 900 km from the source, it is not possible to quantitatively determine the relative proportions of tephra from the different phases due to the unimodal nature of the deposits (Engwell et al., 2014). However, the rapid decrease in the Plinian

component between 800 and 900 km indicates that ultra-distal tephra deposits (~ 1-2 cm) would have been predominantly co-ignimbrite in origin (Pyle et al., 2006).

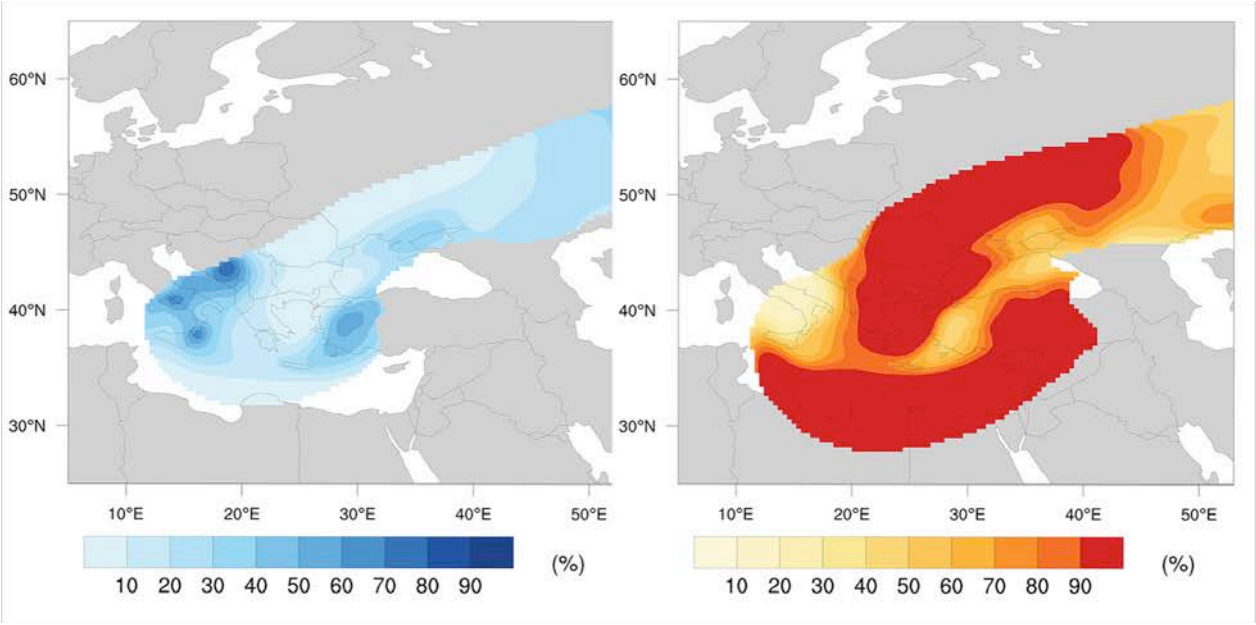

Figure 66. Contribution (%) from the Plinian (left) and co-ignimbrite (right) phases to the CI tephra deposit (extracted from Marti et al., 2016).

The inclusion of the gravity-driven transport improves tephra distribution in proximal areas reducing the overall RMSE by ~20% and the bias by ~20% (0.28 to 0.21). Contrary to other large explosive volcanic eruptions (e.g. Mt. Pinatubo - Costa et al. (2013); Toba Tuff - Costa et al. (2014), where cloud spreading and spinning velocities exceed typical stratospheric wind speeds (Baines and Sparks, 2005), gravity-current transport was dominant for the first hour only, producing an umbrella cloud radius of ~100 km upwind. This result is in agreement with findings of Giaccio et al. (2012), who reported the absence of tephra deposits associated with the CI event at the Sulmona intermountain basin, less than 150 km north of the vent, suggesting CI tephra transport was dominated by wind advection. An explanation for this phenomenon is associated with the inferred strong stratospheric winds (~90 m/s) above the vent, which could have prevailed over the effect of the spreading umbrella cloud (Fig 66). Stratospheric wind speed values above the vent are consistent with the mean of the 10 best meteorological fields found by Costa et al. (2012), which ranged from ~55 to ~95 m/s. This could support the idea that during the last Glacial period, winds were stronger than those in present-day (Dietrich et al., 2015). The passive transport dominance during the CI eruption can also explain the good fit reported in Costa et al. (2012), in which the effect of the gravity current in the umbrella cloud was not considered.

From a climatic perspective, recent studies indicate that the stratospheric aerosol cloud generated from the CI event would have induced a “volcanic winter” (Rampino et al., 1988) with a cooling effect of ~ 6-9ºC in Eastern Europe (Black et al., 2015). Using the total magma volume reported in this chapter (Table 17), and the CI melt composition (Signorelli et al., 2001), this work estimates (after Self *et al.*, 2004) the

amount of sulphur dioxide (SO_2) released by the eruption to be 168-180 Tg of SO_2 (84.5-90 Tg S), most of which reached the stratosphere assuming negligible release in the troposphere (Self, 2004). Table 18 summarizes the volatile release estimates for each phase of the CI eruption. Estimates are consistent with sulphate deposition records of the GISP2 ice core (Zielinski et al., 1996). These values represent a 10-15% decrease compared to previous CI reconstructions as a single-phase event (Costa et al., 2012) and are three times higher than those estimated for the largest historic eruption, the 1815 Tambora event (Self, 2004). Estimates of chlorine (Cl) and fluorine (F) are also calculated using the same methodology, taking into account the difference between concentrations dissolved in melt inclusions and those in matrix glass (Pappalardo et al., 2008). The amount of chemicals leached into the soil are calculated using volume estimations for the proximal pyroclastic density current deposits (Pyle et al., 2006).

Chemical	Stratospheric volatiles (Tg)			Leached into the soil (Tg) (by proximal PDC)
	Plinian phase	Co-ignimbrite phase	Combined phases	
SO_2 aerosols	88-92	248-264	336-356	n.a.
SO_2	44-46	124-132	168-178	273-289
Fluoride	243-256	693-731	936-987	1,519-3,384
Chloride	340-359	970-1,024	1,310-1,383	2,362-4,738

Table 18. Chemical release estimates by each phase of the CI eruption. Left: estimation of stratospheric volatiles after Self *et al*. (2004); Right: chemicals leached into the soil considering volume estimations for the proximal pyroclastic density current deposits after Pyle *et al*. (2006).

For large volcanic eruptions like the CI, stratospheric injection of SO_2 is the principal atmospheric and global impact. In the stratosphere, SO_2 is converted to sulphuric acid (H_2SO_4), which condenses rapidly to form fine sulphate aerosols that block incoming solar radiation and contribute to ozone destruction. Assuming a conversion efficiency (SO_2 to sulphate aerosols) of ~86% (McCormick et al., 1995; Self, 2004), the CI eruption would have yielded a maximum of 336–356 Tg of sulphate aerosols. These results are an order of magnitude greater than those found for the Mount Pinatubo eruption (McCormick et al., 1995), and are comparable with those of the Bishop Tuff eruption (Scaillet et al., 2004).

The environmental stress that followed the CI eruption, aggravated by the onset of the Heinrich Event 4, provides a link between this exceptional volcanic eruption and the comprehensively discussed Middle to Upper Palaeolithic transition (Fedele et al., 2007; Giaccio et al., 2012; Golovanova et al., 2010; Zilhão, 2006). Despite a long history of investigation, considerable debate still focuses on whether Neanderthals became extinct as a result of climate change or due to competition with anatomically modern humans (Banks et al., 2008; Fedele et al., 2003). According to recent studies, a stratospheric aerosol cloud of the size indicated by our CI simulations would have induced a cooling effect of ~ 6-9 ºC in eastern Europe and Northern Asia, 2-4°C in Western Europe (Black et al., 2015), and ~ 1-2 ºC globally (Timmreck et al., 2010), with an e-folding decay time of approximately 1 year (Robock, 2003). However, this "volcanic winter" (Rampino et al., 1988) would not have been sufficient to trigger dramatic changes in Upper

Palaeolithic European populations on a larger scale (Black et al., 2015). Archaeological records indicate that anatomically modern humans from Central Asia and the Middle East first populated the European continent prior to the CI eruption, suggesting contemporaneity with Neanderthals (Fedele et al., 2003). Tephra fallout from the eruption would have reduced the area available for human settlement in Europe by up to 30% (Fig. 67), causing a halt in the westward dispersal of modern human groups and leading to a significant "genetic bottleneck" (Zilhão, 2006). However, the removal of a large part of this tephra by erosion, the short acid deposition phase (1-2 years; Black et al., 2015), and the availability of nutrient reserves in buried topsoils, would have allowed for a rapid (~ 10 years) ecosystem recovery (Arnalds, 2013) in most areas away from the source. For example, the effect on net primary productivity following deposition of 5 – 10 cm of tephra from the 1980 eruption of Mount St. Helens was similar to that of subsequent yearly weather fluctuations (Pfitsch and Bliss, 1988). This being considered, it is possible that modern humans would have gravitated towards repopulating these recovered areas rather than resuming their westward dispersal, permitting prolonged Neanderthal survival in South-Western Europe. This assumption is consistent with the existing consensus that Neanderthal populations persisted in southern Europe, particularly in southern Iberia, well after the CI eruption (Zilhão, 2006). Furthermore, climatic changes from the Heinrich event 4 briefly created a biogeographic barrier between the Neanderthals and modern humans as described in the "Ebro Frontier" model (Zilhão, 2000). Demographic pressure over this frontier after the reinstatement of modern human groups in central and Eastern Europe would have culminated in the assimilation of the last Neanderthal refugia through expansion from across the Pyrenees.

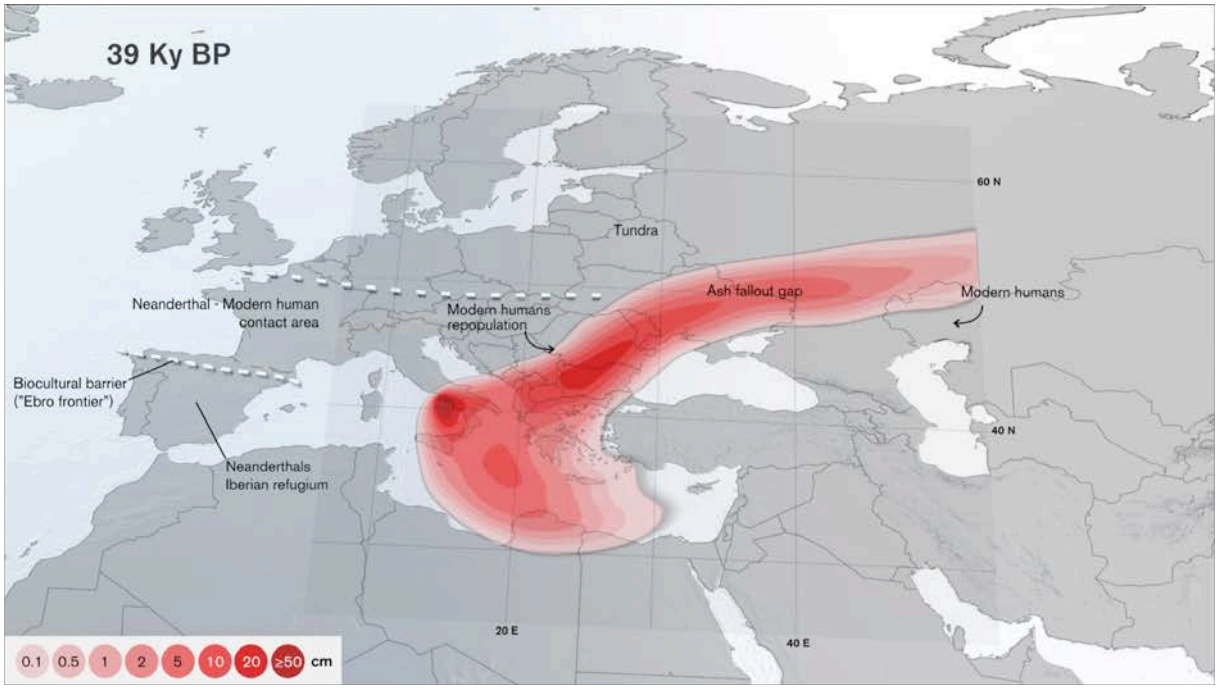

Figure 67. Campanian Ignimbrite's contribution to the Middle to Upper Palaeolithic transition. Tephra fallout, together with the attendant episode of Fenno-Scandinavian ice cap and peripheral tundra advance on land (top dashed line), suggests a reduction of the area available for human settlement in Europe of up to 30% (represented by the ash fallout gap with isopach tephra deposits

in cm). Anatomically modern humans would have gravitated towards repopulating this gap after ecosystem recovery, rather that overcoming new biogeographical frontiers, leading to an instance of prolonged (extracted from Marti et al., 2016).

5.6 Summary and conclusions

The 39 ka Campanian Ignimbrite (CI) super-eruption was the largest volcanic eruption of the past 200 ka in Europe. Tephra deposits indicate two distinct plume forming phases, Plinian and co-ignimbrite, characteristic of many caldera-forming eruptions. Previous numerical studies have characterized the eruption as a single-phase event, potentially leading to inaccurate assessment of eruption dynamics. To reconstruct the volume, intensity, and duration of the tephra dispersal, a computational inversion method was applied to explicitly account for the Plinian and co-ignimbrite phases and for gravitational spreading of the umbrella cloud. To verify the consistency of our results, an additional single-phase inversion was performed using an independent thickness dataset. Our better-fitting two-phase model suggests a higher mass eruption rate than previous studies, and estimates that 3/4 of the total fallout volume is co-ignimbrite in origin. Gravitational spreading of the umbrella cloud dominates tephra transport within the first hundred kilometres due to strong stratospheric winds in our best-fit wind model. Finally, tephra fallout impacts would have interrupted the westward migration of modern hominid groups in Europe, possibly supporting the hypothesis of prolonged Neanderthal survival in South-Western Europe during the Middle to Upper Palaeolithic transition.

An interactive website providing a moderated explanation of this methodology and its results is available to the general public at: (http://www.bsc.es/viz/campanian_ignimbrite).

Chapter 6

6 Conclusions and future research

A detailed discussion of the results and their conclusions were included for each chapter. The following sections identify the main conclusions of the Ph.D. research and highlights emerging areas and future challenges related to volcanic ash forecasting.

6.1 Main conclusions

The research conducted in this Ph.D. dissertation has focused on the implementation and evaluation of NMMB-MONARCH-ASH, a new on-line meteorological and atmospheric chemistry transport model to simulate the emission, transport and deposition of tephra particles released from volcanic eruptions. Five main conclusions are drawn from this work:

1. **NMMB-MONARCH-ASH is the first on-line system designed to predict ash cloud trajectories, concentration of ash at relevant flight levels, and the expected deposit thickness for both regional and global domains in research and operational set-ups**. The model has demonstrated the ability to remove most inconsistencies found in traditional off-line modeling systems, showing to be robust and scalable to arbitrary domain sizes and numbers of processors – See Chapter 2.

2. **The model is capable to reproduce the spatial and temporal dispersal variability of the ash cloud and tephra deposits, showing promising results and improving the performance from well-known off-line dispersal models traditionally employed in several operational settings** (*cases: 2001 Mt. Etna and 2011 Cordón Caulle eruptions*). For example NMMB-MONARCH-ASH improved the tephra distribution results from FALL3D simulations for the same event (R^2; 0.80/0.62), reducing the RMSE (0.014/0.24) and bias (0.02/0.6) by an order of magnitude (*case: 2001 Mt. Etna eruption*) – See Chapter 2.

3. Traditional off-line forecasts employed in operational model setups can result in significant uncertainties due to model and numerical errors. **The on-line vs. off-line strategies available in NMMB-MONARCH-ASH have demonstrated that off-line forecasts can fail to reproduce up to 45-70% of the ash cloud of an on-line forecast. The uncertainty associated to off-line systems is found to be as relevant (i.e. same order of magnitude) as those uncertainties attributed to the source term** (*cases: synthetic, 2010 Eyjafjallajökull, and 2011 Cordón Caulle eruptions)* – See Chapter 3.

4. On-line modeling strategies are preferred over traditional off-line forecasts in situations where meteorological conditions are fluctuating rapidly in time, two-way feedbacks are significant, or long-range ash cloud dispersal predictions are necessary. **A global application of NMMB-**

MONARCH-ASH has demonstrated, for the first tine, that volcanic ash emitted from Antarctic volcanoes could potentially encircle the globe, leading to significant consequences for global aviation safety, and showing that performing proper hazard assessment on this region is crucial to understand the patterns of ash distribution at high southern latitudes (*case: 1970-like Deception Island eruptive scenario*) – See Chapter 4.

5. Employing off-line modeling systems might be more convenient in terms of computing time or resources in cases where multiple VATDM executions are necessary without the prerequisite of re-running the meteorological component, e.g. to update the source term whenever the eruption conditions vary, for inverse modeling of ash, or to perform an ensemble forecast. **A novel computational intensive inversion approach has been developed to reconstruct, for the first time, the duration and contribution of the two phases of the Campanian Ignimbrite super-eruption. This approach has employed hundreds of FALL3D off-line simulations to improve modeled tephra distribution across the dispersal area from single phase reconstructions (R^2; 0.81/0.77), reducing RMSE by ~33% (0.18/0.27) and bias by ~52% (0.21/0.47). The better-fitting two-phase model suggests a higher mass eruption rate than previous studies (75% increase), lower total volume (15% decrease) and shorter duration (5 times) of the climatic phase, and estimates that 3/4 of the total fallout volume is co-ignimbritic in origin** (case: *39 ka Campanian Ignimbrite*) – See Chapter 5.

6.2 Future research and recommendations

This section proposes further research in three challenges related to volcanic ash forecasting:

1. **To employ computationally efficient on-line dispersal models for operational forecast of volcanic ash.** To date, all operational ash forecast systems follow the off-line approach and the few existing on-line atmospheric chemistry and transport models adapted to volcanic ash are still restricted to a research level. However, the increase of computational power in recent years and the fact that the total computing time required to run an on-line coupled model is not substantially larger, the benefits of the traditional off-line systems are at question. The results of this Ph.D. thesis advocate that operational groups responsible for real-time advisories for aviation should consider explore and consider on-line coupled models.

2. **To quantify the feedback effect of dense volcanic ash clouds on the radiative budget and regional meteorology**. Volcanic pollution affects the energy balance of the atmosphere whilst the dust and aerosols remain in the stratosphere. Despite that for most volcanic eruptions the influence on the radiative budget is minor (no effect or minor local/regional effects), in some cases (e.g. large explosive eruptions, super-eruptions) the impact of tropospheric volcanic aerosol can be significant, becoming a regional (or even global) radiative climate forcing. According to

the IPCC (2013) aerosols (including those from volcanic eruptions) and their interactions with clouds contribute to the largest uncertainties in the estimation of the Earth's changing energy budget. Future versions of NMMB-MONARCH-ASH foresee the implementation of volcanic particles within the radiative transfer model of NMMB-MONARCH.

3. **To pioneer tools to support managing aviation risk from ash hazards**. Impact analysis tools are necessary to prevent aircraft flying into ash clouds, which could result in catastrophic impacts. The aviation community is concerned about the detection and tracking of volcanic ash clouds to provide timely warnings to aircrafts and airports. The burden on airline operators is to perform dynamic risk assessments, including during the pre-eruptive phase. Finding the right balance between ensuring safety of flight (recognizing and avoiding hazardous airspace) and implementing efficiency of flight (minimizing unnecessary diversions and re-routing) is an ongoing challenge. The BSC is currently working on a software tool called SORT-ATM (Solutions of Real-Time for Air Traffic Management) aimed to fulfill this challenge. SORT-ATM is a user-friendly software application capable to provide customer-based solutions for Air Traffic Management during emergency situations involving atmospheric natural hazards. The impact assessment is based on calculations of a unique algorithm that employs in-house atmospheric dispersion models (e.g. FALL3D, NMMB-MONARCH-ASH), parameters for flight plan configurations and schedule, aircraft specifics, forecasted weather conditions and other relevant air traffic management and asset data from clients. The expected release date for this software is January 1st, 2018.

References

Aida, I.: Reliability of a tsunami source model derived from fault parameters., J. Phys. Earth, 26, 57–73, doi:10.4294/jpe1952.26.57, 1978.

Alfano, F., Bonadonna, C., Delmelle, P. and Costantini, L.: Insights on tephra settling velocity from morphological observations, J. Volcanol. Geotherm. Res., 208(3–4), 86–98, doi:10.1016/j.jvolgeores.2011.09.013, 2011.

Almendros, J., Carmona, E., Jiménez, V., Díaz-Moreno, A., Lorenzo, F., Berrocoso, M., de Gil, A., Fernández-Ros, A., Rosado, B., Prates, G. and Peci, L. M.: Deception Island: Sustained deformation and large increase in seismic activity during the 2014-2015 survey, in Proceedings Expert Group on Antarctic Volcanism (ANTVOLC), SCAR, Catania, Italy., 2015.

Ames, W.: Numerical methods for partial differential equations, Nelson. London., 1969.

Ansmann, A., Tesche, M., Groß, S., Freudenthaler, V., Seifert, P., Hiebsch, A., Schmidt, J., Wandinger, U., Mattis, I., Müller, D. and Wiegner, M.: The 16 April 2010 major volcanic ash plume over central Europe: EARLINET lidar and AERONET photometer observations at Leipzig and Munich, Germany, Geophys. Res. Lett., 37(13), 1–5, doi:10.1029/2010GL043809, 2010.

Arakawa, A. and Lamb, V.: Computational design of the basic dynamical processes of the UCLA general circulation model, Methods Comput. Phys., 17, 173–265, 1977.

Arason, P., Petersen, G. N. and Bjornsson, H.: Observations of the altitude of the volcanic plume during the eruption of Eyjafjallajökull, April–May 2010, Earth Syst. Sci. Data, 3(1), 9–17, doi:10.5194/essd-3-9-2011, 2011.

Arastoopour, H., Wang, C.-H. and Weil, S. A.: Particle-particle interaction force in a dilute gas-solid system, Chem. Eng. Sci., 37(9), 1379–1386, doi:10.1016/0009-2509(82)85010-0, 1982.

Armienti, P., Macedonio, G. and Pareschi, M. T.: A numerical model for simulation of tephra transport and deposition; applications to May 18, 1980, Mount St. Helens eruption, J. Geophys. Res., 93(B6), 6463–6476, doi:10.1029/JB093iB06p06463, 1988.

Arnalds, O.: The influence of volcanic tephra (ash) on ecosystems, Adv. Agron., 121, 331–380, doi:10.1016/B978-0-12-407685-3.00006-2, 2013.

Badia, A., Jorba, O., Voulgarakis, A., Dabdub, D., Pérez García-Pando, C., Hilboll, A., Gonçalves, M. and Janjic, Z.: Description and evaluation of the Multiscale Online Nonhydrostatic AtmospheRe CHemistry model (NMMB-MONARCH) version 1.0: gas-phase chemistry at global scale, Geosci. Model Dev., 10(2), 609–638, doi:10.5194/gmd-10-609-2017, 2017.

Bagheri, G. and Bonadonna, C.: Aerodynamics of Volcanic Particles, Volcan. Ash, 39–52, doi:10.1016/B978-0-08-100405-0.00005-7, 2016a.

Bagheri, G. and Bonadonna, C.: On the drag of freely falling non-spherical particles, Powder Technol., 301, 526–544, doi:10.1016/j.powtec.2016.06.015, 2016b.

Baines, P. and Sparks, R. S. J.: Dynamics of giant volcanic ash clouds from supervolcanic eruptions, Geophys. Res. Lett., 32(December), 1–4, doi:10.1029/2005GL024597, 2005.

Baklanov, A.: Integrated Meteorology Chemistry Models: Challenges, gaps, needs and future directions, White Pap. Draft, doi:10.5194/acp-14-317-2014, 2014.

Baklanov, A., Mahura, A. and Sokhi, R.: Integrated Systems of Meso-Meteorological and Chemical Transport Models, Springer Berlin Heidelberg. [online] Available from: https://books.google.es/books?id=hseg5tsp-qAC, 2011.

Baklanov, A., Schlünzen, K., Suppan, P., Baldasano, J. M., Brunner, D., Aksoyoglu, S., Carmichael, G., Douros, J., Flemming, J., Forkel, R., Galmarini, S., Gauss, M., Grell, G., Hirtl, M., Joffre, S., Jorba, O., Kaas, E., Kaasik, M., Kallos, G., Kong, X., Korsholm, U., Kurganskiy, A., Kushta, J., Lohmann, U., Mahura, A., Manders-Groot, A., Maurizi, A., Moussiopoulos, N., Rao, S. T., Savage, N., Seigneur, C., Sokhi, R. S., Solazzo, E., Solomos, S., Sørensen, B., Tsegas, G., Vignati, E., Vogel, B. and Zhang, Y.: Online coupled regional meteorology chemistry models in Europe: Current status and prospects, Atmos. Chem. Phys., 14(November 2013), 317–398, doi:10.5194/acp-14-317-2014, 2014.

Balis, D., Koukouli, M.-E., Siomos, N., Dimopoulos, S., Mona, L., Pappalardo, G., Marenco, F., Clarisse, L.,

Ventress, L. J., Carboni, E., Grainger, R. G., Wang, P., Tilstra, G., van der A, R., Theys, N. and Zehner, C.: Validation of ash optical depth and layer height retrieved from passive satellite sensors using EARLINET and airborne lidar data: the case of the Eyjafjallajökull eruption, Atmos. Chem. Phys., 16(9), 5705–5720, doi:10.5194/acp-16-5705-2016, 2016.

Banks, W., D'Errico, F., Peterson, A., Kageyama, M., Sima, A. and Sánchez-Goñi, M.: Neanderthal extinction by competitive exclusion, PLoS One, 3(12), 1–8, doi:10.1371/journal.pone.0003972, 2008.

Barberi, F., Innocenti, F., Lirer, L., Munno, R., Pescatore, T. and Santacroce, R.: The campanian ignimbrite: a major prehistoric eruption in the Neapolitan area (Italy), Bull. Volcanol., 41(1), 10–31, doi:10.1007/BF02597680, 1978.

Barsotti, S., Neri, A. and Scire, J. S.: The VOL-CALPUFF model for atmospheric ash dispersal: 1. Approach and physical formulation, J. Geophys. Res., 113(B3), B03208, doi:10.1029/2006JB004623, 2008.

Barsotti, S., Andronico, D., Neri, A., Del Carlo, P., Baxter, P. J., Aspinall, W. P. and Hincks, T.: Quantitative assessment of volcanic ash hazards for health and infrastructure at Mt. Etna (Italy) by numerical simulation, J. Volcanol. Geotherm. Res., 192(1–2), 85–96, doi:10.1016/j.jvolgeores.2010.02.011, 2010.

Bartolini, S., Geyer, A., Martí, J., Pedrazzi, D. and Aguirre-Díaz, G.: Volcanic hazard on Deception Island (South Shetland Islands, Antarctica), J. Volcanol. Geotherm. Res., 285, 150–168, doi:https://doi.org/10.1016/j.jvolgeores.2014.08.009, 2014.

Beckett, F., Kylling, A., Sigurðardóttir, G., von Löwis, S. and Witham, C.: Quantifying the mass loading of particles in an ash cloud remobilised from tephra deposits on Iceland, Atmos. Chem. Phys. Discuss., (August), 1–31, doi:10.5194/acp-2016-689, 2016.

Bender, N. A., Crosbie, K. and Lynch, H. J.: Patterns of tourism in the Antarctic Peninsula region: a 20-year analysis, Antarct. Sci., 28(3), 194–203, doi:DOI: 10.1017/S0954102016000031, 2016.

Bergmann, I. and Dobslaw, H.: Short-term transport variability of the Antarctic Circumpolar Current from satellite gravity observations, J. Geophys. Res. Ocean., 117(C5), doi:10.1029/2012JC007872, 2012.

Betts, A. K. and Miller, M. J.: A new convective adjustment scheme. Part II: Single column tests using GATE wave, BOMEX, ATEX and arctic air-mass data sets, Q. J. R. Meteorol. Soc., 112(473), 693–709, doi:10.1002/qj.49711247308, 1986.

Biass, S. and Bonadonna, C.: A quantitative uncertainty assessment of eruptive parameters derived from tephra deposits: The example of two large eruptions of Cotopaxi volcano, Ecuador, Bull. Volcanol., 73(1), 73–90, doi:10.1007/s00445-010-0404-5, 2011.

Black, B., Neely, R. and Manga, M.: Campanian Ignimbrite volcanism, climate, and the final decline of the Neanderthals, Geology, 43(5), 1–4, doi:10.1130/G36514.1, 2015.

Bonadonna, C. and Costa, A.: Modeling tephra sedimentation from volcanic plumes, in Modeling Volcanic Processes, pp. 173–202., 2013a.

Bonadonna, C. and Costa, A.: Plume height, volume, and classification of explosive volcanic eruptions based on the Weibull function, Bull. Volcanol., 75, 1–19, doi:10.1007/s00445-013-0742-1, 2013b.

Bonadonna, C. and Houghton, B. F.: Total grain-size distribution and volume of tephra-fall deposits, Bull. Volcanol., 67(June 1996), 441–456, doi:10.1007/s00445-004-0386-2, 2005.

Bonadonna, C. and Phillips, J. C.: Sedimentation from strong volcanic plumes, J. Geophys. Res., 108(B7), 2340, doi:10.1029/2002JB002034, 2003.

Bonadonna, C., Ernst, G. G. J. and Sparks, R. S. J.: Thickness variations and volume estimates of tephra fall deposits: the importance of particle Reynolds number, J. Volcanol. Geotherm. Res., 81(3–4), 173–187, doi:10.1016/S0377-0273(98)00007-9, 1998.

Bonadonna, C., Mayberry, G. C., Calder, E. S., Sparks, R. S. J., Choux, C., Jackson, P., Lejeune, a. M., Loughlin, S. C., Norton, G. E., Rose, W., Ryan, G. and Young, S. R.: Tephra fallout in the eruption of Soufriere Hills Volcano, Montserrat, Geol. Soc. London, Mem., 21(1), 483–516, doi:10.1144/GSL.MEM.2002.021.01.22, 2002.

Bonadonna, C., Connor, C., Houghton, B. F., Connor, L., Byrne, M., Laing, A. and Hincks, T. K.: Probabilistic modeling of tephra dispersal: Hazard assessment of a multiphase rhyolitic eruption at Tarawera, New Zealand, J. Geophys. Res. B Solid Earth, 110(3), 1–21, doi:10.1029/2003JB002896,

2005.

Bonadonna, C., Folch, A., Loughlin, S. and Puempel, H.: Report on the IAVCEI-WMO workshop on Ash Dispersal Forecast and Civil Aviation, IUGG Newsl., 11(6), 6–7, 2010.

Bonadonna, C., Genco, R., Gouhier, M., Pistolesi, M., Cioni, R., Alfano, F., Hoskuldsson, A. and Ripepe, M.: Tephra sedimentation during the 2010 Eyjafjallajkull eruption (Iceland) from deposit, radar, and satellite observations, J. Geophys. Res. Solid Earth, 116(12), doi:10.1029/2011JB008462, 2011.

Bonadonna, C., Folch, A., Loughlin, S. and Puempel, H.: Future developments in modelling and monitoring of volcanic ash clouds: Outcomes from the first IAVCEI-WMO workshop on Ash Dispersal Forecast and Civil Aviation, Bull. Volcanol., 74(1), 1–10, doi:10.1007/s00445-011-0508-6, 2012.

Bonadonna, C., Webley, P., Hort, M., Folch, A., Loughlin, S. and Puempel, H.: 2 nd IUGG-WMO Workshop on Ash Dispersal Forecast and Civil Aviation, Consensual Document. [online] Available from: https://vhub.org/resources/add-contribution/3343, 2014.

Bonadonna, C., Biass, S. and Costa, A.: Physical characterization of explosive volcanic eruptions based on tephra deposits: Propagation of uncertainties and sensitivity analysis, J. Volcanol. Geotherm. Res., doi:10.1016/j.jvolgeores.2015.03.009, 2015a.

Bonadonna, C., Cioni, R. and Pistolesi, M.: Sedimentation of long-lasting wind-affected volcanic plumes : the example of the 2011 rhyolitic Cordón Caulle eruption, Chile, Bull. Volcanol., doi:10.1007/s00445-015-0900-8, 2015b.

Boughton, B. A., Delaurentis, J. M. and Dunn, W. E.: A stochastic model of particle dispersion in the atmosphere, Boundary-Layer Meteorol., 40(1), 147–163, doi:10.1007/BF00140073, 1987.

Branca, S. and Del Carlo, P.: Types of eruptions of Etna volcano AD 1670-2003: Implications for short-term eruptive behaviour, Bull. Volcanol., 67(8), 732–742, doi:10.1007/s00445-005-0412-z, 2005.

Brown, R., Bonadonna, C. and Durant, A.: A review of volcanic ash aggregation, Phys. Chem. Earth, 45–46(January), 65–78, doi:10.1016/j.pce.2011.11.001, 2012.

Burns, F. A., Bonadonna, C., Pioli, L., Cole, P. D. and Stinton, A.: Ash aggregation during the 11 February 2010 partial dome collapse of the Soufrière Hills Volcano, Montserrat, J. Volcanol. Geotherm. Res., 335, 92–112, doi:https://doi.org/10.1016/j.jvolgeores.2017.01.024, 2017.

Bursik, M.: Effect of wind on the rise height of volcanic plumes, Geophys. Res. Lett., 28(18), 3621–3624, doi:10.1029/2001GL013393, 2001.

Bursik, M., Sparks, R. S. J., Gilbert, J. S. and Carey, S. N.: Sedimentation of tephra by volcanic plumes: I. Theory and its comparison with a study of the Fogo A plinian deposit, Sao Miguel (Azores), Bull. Volcanol., 54(4), 329–344, doi:10.1007/BF00301486, 1992.

Carazzo, G., Kaminski, E. and Tait, S.: The timing and intensity of column collapse during explosive volcanic eruptions, Earth Planet. Sci. Lett., 411, 208–217, doi:10.1016/j.epsl.2014.12.006, 2015.

Carey, S. and Sigurdsson, H.: The intensity of plinian eruptions, Bull. Volcanol., 51(1), 28–40, doi:10.1007/BF01086759, 1989.

Carey, S. and Sparks, R. S. J.: Quantitative models of the fallout and dispersal of tephra from volcanic eruption columns, Bull. Volcanol., 48(2–3), 109–125, doi:10.1007/BF01046546, 1986.

Carn, S. A. and Krotkov, N. A.: Chapter 12 – Ultraviolet Satellite Measurements of Volcanic Ash, in Volcanic Ash, pp. 217–231, Elsevier., 2016.

Cas, R. and Wright, J.: Volcanic Successions: Modern and Ancient. A geological approach to processes, products and successions, 1st ed., Springer Netherlands., 1987.

Casadevall, T. J.: Volcanic Hazards and Aviation Safety : Lessons of the Past Decade., 1993.

Cashman, K. and Rust, A.: Volcanic Ash: Generation and Spatial Variations, in Volcanic Ash, pp. 5–22, Elsevier., 2016.

Cerminara, M.: The Multiphase Buoyant Plume Solution of the Dusty Gas Model., 2015.

Cerminara, M., Esposti Ongaro, T. and Berselli, L. C.: ASHEE-1.0: A compressible, equilibrium-Eulerian model for volcanic ash plumes, Geosci. Model Dev., 9(2), 697–730, doi:10.5194/gmd-9-697-2016, 2016.

Chen, W. R. and Zhao, L. R.: Review - Volcanic Ash and its Influence on Aircraft Engine Components, Procedia Eng., 99, 795–803, doi:10.1016/j.proeng.2014.12.604, 2015.

Civetta, L., Orsi, G., Pappalardo, L., Fisher, R., Heiken, G. and Ort, M.: Geochemical zoning, mingling, eruptive dynamics and depositional processes — the Campanian Ignimbrite, Campi Flegrei caldera, Italy, J. Volcanol. Geotherm. Res., 75(2), 183–219, doi:10.1016/S0377-0273(96)00027-3, 1997.

Clarisse, L. and Prata, F.: Chapter 11 – Infrared Sounding of Volcanic Ash, in Volcanic Ash, pp. 189–215, Elsevier., 2016.

Clarkson, R. J., Majewicz, E. J. E. and Mack, P.: A re-evaluation of the 2010 quantitative understanding of the effects volcanic ash has on gas turbine engines, Proc. Inst. Mech. Eng. Part G J. Aerosp. Eng., 230(12), 2274–2291, doi:10.1177/0954410015623372, 2016.

Collini, E., Osores, M. S., Folch, A., Viramonte, J., Villarosa, G. and Salmuni, G.: Volcanic ash forecast during the June 2011 Cordón Caulle eruption, Nat. Hazards, 66, 389–412, doi:10.1007/s11069-012-0492-y, 2013.

Connor, L. and Connor, C.: Inversion is the Key to Dispersion : Understanding Eruption Dynamics by Inverting Tephra Fallout, Special Publications of IAVCEI, 1. Geological Society, London, pp. 231–242., 2006.

Cornell, W., Carey, S. and Sigurdsson, H.: Computer simulation of transport and deposition of the Campanian Y-5 ash, J. Volcanol. Geotherm. Res., 17, 89–109, 1983.

Costa, A., Macedonio, G. and Folch, A.: A three-dimensional Eulerian model for transport and deposition of volcanic ashes, Earth Planet. Sci. Lett., 241, 634–647, doi:10.1016/j.epsl.2005.11.019, 2006.

Costa, A., Folch, A. and MacEdonio, G.: A model for wet aggregation of ash particles in volcanic plumes and clouds: 1. Theoretical formulation, J. Geophys. Res. Solid Earth, 115, 1–14, doi:10.1029/2009JB007175, 2010.

Costa, A., Folch, A., Macedonio, G., Giaccio, B., Isaia, R. and Smith, V. C.: Quantifying volcanic ash dispersal and impact of the Campanian Ignimbrite super-eruption, Geophys. Res. Lett., 39(10), L10310, doi:10.1029/2012GL051605, 2012.

Costa, A., Folch, A. and Macedonio, G.: Density-driven transport in the umbrella region of volcanic clouds : Implications for tephra dispersion models, Geophys. Res. Lett., 40(July), 4823–4827, doi:10.1002/grl.50942, 2013.

Costa, A., Smith, V. C., Macedonio, G. and Matthews, N.: The magnitude and impact of the Youngest Toba Tuff super-eruption, Front. Earth Sci., 2(August), 1–8, doi:10.3389/feart.2014.00016, 2014.

Costa, A., Pioli, L. and Bonadonna, C.: Assessing tephra total grain-size distribution: Insights from field data analysis, Earth Planet. Sci. Lett., 443(September), 90–107, doi:10.1016/j.epsl.2016.02.040, 2016a.

Costa, A., Suzuki, Y., Cerminara, M., Devenish, B. J., Esposti Ongaro, T., Herzog, M., Van Eaton, A., Denby, L., Bursik, M., De' Michieli Vitturi, M., Engwell, S., Neri, A., Barsotti, S., Folch, A., Macedonio, G., Girault, F., Carazzo, G., Tait, S., Kaminski, É., Mastin, L., Woodhouse, M., Phillips, J., Hogg, A., Degruyter, W. and Bonadonna, C.: Overview of the Results of the Eruption Column Model Intercomparison Exercise, J. Volcanol. Geotherm. Res., doi:10.1016/j.jvolgeores.2016.01.017, 2016b.

Cox, P. M., Betts, R. a, Jones, C. D., Spall, S. a and Totterdell, I. J.: Acceleration of global warming due to carbon-cycle feedbacks in a coupled climate model., Nature, 408(6809), 184–187, doi:10.1038/35041539, 2000.

D'Amours, R., Malo, A., Servranckx, R., Bensimon, D., Trudel, S. and Gauthier-Bilodeau, J.-P.: Application of the atmospheric Lagrangian particle dispersion model MLDP0 to the 2008 eruptions of Okmok and Kasatochi volcanoes, J. Geophys. Res., 115, D00L11, doi:10.1029/2009JD013602, 2010.

Dacre, H. F., Grant, A. L. M., Hogan, R. J., Belcher, S. E., Thomson, D. J., Devenish, B. J., Marenco, F., Hort, M. C., Haywood, J. M., Ansmann, A., Mattis, I. and Clarisse, L.: Evaluating the structure and magnitude of the ash plume during the initial phase of the 2010 Eyjafjallajökull eruption using lidar observations and NAME simulations, J. Geophys. Res. Atmos., 116(14), doi:10.1029/2011JD015608, 2011.

Darwin VAAC: Satellite image of path of the Cordon Caulle ash cloud around the southern hemisphere from 5-12 June 2011, Bur. Meteorol. [online] Available from: http://www.bom.gov.au/info/vaac/cordon_caulle.shtml, 2011.

De'Michieli Vitturi, M., Neri, A. and Barsotti, S.: PLUME-MoM 1.0: A new integral model of volcanic plumes based on the method of moments, Geosci. Model Dev., 8(8), 2447–2463, doi:10.5194/gmd-8-

2447-2015, 2015.

Degruyter, W. and Bonadonna, C.: Improving on mass flow rate estimates of volcanic eruptions, Geophys. Res. Lett., 39(May), 1–6, doi:10.1029/2012GL052566, 2012.

Dellino, P., Mele, D., Bonasia, R., Braia, G., La Volpe, L. and Sulpizio, R.: The analysis of the influence of pumice shape on its terminal velocity, Geophys. Res. Lett., 32(October), 1–4, doi:10.1029/2005GL023954, 2005.

Devenish, B. J.: Using simple plume models to refine the source mass flux of volcanic eruptions according to atmospheric conditions, J. Volcanol. Geotherm. Res., 256, 118–127, doi:10.1016/j.jvolgeores.2013.02.015, 2013.

Devenish, B. J., Rooney, G. G., Webster, H. N. and Thomson, D. J.: The entrainment rate for buoyant plumes in a crossflow, Boundary-Layer Meteorol., 134(3), 411–439, doi:10.1007/s10546-009-9464-5, 2010.

Devenish, B. J., Francis, P. N., Johnson, B. T., Sparks, R. S. J. and Thomson, D. J.: Sensitivity analysis of dispersion modeling of volcanic ash from Eyjafjallajökull in May 2010, J. Geophys. Res. Atmos., 117(D20), doi:10.1029/2011JD016782, 2012.

Dietrich, S., Werner, M. and Lohmann, G.: More Variable and Stronger Winds during the Last Glacial, in : EGU General Assembly Conference Abstracts, vol. 17, p. 15486., 2015.

Dioguardi, F., Dürig, T., Engwell, S. L., Gudmundsson, M. T. and Loughlin, S. C.: Investigating Source Conditions and Controlling Parameters of Explosive Eruptions: Some Experimental-Observational-Modelling Case Studies, in Updates in Volcanology - From Volcano Modelling to Volcano Geology, pp. 141–162., 2016.

Dioguardi, F., Mele, D., Dellino, P. and Dürig, T.: The terminal velocity of volcanic particles with shape obtained from 3D X-ray microtomography, J. Volcanol. Geotherm. Res., 329, 41–53, doi:10.1016/j.jvolgeores.2016.11.013, 2017.

Doms, G., Förstner, J., Heise, E., Herzog, H.-J., Mironov, D., Raschendorfer, M., Reinhardt, T., Ritter, B., Schrodin, R., Schulz, J.-P. and Vogel, G.: A Description of the Nonhydrostatic Regional COSMO Model Part II : Physical Parameterization., 2011.

Van Eaton, A. R. and Wilson, C. J. N.: The nature, origins and distribution of ash aggregates in a large-scale wet eruption deposit: Oruanui, New Zealand, J. Volcanol. Geotherm. Res., 250, 129–154, doi:10.1016/j.jvolgeores.2012.10.016, 2013.

Van Eaton, A. R., Muirhead, J. D., Wilson, C. J. N. and Cimarelli, C.: Growth of volcanic ash aggregates in the presence of liquid water and ice: an experimental approach, Bull. Volcanol., 74(9), 1963–1984, doi:10.1007/s00445-012-0634-9, 2012a.

Van Eaton, A. R., Mastin, L. G., Herzog, M., Schwaiger, H. F., Schneider, D. J., Wallace, K. L. and Clarke, A. B.: Hail formation triggers rapid ash aggregation in volcanic plumes., Nat. Commun., 6, 7860, doi:10.1038/ncomms8860, 2015.

Van Eaton, A., Herzog, M., Wilson, C. J. N. and McGregor, J.: Ascent dynamics of large phreatomagmatic eruption clouds: The role of microphysics, J. Geophys. Res. Solid Earth, 117(3), 1–23, doi:10.1029/2011JB008892, 2012b.

Eckermann, S.: Hybrid $\sigma - p$ Coordinate Choices for a Global Model, Mon. Weather Rev., 137(1), 224–245, doi:10.1175/2008MWR2537.1, 2009.

Ek, M. B., Mitchell, K. E., Lin, Y., Rogers, E., Grunmann, P., Koren, V., Gayno, G. and Tarpley, J. D.: Implementation of Noah land surface model advances in the National Centers for Environmental Prediction operational mesoscale Eta model, J. Geophys. Res. Atmos., 108(D22), doi:10.1029/2002JD003296, 2003.

Elissondo, M., Baumann, V., Bonadonna, C., Pistolesi, M., Cioni, R., Bertagnini, A., Biass, S., Herrero, J. C. and Gonzalez, R.: Chronology and impact of the 2011 Cordon Caulle eruption, Chile, Nat. Hazards Earth Syst. Sci., 16(3), 675–704, doi:10.5194/nhess-16-675-2016, 2016.

Emeis, S., Forkel, R., Junkermann, W., Schäfer, K., Flentje, H., Gilge, S., Fricke, W., Wiegner, M., Freudenthaler, V., Groβ, S., Ries, L., Meinhardt, F., Birmili, W., Münkel, C., Obleitner, F. and Suppan, P.: Measurement and simulation of the 16/17 April 2010 Eyjafjallajökull volcanic ash layer dispersion in the northern Alpine region, Atmos. Chem. Phys., 11(6), 2689–2701, doi:10.5194/acp-11-2689-2011,

2011.

Engwell, S., Mastin, M., Sara, B., Augusto, N., Folch, A., Stunder, B. and Witham, C.: Improving the global Eruption Source Parameters Database : Where do we go from here ?, 2016.

Engwell, S. L., Sparks, R. S. J. and Carey, S.: Physical characteristics of tephra layers in the deep sea realm: the Campanian Ignimbrite eruption, Geol. Soc. London, Spec. Publ., 398(1), 47–64, doi:10.1144/SP398.7, 2014.

Esposti Ongaro, T. and Cerminara, M.: Non-equilibrium processes in ash-laden volcanic plumes: new insights from 3D multiphase flow simulations, J. Volcanol. Geotherm. Res., doi:10.1016/j.jvolgeores.2016.04.004, 2015.

Esposti Ongaro, T., Cavazzoni, C., Erbacci, G., Neri, A. and Salvetti, M. V.: A parallel multiphase flow code for the 3D simulation of explosive volcanic eruptions, Parallel Comput., 33(7–8), 541–560, doi:10.1016/j.parco.2007.04.003, 2007.

Eychenne, J., Le Pennec, J., Troncoso, L., Gouhier, M. and Nedelec, J.: Causes and consequences of bimodal grain-size distribution of tephra fall deposited during the August 2006 Tungurahua eruption (Ecuador), Bull. Volcanol., 74(August 2006), 187–205, doi:10.1007/s00445-011-0517-5, 2012.

Eychenne, J., Cashman, K., Rust, A. and Durant, A.: Impact of the lateral blast on the spatial pattern and grain size characteristics of the 18 May 1980 Mount St. Helens fallout deposit, J. Geophys. Res. Solid Earth, doi:10.1002/2015JB012116, 2015.

Fedele, F., Giaccio, B., Isala, R. and Orsi, G.: The Campanian ignimbrite eruption, Heinrich event 4, and Palaeolithic change in Europe: a high-resolution investigation, edited by C. Oppenheimer and A. Robock, American Geophysical Union., 2003.

Fedele, F., Giaccio, B. and Isaia, R.: The Campanian Ignimbrite factor: towards a reappraisal of the Middle to Upper Palaeolithic “transition,” in Living Under the Shadow: The Cultural Impacts of Volcanic Eruptions, edited by J. Grattan and R. Torrence, pp. 19–41, Left Coast Press, Walnutt Creek, California., 2007.

Ferrier, B., Jin, Y., Lin, Y., Black, T., Rogers, E. and DiMego, G.: Implementation of a new frid-scale cloud and precipitation shceme in the NCEP Eta Model, in Proc. 15th Conf. on Numerical Weather Prediction; San Antonio; 12–16 August 2002; TX, pp. 280–283, American Meteorological Society., 2002.

Fisher, R., Orsi, G., Ort, M. and Heiken, G.: Mobility of a large-volume pyroclastic flow — emplacement of the Campanian ignimbrite, Italy, J. Volcanol. Geotherm. Res., 56(3), 205–220, doi:http://dx.doi.org/10.1016/0377-0273(93)90017-L, 1993.

Fisher, R. V. and Schmincke, H.-U.: Pyroclastic Rocks., 1984.

Fitzsimmons, K., Hambach, U., Veres, D. and Iovita, R.: The Campanian Ignimbrite eruption: new data on volcanic ash dispersal and its potential impact on human evolution., PLoS One, 8(6), e65839, doi:10.1371/journal.pone.0065839, 2013.

Flentje, H., Claude, H., Elste, T., Gilge, S., Köhler, U., Plass-Dülmer, C., Steinbrecht, W., Thomas, W., Werner, A. and Fricke, W.: The Eyjafjallajökull eruption in April 2010 - Detection of volcanic plume using in-situ measurements, ozone sondes and lidar-ceilometer profiles, Atmos. Chem. Phys., 10(20), 10085–10092, doi:10.5194/acp-10-10085-2010, 2010.

Folch, A.: A review of tephra transport and dispersal models: Evolution, current status, and future perspectives, J. Volcanol. Geotherm. Res., 235–236, 96–115, doi:10.1016/j.jvolgeores.2012.05.020, 2012.

Folch, A. and Sulpizio, R.: Evaluating long-range volcanic ash hazard using supercomputing facilities: application to Somma-Vesuvius (Italy), and consequences for civil aviation over the Central Mediterranean Area, Bull. Volcanol., 72(9), 1039–1059, doi:10.1007/s00445-010-0386-3, 2010.

Folch, A., Costa, A. and Macedonio, G.: FALL3D: A computational model for transport and deposition of volcanic ash, Comput. Geosci., 35, 1334–1342, doi:10.1016/j.cageo.2008.08.008, 2009.

Folch, A., Costa, A. and Macedonio, G.: A model for wet aggregation of ash particles in volcanic plumes and clouds: 1. Theoretical formulation, J. Geophys. Res. Solid Earth, 115, 1–16, doi:10.1029/2009JB007175, 2010.

Folch, A., Costa, A. and Basart, S.: Validation of the FALL3D ash dispersion model using observations of

the 2010 Eyjafjallajökull volcanic ash clouds, Atmos. Environ., 48, 165–183, doi:http://dx.doi.org/10.1016/j.atmosenv.2011.06.072, 2012.

Folch, A., Mingari, L., Osores, M. S. and Collini, E.: Modeling volcanic ash resuspension - Application to the 14-18 October 2011 outbreak episode in central Patagonia, Argentina, Nat. Hazards Earth Syst. Sci., 14(1), 119–133, doi:10.5194/nhess-14-119-2014, 2014.

Folch, A., Costa, A. and Macedonio, G.: FPLUME-1.0: An integral volcanic plume model accounting for ash aggregation, Geosci. Model Dev., 9(1), 431–450, doi:10.5194/gmd-9-431-2016, 2016a.

Folch, A., Costa, A. and MacEdonio, G.: User's manual - FALL3D 7.1. [online] Available from: http://datasim.ov.ingv.it/download/fall3d/manual-fall3d-7.1.pdf, 2016b.

Freitas, S. R., Longo, K. M., Alonso, M. F., Pirre, M., Marecal, V., Grell, G., Stockler, R. and Mello, R. F.: Geoscientific Model Development PREP-CHEM-SRC – 1 . 0 : a preprocessor of trace gas and aerosol emission fields for regional and global atmospheric chemistry models, , 419–433, doi:10.5194/gmd-4-419-2011, 2011.

Fretzdorff, S. and Smellie, J. L.: Electron microprobe characterization of ash layers in sediments from the central Bransfield basin (Antarctic Peninsula): evidence for at least two volcanic sources, Antarct. Sci., 14(4), 412–421, doi:DOI: 10.1017/S0954102002000214, 2002.

Gadd, A.: An economical explicit integration scheme. Tech. Note 44. UK Meteorological Office., 1974.

Galmarini, S., Bonnardot, F., Jones, A., Potempski, S., Robertson, L. and Martet, M.: Multi-model vs. EPS-based ensemble atmospheric dispersion simulations: A quantitative assessment on the ETEX-1 tracer experiment case, Atmos. Environ., 44(29), 3558–3567, doi:10.1016/j.atmosenv.2010.06.003, 2010.

Ganser, G. H.: A rational approach to drag prediction of spherical and nonspherical particles, Powder Technol., 77(2), 143–152, doi:http://dx.doi.org/10.1016/0032-5910(93)80051-B, 1993.

Geisinger, A., Behrendt, A., Wulfmeyer, V., Strohbach, J., Förstner, J., Potthast, R. and Mattis, I.: A Backscatter Lidar Forward Operator for Particle-Representing Atmospheric Chemistry Models, Atmos. Chem. Phys. Discuss., 1–45, doi:10.5194/acp-2016-609, 2016.

Giaccio, B., Nomade, S., Wulf, S., Isaia, R., Sottili, G., Cavuoto, G., Galli, P., Messina, P., Sposato, A., Sulpizio, R. and Zanchetta, G.: The late MIS 5 Mediterranean tephra markers: a reappraisal from peninsular Italy terrestrial records, Quat. Sci. Rev., 56(October 2015), 31–45, doi:10.1016/j.quascirev.2012.09.009, 2012.

Girault, F., Carazzo, G., Tait, S., Ferrucci, F. and Kaminski, É.: The effect of total grain-size distribution on the dynamics of turbulent volcanic plumes, Earth Planet. Sci. Lett., 394, 124–134, doi:10.1016/j.epsl.2014.03.021, 2014.

Golovanova, L., Doronichev, V., Cleghorn, N., Koulkova, M., Sapelko, T. and Shackley, S.: Significance of Ecological Factors in the Middle to Upper Paleolithic Transition, Curr. Anthropol., 51(5), 655–691, doi:10.1086/656185, 2010.

Grell, G. and Baklanov, A.: Integrated modeling for forecasting weather and air quality: A call for fully coupled approaches, Atmos. Environ., 45(38), 6845–6851, doi:10.1016/j.atmosenv.2011.01.017, 2011.

Grell, G. a., Knoche, R., Peckham, S. E. and McKeen, S. a.: Online versus offline air quality modeling on cloud-resolving scales, Geophys. Res. Lett., 31(April), 6–9, doi:10.1029/2004GL020175, 2004.

Grell, G. a., Peckham, S. E., Schmitz, R., McKeen, S. a., Frost, G., Skamarock, W. and Eder, B.: Fully coupled "online" chemistry within the WRF model, Atmos. Environ., 39, 6957–6975, doi:10.1016/j.atmosenv.2005.04.027, 2005.

Grell, G. A., Emeis, S., Stockwell, W. R., Schoenemeyer, T., Forkel, R., Michalakes, J., Knoche, R. and Seidl, W.: Application of a multiscale, coupled MM5/chemistry model to the complex terrain of the VOTALP valley campaign, Atmos. Environ., 34(9), 1435–1453, doi:10.1016/S1352-2310(99)00402-1, 2000.

Griggs, A. J., Davies, S. M., Abbott, P. M., Coleman, M., Palmer, A. P., Rasmussen, T. L. and Johnston, R.: Visualizing tephra deposits and sedimentary processes in the marine environment: The potential of X-ray microtomography, Geochemistry, Geophys. Geosystems, 16(12), 4329–4343, doi:10.1002/2015GC006073, 2015.

Gudmundsson, M. T., Thordarson, T., Höskuldsson, Á., Larsen, G., Björnsson, H., Prata, F. J., Oddsson, B.,

Magnússon, E., Högnadóttir, T., Petersen, G. N., Hayward, C. L., Stevenson, J. a. and Jónsdóttir, I.: Ash generation and distribution from the April-May 2010 eruption of Eyjafjallajökull, Iceland, Sci. Rep., 2, 1–12, doi:10.1038/srep00572, 2012.

Guffanti, M., Mayberry, G. C., Casadevall, T. and Wunderman, R.: Volcanic hazards to airports, Nat. Hazards, 51(2), 287–302, doi:10.1007/s11069-008-9254-2, 2009.

Han, J. and Pan, H.-L.: Revision of Convection and Vertical Diffusion Schemes in the NCEP Global Forecast System, Weather Forecast., 26(4), 520–533, doi:10.1175/WAF-D-10-05038.1, 2011.

Hasager, C. B., Birmili, W., Pappalardo, G. and Prata, F.: Atmospheric implications of the volcanic eruptions of Eyjafjallajökull, Iceland 2010, Spec. Issue, Atmos. Chem. Phys. [online] Available from: http://www.atmos-chem-phys.net/special issue212.html, 2010.

Haustein, K., Pérez, C., Baldasano, J. M., Jorba, O., Basart, S., Miller, R. L., Janjic, Z., Black, T., Nickovic, S., Todd, M. C., Washington, R., Müller, D., Tesche, M., Weinzierl, B., Esselborn, M. and Schladitz, a.: Atmospheric dust modeling from meso to global scales with the online NMMB/BSC-Dust model - Part 2: Experimental campaigns in Northern Africa, Atmos. Chem. Phys., 12, 2933–2958, doi:10.5194/acp-12-2933-2012, 2012.

Heiken, G.: Atlas of Volcanic Ash., 1974.

Heinold, B., Tegen, I., Wolke, R., Ansmann, A., Mattis, I., Minikin, A., Schumann, U. and Weinzierl, B.: Simulations of the 2010 Eyjafjallajökull volcanic ash dispersal over europe using COSMO-MUSCAT, Atmos. Environ., 48, 195–204, doi:10.1016/j.atmosenv.2011.05.021, 2012.

Heinrich, H.: Origin and consequences of cyclic ice rafting in the Northeast Atlantic Ocean during the past 130,000 years, Quat. Res., 29(2), 142–152, doi:10.1016/0033-5894(88)90057-9, 1988.

Herzog, M., Oberhuber, J. M. and Graf, H.-F. H.-F.: A Prognostic Turbulence Scheme for the Nonhydrostatic Plume Model ATHAM, J. Atmos. Sci., 60(22), 2783–2796 [online] Available from: http://dx.doi.org/10.1175/1520-0469(2003)060%3C2783:APTSFT%3E2.0.CO;2, 2003.

Hewett, T. A., Fay, J. A. and Hoult, D. P.: Laboratory experiments of smokestack plumes in a stable atmosphere, Atmos. Environ., 5(9), 767–789, doi:10.1016/0004-6981(71)90028-X, 1971.

Hurst, A. W.: Estimating Fallout ASHFALL – A Computer Program for Estimating Volcanic Ash Fallout Report and Users Guide., 1994.

Ibáñez, J. M., Almendros, J., Carmona, E., Martínez-Arévalo, C. and Abril, M.: The recent seismo-volcanic activity at Deception Island volcano, Deep. Res. Part II Top. Stud. Oceanogr., 50(10–11), 1611–1629, doi:10.1016/S0967-0645(03)00082-1, 2003.

Institute of Earth Sciences: Eruption in Eyjafjallajökull 2010, [online] Available from: http://earthice.hi.is/eruption_eyjafjallajokull_2010, 2010.

Iwasaki, T., Maki, T. and Katayama, K.: Tracer transport model at Japan meteorological agency and its application to the ETEX data, Atmos. Environ., 32(24), 4285–4295, doi:10.1016/S1352-2310(98)00171-X, 1998.

Janjic, Z.: Pressure gradient force and advection scheme used for forecasting with steep and small scale topography, Beiträge zur Phys. der Atmosphäre, 50(1), 186–199, 1977.

Janjic, Z.: Forward-backward scheme modified to prevent two-grid-interval noise and its application in sigma coordinate models, Contrib. Atmos. Phys, 52, 69–84, 1979.

Janjic, Z.: Nonlinear Advection Schemes and Energy Cascade on Semi-Staggered Grids, Mon. Weather Rev., 112, 1234–1245, doi:10.1175/1520-0493(1984)112<1234:NASAEC>2.0.CO;2, 1984.

Janjic, Z.: The Step-Mountain Coordinate: Physical Package, Mon. Weather Rev., 118(7), 1429–1443, doi:10.1175/1520-0493(1990)118<1429:TSMCPP>2.0.CO;2, 1990.

Janjic, Z.: The Step-Mountain Eta Coordinate Model: Further Developments of the Convection, Viscous Sublayer, and Turbulence Closure Schemes, Mon. Weather Rev., 122(5), 927–945, doi:10.1175/1520-0493(1994)122<0927:TSMECM>2.0.CO;2, 1994.

Janjic, Z.: The Mellor-Yamada level 2.5 turbulence closure scheme in the NCEP Eta Model, WORLD Meteorol. Organ. TD, 4–14, 1996.

Janjic, Z.: Nonsingular Implementation of the Mellor-Yamada Level 2.5 Scheme in the NCEP Meso model, Natl. Centers Environ. Predict., 61 [online] Available from:

http://www.emc.ncep.noaa.gov/officenotes/newernotes/on437.pdf, 2001.

Janjic, Z.: A nonhydrostatic model based on a new approach, Meteorol. Atmos. Phys., 82, 271–285, doi:10.1007/s00703-001-0587-6, 2003.

Janjic, Z.: A unified model approach from meso to global scales, in EGU General Assembly Conference Abstracts, vol. 7, European Geosciences Union 2005., 2005.

Janjic, Z.: Further development of the unified multiscale Eulerian model for a broad range of spatial and temporal scales within the new National Environmental Modeling System, in EGU General Assembly Conference Abstracts, vol. 11, p. 1587, EGU General Assembly 2009., 2009.

Janjic, Z. and Black, T.: An ESMF unified model for a broad range of spatial and temporal scales, in EGU General Assembly Conference Abstracts, vol. 9, European Geosciences Union., 2007.

Janjic, Z. and Gall, R.: Scientific documentation of the NCEP nonhydrostatic multiscale model on the B grid (NMMB). Part 1 Dynamics., NCAR Technical Note., 2012.

Janjic, Z., Gerrity, J. and Nickovic, S.: An Alternative Approach to Nonhydrostatic Modeling, Part III: Nonlinear Mountain Wave Test, World Meteorol. Organ. TD, 5–15, 2000.

Janjic, Z., Gerrity, J. and Nickovic, S.: An Alternative Approach to Nonhydrostatic Modeling, Mon. Weather Rev., 129(5), 1164–1178, doi:10.1175/1520-0493(2001)129<1164:AAATNM>2.0.CO;2, 2001.

Janjic, Z., Black, T., Rogers, E., Chuang, H. and DiMego, G.: The NCEP nonhydrostatic mesoscale forecasting model, in 10th Conference on Mesoscale Processes, Portland, OR, Amer. Meteor. Soc., 2003.

Janjic, Z., Huang, H. and Lu, S.: A unified atmospheric model suitable for studying transport of mineral aerosols from meso to global scales, IOP Conf. Ser. Earth Environ. Sci., 7, 12011, doi:10.1088/1755-1307/7/1/012011, 2009.

Janjic, Z., Janjic, T. and Vasic, R.: A Class of Conservative Fourth-Order Advection Schemes and Impact of Enhanced Formal Accuracy on Extended-Range Forecasts, Mon. Weather Rev., 139(1973), 1556–1568, doi:10.1175/2010MWR3448.1, 2011.

Jay, J., Costa, F., Pritchard, M., Lara, L., Singer, B. and Herrin, J.: Erratum to “Locating magma reservoirs using InSAR and petrology before and during the 2011-2012 Cordón Caulle silicic eruption,” Earth Planet. Sci. Lett., 395, 254–266, doi:10.1016/j.epsl.2014.07.021, 2014.

Jöckel, P., von Kuhlmann, R., Lawrence, M. G., Steil, B., Brenninkmeijer, C. M., Crutzen, P. J., Rasch, P. J. and Eaton, B.: On a fundamental problem in implementing flux-form advection schemes for tracer transport in 3-dimensional general circulation and chemistry transport models, Q. J. R. Meteorol. Soc., 127(September 2015), 1035–1052, doi:10.1002/qj.49712757318, 2001.

Johnson, C. G., Hogg, A. J., Huppert, H. E., Sparks, R. S. J., Phillips, J. C., Slim, A. C. and Woodhouse, M. J.: Modelling intrusions through quiescent and moving ambients, J. Fluid Mech., 771(May), 370–406, doi:10.1017/jfm.2015.180, 2015.

Jolliffe, I. T. and Stephenson, D. B.: Forecast Verification: A Practitioner’s Guide in Atmospheric Science, 2nd ed., John Wiley & Sons, Ltd, Chichester, UK., 2012.

Jones, A. R., Thomson, D. J., Hort, M. and Devenish, B. J.: The U.K. Met Office’s next-generation atmospheric dispersion model, NAME III, in Air Pollution Modeling and its Application XVII (Proceedings of the 27th NATO/CCMS International Technical Meeting on Air Pollution Modelling and its Application), edited by B. C. and N. A, pp. 580–589, Springer., 2007.

Jorba, O., Dabdub, D., Blaszczak-Boxe, C., Pérez, C., Janjic, Z., Baldasano, J. M., Spada, M., Badia, A. and Gonçalves, M.: Potential significance of photoexcited NO2 on global air quality with the NMMB/BSC chemical transport model, J. Geophys. Res., 117(August), doi:10.1029/2012JD017730, 2012.

Kalnay, E., Kanamitsu, M. and Baker, W. E.: Global Numerical Weather Prediction at the National Meteorological Center, Bull. Am. Meteorol. Soc., 71(3), 1410–1428, doi:10.1175/1520-0434(1989)004<0286:HONWPA>2.0.CO;2, 1990.

Kidder, S. and VonderHaar, T.: Satellite meteorology: an introduction, Academic Press, NY., 1995.

Koyaguchi, T. and Ohno, M.: Reconstruction of eruption column dynamics on the basis of grain size of tephra fall deposits: 1. Methods, J. Geophys. Res. Solid Earth, 106(B4), 6499–6512, doi:10.1029/2000JB900426, 2001.

Koyaguchi, T., Suzuki, Y. and Kozono, T.: Effects of the crater on eruption column dynamics, J. Geophys.

Res. Solid Earth, 115, 1–26, doi:10.1029/2009JB007146, 2010.

Langmann, B.: Numerical modelling of regional scale transport and photochemistry directly together with meteorological processes, Atmos. Environ., 34(21), 3585–3598, doi:10.1016/S1352-2310(00)00114-X, 2000.

Langmann, B.: Interactive numerical modeling of the atmospheric water cycle and volcanic ash aggregation, in 2nd IUGG-WMO workshop on Ash dispersal forecast and civil aviation, World Meteorological Organization., 2013.

Langmann, B., Folch, A., Hensch, M. and Matthias, V.: Volcanic ash over Europe during the eruption of Eyjafjallajökull on Iceland, April–May 2010, Atmos. Environ., 48, 1–8, doi:10.1016/j.atmosenv.2011.03.054, 2012.

Larson, J., Jacob, R. and Ong, E.: The Model Coupling Toolkit: A New Fortran90 Toolkit for Building Multiphysics Parallel Coupled Models, Int. J. High Perform. Comput. Appl. , 19(3), 277–292, doi:10.1177/1094342005056115, 2005.

Leadbetter, S. J., Hort, M. C., von Löwis, S., Weber, K. and Witham, C. S.: Modeling the resuspension of ash deposited during the eruption of Eyjafjallajökull in spring 2010, J. Geophys. Res. Atmos., 117(D20), doi:10.1029/2011JD016802, 2012.

Legg, B. J. and Raupach, M. R.: Markov-chain simulation of particle dispersion in inhomogeneous flows: The mean drift velocity induced by a gradient in Eulerian velocity variance, Boundary-Layer Meteorol., 24(1), 3–13, doi:10.1007/BF00121796, 1982.

Lin, J. C.: Lagrangian Modeling of the Atmosphre: An Introduction, in Lagrangian Modeling of the Atmosphere, pp. 1–11, American Geophysical Union., 2012.

Liu, E. J., Cashman, K. V., Beckett, F. M., Witham, C. S., Leadbetter, S. J., Hort, M. C. and Guðmundsson, S.: Ash mists and brown snow: Remobilization of volcanic ash from recent Icelandic eruptions, J. Geophys. Res. Atmos., 119(15), 9463–9480, doi:10.1002/2014JD021598, 2014.

Liu, E. J., Oliva, M., Antoniades, D., Giralt, S., Granados, I., Pla-Rabes, S., Toro, M. and Geyer, A.: Expanding the tephrostratigraphical framework for the South Shetland Islands, Antarctica, by combining compositional and textural tephra characterisation, Sediment. Geol., 340, 49–61, doi:10.1016/j.sedgeo.2015.08.002, 2016.

Lorenz, E. N.: Energy and numerical weather prediction, Tellus, 12, 364–373, 1960.

Macedonio, G., Costa, A. and Longo, A.: A computer model for volcanic ash fallout and assessment of subsequent hazard, Comput. Geosci., 31(7), 837–845, doi:10.1016/j.cageo.2005.01.013, 2005.

Macedonio, G., Costa, A. and Folch, A.: Uncertainties in volcanic plume modeling: A parametric study using FPLUME, J. Volcanol. Geotherm. Res., 326, 92–102, doi:10.1016/j.jvolgeores.2016.03.016, 2016.

Mackie, S., Cashman, K., Ricketts, H., Rust, A. and Watson, M.: Volcanic ash - Hazard observation, Elsevier., 2016.

Mailler, S., Menut, L., Khvorostyanov, D., Valari, M., Couvidat, F., Siour, G., Turquety, S., Briant, R., Tuccella, P., Bessagnet, B., Colette, A., Létinois, L. and Meleux, F.: CHIMERE-2016: From urban to hemispheric chemistry-transport modeling, Geosci. Model Dev. Discuss., (September), 1–41, doi:10.5194/gmd-2016-196, 2016.

Martet, M., Josse, M., Peuch, M. and Bonnardot, M.: MOCAGE-accident : From research to operational applications, in EMS Annual Meeting Abstracts, vol. 6, p. 2009., 2009.

Marti, A., Folch, A. and Jorba, O.: On-line coupling of volcanic ash with multiscale meteorological models: a case for 1991 Mt. Pinatubo, in IAVCEI 2013 Scientific Assembly, Kagoshima, Japan., 2013.

Marti, A., Folch, A. and Jorba, O.: On-line coupling of volcanic ash and aerosols transport with multi-scale meteorological models: a case for 2008 Chaitén eruption, in Cities on Volcanoes 8, Jakarta, Indonesia., 2014.

Marti, A., Folch, A., Costa, A. and Engwell, S. L.: A novel approach to reconstruct the plinian and co-ignimbrite phases of large eruptions - Campanian Ignimbrite, 2nd BSC Int. Dr. Symp., (May), 81–82, 2015.

Marti, A., Folch, A., Costa, A. and Engwell, S.: Reconstructing the plinian and co-ignimbrite sources of large volcanic eruptions: A novel approach for the Campanian Ignimbrite, Sci. Rep., 6, 21220,

doi:10.1038/srep21220, 2016.

Marti, A., Folch, A., Jorba, O. and Janjic, Z.: Volcanic ash modeling with the online NMMB-MONARCH-ASH v1.0 model: model description, case simulation, and evaluation, Atmos. Chem. Phys., 17(6), 4005–4030, doi:10.5194/acp-17-4005-2017, 2017.

Martí, J., Geyer, A. and Aguirre-Diaz, G.: Origin and evolution of the Deception Island caldera (South Shetland Islands, Antarctica), Bull. Volcanol., 75(6), 1–18, doi:10.1007/s00445-013-0732-3, 2013.

Mastin, L. G.: A user-friendly one-dimensional model for wet volcanic plumes, Geochemistry, Geophys. Geosystems, 8(3), doi:10.1029/2006GC001455, 2007.

Mastin, L. G.: Testing the accuracy of a 1-D volcanic plume model in estimating mass eruption rate, J. Geophys. Res. Atmos., 119(5), 2474–2495, doi:10.1002/2013JD020604, 2014.

Mastin, L. G., Guffanti, M., Servranckx, R., Webley, P., Barsotti, S., Dean, K., Durant, A., Ewert, J. W., Neri, A., Rose, W., Schneider, D., Siebert, L., Stunder, B., Swanson, G., Tupper, A., Volentik, A. and Waythomas, C. F.: A multidisciplinary effort to assign realistic source parameters to models of volcanic ash-cloud transport and dispersion during eruptions, J. Volcanol. Geotherm. Res., 186(1–2), 10–21, doi:10.1016/j.jvolgeores.2009.01.008, 2009.

Mastin, L. G., Schwaiger, H., Schneider, D., Wallace, K. L., Schaefer, J. and Denlinger, R. P.: Injection, transport, and deposition of tephra during event 5 at Redoubt Volcano, 23 March, 2009, J. Volcanol. Geotherm. Res., 259, 201–213, doi:10.1016/j.jvolgeores.2012.04.025, 2013.

Mastin, L. G., Van Eaton, A. and Lowenstern, J.: Modeling ash fall distribution from a Yellowstone supereruption, Geochemistry, Geophys. Geosystems, 15(8), 3459–3475, doi:10.1002/2014GC005469, 2014.

Mastin, L. G., Van Eaton, A. R. and Durant, A. J.: Adjusting particle-size distributions to account for aggregation in tephra-deposit model forecasts, Atmos. Chem. Phys., 16(14), 9399–9420, doi:10.5194/acp-16-9399-2016, 2016.

Matthias, V., Aulinger, A., Bieser, J., Cuesta, J., Geyer, B., Langmann, B., Serikov, I., Mattis, I., Minikin, A., Mona, L., Quante, M., Schumann, U. and Weinzierl, B.: The ash dispersion over Europe during the Eyjafjallajökull eruption - Comparison of CMAQ simulations to remote sensing and air-borne in-situ observations, Atmos. Environ., 48(April 2010), 184–194, doi:10.1016/j.atmosenv.2011.06.077, 2012.

McCormick, M. P., Thomason, L. W. and Trepte, C. R.: Atmospheric effects of the Mt Pinatubo eruption, Nature, 373(6513), 399–404 [online] Available from: http://dx.doi.org/10.1038/373399a0, 1995.

Mellor, G. L. and Yamada, T.: Development of a turbulence closure model for geophysical fluid problems, Rev. Geophys., 20(4), 851–875, doi:10.1029/RG020i004p00851, 1982.

Mesinger, F.: Forward-backward scheme, and its use in a limited area model., Beitr. Phys. Atmos., 50, 200–210, 1977.

Michalakes, J., Chen, S., Dudhia, J., Hart, L., Klemp, J., Middlecoff, J. and Skamarock, W.: Development of a Next Generation Regional Weather Research and Forecast Model, Proc. Ninth ECMWF Work. Use High Perform. Comput. Meteorol., 269–276, 2000.

Miller, T. P. and Casadevall, T. J.: Volcanic ash hazards to aviation in: Encyclopedia of Volcanoes, edited by H. Sigurdsson, Academic Press, Cambridge., 2000.

Mlawer, E., Taubman, S., Brown, P., Iacono, M. and Clough, S.: Radiative transfer for inhomogeneous atmospheres: RRTM, a validated correlated-k model for the longwave, J. Geophys. Res. Atmos., 102(D14), 16663–16682, doi:10.1029/97JD00237, 1997.

Mona, L. and Marenco, F.: Lidar Observations of Volcanic Particles, in Volcanic Ash, pp. 161–173, Elsevier., 2016.

Monin, A. S. and Obukhov, A. M.: Basic laws of turbulent mixing in the surface layer of the atmosphere, Contrib. Geophys. Inst. Acad. Sci. USSR, 24(151), 163–187, 1954.

Moreton, S. G. and Smellie, J. L.: Identification and correlation of distal tephra layers in deep-sea sediment cores, Scotia Sea, Antarctica, Ann. Glaciol., 27, 285–289, doi:DOI: 10.1017/S0260305500017596, 1998.

Morton, B. R., Taylor, G. and Turner, J. S.: Turbulent Gravitational Convection from Maintained and Instantaneous Sources, Proc. R. Soc. London A Math. Phys. Eng. Sci., 234(1196), 1–23, 1956.

Mosca, S., Graziani, G., Klug, W., Bellasio, R. and Bianconi, R.: A statistical methodology for the

evaluation of long-range dispersion models: an application to the ETEX exercise, Atmos. Environ., 32(24), 4307–4324, doi:10.1016/S1352-2310(98)00179-4, 1998.

Myhre, G., Shindell, D., Bréon, F. M., Collins, W., Fuglestvedt, J., Huang, J., Koch, D., Lamarque, J.-F., Lee, D., Mendoza, B., Nakajima, T., Robock, A., Stephens, G., Takemura, T. and Zhan, H.: 2013: Anthropogenic and Natural Radiative Forcing, Clim. Chang. 2013 Phys. Sci. Basis. Contrib. Work. Gr. I to Fifth Assess. Rep. Intergov. Panel Clim. Chang., 659–740, doi:10.1017/ CBO9781107415324.018, 2013.

Oberhuber, J., Herzog, M., Graf, H. . and Schwanke, K.: Volcanic plume simulation on large scales, J. Volcanol. Geotherm. Res., 87(1–4), 29–53, doi:10.1016/S0377-0273(98)00099-7, 1998.

Orheim, O.: A 200-year record of glacier mass balance at Deception Island, southwest Atlantic Ocean, and its bearing on models of global climatic change, Res. Found. Inst. Polar Stud. Ohio State Univ., (42), 118 [online] Available from: https://kb.osu.edu/dspace/handle/1811/51272, 1972.

Osores, M. S., Folch, A., Ruiz, J. and Collini, E.: Estimación de alturas de columna eruptiva a partir de imáges captadas por el sensor IMAGER del GOES-13, y su empleo para el pronóstico de dispersión y depóstio de cenizas volcánicas sobre Argentina, in XIX Congreso Geologico Argentino., 2014.

Osores, M. S., Collini, E., Mingari, L., Folch, A., Ruiz, L., Toyos, G., Pujol, G., Farias, C., Alexander, P., Suaya, M., Schonholz, T., Viramonte, J. G. and Villarosa, G.: Volcanic Ash Dispersion Modeling, Forecasting and Remote Sensing in Argentina. Recent and future developments, in IUGG - VW04 Remote Sensing and Modelling of Volcanic Ash in Latin America, International Union of Geodesy and Geophysics (IUGG), Czech Republic., 2015.

Oxford Economics: The economic impacts of air travel restrictions due to volcanic ash., 2010.

Pallàs, R., Smellie, J. L., Casas, J. M. and Calvet, J.: Using tephrochronology to date temperate ice: correlation between ice tephras on Livingston Island and eruptive units on Deception Island volcano (South Shetland Islands, Antarctica), The Holocene, 11(2), 149–160, doi:10.1191/095968301669281809, 2001.

Pan, H.-L. and Mahrt, L.: Interaction between soil hydrology and boundary-layer development, Boundary-Layer Meteorol., 38(1), 185–202, doi:10.1007/BF00121563, 1987.

Pappalardo, G., Mona, L., D'Amico, G., Wandinger, U., Adam, M., Amodeo, A., Ansmann, A., Apituley, A., Alados Arboledas, L., Balis, D., Boselli, A., Bravo-Aranda, J. A., Chaikovsky, A., Comeron, A., Cuesta, J., De Tomasi, F., Freudenthaler, V., Gausa, M., Giannakaki, E., Giehl, H., Giunta, A., Grigorov, I., Groß, S., Haeffelin, M., Hiebsch, A., Iarlori, M., Lange, D., Linné, H., Madonna, F., Mattis, I., Mamouri, R.-E., McAuliffe, M. A. P., Mitev, V., Molero, F., Navas-Guzman, F., Nicolae, D., Papayannis, A., Perrone, M. R., Pietras, C., Pietruczuk, A., Pisani, G., Preißler, J., Pujadas, M., Rizi, V., Ruth, A. A., Schmidt, J., Schnell, F., Seifert, P., Serikov, I., Sicard, M., Simeonov, V., Spinelli, N., Stebel, K., Tesche, M., Trickl, T., Wang, X., Wagner, F., Wiegner, M. and Wilson, K. M.: Four-dimensional distribution of the 2010 Eyjafjallajökull volcanic cloud over Europe observed by EARLINET, Atmos. Chem. Phys., 13(8), 4429–4450, doi:10.5194/acp-13-4429-2013, 2013.

Pappalardo, L., Ottolini, L. and Mastrolorenzo, G.: The Campanian Ignimbrite (southern Italy) geochemical zoning: Insight on the generation of a super-eruption from catastrophic differentiation and fast withdrawal, Contrib. to Mineral. Petrol., 156(4), 1–26, doi:10.1007/s00410-007-0270-0, 2008.

Pavolonis, M.: Volcanic Ash Algorithm Intercomparison (SCOPE-Nowcasting PP2). World Meteorological Society., 2016.

Pavolonis, M., Heidinger, A. and Sieglaff, J.: Automated retrievals of volcanic ash and dust cloud properties from upwelling infrared measurements, J. Geophys. Res. Atmos., 118(3), 1436–1458, doi:10.1002/jgrd.50173, 2013.

Pedrazzi, D., Aguirre-Díaz, G., Bartolini, S., Martí, J. and Geyer, A.: The 1970 eruption on Deception Island (Antarctica): eruptive dynamics and implications for volcanic hazards, J. Geol. Soc. , 171(6), 765–778, doi:10.1144/jgs2014-015, 2014.

Pérez, C., Haustein, K., Janjic, Z., Jorba, O., Huneeus, N., Baldasano, J. M., Black, T., Basart, S., Nickovic, S., Miller, R. L., Perlwitz, J. P., Schulz, M. and Thomson, M. J.: Atmospheric dust modeling from meso to global scales with the online NMMB/BSC-Dust model; Part 1: Model description, annual simulations and evaluation, Atmos. Chem. Phys., 11, 13001–13027, doi:10.5194/acp-11-13001-2011, 2011.

Perrotta, A. and Scarpati, C.: Volume partition between the plinian and co-ignimbrite air fall deposits of the Campanian Ignimbrite eruption, Mineral. Petrol., 79, 67–78, doi:10.1007/s00710-003-0002-8, 2003.

Pfeiffer, T., Costa, A. and Macedonio, G.: A model for the numerical simulation of tephra fall deposits, J. Volcanol. Geotherm. Res., 140, 273–294, doi:10.1016/j.jvolgeores.2004.09.001, 2005.

Pfitsch, W. A. and Bliss, L. C.: Recovery of net primary production in subalpine meadows of Mount St. Helens following the 1980 eruption, Can. J. Bot., 66(5), 989–997, doi:10.1139/b88-142, 1988.

Pielke, R. a, Cotton, W. R., Walko, R. L., Tremback, C. J., Lyons, W. a, Grasso, L. D., Nicholls, M. E., Moran, M. D., Wesley, D. a, Lee, T. J. and Copeland, J. H.: A comprehensive meteorological modeling system-RAMS, Meteor. Atmos. Phys., 91(49), 69–91, 1992.

Pistolesi, M., Cioni, R., Bonadonna, C., Elissondo, M., Baumann, V., Bertagnini, A., Chiari, L. and Gonzales, R.: Complex dynamics of small-moderate volcanic events : the example of the 2011 rhyolitic Cordón Caulle eruption , Chile, Bull. Volcanol., 77(3), doi:10.1007/s00445-014-0898-3, 2015.

Pouget, S., Bursik, M., Johnson, C. G., Hogg, A. J., Phillips, J. C. and Sparks, R. S. J.: Interpretation of umbrella cloud growth and morphology: implications for flow regimes of short-lived and long-lived eruptions, Bull. Volcanol., 78(1), 1–19, doi:10.1007/s00445-015-0993-0, 2016a.

Pouget, S., Bursik, M., Singla, P. and Singh, T.: Sensitivity analysis of a one-dimensional model of a volcanic plume with particle fallout and collapse behavior, J. Volcanol. Geotherm. Res., doi:10.1016/j.jvolgeores.2016.02.018, 2016b.

Prata, A. J.: Infrared radiative transfer calculations for volcanic ash clouds, Geophys. Res. Lett., 16(11), 1293–1296, doi:10.1029/GL016i011p01293, 1989a.

Prata, A. J.: Observations of volcanic ash clouds in the 10-12 μm window using AVHRR/2 data, Int. J. Remote Sens., 10(4–5), 751–761, doi:10.1080/01431168908903916, 1989b.

Prata, A. J.: Volcanic information derived from satellite data: Algorithm Theoretical Basis Document I., 2011.

Prata, A. J. and Bernardo, C.: Retrieval of sulfur dioxide from a ground-based thermal infrared imaging camera, Atmos. Meas. Tech., 7(9), 2807–2828, doi:10.5194/amt-7-2807-2014, 2014.

Prata, A. J. and Prata, A. T.: Eyjafjallajökull volcanic ash concentrations determined using Spin Enhanced Visible and Infrared Imager measurements, J. Geophys. Res. Atmos., 117(6), 1–24, doi:10.1029/2011JD016800, 2012.

Prata, F., Woodhouse, M., Huppert, H. E., Prata, A., Thordarson, T. and Carn, S.: Atmospheric processes affecting the separation of volcanic ash and SO₂ in volcanic eruptions: Inferences from the May 2011 Grímsvötn eruption, Atmos. Chem. Phys. Discuss., (February), 1–34, doi:10.5194/acp-2017-95, 2017.

Pyle, D.: The thickness, volume and grainsize of tephra fall deposits, Bull. Volcanol., 51(1), 1–15, doi:10.1007/BF01086757, 1989.

Pyle, D., Ricketts, G., Margari, V., Van Andel, T., Sinitsyn, A., Praslov, N. and Lisitsyn, S.: Wide dispersal and deposition of distal tephra during the Pleistocene “Campanian Ignimbrite/Y5” eruption, Italy, Quat. Sci. Rev., 25(21–22), 2713–2728, doi:10.1016/j.quascirev.2006.06.008, 2006.

Raga, G. B., Baumgardner, D., Ulke, a. G., Torres Brizuela, M. and Kucienska, B.: The environmental impact of the Puyehue-Cordon Caulle 2011 volcanic eruption on Buenos Aires, Nat. Hazards Earth Syst. Sci., 13, 2319–2330, doi:10.5194/nhess-13-2319-2013, 2013.

Rampino, M. R., Self, S. and Stothers, R.: Volcanic Winters, Annu. Rev. Earth Planet. Sci., 16(1), 73–99, doi:10.1146/annurev.ea.16.050188.000445, 1988.

Reckziegel, F., Bustos, E., Mingari, L., Báez, W., Villarosa, G., Folch, A., Collini, E., Viramonte, J., Romero, J. and Osores, M. S.: Forecasting volcanic ash dispersal and coeval resuspension during the April–May 2015 Calbuco eruption, J. Volcanol. Geotherm. Res., 321, 44–57, doi:http://dx.doi.org/10.1016/j.jvolgeores.2016.04.033, 2016.

Renner, E. and Wolke, R.: Modelling the formation and atmospheric transport of secondary inorganic aerosols with special attention to regions with high ammonia emissions, Atmos. Environ., 44(15), 1904–1912, doi:10.1016/j.atmosenv.2010.02.018, 2010.

Rieger, D., Bangert, M., Bischoff-Gauss, I., Förstner, J., Lundgren, K., Reinert, D., Schröter, J., Vogel, H.,

Zängl, G., Ruhnke, R. and Vogel, B.: ICON–ART 1.0 – a new online-coupled model system from the global to regional scale, Geosci. Model Dev., 8(6), 1659–1676, doi:10.5194/gmd-8-1659-2015, 2015.

Robock, A.: Volcanoes: Role in climate, edited by J. J. Holton, A. Curry, and J. Pyle, Academic Press, London., 2003.

Roobol, M. J.: The volcanic hazard at Deception Island, South Shetland Islands, Br. Antarct. Surv. Bull., 51, 237–245, 1982.

Rood, R. B.: Numerical advection algorithms and their role in atmospheric transport and chemistry models, Rev. Geophys., 25(1), 71–100, doi:10.1029/RG025i001p00071, 1987.

Rose, W. and Durant, A.: Fine ash content of explosive eruptions, J. Volcanol. Geotherm. Res., 186(1–2), 32–39, doi:10.1016/j.jvolgeores.2009.01.010, 2009.

Rosi, M. and Vezzoli, L.: Plinian pumice fall deposit of the Campanian Ignimbrite eruption (Phlegrean Fields, Italy), J. Volcanol. Geotherm. Res., 91, 179–198, 1999.

Russell, A. and Dennis, R.: NARSTO critical review of photochemical models and modeling, Atmos. Environ., 34(12–14), 2283–2324, doi:10.1016/S1352-2310(99)00468-9, 2000.

Savre, J., Percival, J. R., Herzog, M. and Pain, C.: Two-Dimensional Evaluation of ATHAM-Fluidity, a Nonhydrostatic Atmospheric Model Using Mixed Continuous/Discontinuous Finite Elements and Anisotropic Grid Optimization, Mon. Weather Rev., 144(11), 4349–4372, doi:10.1175/MWR-D-15-0398.1, 2016.

Scaillet, B., Luhr, J. and Carroll, M.: Petrological and Volcanological Constraints on Volcanic Sulfur Emissions to the Atmosphere, edited by A. Robock and C. Oppenheimer, Volcanism Earth's Atmos., 11–40, 2004.

Scaini, C., Folch, A. and Navarro, M.: Tephra hazard assessment at Concepcion Volcano, Nicaragua, J. Volcanol. Geotherm. Res., 219–220, 41–51, doi:10.1016/j.jvolgeores.2012.01.007, 2012.

Schmid, R.: Descriptive nomenclature and classification of pyroclastic deposits and fragments, Geol. Rundschau, 70(2), 794–799, doi:10.1007/BF01822152, 1981.

Schmidt, A., Fristad, K. and Elkins-Tanton, L.: Volcanism and Global Environmental Change, edited by A. Schmidt, K. Fristad, and L. Elkins-Tanton, Cambridge University Press., 2015.

Schumann, U., Weinzierl, B., Reitebuch, O., Schlager, H., Minikin, A., Forster, C., Baumann, R., Sailer, T., Graf, K., Mannstein, H., Voigt, C., Rahm, S., Simmet, R., Scheibe, M., Lichtenstern, M., Stock, P., Rüba, H., Schäuble, D., Tafferner, A., Rautenhaus, M., Gerz, T., Ziereis, H., Krautstrunk, M., Mallaun, C., Gayet, J. F., Lieke, K., Kandler, K., Ebert, M., Weinbruch, S., Stohl, A., Gasteiger, J., Gro, S., Freudenthaler, V., Wiegner, M., Ansmann, A., Tesche, M., Olafsson, H. and Sturm, K.: Airborne observations of the Eyjafjalla volcano ash cloud over Europe during air space closure in April and May 2010, Atmos. Chem. Phys., 11(5), 2245–2279, doi:10.5194/acp-11-2245-2011, 2011.

Schwaiger, H., Denlinger, R. P. and Mastin, L. G.: Ash3d: A finite-volume, conservative numerical model for ash transport and tephra deposition, J. Geophys. Res. Solid Earth, 117(4), 1–20, doi:10.1029/2011JB008968, 2012.

Scollo, S., Del Carlo, P. and Coltelli, M.: Tephra fallout of 2001 Etna flank eruption: Analysis of the deposit and plume dispersion, J. Volcanol. Geotherm. Res., 160(1–2), 147–164, doi:10.1016/j.jvolgeores.2006.09.007, 2007.

Scollo, S., Tarantola, S., Bonadonna, C., Coltelli, M. and Saltelli, A.: Sensitivity analysis and uncertainty estimation for tephra dispersal models, J. Geophys. Res. Solid Earth, 113, 1–17, doi:10.1029/2007JB004864, 2008.

Scollo, S., Kahn, R. A., Nelson, D. L., Coltelli, M., Diner, D. J., Garay, M. J. and Realmuto, V. J.: MISR observations of Etna volcanic plumes, J. Geophys. Res. Atmos., 117(6), 1–13, doi:10.1029/2011JD016625, 2012.

Searcy, C., Dean, K. and Stringer, W.: PUFF: A high-resolution volcanic ash tracking model, J. Volcanol. Geotherm. Res., 80(1–2), 1–16, doi:10.1016/S0377-0273(97)00037-1, 1998.

Self, S.: Magma volume, volatile emissions, and stratospheric aerosols from the 1815 eruption of Tambora, Geophys. Res. Lett., 31(20), L20608, doi:10.1029/2004GL020925, 2004.

Self, S.: The effects and consequences of very large explosive volcanic eruptions., Philos. Trans. A. Math.

Phys. Eng. Sci., 364(June), 2073–2097, doi:10.1098/rsta.2006.1814, 2006.

Signorelli, S., Vaggelli, G., Romano, C. and Carroll, M.: Volatile element zonation in Campanian Ignimbrite magmas (Phlegrean Fields, Italy): evidence from the study of glass inclusions and matrix glasses, Contrib. to Mineral. Petrol., 140, 543–553, doi:10.1007/s004100000213, 2001.

Simmons, a. J. and Burridge, D. M.: An Energy and Angular-Momentum Conserving Vertical Finite-Difference Scheme and Hybrid Vertical Coordinates, Mon. Weather Rev., 109, 758–766, doi:10.1175/1520-0493, 1981.

Skamarock, W. C., Klemp, J. B., Dudhi, J., Gill, D. O., Barker, D. M., Duda, M. G., Huang, X.-Y., Wang, W. and Powers, J. G.: A Description of the Advanced Research WRF Version 3, Tech. Rep., (June), 113, doi:10.5065/D6DZ069T, 2008.

Smellie, J. L.: The upper Cenozoic tephra record in the south polar region: a review, Glob. Planet. Change, 21(1–3), 51–70, doi:10.1016/S0921-8181(99)00007-7, 1999.

Smellie, J. L.: The 1969 subglacial eruption on Deception Island (Antarctica): events and processes during an eruption beneath a thin glacier and implications for volcanic hazards, Geol. Soc. London, Spec. Publ. , 202(1), 59–79, doi:10.1144/GSL.SP.2002.202.01.04, 2002.

Smith, T. A., Campbell, T. J., Allard, R. A. and Carroll, S. N.: User's Guide for the Coupled Ocean/Atmospheric Mesoscale Prediction System (COAMPS) Version 5.0., 2012.

Sommer, B.: Ash Cloud from Chilean volcano entering New Zealand Airspace, Civ. Aviat. Auth. New Zeal. [online] Available from: https://www.caa.govt.nz/publicinfo/med_rel_Ash_Cloud.htm, 2011.

Spada, M., Jorba, O., Pérez, C., Janjic, Z. and Baldasano, J. M.: Modeling and evaluation of the global sea-salt aerosol distribution: Sensitivity to emission schemes and resolution effects at coastal/orographic sites, Atmos. Chem. Phys., 13, 11735–11755, doi:10.5194/acp-13-11735-2013, 2013.

Spada, M., Jorba, O., Pérez, C., Janjic, Z. and Baldasano, J. M.: On the evaluation of global sea-salt aerosol models at coastal/orographic sites, Atmos. Environ., 101, 41–48, doi:10.1016/j.atmosenv.2014.11.019, 2015.

Sparks, R. S. J.: The dimensions and dynamics of volcanic eruption columns, Bull. Volcanol., 48(1), 3–15, doi:10.1007/BF01073509, 1986.

Sparks, R. S. J. and Huang, T. C.: The volcanological significance of deep-sea ash layers associated with ignimbrites, Geol. Mag., 117(5), 425–436, 1980.

Sparks, R. S. J. and Walker, G. P. L.: The significance of vitric-enriched air-fall ashes associated with crystal-enriched ignimbrites, J. Volcanol. Geotherm. Res., 2(4), 329–341, 1977.

Sparks, R. S. J., Wilson, L. and Hulme, G.: Theoretical modeling of the generation, movement, and emplacement of pyroclastic flows by column collapse, J. Geophys. Res. Solid Earth, 83(B4), 1727–1739, doi:10.1029/JB083iB04p01727, 1978.

Sparks, R. S. J., Bursik, M., Ablay, G. J., Thomas, R. M. E. and Carey, S.: Sedimentation of tephra by volcanic plumes. Part 2: controls on thickness and grain-size variations of tephra fall deposits, Bull. Volcanol., 54(8), 685–695, doi:10.1007/BF00430779, 1992.

Sparks, R. S. J., Bursik, M., Carey, S., Gilbert, J., Glaze, L., Sigurdsson, H. and Woods, A.: Volcanic Plumes, 1 edition., John Wiley, Chichester, U.K., 1997.

Sparks, R. S. J., Self, S., Grattan, J., Oppenheimer, C., Pyle, D. and Rymer, H.: Super-eruptions: Global Effects and Future Threats: Report of a Geological Society of London working group., 2005.

Stein, A. F., Draxler, R. R., Rolph, G. D., Stunder, B., Cohen, M. D. and Ngan, F.: NOAA's HYSPLIT atmospheric transport and dispersion modeling system, Bull. Am. Meteorol. Soc., (February), 150504130527006, doi:10.1175/BAMS-D-14-00110.1, 2015.

Stohl, A., Forster, C., Frank, A., Seibert, P. and Wotawa, G.: Technical note: The Lagrangian particle dispersion model FLEXPART version 6.2, Atmos. Chem. Phys., 5(9), 2461–2474, doi:10.5194/acp-5-2461-2005, 2005.

Stohl, A., Prata, A. J., Eckhardt, S., Clarisse, L., Durant, A., Henne, S., Kristiansen, N. I., Minikin, A., Schumann, U., Seibert, P., Stebel, K., Thomas, H. E., Thorsteinsson, T., Torseth, K. and Weinzierl, B.: Determination of time-and height-resolved volcanic ash emissions and their use for quantitative ash dispersion modeling: The 2010 Eyjafjallajökull eruption, Atmos. Chem. Phys., 11(9), 4333–4351,

doi:10.5194/acp-11-4333-2011, 2011.

Stuefer, M., Freitas, S. R., Grell, G., Webley, P., Peckham, S. and McKeen, S. a.: Inclusion of Ash and SO2 emissions from volcanic eruptions in WRF-CHEM: development and some applications, Geosci. Model Dev., 5, 2571–2597, doi:10.5194/gmdd-5-2571-2012, 2013.

Sulpizio, R., Folch, A., Costa, A., Scaini, C. and Dellino, P.: Hazard assessment of far-range volcanic ash dispersal from a violent Strombolian eruption at Somma-Vesuvius volcano, Naples, Italy: Implications on civil aviation, Bull. Volcanol., 74(9), 2205–2218, doi:10.1007/s00445-012-0656-3, 2012.

Suzuki, T.: A theoretical model for dispersion of tephra, in In Arc Volcanism: Physics and Tectonics, pp. 93–113, Terra Scientific Publishing Company, Tokyo., 1983.

Suzuki, Y.: A numerical study of turbulent mixing in eruption clouds using a three-dimensional fluid dynamics model, J. Geophys. Res., 110(B8), 201, doi:10.1029/2004JB003460, 2005.

Suzuki, Y. and Koyaguchi, T.: A three-dimensional numerical simulation of spreading umbrella clouds, J. Geophys. Res., 114, 1–18, doi:10.1029/2007JB005369, 2009.

Suzuki, Y. J., Costa, A., Cerminara, M., Esposti Ongaro, T., Herzog, M., Van Eaton, A. R. and Denby, L. C.: Inter-comparison of three-dimensional models of volcanic plumes, J. Volcanol. Geotherm. Res., 326, 26–42, doi:10.1016/j.jvolgeores.2016.06.011, 2016.

Thorarinsson, S.: Tephrochronological studies in Iceland, Geogr. Ann., 26, 1–217, doi:10.2307/519916, 1944.

Timmreck, C., Graf, H., Lorenz, S., Niemeier, U., Zanchettin, D., Matei, D., Jungclaus, J. and Crowley, T.: Aerosol size confines climate response to volcanic super-eruptions, Geophys. Res. Lett., 37(September), 1–5, doi:10.1029/2010GL045464, 2010.

Torrecillas, C., Berrocoso, M. and García-García, A.: The Multidisciplinary Scientific Information Support System (SIMAC) for Deception Island, in Antarctica: Contributions to Global Earth Sciences, edited by D. K. Fütterer, D. Damaske, G. Kleinschmidt, H. Miller, and F. Tessensohn, pp. 397–402, Springer Berlin Heidelberg, Berlin, Heidelberg., 2006.

Toyos, G., Mingari, L., Pujol, G. and Villarosa, G.: Investigating the nature of an ash cloud event in Southern Chile using remote sensing: volcanic eruption or resuspension?, Remote Sens. Lett., 8(2), 146–155, doi:10.1080/2150704X.2016.1239281, 2017.

Turner, J. S.: Buoyancy Effects in Fluids, Cambridge University Press., 1973.

Ulke, A. G., Torres Brizuela, M. M., Raga, G. B. and Baumgardner, D.: Aerosol properties and meteorological conditions in the city of Buenos Aires, Argentina, during the resuspension of volcanic ash from the Puyehue-Cordón Caulle eruption, Nat. Hazards Earth Syst. Sci., 16(9), 2159–2175, doi:10.5194/nhess-16-2159-2016, 2016.

De Vivo, B., Rolandi, G., Gans, P. B., Calvert, A., Bohrson, W., Spera, F. J. and Belkin, H.: New constraints on the pyroclastic eruptive history of the Campanian volcanic Plain (Italy), Mineral. Petrol., 73, 47–65, doi:10.1007/s007100170010, 2001.

Vukovic, A., Rajkovic, B. and Janjic, Z.: Land Ice Sea Surface Model: Short Description and Verification, in 2010 International Congress on Environmental Modelling and Software Modelling for Environment's Sake, Fifth Biennial Meeting, Ottawa, Canada, 5–8 July 2010., 2010.

Webster, H. N., Thomson, D. J., Johnson, B. T., Heard, I. P. C., Turnbull, K., Marenco, F., Kristiansen, N. I., Dorsey, J., Minikin, A., Weinzierl, B., Schumann, U., Sparks, R. S. J., Loughlin, S. C., Hort, M. C., Leadbetter, S. J., Devenish, B. J., Manning, A. J., Witham, C. S., Haywood, J. M. and Golding, B. W.: Operational prediction of ash concentrations in the distal volcanic cloud from the 2010 Eyjafjallajökull eruption, J. Geophys. Res. Atmos., 117(2), 1–17, doi:10.1029/2011JD016790, 2012.

Wernli, H., Paulat, M., Hagen, M. and Frei, C.: SAL—A Novel Quality Measure for the Verification of Quantitative Precipitation Forecasts, Mon. Weather Rev., 136(11), 4470–4487, doi:10.1175/2008MWR2415.1, 2008.

Wessel, P. and Smith, W. H. F.: Free software helps map and display data, Eos, Trans. Am. Geophys. Union, 72(41), 441–441, doi:10.1029/90EO00319, 1991.

Wilkins, K. L., Watson, I. M., Kristiansen, N. I., Webster, H. N., Thomson, D. J., Dacre, H. F. and Prata, A. J.: Using data insertion with the NAME model to simulate the 8 May 2010 Eyjafjallajökull volcanic ash

cloud, J. Geophys. Res. Atmos., 121(1), 306–323, doi:10.1002/2015JD023895, 2016.

Wilson, C. J. N.: Supereruptions and Supervolcanoes: Processes and Products, Elements, 4(1), 29–34, doi:10.2113/GSELEMENTS.4.1.29, 2008.

Wilson, L.: Explosive Volcanic Eruptions—III. Plinian Eruption Columns, Geophys. J. R. Astron. Soc., 45(3), 543–556, doi:10.1111/j.1365-246X.1976.tb06909.x, 1976.

Wilson, L. and Huang, T. C.: The influence of shape on the atmospheric settling velocity of volcanic ash particles, Earth Planet. Sci. Lett., 44(2), 311–324, doi:10.1016/0012-821X(79)90179-1, 1979.

Wilson, L. and Walker, G. P. L.: Explosive volcanic eruptions - VI. Ejecta dispersal in plinian eruptions: the control of eruption conditions and atmospheric properties, Geophys. J. R. Astron. Soc., 89(2), 657–679, doi:10.1111/j.1365-246X.1987.tb05186.x, 1987.

Wilson, T., Stewart, C., Bickerton, H., Baxter, P., Outes, V., Villarosa, G. and Rovere, E.: Impacts of the June 2011 Puyehue-Cordón Caulle volcanic complex eruption on urban infrastructure, agriculture and public health., 2013.

Witham, C. S., Hort, M. C., Potts, R., Servranckx, R., Husson, P. and Bonnardot, F.: Comparison of VAAC atmospheric dispersion models using the 1 November 2004 Grimsvötn eruption, Meteorol. Appl., 14(1), 27–38, doi:10.1002/met.3, 2007.

Woodhouse, M., Hogg, a. J., Phillips, J. C. and Sparks, R. S. J.: Interaction between volcanic plumes and wind during the 2010 Eyjafjallajökull eruption, Iceland, J. Geophys. Res. Solid Earth, 118, 92–109, doi:10.1029/2012JB009592, 2013.

Woods, A.: The fluid dynamics and thermodynamics of eruption columns, Bull. Volcanol., 50(3), 169–193, doi:10.1007/BF01079681, 1988.

Woods, A. and Wohletz, K.: Dimensions and dynamics of co-ignimbrite eruption columns, Nature, 354, 56–58, 1991.

Zhang, L., Gong, S., Padro, J. and Barrie, L.: A size-segregated particle dry deposition scheme for an atmospheric aerosol module, Atmos. Environ., 35, 549–560, doi:10.1016/S1352-2310(00)00326-5, 2001.

Zhang, Y.: Online-coupled meteorology and chemistry models: history, current status, and outlook, Atmos. Chem. Phys., 8, 2895–2932, doi:10.5194/acp-8-2895-2008, 2008.

Zhu, L., Li, J., Zhao, Y., Gong, H. and Li, W.: Retrieval of volcanic ash height from satellite-based infrared measurements, J. Geophys. Res. Atmos., doi:10.1002/2016JD026263, 2017.

Zielinski, G., Mayewski, P. A., Meeker, L. D., Whitlow, S. and Twickler, M. S.: A 110,000-Yr Record of Explosive Volcanism from the GISP2 (Greenland) Ice Core, Quat. Res., 45(45), 109–118, doi:10.1006/qres.1996.0013, 1996.

Zilhão, J.: The Ebro Frontier : A Model for the Late Extinction of Iberian Neanderthals, Neanderthals edge150th Anniv. Conf. Forbes' Quarr. Discov. Gibraltar, (1977), 111–121, doi:10.1109/ICELMACH.2008.4800248, 2000.

Zilhão, J.: Neandertals and moderns mixed, and it matters, Evol. Anthropol., 15, 183–195, doi:10.1002/evan.20110, 2006.

Zilitinkevich, S.: Bulk characteristics of turbulence in the atmospheric planetary boundary layer, Tr. GGO, 167, 49–52, 1965a.

Zilitinkevich, S.: Vertical turbulent exchange in the atmospheric surface layer (Vertical turbulent mixing in surface layer of atmosphere for equilibrium and nonequilibrium stratified flow), Tr. GGO, 167, 49–52, 1965b.